ROYAUME DU MAROC
Université Mohammed V - RABAT -
جامعة محمد الخامس – الرباط –
Faculté des sciences
كلية العلوم
CENTRE D'ETUDES DOCTORALES - SCIENCES ET TECHNOLOGIES

N° d'ordre : 3748

# THESE

En vue de l'obtention du : **DOCTORAT**

**Structure de Recherche** : Équipe de Sciences de la Matière et du Rayonnements
**Discipline** : Physique
**Spécialité** : Physique des Hautes Énergies

*Présentée et soutenue le 19/01/2023 par :*

**Hassnae EL JARRARI**

## Dark Photon Searches from Higgs Boson and Heavy Boson Decays Using *pp* Collisions Recorded at 13 TeV with the ATLAS Detector at the LHC and Performance Evaluation of the Low Gain Avalanche Detectors for the HL-LHC ATLAS High-Granularity Timing Detector

*Jury de thèse composé de:*

| | | |
|---|---|---|
| *Peter JENNI* | *PES, Albert-Ludwigs-Universität Freiburg, Germany* | *Président* |
| *Rachid AHL LAAMARA* | *PH, Université Mohammed V, Faculté des Sciences, Rabat* | *Rapporteur/Examinateur* |
| *Nour-eddine FETTOUHI* | *PES, Université Mohammed V, Faculté des Sciences, Rabat* | *Rapporteur/Examinateur* |
| *Abdelilah MOUSSA* | *PES, Université Mohammed I, Faculté des Sciences, Oujda* | *Rapporteur/Examinateur* |
| *Rajaa CHERKAOUI EL MOURSLI* | *PES, Université Mohammed V, Faculté des Sciences, Rabat* | *Examinateur* |
| *Andreas HOECKER* | *PES, Conseil Européen pour la Recherche Nucléaire, Suisse* | *Examinateur* |
| *Rachid MAZINI* | *PES, Académie des sciences de Taiwan* | *Co-Encadrant* |
| *Yahya TAYALATI* | *PES, Université Mohammed V, Faculté des Sciences, Rabat* | *Directeur de thèse* |

Année Universitaire : 2022/2023

*To my parents, my sister and my brothers*
*for their endless love, encouragements and support*

*To my former teachers and supervisors*
*My friends and colleagues*

*To every curious mind*
*Knowledge has no limit*

# *Acknowledgements*

This thesis has been an immense and challenging six years journey full of incredibly enriching experiences. There are certainly people who were responsible for making it such a special adventure that I would like to take the opportunity to sincerely thank in this section. First and foremost, I would like to thank my supervisor Prof. **Yahya Tayalati** (PES, Faculté des Sciences, Rabat) for offering me the opportunity to pursue a PhD at Mohammed V University on the ATLAS experiment at the LHC. I'm so grateful for the time he dedicated to set me on my path and for his careful guidance, encouragement and precious advice along the way.

I would also wish to express my gratitude, appreciation and thanks to my co-supervisor Prof. **Rachid Mazini** (PES, Académie des sciences de Taiwan), who took care in introducing me to the physics analysis techniques and encouraged me to get involved in detector hardware development and operations. He guided my progress with his great knowledge and support. It was always an enriching experience to discuss with him my progress and to have brilliant conversations about physics and beyond.

I should highlight the unique opportunity of being the recipient of the ATLAS PhD Grant that allowed me to be based at CERN for the period of 2020-2021. I am extremely grateful to the former ATLAS collaboration spokesperson Prof. **Peter Jenni** (PES, Albert-Ludwigs-Universität Freiburg) and the CERN director-general Prof. Fabiola Gianotti (PES, CERN) for establishing this grant from their award funds. I would like to thank Prof. **Peter Jenni** again for always checking on me, especially during the COVID pandemic. I was always happy to receive his friendly greetings and advice about my ongoing work. I would also like to thank him for the honour of accepting to be the president of my thesis jury.

Thank you to my manuscript committee, Prof. **Rachid Ahl Laamara** (PH, Faculté des Sciences, Rabat), Prof. **Nour-Eddine Fettouhi** (PES, Faculté des Sciences, Rabat) and Prof. **Abedlillah Moussa** (PH, Faculté des Sciences, Oujda) for offering their time to review my thesis, for their careful reading and helpful comments. I would also like to thank Prof. **Rajaa Cherkaoui El Moursli** for accepting to be the examiner of my thesis.

I would like to express my sincere gratitude to the ATLAS collaboration Spokesperson Prof. **Andreas Hoecker** (PES, CERN), for financing my stay at CERN for three months in 2022 and for accepting to be the examiner and attend my thesis defence in person.

I'd also like to thank my technical supervisor and my advisor during my qualification in the TRT group, Prof. **Fred Luehring** (PES, Indiana University) and Dr. **Philippe Calfayan** (Indiana University) for helping me learn more about the TRT and the reconstruction software. Along the way, I had the great opportunity to join the STEP program at the ICTP with Prof. **Bobby Acharya** (PES, King's College London) with whom I was able to start my stay at CERN for a more enlightening working environment.

I would like to thank the whole ATLAS collaboration, all the directors, organizers and lecturers of the different summer schools I attended, in Namibia, Pakistan, Jefferson Lab and Brookhaven National Lab in the USA, ESIPAP in France and ICFA in India. Thank you to all my ESMAR colleagues in Rabat and my colleagues from summer schools and from CERN for all the interesting discussions we had. I would like to thank Prof. **Bengt LUND-JENSEN** (PES, KTH Royal Institute of Technology in Stockholm) for supporting the ATLAS Moroccan group through the Swedish Research Council, we are grateful for their generous funding. I am especially grateful to my family and friends for their support throughout my PhD studies. I thank you all.

# *Abstract*

This PhD thesis includes two main topics, the first one is related to the search for dark photons. Two different searches were performed at a centre-of-mass energy of $\sqrt{s} = 13$ TeV using the LHC Run-2 integrated luminosity of 139 fb$^{-1}$ recorded by the ATLAS detector, the first search concerns dark photons from the SM Higgs boson decay, produced together with a $Z$ boson, this search resulted in setting the best experimental limit corresponding to an observe (expected) upper limit on the $BR(H \to \gamma\gamma_d)$ of 2.28% (2.82%) set at 95% confidence level (CL). To broaden the exploration of this predicted dark matter particle, a second search was carried out considering some heavy Higgs bosons with masses ranging from 400 GeV to 3 TeV, produced either in gluon-gluon Fusion (ggF) or in Vector-Boson-Fusion (VBF) modes. The exclusion limits at 95% CL on the $\sigma \times BR(H \to \gamma\gamma_d)$ for the combined ggF+VBF productions are found to be in the range from [1.44,24.2]fb ([1.68,28.1]fb) observed (expected) respectively. The second main topic concerns a new timing detector called the High Granularity Timing Detector that will be installed in the ATLAS detector to mitigate pile-up effects during the High Luminosity upgrade of the LHC. LGAD sensors from different vendors have been measured in beam test campaigns during the years 2018 and 2019 at CERN and DESY. The results obtained in terms of the collected charge, time resolution, hit efficiency as well as the charge uniformity as a function of the position of the incident particle inside the sensor pad are included.

**Keywords:** CERN, LHC, ATLAS, Higgs boson, dark photon, ggF, VBF, HGTD, LGAD.

# *Résumé*

Cette thèse de doctorat porte sur la recherche de photons sombres. Deux recherches différentes ont été effectuées à une énergie de centre de masse de $\sqrt{s} = 13$ TeV en utilisant la luminosité totale intégrée durant le Run-2 du LHC de 139 fb$^{-1}$ collectée par le détecteur ATLAS, la première concerne une recherche de photons sombres provenant de la désintégration du boson de Higgs, produit conjointement avec un boson $Z$. Cette recherche a produit la meilleure limite expérimentale sur cette désintégration probable du boson de Higgs. La limite observée (attendue) obtenue sur le rapport de branchement BR$(H \rightarrow \gamma\gamma_d)$ est de 2.28% ($2.82^{+1.33}_{-0.84}$%) fixée à 95% CL pour le $\gamma_d$ de masse 0 GeV. Pour élargir l'exploration de cette particule prédite de matière noire, une deuxième recherche de photons sombres sans masse a été effectuée en considérant certains bosons lourds de type Higgs avec des masses allant de 400 GeV à 3 TeV produits soit en fusion gluon-gluon $ggF$ soit en fusion vecteur-boson $VBF$. Les limites d'exclusion à un niveau de confiance de 95 % sur la valeur $\sigma \times BR(H \rightarrow \gamma\gamma_d)$ pour la production combinée $ggF + VBF$ du boson de Higgs lourd sont comprises entre 1.44 (1.68 fb) et 24.2 (28.1 fb) observée (prévue) respectivement. De plus, cette thèse inclue un travail porté sur un nouveau détecteur de temps fortement segmenté appelé HGTD qui sera installé dans le détecteur ATLAS pour atténuer les effets d'empilement pendant la mise à niveau du LHC à haute luminosité. Les performances de plusieurs capteurs LGAD ont été mesurées lors de campagnes d'essais de faisceaux au cours des années 2018 et 2019 au CERN et a DESY. Les résultats obtenus avec les données enregistrées par un oscilloscope synchronisé avec un télescope de faisceau, telles que la charge collectée, la résolution temporelle, l'efficacité du coup, ainsi que l'uniformité de la charge en fonction de la position de la particule incidente à l'intérieur du capteur, sont documentés.

**Mots-clés:** CERN, LHC, ATLAS, HGTD, LGAD, photon sombre, boson de Higgs, matière noire.

# *Résumé étendu*

Cette thèse de doctorat comprend quatre grandes sections, la première présente le cadre théorique qui sous-tend le sujet de cette thèse, en expliquant les notions théoriques de la physique des particules et en mettant l'accent sur le modèle standard et la physique d'au-delà du modèle standard, comme la matière noire et les photons sombres. La deuxième section présente la configuration expérimentale du détecteur ATLAS au Grand collisionneur de hadrons au CERN ainsi que la reconstruction des différentes particules produites dans les collisions proton-proton. La troisième section représente le sujet principal de cette thèse, la recherche de photons sombres. Deux recherches différentes ont été effectuées à une énergie de centre de masse de $\sqrt{s} = 13$ TeV en utilisant la luminosité totale intégrée durant le Run-2 du LHC de 139 fb$^{-1}$ enregistrée par le détecteur ATLAS, la première concerne une recherche de photons sombres provenant de la désintégration du boson de Higgs, produit conjointement avec un boson $Z$. Un balayage sur la masse de photons sombres a été effectué, allant de sans-masse (0 GeV) jusqu'à 40 GeV. Cette recherche a produit la meilleure limite expérimentale sur cette désintégration probable du boson de Higgs. La limite observée (attendue) obtenue sur le rapport de branchement BR$(H \rightarrow \gamma\gamma_d)$ est de 2.28% ($2.82^{+1.33}_{-0.84}$%) fixée à 95% CL pour le $\gamma_d$ de masse 0 GeV. Pour élargir l'exploration de cette particule prédite de matière noire, une deuxième recherche de photons sombres sans masse a été effectuée en considérant certains bosons lourds de type Higgs avec des masses allant de 400 GeV à 3 TeV produits soit en fusion gluon-gluon $ggF$ soit en fusion vecteur-boson $VBF$. Les limites d'exclusion à un niveau de confiance de 95 % sur la valeur $\sigma \times BR(H \rightarrow \gamma\gamma_d)$ pour la production combinée $ggF + VBF$ du boson de Higgs lourd sont comprises entre 1.44 (1.68 fb) et 24.2 (28.1 fb) observée (prévue) respectivement, avec la limite la plus élevée correspondant à un boson lourd d'une masse de 400 GeV et la limite la plus basse correspondant au boson le plus lourd. Les limites pour les modes de production séparés $ggF$ et $VBF$ ainsi que les masses intermédiaires du boson de Higgs sont aussi fournies. La quatrième section de cette thèse concerne un nouveau détecteur de temps fortement segmenté appelé HGTD qui sera installé dans le détecteur ATLAS pour atténuer les effets d'empilement pendant la mise à niveau du LHC à haute luminosité. La conception du HGTD repose sur l'utilisation de détecteurs d'avalanche à faible gain appelés (LGAD), d'une épaisseur active de 50 µm, qui permettent de mesurer avec une grande précision le temps d'arrivée des particules. Le HGTD améliorera l'attribution des vertex aux particules en mesurant le temps de parcours avec une résolution allant d'environ 30 ps au début des opérations du HL-LHC jusqu'à 70 ps à la fin. Les performances de plusieurs capteurs LGAD non irradiés, ainsi qu'irradiés par des neutrons et des protons, provenant de différents fournisseurs, ont été mesurées lors de campagnes d'essais de faisceaux au cours des années 2018 et 2019 au Super Proton Synchrotron (SPS) du CERN et au Deutsches Elektronen-Synchrotron (DESY). Les résultats obtenus avec les données enregistrées par un oscilloscope synchronisé avec un télescope de faisceau qui fournit des informations sur la position des particules avec une résolution de quelques $\mu$m, telles que la charge collectée, la résolution temporelle, l'efficacité du coup, ainsi que l'uniformité de la charge en fonction de la position de la particule incidente à l'intérieur du capteur, sont documentés dans cette section. De plus, cette thèse inclut en annexe le projet de qualification portée sur un sous-détecteur interne de ATLAS appelé Transition-Radiation-Tracker (TRT), une étude systématique a été réalisée afin d'identifier les sources de plusieurs divergences observées dans les données xAOD du TRT par rapport aux formats de calibration. Ce travail a permis d'identifier l'origine du problème et la correction proposée a permet un meilleur accord entre toutes les variables du TRT.

# List of Tables

# List of Figures

# Contents

# Introduction

There is strong astrophysical evidence suggesting the existence of DM with a density about five times higher than ordinary baryonic matter [1]. However, many of its properties, such as its fundamental nature, are unknown. It is plausible that DM is a component of a larger "dark sector", which is weakly coupled to the SM and possesses a rich internal structure and interactions. Existing models propose a dark sector that contains few or many particles, some providing ideal candidates for DM. The interaction of these dark states can be Yukawa-like, mediated by dark gauge bosons or both.

The dark and visible sectors may interact through a portal offering a potential experimental signature. The form of this portal can be classified according to the dimension of its operators. The best motivated and most studied models contain operators whose forms depend on the spin of the portal mediator: vector (spin 1), neutrino (spin 1/2), Higgs boson (scalar) or axion (pseudo-scalar) [2].

The vector portal used in this thesis is where the interaction results from the kinetic mixing between one dark and one visible Abelian gauge boson. The visible photon is taken to be the boson of the $U(1)$ gauge group of electromagnetism, or the hyper-charge in the regime above the electroweak symmetry breaking scale, while the dark photon is identified as the boson of an extra $U(1)_D$ symmetry. This mixing is always possible because the field strengths of two Abelian gauge fields can be multiplied together to give a dimension-four operator [3]. The existence of such an operator means that the two gauge bosons mix as they propagate [4]. This kinetic mixing provides the portal linking the dark and visible sectors and makes the experimental detection of the dark photon possible.

The massless and the massive dark photons, whose theoretical frameworks as well as experimental signatures are quite distinct, give rise to dark sectors with different phenomenological and experimental features. The massive dark photon has received most of the attention so far because it couples directly to the SM currents and is more readily accessible in experimental searches [5, 6, 7, 8, 9]. The massless dark photon arises from a sound theoretical framework [10, 2], it does not couple directly to any of the SM currents and interacts instead with ordinary matter only through operators of dimension higher than four. It provides, with respect to the massive case, a comparably rich, if perhaps more challenging, experimental target.

Looking beyond particle physics and towards cosmology, dark photons may solve small-scale structure formation problems [11]. In astroparticle physics, dark photons may induce the Sommerfeld enhancement of the DM annihilation cross-section needed to explain the PAMELA-Fermi-AMS2 positron anomaly [12]. They may also assist light DM annihilation to reach the phenomenologically required magnitude, and make asymmetric DM scenarios phenomenologically viable [13, 14].

This thesis targets dark photons predicted by a new model generating exponentially spread SM Yukawa couplings from unbroken $U(1)_D$ quantum numbers in the dark sector [15]. This approach transfers non-perturbative flavour- and chiral-symmetry breaking from the dark to the visible sector via heavy scalar messenger fields that might produce new physics signals at the LHC. For massless dark photons, the $U(1)_D$ kinetic mixing with $U(1)$ can be tuned away on shell, in agreement with all existing constraints [16, 17], while off-shell contributions give rise to higher-dimensional contact operators strongly suppressed by the scale of the heavy messenger mass. A potential discovery process

for dark photons proceeding via Higgs-boson production in the ATLAS detector at the LHC is presented in this thesis. Thanks to the non-decoupling properties of the Higgs boson, a branching ratio of $H \to \gamma\gamma_d$ with values up to a few per cent is possible for a massless dark photon as well as for heavy dark-sector scenarios. The corresponding signature consists of a photon with an energy $E_\gamma = m_H/2$ in the Higgs boson centre-of-mass frame and a similar amount of missing transverse momentum ($E_{\mathrm{T}}^{\mathrm{miss}}$) which originates from the escaping $\gamma_d$ [14]. Moreover, in the unbroken $U(1)_D$ scenarios, the two-body decay $H \to \gamma\gamma_d$ can be enhanced despite existing theoretical constraints [13], providing a very distinctive signature of a single photon plus missing transverse momentum at the Higgs boson mass resonance. If such a signature is discovered at the LHC, CP invariance will imply the spin-1 nature of the missing particle, excluding axions or other ultra-light scalar particles.

The photon plus $E_{\mathrm{T}}^{\mathrm{miss}}$ signature has been extensively studied by the LHC experiments [18, 19, 20]. In the particular case of massless $\gamma_d$, searches in Higgs boson decays were performed at the LHC in $pp$ collisions at a centre-of-mass energy of 13 TeV. The CMS experiment has probed this decay channel using Higgs boson events produced in association with a $Z$ boson $ZH(Z \to \ell^+\ell^-)$ with an integrated luminosity of 137 fb$^{-1}$ [21], or via vector-boson fusion (VBF) production [22] (with 130 fb$^{-1}$) setting an observed (expected) upper limit on the BR($H \to \gamma\gamma_d$) at the 95% confidence level (CL) of 4.6% (3.6%) and 3.5% (2.8%) respectively. ATLAS has set an observed (expected) limit on the $H \to \gamma\gamma_d$ branching ratio, using the VBF production mode with an integrated luminosity of 139 fb$^{-1}$, to 1.8% (1.7%) at the 95% CL [23].

Two new dark photon searches performed using the full LHC *Run 2* dataset corresponding to 139 fb$^{-1}$ of $pp$ collisions recorded between 2015 and 2018 by the ATLAS detector at a centre-of-mass energy of $\sqrt{s} = 13$ TeV are the main physics subject of this thesis as presented in Section III. The first search targets massless and massive dark photons from the SM Higgs boson decay with a mass of $m_H = 125$ GeV, produced together with a $Z$ boson. Leptons from the $Z$ boson decay are used to trigger the event and provide a mass constraint. The transverse mass $m_{\mathrm{T}}$ of the $\gamma - E_{\mathrm{T}}^{\mathrm{miss}}$ system presents a kinematic edge at the Higgs boson mass and is included as a variable of interest in the boosted decision tree (BDT) score that is exploited to enhance the search sensitivity. The kinematics of these events allow the search for $\gamma_d$ in the [0-40] GeV mass range. To broaden the exploration of this predicted dark matter particle, a second search for massless dark photons was carried out considering some heavy Higgs bosons with masses ranging from 400 GeV to 3 TeV produced either in gluon-gluon Fusion $ggF$ or in Vector-Boson-Fusion $VBF$ production modes. The final state consists of a high amount of $E_{\mathrm{T}}^{\mathrm{miss}}$ well separated from a photon with high transverse momentum ($p_{\mathrm{T}}$).

Several searches for new physics beyond the SM have been carried out at the LHC experiments using the existing data of Run1 and Run2, so far, no hint has been observed. If this is due to new processes occurring only at very low rates, more data is necessary in order to discover them. Thus, after the ongoing *Run 3*, the LHC will be upgraded to provide an even higher instantaneous luminosity, increasing the data collection rate. To cope with the challenging environment, a new timing detector called the High Granularity Timing Detector (HGTD) will be installed in the ATLAS detector to mitigate pile-up effects during the High Luminosity (HL) upgrade of the LHC. The design of the HGTD is based on the use of Low Gain Avalanche Detectors (LGADs), with an active thickness of 50 µm, that allow measuring with high-precision the time of arrival of particles. The HGTD will improve the particle-vertex assignment by measuring the track time with a resolution ranging from approximately 30 ps at the beginning of the HL-LHC operations to 70 ps at the end. Performances of several unirradiated, as well as neutron- and proton-irradiated, LGAD sensors from different vendors have been measured in beam test campaigns during the years 2018 and 2019 at the CERN Super Proton Synchrotron (SPS) and the Deutsches Elektronen-Synchrotron (DESY). The results obtained with data recorded by an oscilloscope synchronised with a beam telescope which provides particle position information within a resolution of a few $\mu$m such as the collected charge, time resolution, hit efficiency as well as the charge uniformity as a function of the position of the incident particle inside the sensor pad are documented Section IV of this thesis.

# Part I

# THEORETICAL FRAMEWORK

# 1 From Classical to Modern Physics

**Classical Physics:** Classical mechanics is valid for systems where all velocities are much less than the velocity of light. If the velocities are close to the velocity of light, classical mechanics must be replaced by relativistic mechanics, introduced by Albert Einstein in 1905. In the theory of relativity, the speed of light is a fundamental constant: $c = 299792458 m/s$ and the flow of time depends on the reference system, Energy and mass are related to each other —mass is considered "frozen" energy. At rest, the corresponding energy of a mass is given by the equation of Einstein: $E = mc^2$.
*Electrodynamics:* is another important classical field of physics, which describes the behaviour of electric charges and electromagnetic fields. The theory of classical electrodynamics was introduced by James Clerk Maxwell in 1864 and its basic equations are the Maxwell equations [24].

**Modern Physics:** *Quantum Mechanics:* is an important branch of modern physics, it started in 1900 when Max Planck wrote a paper on the quantization of energy in electromagnetic processes. He introduced the new fundamental constant $h$. In 1905 Albert Einstein proposed that the energy of light is quantized. Light is a collection of particles, which are called photons. The energy of a photon is given by the product of Planck's constant $h$ and the frequency of the light. In 1924 Louis de Broglie published a theory of matter waves. A particle, e.g. an electron, is at the same time also a wave, just like the case of a photon. The wavelength is given by the ratio of Planck's constant and the momentum of the electron. Thus electrons and photons are similar, but photons move at the speed of light, while electrons can have any speed smaller than the speed of light. Werner Heisenberg discovered in 1927 that in quantum physics, observables can not be precisely determined; they have a fundamental uncertainty, which is related to Planck's constant $h$. For example, the product of the uncertainty of the position of a particle and the uncertainty of the momentum can not be smaller than Planck's constant: $\delta x \times \delta p \sim h$. In 1926 Erwin Schrödinger introduced wave mechanics. He interpreted matter waves as the wave functions of particles. The time evolution of these wave functions is described by a differential equation, the Schrödinger equation. He showed that his wave mechanics is equivalent to matrix mechanics. Max Born interpreted the square of the wave function as the probability density. In 1914 James Chadwick discovered that energy and momentum were not conserved in the beta decay of atomic nuclei. For many years this phenomenon was not understood. In 1930 Wolfgang Pauli suggested that in beta decay not only an electron was emitted, but also a neutral particle, which could not be observed. The energy and the momentum of this particle, later called the neutrino, would be the observed missing energy and momentum. Pauli assumed that neutrinos could never be observed directly. But in 1956 they were discovered by Clyde Cowan and Frederick Reines while investigating the neutrino emission of a big reactor in South Carolina [24].
*Quantum Field Theory (QFT):* started with Dirac's work on the quantum extension of Maxwell's classical theory [25] and is defined as the quantum mechanics of continuous systems. QFT is arguably

the most far-reaching and beautiful physical theory ever constructed, with aspects more stringently tested and verified to greater precision than any other theory in physics, it is also considered the most successful physical framework that extends the physical laws of the subatomic world (quantum mechanics) to extremely high energies and fast speeds (Einstein's theory of special relativity). More specifically, QFT becomes relevant when measuring distances that are smaller than the Compton wavelength of a relativistic particle ($\lambda_C = \frac{o\hbar}{mc}$). In the context of QFT, space-time is populated with mathematical constructs called fields, $\phi(x)$. These fields carry out certain quantum numbers and can be used to create or annihilate particles. QFT can adequately explain the interactions of three of the four known fundamental forces in the universe [26]. Every particle and every wave in the Universe is simply an excitation of a quantum.
*Quantum Electrodynamics (QED):* In 1929 Werner Heisenberg and Wolfgang Pauli went one step further from quantum physics and quantized the electromagnetic field, which started the development of QED. In this theory, electromagnetic forces are generated by the exchange of photons. The Schrödinger equation cannot be used to describe relativistic effects, since it contains the second derivatives of the three-dimensional space, but only the first derivative of time. A relativistic field equation was introduced by Paul Dirac in 1928. In the Dirac equation, only the first derivatives concerning space and time appear. Dirac noticed that his equation was only consistent if the electron has an antiparticle, later called the positron. The positron was discovered in 1932 in the cosmic rays. In QED, there is a serious problem, an electron can emit virtual photons, but can also absorb them afterwards. If one calculates this process, one obtains a divergent result - the charge and also the mass of an electron are infinite. This problem was solved by Julian Schwinger, Richard Feynman and Freeman Dyson. An electron without electromagnetic interaction has a "naked mass" and a "naked charge". If the electromagnetic interaction is introduced, the contributions to the mass and the charge are infinite. If one assumes that the naked mass and the naked charge are also infinite, but with a negative sign, the sum of the naked mass plus the corrections should be equal to the observed mass of the electron. The same can be done for the charge. Then all infinities disappeared, due to the normalisation of the mass and the charge.
*Quantum Chromodynamics (QCD)* The atomic nuclei are bound states of protons and neutrons. But these nucleons are not elementary, but consist of quarks. A proton is a bound state of three quarks. Two different quarks are needed to describe all atomic nuclei, the up quarks and the down quarks. The electric charge of the up quark is $(+2/3)e$, the charge of the down quark is $(-1/3)e$— the electric charge of the proton is (+e). The interactions among the quarks are described by the theory of QCD, introduced by Murray Gell-Mann in 1972. The forces among the quarks are generated by the exchange of the gauge bosons of QCD, the gluons. The quarks and gluons do not exist as free particles they are permanently confined in the hadrons. The quarks can be observed indirectly in the scattering of electrons and atomic nuclei. Such experiments were started in 1967 at the Stanford Linear Accelerator Center in California [24].

Moreover, QFT became fully developed in QED. It has been united with statistical mechanics through Feynman's path integral, and its domain has been expanded to cover particle physics, condensed-matter physics, astrophysics, and wherever path integrals are spoken [27]. QED, with its extremely accurate and well-tested predictions, and the standard model of electroweak and chromodynamic (nuclear) forces are examples of successful theories. The concept of the renormalization group has given us a new perspective on field theory in general and on critical phenomena in particular. At this stage, a strong case can be made that QFT is the mathematical and intellectual framework for describing and understanding all physical phenomena, except possibly for quantum gravity [28].

# 2 The Standard Model of Particle Physics

The Standard Model of particle physics is a theoretical framework that provides a modern understanding of elementary particles and their interactions using a quantum field theoretical approach. The first step towards the Standard Model was Sheldon Glashow's discovery in 1961 of a way to combine electromagnetic and weak interactions. In 1967 Steven Weinberg and Abdus Salam incorporated the Higgs mechanism into Glashow's electroweak interaction, giving it its modern form. The SM was designed to explain all the then-known physics, including the following key ingredients:

- The known interactions relevant to particle physics were three, named electromagnetic (EM), strong and weak interactions. They all conserve energy, momentum and angular momentum.
- The EM interaction is long-range, while the strong and weak interactions are of short range. The first is mediated by a massless particle, the photon, while the weak interaction is expected to be mediated by very heavy charged bosons, not known. The strong interaction was not understood along the lines of the Yukawa theory after the pions did not seem to be elementary
- The known elementary particles were classified as fermions with spin $1/2$ and bosons with spin 1. The lightest of these is the neutrinos and the photon respectively. They have zero mass.
- The zero mass particles are characterised by a quantum number called helicity, which is the orientation of the spin with respect to the momentum. The number of helicity states (polarization) of the photon is two (two transverse polarisations), but the neutrino has only one polarization. More specifically it can only be left-handed (and the anti-neutrino right-handed).
- The particles which feel the strong interaction are called hadrons. The spin $1/2$ hadrons are called baryons. Those that do not feel the strong interaction are called leptons. The first is characterised by a baryon number and the second by a lepton number.
- All the known interactions conserve charge, baryon and lepton number.
- Parity, associated with the symmetry under space inversion, seemed conserved in strong and electromagnetic interactions, but it is maximally violated in weak interactions
- The only interaction the neutrinos feel is the weak interaction.
- The known elementary Fermions are the quarks and leptons and they come into families. The hadrons as *(u, d), (c, s)* and perhaps others and the leptons as $(\nu_e, e^-)$, $((\nu_\mu, \mu^-))$ and perhaps others. Lepton flavour seems to be conserved in all three interactions, but the quark flavour is a little bit violated in weak interactions.

- The quarks carry an additional quantum number called colour, which is responsible for the strong interaction.
- In condensed matter physics the phenomenon of a spontaneous symmetry breaking was known, e.g. spontaneous magnetisation. In other words, even if the symmetry of the interaction between the physical entities has a symmetry, e.g. it is rotationally invariant, the ground state of the system does not respect this symmetry. Thus even in the absence of an external magnetic field, all the elementary dipoles come out aligned at least in a sufficiently small region.
- The notion of spontaneous symmetry breaking was elucidated by the existence of spin-zero particles (scalars) and suggested that the true symmetries of nature, involving the internal degrees of freedom, are not global, holding for all space-time points simultaneously, but local or gauge symmetries.
- All particles are initially characterised by zero mass, but some of them may attain a mass after the spontaneous breakdown of the symmetry by the scalars called Higgs

The current formulation of the successful SM theory that describes three of the four known fundamental forces excluding gravity was finalised in the mid-1970s. An overview of the particle content of the SM is given in 2.1, which was discovered in experimental observations over several decades. The concepts that are used in the description of the interactions, which emerge naturally from the application of symmetry considerations, are introduced in 2.2. The spontaneous symmetry breaking presented in 2.3 is necessary to generate masses for the electroweak gauge bosons. A brief overview of the limitations of the SM is given in 2.4. This chapter follows the references [29, 30, 31], where more detailed explanations, outside of the scope of this thesis, can be found.

## 2.1 Matter Particles and Force Carriers

The matter content of the SM and especially properties like the particles' mass can't be predicted by the theory alone, but originates from experimental observations, even though theoretical prediction lead on several occasions to the discovery of particles. There are 12 known fermionic particles of spin $\frac{1}{2}$ included in the SM that are arranged into three generations of matter. Each generation consists of two types of quarks and two types of leptons. These types differ by their masses between the generations but have similar behaviour with respect to their interactions. An overview of the SM particle spectrum is given in 2.1, listing also their properties like mass, charge and spin. The SM also includes the *anti-matter* variant of each particle, differing by the sign of their charges. The antiparticles are denoted by the same symbols as the particles, but with a bar over the respective symbols. Quarks are massive particles that interact through electromagnetic, weak and strong forces. Up-type quarks have a positive electric charge of $Q = +\frac{2}{3}$ while down-type quarks have a negative electric charge of $Q = -\frac{1}{3}$. Each generation includes one up-type and one down-type quark, called up quark $u$ and down quark $d$ in the first generation, charm $c$ and strange $s$ quark in the second generation and top $t$ and bottom $b$ in the third. Quarks carry colour charge, the source of the strong field, which exists in three states, usually denoted as red, green and blue. Colour-charged particles have never been experimentally observed as free and isolated particles, leading to the assumption that they only occur in colourless bound states, a principle called *confinement*. Combinations of colour charges can cancel to build charge-neutral states when combining a colour and an anti-colour or when bounding all three colour charges. These observable states are called hadrons, where the constituent quarks are combined in a way that assures the overall colour charge of these hadrons to cancel. Hadrons can be either combinations of a quark and anti-quark pair ($q\bar{q}$, where the anti-quark carries an anti-colour charge), called mesons, or exist as three quark states called baryons ($qqq$). Exotic quark states

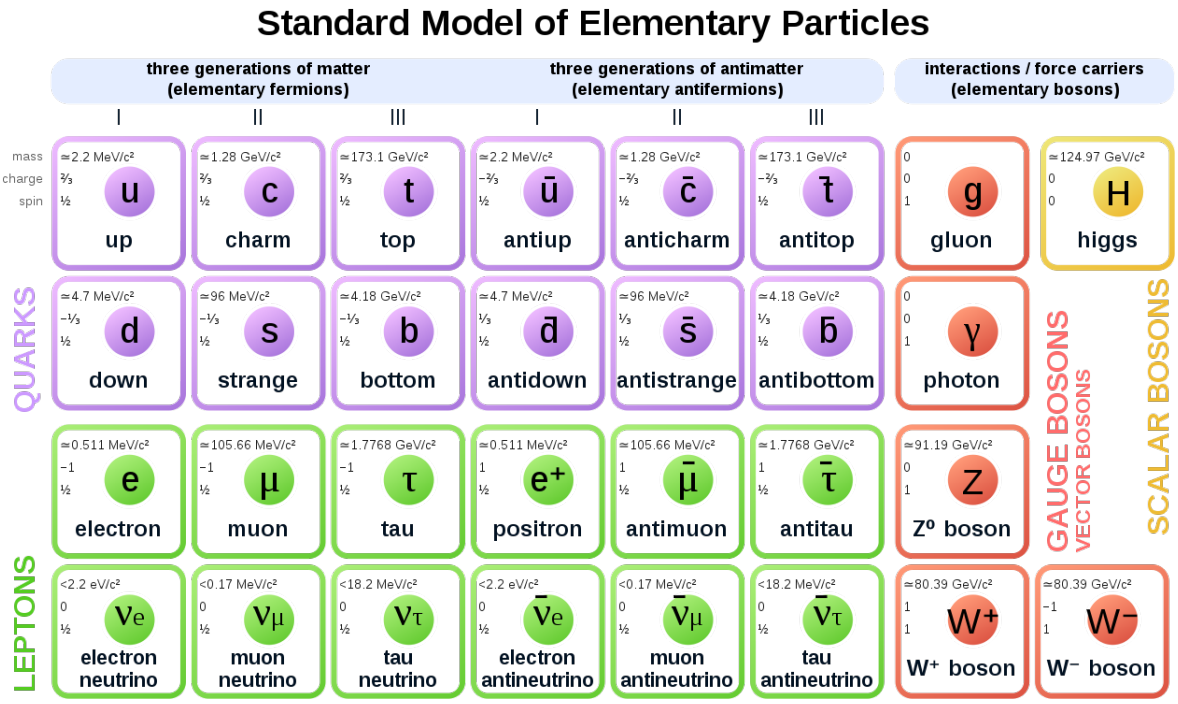


FIGURE 2.1: Standard Model matter and antimatter particles scheme, divided into the three generations leptons, quarks and the gauge bosons. The properties of the particles such as electrical charge, colour, mass and spin are shown [32].

containing more than three quarks have been observed, but always in a colour-neutral form. The two leptons within each generation consist of one electrically charged particle and one uncharged neutrino. While the charged lepton has a mass, in the classical formulation of the SM, the neutrino is considered massless. Experimental observations of neutrino oscillations [33, 34, 35] indicate that neutrinos must have a – although very small – non-vanishing value. Only upper limits on the neutrino masses are available up to today, as indicated in 2.1. The charged lepton, called electron $e$ in the first generation, interacts electromagnetically as well as weakly. The second and third-generation charged leptons are the muon $\mu$ and the tau lepton $\tau$. Neutrinos only interact through weak interaction and due to this characteristic, they typically pass through solid matter with a very low chance of interacting with an atom, making them difficult to detect. Each charged lepton is associated with the neutrino within its generation by carrying the same lepton number. They are thus called the electron neutrino $\nu_e$, muon neutrino $\nu_\mu$ and tau neutrino $\nu_\tau$. In quantum field theory, interactions are mediated by Gauge bosons (see 2.2) of integer spin. Electromagnetism is mediated by the photon and thus it is a long-range interaction due to the vanishing mass of the mediator. The $W^\pm$ and $Z$ bosons are the carriers of the weak force. While the $W^\pm$ boson carries an integer charge, the $Z$ boson is electrically neutral, which means it can only transfer spin, momentum and energy in an interaction. The high masses of the weak bosons cause the weak interaction to be very short-ranged. Gluons mediate the strong force, they are massless, but contrary to photons they carry colour charges themselves.

While in principle all 12 fermions of the SM interact weakly, an important distinction has to be made. The spin of particles can be used to define their helicity. Parallel or anti-parallel alignment of the spin relative to the particle's direction of motion describes right-handed and left-handed fermions, respectively.

## 2.2 Fundamental interactions

Symmetries play an important role in physics. A system is considered to respect a given symmetry if it is invariant under the transformations associated with the symmetry. A physical system is in general described by a Lagrangian density $\mathcal{L}$, which defines the system's dynamics. In the SM it is a set of local Gauge symmetries that transform the originally free theory into an interacting one by introducing vector boson fields that guarantee the theory stays invariant under Gauge transformations. This *Gauge principle* can be illustrated for example for the case of QED, the theory describing phenomena of electrically charged particles and their interactions.

For a free Dirac field $\psi$ with spin $\frac{1}{2}$, mass $m$ and electric charge $q$, the Lagrangian can be written as

$$\mathcal{L} = \bar{\psi}(x)(i\partial_\mu\gamma^\mu - m)\psi(x), \tag{2.1}$$

where $\gamma^\mu, \mu \in 0,1,2,3$, are the Dirac matrices. It is easy to show that $\mathcal{L}$ is invariant under global $U(1)$ transformations

$$\psi \to e^{iq\theta}\psi, \quad \bar{\psi} \to e^{-iq\theta}\bar{\psi}, \tag{2.2}$$

but when promoting the transformation to a local one, meaning that the parameter $\theta$ depends on the space-time coordinates $x$, additional terms appear in the transformed Lagrangian from the derivations:

$$\partial_\mu(e^{iq\theta(x)}\psi) = e^{iq\theta(x)}\partial_\mu\psi + iq(\partial_\mu\theta(x))e^{iq\theta(x)}\psi. \tag{2.3}$$

To assure invariance of the Lagrangian $\mathcal{L}$ under local $U(1)$ transformation a vector field $A_\mu(x)$, which transforms under $U(1)$ according to

$$A_\mu(x) \to A_\mu(x) - \partial_\mu\theta(x), \tag{2.4}$$

is introduced to compensate for the extra terms. The gauge invariant Lagrangian is then built by replacing the derivative, $\partial_\mu$, with the co-variant derivative $D_\mu$, defined as

$$D_\mu\psi = (\partial_\mu + iqA_\mu(x))\psi. \tag{2.5}$$

Rewriting the Lagrangian in the form

$$\mathcal{L} = \bar{\psi}(x)(iD_\mu\gamma^\mu - m)\psi(x), \tag{2.6}$$

it contains terms of the form $\bar{\psi}qA_\mu\gamma^\mu\psi$ that represents an interaction between the field $\psi$ and the vector boson $A_\mu$, where the latter can be identified as the photon. Thus by requiring local symmetry of $\mathcal{L}$, an interaction has been generated via the Gauge principle. Including the kinetic term of the photon field, the total Lagrangian of QED can be written as

$$\mathcal{L}_{\text{QED}} = \bar{\psi}(x)(iD_\mu\gamma^\mu - m)\psi(x) - \frac{1}{4}F_{\mu\nu}(x)F^{\mu\nu}(x) \tag{2.7}$$

with the field tensor $F_{\mu\nu}$ defined as

$$F_{\mu\nu}(x) = \partial_\mu A_\nu(x) - \partial_\nu A_\mu(x). \tag{2.8}$$

The full Gauge symmetry group of the Standard Model is $SU(3)_C \times SU(2)_L \times U(1)_Y$. It can be separated into two parts. The strong interaction is described by quantum chromodynamics, where the interaction is generated by requiring symmetry of the Lagrangian under colour charge transformations, corresponding to the symmetry group $SU(3)_C$, where $C$ refers to the strong colour charge. The electromagnetic and weak interactions are unified into the electroweak interaction that corresponds

to the gauge invariance under $SU(2)_L \times U(1)_Y$ symmetry. $SU(2)_L$ is the weak isospin group acting only on left-handed fermions and $U(1)_Y$ is the weak hyper-charge group.

**Quantum chromodynamics** The gauge bosons associated with $SU(3)_C$ symmetry are the gluons. Equivalently as done for QED, the QCD invariant Lagrangian is constructed by applying the gauge principle. Similarly, a covariant derivative is defined as

$$D_\mu q = (\partial_\mu - i g_s \frac{\lambda_a}{2} G^a_\mu(x))q, \tag{2.9}$$

where q denotes the quark field, $g_s$ is the strong coupling constant, $\lambda_a$ are the generators of $SU(3)_C$ and $G^a_\mu(x)$ defines the gluon fields. A gluon field transforms under $SU(3)_C$ according to

$$G^a_\mu(x) \rightarrow G^a_\mu(x) - \frac{1}{g_s}\partial_\mu \theta^a(x) + f^{abc}\theta_b(x) G_{\mu c}(x) \tag{2.10}$$

in order to guarantee invariance of $\mathcal{L}$ under colour charge transformations, where $f^{abc}$ are the $SU(3)_C$ group structure constants. Due to the different structure of the $SU(3)_C$ group, when writing the QCD Lagrangian

$$\mathcal{L}_{\text{QCD}} = \sum_q \bar{q}(iD_\mu \gamma^\mu - m)q - \frac{1}{4} G^a_{\mu\nu}(x) G^{\mu\nu}_a(x) \tag{2.11}$$

with the gluon field strength tensor

$$G^a_{\mu\nu}(x) = \partial_\mu G^a_\nu(x) - \partial_\nu G^a_\mu(x) + g_s f^{abc} G_{\mu b} G_{\nu c}, \tag{2.12}$$

additional terms comparing to QED appear. These result in self-coupling of the gluons. This means that while being the mediators of the strong force, they also carry colour and couple to themselves in three-gluon or four-gluon interactions.

**Electroweak interactions** Requiring the Lagrangian to be invariant under $SU(2)_L \times U(1)_Y$ gives rise to the electroweak interactions. This group has in total four generators. Three of them are the $SU(2)_L$ generators $T_i = \frac{\sigma_i}{2}$ with $i = 1, 2, 3$ and $\sigma_i$ being the Pauli matrices. The generator of $U(1)_Y$ is $\frac{Y}{2}$. The associated gauge bosons are three weak bosons $W^i_\mu$ for $SU(2)_L$ and $B_\mu$ as the hyper-charge boson of $U(1)_Y$. As mentioned before, only left-handed fermions are affected by $SU(2)_L$ transformations, while right-handed fermions are untouched. The co-variant derivative corresponding to $SU(2)_L \times U(1)_Y$ applied on a generic fermion $f$ is

$$D_\mu f = (\partial_\mu - i g T_i W^i_\mu - i g' \frac{Y}{2} B_\mu) f, \tag{2.13}$$

which generates the electroweak interactions in the Lagrangian terms of the form $\bar{f} D_\mu \gamma_\mu f$. The physical gauge bosons are obtained by a mixing of the electroweak eigenstates, giving their mass eigenstates

$$W^\pm_\mu = \frac{1}{\sqrt{2}}(W^1_\mu \mp i W^2_\mu) \tag{2.14}$$

$$Z_\mu = \cos\theta_W W^3_\mu - \sin\theta_W B_\mu \tag{2.15}$$

$$A_\mu = \sin\theta_W W^3_\mu + \cos\theta_W B_\mu, \tag{2.16}$$

where $\theta_W$ is the Weinberg angle and $\sin\theta_W \equiv \frac{g'^2}{g^2 + g'^2}$.

It is important to note that mass terms resembling the form $m_W^2 W_\mu W^\mu$, as they have been introduced for QCD, are forbidden in the electroweak sector, as they violate the $SU(2)_L \times U(1)_Y$ invariance. Thus in its pure form, the Standard Model gauge group being $SU(3)_C \times SU(2)_L \times U(1)_Y$ would infer massless weak gauge bosons, which is in clear disagreement with the short-range property of the weak interaction as well as the measured masses of the $W$ and $Z$ boson. The solution to this problem is spontaneous symmetry breaking, which will be discussed in the next section.

## 2.3 Spontaneous symmetry breaking and the Higgs Boson

To include the mass terms of the weak bosons, which are forbidden by a purely $SU(2)_L \times U(1)_Y$ invariant electroweak sector, the concept of spontaneous symmetry breaking (SSB) is introduced. A system's symmetry is considered to be spontaneously broken if the interactions of the given system respect the symmetry, but the system's ground state does not. To implement this symmetry breaking, an additional field $\Phi$ is introduced to the theory, which is invariant under $SU(2)_L \times U(1)_Y$, but has a ground state that breaks this symmetry. A possible choice is to require $\Phi$ to be a complex scalar field, that has weak isospin and hyper-charge. Its interactions with the gauge bosons and fermions are generated by applying the gauge principle. To generate a non-vanishing ground state vacuum expectation value for the field $\Phi$, a scalar potential $V(\Phi)$ can be introduced that also generates self-interactions. The field can be written as

$$\Phi = \begin{pmatrix} \phi^+ \\ \phi_0 \end{pmatrix} \tag{2.17}$$

with the complex components $\phi^+$ and $\phi_0$, and the potential is defined to be

$$V(\Phi) = -\mu^2 \Phi^\dagger \Phi + \lambda (\Phi^\dagger \Phi)^2; \;\; \lambda > 0. \tag{2.18}$$

The Lagrangian for this field can be written as

$$\mathcal{L}_{SSB} = (D_\mu \Phi)^\dagger (D^\mu \Phi) - V(\Phi), \tag{2.19}$$

where the covariant derivative has the same form as in 2.13. Since in the case that $(-\mu)^2 > 0$ the ground state of the vacuum is

$$\langle 0|\Phi|0\rangle = 0 \tag{2.20}$$

and no symmetry breaking occurs, $(-\mu)^2 < 0$ has to be required. In this case, the vacuum expectation value that minimises the potential is

$$|\langle 0|\Phi|0\rangle| = \begin{pmatrix} 0 \\ v/\sqrt{2} \end{pmatrix}, \;\; v = \sqrt{\frac{\mu^2}{\lambda}}, \tag{2.21}$$

which is not symmetric under $SU(2)_L \times U(1)_Y$, but retains symmetry under $U(1)_{EM}$. thus achieving the breaking of the symmetry $SU(2)_L \times U(1)_Y \to U(1)_{EM}$.

Using a unitary gauge, the scalar field can be written as

$$\Phi = \begin{pmatrix} 0 \\ \frac{v+h}{\sqrt{2}} \end{pmatrix}, \tag{2.22}$$

where $h$ denotes the physical Higgs boson.

By taking this expression for $\Phi$ and evaluating the kinematic part of 2.19, mass terms for the electroweak bosons of 2.14 and 2.15 are generated. At tree-level prediction, the masses are

$$m_W = \frac{gv}{2}, \quad m_Z = \frac{\sqrt{g^2 + g'^2}v}{2}, \tag{2.23}$$

while leaving the field $A_\mu$, identified as the photon, massless. Masses of the fermions are obtained in the SM by adding the $SU(2)_L \times U(1)_Y$ invariant Yukawa Lagrangian $\mathcal{L}_{\text{Yukawa}}$, which uses the same scalar field introduced in 2.22. For the first generation, the Lagrangian can be written as

$$\mathcal{L}_{\text{Yukawa}} = \lambda_e \tilde{l}_L \Phi e_R + \lambda_u \tilde{u}_L \Phi u_R + \lambda_d \tilde{d}_L \Phi d_R + h.c. \tag{2.24}$$

and equivalent for the 2$^{\text{nd}}$ and 3$^{\text{rd}}$ generation, where $\lambda_i$ are the Yukawa couplings. This defines the fermion masses at tree level via the coupling of the fermions to the scalar field $\Phi$ to be

$$m_f = \lambda_f \frac{v}{\sqrt{2}}. \tag{2.25}$$

The potential term in 2.19 on the other hand results in a mass term of the form $\mu^2 h^2$ for the leftover degree of freedom of the added scalar field and this is identified as the Higgs boson particle. The requirement of a symmetry-breaking ground state has thus led to a $SU(2)_L \times U(1)_Y$ invariant formulation of the masses of both the electroweak gauge bosons as well as the fermions. This is what is commonly referred to as the Brout-Englert-Higgs mechanism [36, 37]. The ground state breaks the symmetry of the system and causes $SU(2)_L \times U(1)_Y$ to be spontaneously broken to $U(1)_{EM}$. As a residual effect of this approach, an additional massive, scalar, bosonic particle is predicted to exist in nature, the Higgs boson.

With the observation of a new scalar boson in 2012 by the CMS and the ATLAS collaborations [38, 39], whose properties appear to be in good agreement with the SM predictions, the Standard Model is considered complete. Continuous measurements of this boson's properties are necessary and of great interest to the particle physics community to ensure the observed boson can indeed be identified with the boson predicted by the SM. Especially the predicted self-coupling of the Higgs boson emerging from 2.19 is an area of intense research since this would allow further investigation of the structure of the potential $V(\Phi)$.

## 2.4 Open points of the SM

Even though the SM is considered as a very successful theory of particle physics that delivers predictions showing unprecedented precision in terms of agreement with experimental measurements, it is by no means a complete theory of nature. There are several structural inconsistencies inherent to the SM that lead to the assumption that further extensions to the SM are needed. Additionally, there are experimental observations that can't be explained in the framework of the SM in its current form. A non-exhausting list of open points of both aspects is discussed in this section.

**Structural inconsistencies:** The *gauge hierarchy problem* raises the question of why the Higgs boson mass is as small as it is. In the calculation of the physical mass of the SM Higgs boson, loop-level diagrams like 2.2 need to be considered in addition to the tree-level mass, which gives correction terms to the mass of the form

$$\Delta m_h^2 \sim -\frac{\lambda_f^2}{8\pi^2}\Lambda^2 + \dots, \tag{2.26}$$

where $\lambda_f$ is the coupling parameter to the respective fermion and $\Lambda$ is the energy scale above which the SM is expected to no longer be a valid theory. If one sets $\Lambda$ to be at the level of the Planck mass $M_{Pl} \sim 1 \times 10^{19}\,\text{GeV}$, a scale at which modifications to the SM and thus new physics are expected from a gravitational point of view, this huge term needs to cancel to arrive at the observed mass of 125 GeV at the electroweak scale. An effect like this is not considered to be a reasonable feature of a theory and in the literature often called *fine tuning*. Setting the cutoff to a lower value $\Lambda \sim 1\,\text{TeV}$ would dismiss the hierarchy problem, therefore, new physics is expected to appear at this scale.

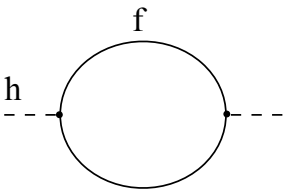


FIGURE 2.2: One-loop radiative correction to the mass of the Higgs boson $h$ by a fermion $f$.

A second very important open point is the apparent absence of *strong CP violation* in QCD. The QCD sector of the SM Lagrangian includes a $CP$ violating term of the form

$$\frac{g_s^2}{32\pi^2}\theta_3 \epsilon^{\mu\nu\rho\sigma} G^a_{\mu\nu} G^a_{\rho\sigma}, \tag{2.27}$$

where $g_s$ is the coupling of the strong interaction, $\theta_3$ is an angle parameter and $\epsilon^{\mu\nu\rho\sigma}$ is defined via total antisymmetry in its four indices. This term contributes to the electric dipole moment of the neutron $d_n$. Since current results limit the dipole moment to $d_n < 10^{-26}\,e\,\text{cm}$ [40], the parameter $\theta_3$ would have to be very tiny, in the order of $\theta_3 \sim 10^{-10}$, which is considered fine-tuning. While the electroweak sector includes $CP$ violation in the CKM mechanism [41], it is not understood why the strong sector does not.

**Observational inconsistencies:** Through the combination of quantum mechanics with special relativity, the existence of antimatter particles that have the same mass as their matter partner, but exhibit opposite charge, is a necessary feature that is also experimentally observed. One of the open questions though is why in the observable universe only matter is found, and all the antimatter that must have been created at the time of the Big Bang has disappeared. There are mechanisms in the SM that differentiate between matter and antimatter, like the CP violating effects, but these are not enough to explain the massive *asymmetry between matter and antimatter* seen in the Universe today.

The fermions masses are described in the SM with terms that couple left- and right-handed fields, as can be seen in 2.24. Neutrinos, being considered massless particles in the classic Standard Model formulation, are included only as left-handed fields in the theory. While a modification of the SM Lagrangian to include right-handed neutrinos and thus *neutrino masses* can be achieved without strong modifications to the overall structure of the SM, the mechanism explaining the large differences between the masses of the electrically charged and uncharged leptons is not yet understood [42, 43].

# 3 Evidence of dark matter from astrophysical observations

The paradigm of dark matter (DM) originates from astrophysical and cosmological observations, which – under the assumption that the physical laws governing the motions of massive objects at large scales are described by *general relativity* – can't be explained with the presence of the observed luminous matter alone. Neither the evolution of the observable universe nor its current state can be explained without the presence of dark matter and dark energy. According to today's understanding, dark matter outweighs visible matter by approximately a factor of 5 to 1. It is called *dark* because of its missing interaction with the electromagnetic field, which manifests in absent absorption, reflection or emission of electromagnetic radiation that is observed in ordinary, baryonic, matter. While dark energy is considered responsible for the expansion of the universe – and will not be further discussed in this work – dark matter denotes the presence of gravitationally interacting matter that does not, or hardly, interact with the known particles of matter described by the SM and represents today the dominant form of matter in the universe.

Experimentally, various possible ways of detecting DM exist, all assuming the existence of microscopic particles constituting the DM. These types of experiments can be broadly grouped into three categories: direct detection, indirect detection and collider searches. *Direct detection* experiments aim at measuring scattering processes between DM particles and atoms in ultra-sensitive low-background experiments. These of course depend on the presence of a DM halo in the Milky Way. *Indirect detection* experiments search for the decay products of dark matter annihilation processes into SM particles like photons in regions of high expected dark matter densities, expected to be found for example at the centre of a galaxy. The searches for DM at (hadron) colliders like the LHC aim at producing DM particles and observing them in events with a missing energy signature. All of the above approaches require an interaction of the dark sector with the Standard Model in addition to the gravitational one.

To this day there is no evidence for non-gravitational interactions of dark matter with SM particles, but some of its properties can nonetheless be inferred from its gravitational effects in astrophysical or cosmological observations. A large amount of different experimental results can be explained simultaneously by postulating the existence of DM and are used to infer its necessary amount in the universe concerning the baryonic matter, a selection of which is mentioned in this chapter. Galactic rotational curves, which can't be explained by visible matter alone, are discussed in 3.1. Observations made via gravitational lensing, among which one finds the famous *Bullet Cluster*, are introduced in 3.2. Results coming from studies of the cosmic microwave background are presented in 3.3.

An alternative approach to the problem of dark matter is a modification of general relativity at large scales. Here one assumes that there is no additional form of matter other than the baryonic one, but that the laws of gravity need to be modified when applied to the levels of galaxies and beyond. While this is also an intensive field of research (see for example, [44, 45, 46] for overviews), it will not be covered within this thesis.

## 3.1 Rotation curves

Rotation curves indicate the velocity profile of stars in spiral galaxies as a function of their distance from the galactic centre. Experimentally, the velocities are obtained by measuring the stars' Doppler shifts. Consulting basic Newtonian mechanics as an approximation to predictions from general relativity, the velocity $v$ of stars in stable orbit is expected to depend on their radial distance $r$ from the centre of the observed galaxy and the radial dependent mass distribution of the galaxy, $M(r)$, following the relation

$$v = \sqrt{\frac{GM(r)}{r}}. \tag{3.1}$$

At a radius far enough from the centre of the galaxy to assume that the galaxies mass is concentrated at lower radii, the mass distribution $M(r)$ becomes constant and the velocity is expected to be proportional to $v \propto 1/\sqrt{r}$. Looking at observations as the rotation curve of galaxy *M33* shown in 3.1, this prediction is contradicted by the data.

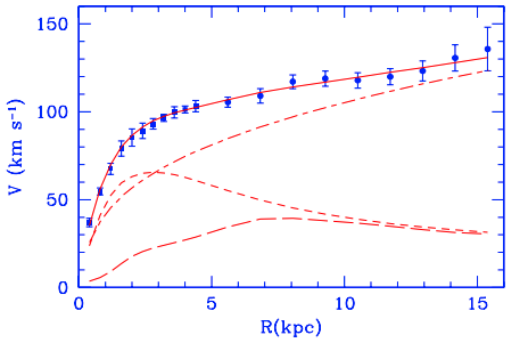


FIGURE 3.1: The rotation curve of the galaxy *M33* is shown as the velocity as a function of the radius from the centre of the galaxy, comparing data (points) with the best-fit model (continuous line). Overlaid are the contributions from the dark matter halo (dashed-dotted line), the stellar disk (short dashed line) and gas (long dashed line) [47].

Even though outside of the luminous part of the galactic disk a considerable amount of gas is expected, the observed behaviour of the rotational curve for large radii can not be explained by this alone. This observation suggests that the mass distribution of the galaxy continues to grow with radius, behaving like $M(r) \propto r$. This is a behaviour that is fundamentally different to the expected behaviour of luminous matter. It is thus considered as strong evidence that spiral galaxies are embedded in extended halos of an additional, otherwise not detectable matter component: dark matter. More examples of rotation curves exhibiting the same behaviour can be found for example in [48].

## 3.2 Gravitational lensing and the bullet cluster

In the general relativistic description of gravitation, space-time is bent by the presence of matter. One of the consequences of this bending is that light travels not on straight lines in a euclidean sense, but on the geodesics defined by the bent space-time geometry. When a large mass sits between a light emitter and an observer, the interjacent matter thus acts as a lens, leading to the distortion of the original image of an object into either complete or fractional *Einstein rings*. Studying observed gravitational lensing effects allows for inferring the amount and distribution of matter necessary to explain visible patterns.

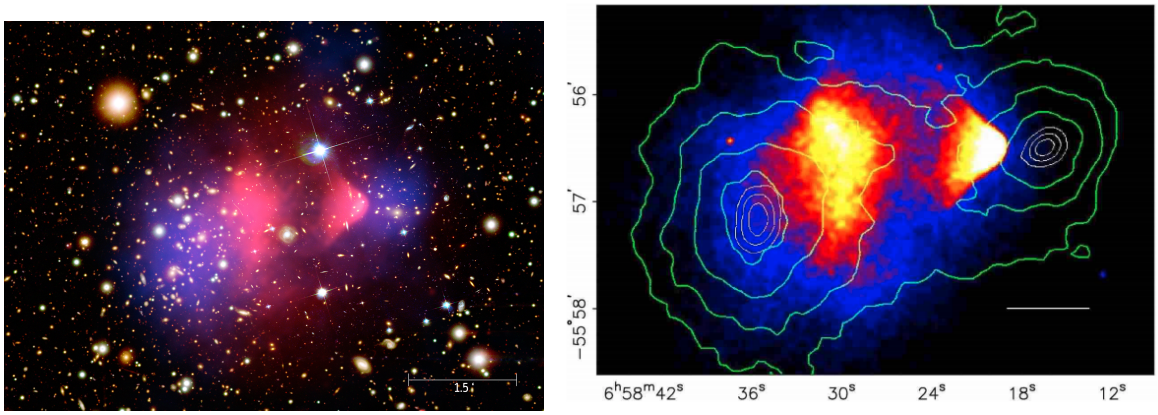


(a) (b)

FIGURE 3.2: The composite image (a) shows the galaxy cluster 1E 0657-56, also known as the *bullet cluster*, formed after the collision of two large clusters of galaxies. Hot gas detected from X-ray emission is illustrated as two pink clumps in the image and contains most of the baryonic matter in the two clusters, mainly in the form of gas, while galaxies are shown in orange and white. The blue clumps sit where most of the mass in the clusters is found, inferring its distribution from gravitational lensing. The mass distribution inferred from gravitational lensing is shown in (b) with green contour lines, that denote the surface mass density peaks. Most of the matter in the clusters is separate from the normal matter, giving direct evidence that nearly all of the matter in the clusters is dark. [49].

A famous example of such an inferred mass distribution comes from the so-called *bullet cluster*. It denotes a system of two galaxy clusters that underwent a collision process. Due to the vast space between the individual galaxies, the stellar components pass through each other with hardly any interaction. Galaxy clusters also contain large quantities of intergalactic gas, which exceeds the mass coming from stars by a factor of roughly 6. The gas interacts electromagnetically, slows down and gets deformed. The shape resulting from the collision can be seen in 3.2a, shown in pink colour.

Using gravitational lensing effects, the mass distribution can be determined. The slowed-down gas, which can be observed from the X-ray spectrum, is – when considering baryonic matter alone – expected to define the peaks of the mass distribution, as it contributes more than the stellar masses. The observed mass distributions, however (3.2b, green contours) show the peaks of this distribution sitting within the centres of the clusters, which can be interpreted as an abundance of non-luminous matter that does not interact with itself or ordinary matter. Dark matter that is assumed to be at most weakly interacting, provides a viable explication to this observation, which has been found in several galaxy cluster collisions [50, 51].

## 3.3 Cosmic microwave background

The cosmic microwave background (CMB) can be understood as leftover radiation originating from the early universe. When the universe has sufficiently expanded and thus sufficiently cooled down for electrons and protons to combine into neutral hydrogen and helium atoms, the universe becomes optically transparent and electromagnetic radiation starts to propagate freely through the universe. From the time of this decoupling (at $T \sim 3000\,\mathrm{K}$) the temperature of the universe decreased due to cosmic expansion, redshifting the spectrum of the background radiation observed today into the range of radio waves. The measured radiation corresponds to a mean temperature of $T = 2.7255(6)\,\mathrm{K}$ [41]. One of the most recent surveys of the CMB was carried out by the Planck collaboration [52], providing

sky maps of the CMB, resolving angular variations in the temperature at the $10^{-5}$ level. These fluctuations are visualised in maps like 3.3a.

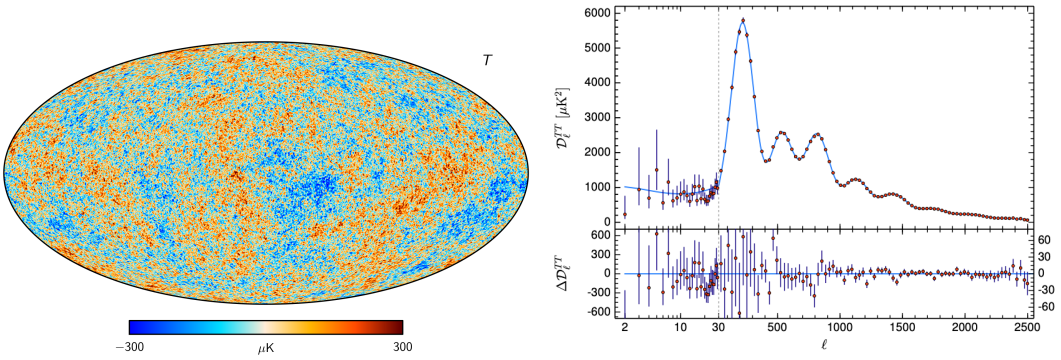


(a) (b)

FIGURE 3.3: An intensity map of the CMB is shown in (a), (b) presents the extracted temperature power spectrum [53, 54].

The temperature fluctuations originate from density variations in the early universe. Photons escaping from denser regions need to overcome the well of the gravitational potential in these regions, leading to an additional redshift. These higher-density zones are necessary to explain the initial clumping of matter that causes large-scale structures found today in the cosmos to form. The fluctuations can be interpreted by expanding the map into spherical harmonics. 3.3b shows the strength of the fluctuations as a function of the multipole $\ell$, which is proportional to the inverse of an angular scale. The derived distribution is called a temperature power spectrum. The data points can be fitted by a six-parameter $\Lambda$CDM model [55], which takes into account dark energy as a cosmological constant ($\Lambda$) and cold[1] dark matter. The result of the fit is shown in 3.3b, showing excellent agreement between data and model. Cosmological parameters like the fraction of baryonic or dark matter in the universe can be extracted from the fit. The resulting parameters [54] infer the fraction of matter to of the energy content of the universe

$$\Omega_m h^2 = 0.1428 \pm 0.0011 \tag{3.2}$$

where $\Omega_m h^2$ is the total matter density and $h$ is the Hubble parameter. This can be split into the baryonic ($\Omega_b h^2$) and the cold dark matter ($\Omega_c h^2$) component

$$\Omega_b h^2 = 0.02233 \pm 0.00015 \tag{3.3}$$

$$\Omega_c h^2 = 0.1198 \pm 0.0012 \tag{3.4}$$

showing that dark matter contributes with roughly 86 % to the total matter density.

[1] *Cold* dark matter, in contrast to *hot* dark matter, denotes a dark matter that travels at velocities that are small compared to the speed of light.

# 4 The Physics of the Dark Photon

The dark photon is a new gauge boson arising from a symmetry of a hypothetical dark sector comprising particles completely neutral under the SM interactions. The neutrality of ordinary matter makes it blind to this new gauge boson which is invisible. The dark photon can be detected because of its kinetic mixing with the ordinary, visible photon. This kinetic mixing is always possible because the field strengths of two Abelian gauge fields can be multiplied together to give a dimension four operator. The existence of such an operator means that the two gauge bosons can go into each other as they propagate. This kinetic mixing provides the portal linking the dark and visible sectors. It is this portal that makes it possible to detect the dark photon in the experiments. Two kinds of dark photons are predicted: The massless and the massive—whose theoretical frameworks as well as experimental signatures are quite distinct. They give rise to dark sectors with different features; their characteristic physics and experimental searches are best reviewed separately. This chapter follows the references [2, 10], where more detailed explanations could be found.

## 4.1 Massless and Massive Dark Photons

The most general kinetic part of the Lagrangian of two Abelian gauge bosons, described by two gauge groups $U(1)_a$ and $U(1)_b$ is given by Equation 4.1.

$$L_0 = -\frac{1}{4}F_{a\mu\nu}F_a^{\mu\nu} - \frac{1}{4}F_{b\mu\nu}F_b^{\mu\nu} - \frac{\epsilon}{2}F_{a\mu\nu}F_b^{\mu\nu}. \tag{4.1}$$

The gauge boson $A_b^\mu$ is taken to couple to the current $J_\mu$ of ordinary SM matter, the other, $A_a^\mu$, to the current $J_\mu^{'}$, which is made of dark-sector matter, to give the Lagrangian in Equation 4.2.

$$L = eJ_\mu A_b^\mu + e^{'}J_\mu^{'}A_a^\mu. \tag{4.2}$$

With $e$ and $e^{'}$ the respective coupling constants. To discuss the physics arising from the Lagrangians in Eqs 4.1 and 4.2, it is useful to identify from the very beginning two kinds of dark photons:

- the **massless** kind, which does not couple directly to any of the SM currents and interacts instead with ordinary matter only through operators of dimensions higher than four;
- the **massive** kind, which couples to ordinary matter through a current (with arbitrary charge), that is, a renormalisable operator of dimension four. The massless limit of this case does not correspond to the massless case above.

Because of their different coupling to SM particles, the two kinds are best discussed separately. As first discussed in [56] in this case the classical Lagrangian can be diagonalised. What happens at the quantum level and how the mixing manifests itself has been analysed in detail in [57] for the unbroken gauge theory as well as the spontaneously broken case [58]

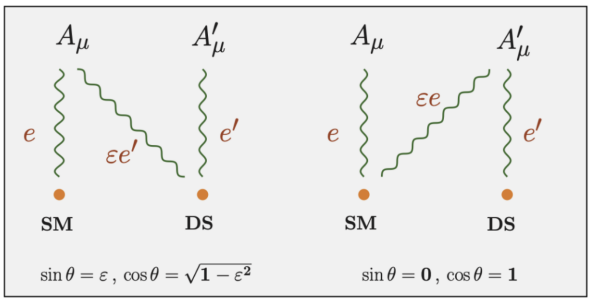


FIGURE 4.1: Scheme of the coupling of the ordinary ($A_\mu$) and dark ($A'_\mu$) photon to the SM and dark-sector (DS) particles for the two choices of the angle $\theta$ discussed in the main text. $e$ and $e'$ are the couplings of the ordinary and dark photons to their respective sectors

The kinetic terms in Eq 4.1 can be diagonalised by rotating the gauge fields as

$$\begin{pmatrix} A_a^\mu \\ A_b^\mu \end{pmatrix} = \begin{pmatrix} \dfrac{1}{\sqrt{1-\varepsilon^2}} & 0 \\ -\dfrac{\varepsilon}{\sqrt{1-\varepsilon^2}} & 1 \end{pmatrix} \begin{pmatrix} \cos\theta & -\sin\theta \\ \sin\theta & \cos\theta \end{pmatrix} \begin{pmatrix} A'^\mu \\ A^\mu \end{pmatrix} \tag{4.3}$$

where now $A^\mu$ is identified with the ordinary photon and $A'^\mu$ with the dark photon. The additional orthogonal rotation in Eq 4.3 is always possible and introduces an angle $\theta$ which is arbitrary as long as the gauge bosons are massless.

After the rotation in Eq 4.3, the interaction Lagrangian in Eq 4.2 becomes:

$$\mathcal{L}' = \left[\frac{e'\cos\theta}{\sqrt{1-\varepsilon^2}} J'_\mu + e\left(\sin\theta - \frac{\varepsilon\cos\theta}{\sqrt{1-\varepsilon^2}}\right) J_\mu\right] A'^\mu + \left[-\frac{e'\sin\theta}{\sqrt{1-\varepsilon^2}} J'_\mu + e\left(\cos\theta + \frac{\varepsilon\sin\theta}{\sqrt{1-\varepsilon^2}}\right) J_\mu\right] A^\mu. \tag{4.4}$$

By choosing $\sin\theta = 0\,(\cos\theta = 1)$ (see right-side of Fig. 4.1), the ordinary photon $A_\mu$ couples only to the ordinary current $J_\mu$ while the dark photon couples to both the ordinary and the dark current $J'_\mu$, the former with strength $\varepsilon e/\sqrt{1-\varepsilon^2}$ proportional to the mixing parameter $\varepsilon$. The Lagrangian is, therefore:

$$\boxed{\mathcal{L}' = \left[\frac{e'}{\sqrt{1-\varepsilon^2}} J'_\mu - \frac{e\varepsilon}{\sqrt{1-\varepsilon^2}} J_\mu\right] A'^\mu + e J_\mu A^\mu} \tag{4.5}$$

On the other hand, with the choice $\sin\theta = \varepsilon$ and $\cos\theta = \sqrt{1-\varepsilon^2}$ (see left-side of Fig. 4.1), the opposite situation with the dark photon occurs, it only couples to the dark current and the ordinary photon to both currents, with strength $\varepsilon e/\sqrt{1-\varepsilon^2}$ to the dark one. This latter coupling between the dark-sector matter to the ordinary photon is called a *milli-charge*. Its value is experimentally known to be small [59]. The dark photon sees ordinary matter only through the effect of operators like the magnetic moment or the charge form factors (of dimension higher than four). This is the choice defining the massless dark photon proper:

$$\boxed{\mathcal{L}' = e' J'_\mu A'^\mu + \left[-\frac{e'\varepsilon}{\sqrt{1-\varepsilon^2}} J'_\mu + \frac{e}{\sqrt{1-\varepsilon^2}} J_\mu\right] A^\mu} \tag{4.6}$$

If the gauge symmetry is spontaneously broken, the diagonalisation of the mass terms locks the angle $\theta$ to the value required by the rotation of the gauge fields to the mass eigenstates and therefore, none of the two currents only couples to one of the two gauge bosons.

This is also the case when the $U(1)$ gauge bosons acquire a mass using the Stueckelberg Lagrangian (see [60] for a review and the relevant references)

$$\mathcal{L}_{Stu} = -\frac{1}{2}M_a^2 A_{a\mu}A_a^\mu - \frac{1}{2}M_b^2 A_{b\mu}A_b^\mu - M_a M_b A_{a\mu}A_b^\mu \tag{4.7}$$

In this case, as in the spontaneously broken case, the angle $\theta$ is fixed and equal to

$$\sin\theta = \frac{\delta\sqrt{1-\varepsilon^2}}{\sqrt{1-2\delta\varepsilon+\delta^2}} \quad \cos\theta = \frac{1-\delta\varepsilon}{\sqrt{1-2\delta\varepsilon+\delta^2}} \tag{4.8}$$

where $\delta = M_b/M_a$, and the rotating of the fields becomes limited compared to 4.3. The Lagrangian in 4.4 becomes

$$\mathcal{L}'' = \frac{1}{\sqrt{1-2\delta\varepsilon+\delta^2}}\left[\frac{e'(1-\delta\varepsilon)}{\sqrt{1-\varepsilon^2}}J'_\mu + \frac{e(\delta-\varepsilon)}{\sqrt{1-\varepsilon^2}}J_\mu\right]A'^\mu + \frac{1}{\sqrt{1-2\delta\varepsilon+\delta^2}}\left[eJ_\mu - \delta e' J'_\mu\right]A^\mu \tag{4.9}$$

The case of spontaneously broken symmetry can be distinguished from the Stueckelberg mass terms because the former will give rise to processes in which the dark photon is produced together with the dark Higgs boson, the vacuum expectation value of which hides the symmetry. Whereas the Lagrangian in 4.9 is the most general, the simplest and most frequently discussed case consists in giving mass directly to only one of the $U(1)$ gauge bosons so that, for instance, $M_b = 0$ in 4.7, the mass states are already diagonal. Even in this simple case, the mass term removes the freedom of choosing the angle $\theta$ in 4.3. With this choice, $\delta = 0$ in 4.9, the ordinary photon couples only to ordinary matter and the massive dark photon is characterized by a direct coupling to the electromagnetic current of the SM particles (in addition to that to dark-sector matter) and described by the Lagrangian

$$\mathcal{L} \supset -\frac{e\varepsilon}{\sqrt{1-\varepsilon^2}}J_\mu A'^\mu \simeq -e\,\varepsilon\,J_\mu A'^\mu \tag{4.10}$$

as in 4.5 above. This is the choice defining the massive dark photon. The coupling of the massive dark photon to SM particles is not quantized—taking the arbitrary value $e\varepsilon$. Because of this direct current-like coupling to ordinary matter, it is the spontaneously broken or Stueckelberg massive dark photon that is mostly discussed in the literature and considered in the experimental proposals. The massive dark photon has the same couplings as the massless dark photon after choosing $\sin\theta = 0$ (right-side of Fig. 4.1); this case, therefore, represents the limit of vanishing mass of the massive dark photon. On the contrary, the massless dark photon proper—corresponding to the choice $\tan\theta = \left[\varepsilon/\sqrt{1-\varepsilon^2}\right]$—is not related to any limiting case of the massive dark photon. There are no electromagnetic milli-charged particles in the massive case; they are present only if both $U(1)$ gauge groups are spontaneously broken (or equivalently $M_b \neq 0$ in the Stueckelberg Lagrangian in 4.7)—which is not the case of our world where the photon is massless.

## 4.2 Massless dark photon: Higher-order operators

The massless dark photon does not interact directly with the currents of the SM fermions. The higher-order operators through which the interaction with ordinary matter $\psi^i$ takes place starting with the dimension-five operators in the Lagrangian

$$\mathcal{L} = \frac{e_D}{2\Lambda_5}\overline{\psi}^i \sigma_{\mu\nu}\left(\mathbb{D}_M^{ij} + i\gamma_5 \mathbb{D}_E^{ij}\right)\psi^j F'^{\mu\nu} \tag{4.11}$$

where $F'_{\mu\nu}$ is the field strength associated to the dark photon field $A'_\mu$, and $\sigma_{\mu\nu} = i/2\,[\gamma_\mu, \gamma_\nu]$. The operator proportional to the coefficient $\mathbb{D}_M$ is the magnetic dipole moment and that proportional to the coefficient $\mathbb{D}_E$ is the electric dipole moment. The indices $i$ and $j$ in the fermion fields keep track of the flavour and thus allow for flavour off-diagonal transitions.

The dimension-five operators in Eq 4.11 are best seen as operators of dimension six with the gauge group $SU(2)_L$ taken as the unbroken symmetry of the Lagrangian and the SM fermion grouped, like in the SM, into doublets $\psi_L$ and singlets $\psi_R$. In this case, the operators contain the Higgs boson field and can be written as

$$\boxed{\mathcal{L} = \frac{e_D}{2\Lambda^2}\overline{\psi}_L^i \sigma_{\mu\nu}\left(\mathbb{D}_M^{ij} + i\gamma_5 \mathbb{D}_E^{ij}\right) H\psi_R^j F'^{\mu\nu} + \text{H.c.}} \tag{4.12}$$

The effective scale is accordingly modulated by the vacuum expectation value (VEV) $v_h$ of the Higgs boson. This VEV keeps track of the chirality breaking, with the whole operator vanishing as $v_h$ goes to zero.

The magnetic dipole $\mathbb{D}_M$ term is retained and the electric dipole term proportional to $\mathbb{D}_E$ is set to zero. The inclusion of the latter would require the further assumption of CP-odd physics which is premature at the moment.

Considering the dimension-six operators

$$\mathcal{L}' = \frac{e_D}{2\Lambda^2}\,\overline{\psi}^i\,\gamma_\mu(\mathbb{R}_r^{ij} + i\gamma_5\,\mathbb{R}_a^{ij})D_\nu\psi^j\,F'^{\mu\nu} \tag{4.13}$$

where the form factor $\mathbb{R}_r$ is related to the charge radius of the fermion; the term $\mathbb{R}_a$ is sometime referred to as the *anapole*.

The operator in Eq 4.13 contributes, via the equations of motion, to four-fermion operators—which are accounted for in the effective field theory of the dimension-six operators [61] but are not relevant for the massless dark photon interaction to ordinary matter—and to the form factors of the interaction if the particles are off-shell.

## 4.3 Dark matter and the dark photon

Dark matter is part of the dark sector. The interplay between the dark photon and dark matter opens new windows on its physics and gives further constraints. Whereas in most scenarios dark matter is one of the fermion (or scalar) states in this sector, there also exists the possibility that dark matter could be a very light vector boson like the massive dark photon itself.

### 4.3.1 Massless dark photon and galaxy dynamics

Models of the self-interacting dark matter charged under Abelian or non-Abelian gauge groups and interacting through the exchange of massless as well as massive particles have a long history.[1]

The most obvious obstacle to having the dark matter in the dark sector interacting via a long-range force as the one carried by the massless dark photon comes from the essentially collisionless dynamics of galaxies and the ellipticity of their dark-matter halo.

The most severe observational limits come from the present dark matter density distribution in collapsed dark matter structures, rather than effects in the early Universe or the early stages of structure formation [68, 69, 79].

Bounds have been derived from the dynamics in merging clusters, such as the Bullet Cluster [85], the tidal disruption of dwarf satellites along their orbits in the host halo, and kinetic energy exchanges among dark matter particles in virialized halos. The latter turns out to be the most constraining bound, noticing that self-interactions tend to isotropize dark matter velocity distributions, while there are galaxies whose gravitational potentials show a triaxial structure with significant velocity anisotropy; limits have been computed, with subsequent refinements, via estimating an isotropization timescale (through hard scattering and cumulative effects of many interactions, also taking into account Debye screening) and comparison to the estimated age of the object [69], or following more closely the evolution of the velocity anisotropy due to the energy transfer [84]. The ellipticity profile inferred for the galaxy NGC720, according to [84] sets a limit of about

$$m_\chi \left(\frac{0.01}{\alpha_d}\right)^{2/3} \gtrsim 300\text{GeV} \tag{4.14}$$

where $m_\chi$ stands for the dark matter mass and the $\alpha_d$ scaling quoted is approximate and comes from the leading $m_\chi$ over $\alpha_s$ scaling in the expression for the isotropization timescale.

The limit in Eq 4.14 is subject to several uncertainties and assumptions; it is less stringent than earlier results, such as the original bound from soft scattering quoted in [68],

$$\frac{G_N m_\chi^4 N}{8\alpha_D^2} \gtrsim 50 \log \frac{G_N m_\chi^2 N}{2\alpha_D} \tag{4.15}$$

where $N$ is the number of dark-matter particles and $G_N$ is Newton's constant, as well about a factor of 3.5 weaker than [69] (see, also, [86, 87]). On the other hand, results on galaxies from $N$-body simulations in self-interacting dark matter cosmologies [88], which take into account predicted ellipticities and dark matter densities in the central regions, seem to go in the direction of milder constraints, about at the same level or slightly weaker than the value quoted in Eq 4.14—again subject to uncertainties, such as the role played by the central baryonic component of NGC720.

[1] The literature on the subject is already very extensive, see, for example, [62, 63, 64, 65, 66, 67, 68, 69, 70, 71, 72, 73, 74, 75, 76, 77, 78, 79, 80, 81, 82, 83, 84].

Interacting dark matter can form bound states. The phenomenology of such atomic dark matter [71] has been discussed in the literature, see [79] and references therein.

### 4.3.2 Massless dark photon and dark-matter relic density

All the stable fields within the dark sector provide a multicomponent candidate for dark matter whose relic density depends on the value of their couplings to the dark photons and SM fermions (into which they may annihilate, depending on the UV model) and masses.

Not all of the dark fermions contribute to the relic density. If these fermions are relatively light, their dominant annihilation is into dark photons.

$$\chi\chi \to A'A' \tag{4.16}$$

with a rate given by

$$\langle \sigma_{\chi\chi\to A'A'} v \rangle = \frac{2\pi\alpha_d^2}{m_\chi^2} \tag{4.17}$$

For a strength $\alpha_d \simeq 0.01$, all fermions with masses up to around 1 TeV have a large cross-section and their relic density.

$$\Omega_\chi h^2 \approx \frac{2.5\times 10^{-10}\ \mathrm{GeV}^{-2}}{\langle \sigma_{\chi\chi\to A'A'} v \rangle} \tag{4.18}$$

is only a per cent of the critical one; it is roughly $10^{-4}$ the critical one for dark fermions in the 1 GeV range, even less for lighter states. These dark fermions are not part of dark matter; they have (mostly) converted into dark photons by the time the universe reaches our age and can only be produced in high-energy events. This is fortunate because they are ruled out as possible dark matter candidates by the limit on galaxy dynamics.

Heavier dark fermions can be dark matter. The dominant annihilation for these is not into dark photons but into SM fermions via the exchange of some messenger field and is proportional to the corresponding coupling which is denoted $\alpha_L$ —with a thermally averaged cross section approximately given by

$$\langle \sigma_{\chi\chi\to f\bar{f}} v \rangle \simeq \frac{2\pi\alpha_L^2}{m_S^2} \tag{4.19}$$

instead of Eq 4.17. The critical relic density can be reproduced if, assuming thermal production,

$$2\pi\alpha_L^2 \left(\frac{10\,\mathrm{TeV}}{m_S}\right)^2 \simeq 0.1 \tag{4.20}$$

These dark matter fermions belonging to the dark sector are in principle detectable through the long-range exchange of the massless dark photon and its coupling to the magnetic (o electric) dipole moment of SM matter which is induced at the one-loop level in the UV model of the dark sector. The somewhat complementary problem of dark matter having dipole moment and interacting with nuclei through the exchange of a photon has been discussed in [89, 90, 91, 92, 93, 94, 95] This dipole interaction is now included within the basis of the operators in the effective field theory of dark matter detection [96, 97, 98].

# 5 Searches for dark photons

Astrophysics and cosmology provide very stringent limits on the interaction of the dark photon with SM matter. It is understood that all the limits are mostly on the order of magnitude because of intrinsic uncertainties in the astrophysics of stellar medium, supernova dynamics and cosmological processes. In addition, other experimental searches are listed in the following.

## 5.1 Where to search for the massless dark photon ?

The massless dark photon can be searched for in different experiments:

- Flavor physics: This is one of the most promising areas for searching for the dark photon and the dark sector in general because none of the stringent astrophysical constraints applies given the flavour off-diagonal nature of the dipole operator in these cases. Proposals exist for processes in Kaon physics at NA62 [99]. The Kaon decay $K \to \pi A'$ is forbidden by the conservation of angular momentum but the decay $K^+ \to \pi^0\pi^+A'$ is allowed and the estimated branching ratio [100] is within reach of the current sensitivity. The rare decays $K^+ \to \pi^+\nu\bar{\nu}$ [101] and $K_L \to \pi^0\nu\bar{\nu}$ [102] are other two processes where the physics of the dark photon can play a crucial role [103]. Also, Hyperion decays can be used for detecting the production of $A'$ [104] and in the decay of charmed hadrons [105] and BESIII. In addition, decays into invisible states of $B$-mesons at BaBar [106] and Belle [107] and $K_{L,S}$ and other neutral mesons at NA64 [108, 109] can be used to study the dark sector (assuming the invisible states belong to it). These decays are greatly enhanced by the Fermi-Sommerfeld [110, 111] effect due to their interaction with the dark photon—the same way as ordinary decays, like the $\beta$-decay, are enhanced by the same effect—making this another exciting area for searching the dark sector [112].

- Higgs and $Z$ physics: The striking signature of a mono-photon plus missing energy can be used to search Higgs [13, 113, 114] and $Z$-boson [115, 116] decay into a visible and a dark photon. Again, the stringent astrophysical constraints do not apply because the size of the dipole operator is dominated (in the loop diagram) by the heavy-quark contribution's giving raise to the coupling to the dark photon.

- Pair annihilation: Collider experiments at higher energies and luminosity can use the same striking signature of a mono-photon plus missing energy to search for the dark photon. Even

though the dipole interaction is suppressed and severely constrained in this case by the astrophysical and cosmological bounds, it is no more suppressed than the equivalent cross sections for the massive case. Moreover, the dipole operator scales as the centre-of-mass energy in the process and higher energies make it more and more relevant;

- Magnons: An interesting possibility is the use of magnons in ferromagnetic materials and their interaction with dark photons (QUAX proposal) [117, 118]. The estimated sensitivity is again done for axions but can be translated for massless dark photons as in the discussion about stars above.

- Astrophysics: Gravitation waves emitted during the inspiral phase of neutron star collapse can test the presence of other forces besides gravitation. Dipole radiation by even a small amount of charges on the stars modifies the energy emitted; the dark photon is a prime candidate for this kind of correction [119, 120, 121, 122].

## 5.2 Dark Photon Searches at the LHC

The search for dark photons is among the many topics to search for dark matter at the LHC. In this chapter, the main phenomenological and experimental results of the dark photon production via Higgs boson decay at the LHC are summarised.

### 5.2.1 Phenomenology: Higgs boson to dark photon

The Higgs boson is produced in the proton-proton collisions at the LHC through different channels with different cross sections, the main ones are the gluon-gluon Fusion (ggF), the Vector Boson Fusion (VBF) and the associated production of VH, where V is a vector boson and it could be a $Z$ or a $W^+$, $W^-$ boson. At a centre-of-mass energy $\sqrt{s}$ =13 TeV and for a SM Higgs boson of 125 GeV mass, the cross-section of the Higgs boson production in the different channels are given in Table 5.1. Given the differences in the production cross-section of the Higgs boson as well as in the kinematics of each signature, each channel is treated independently.

TABLE 5.1: SM Higgs boson production cross section in the main production channels.

| Higgs boson production mode | ggF | VBF | ZH |
|---|---|---|---|
| Cross-section (pb) | 4.198E+01 | 3.925E+00 | 9.095E-01 |

The high cross-sections of ggF and VBF productions of the Higgs boson Table 5.1, make them the most dominant modes at the LHC, giving rise to the largest production rate for a hypothetical scalar boson with SM Higgs-like couplings for the entire mass range of interest. A person-level simulation study was performed at $\sqrt{s}$ =8 TeV and $\sqrt{s}$ =14 TeV for the $H \to \gamma\gamma_d$, where the Higgs is produced either in the ggF or in the VBF channels respectively as shown in Figure 10.1.

The signal is characterised by a single photon recoiling against missing transverse momentum $\gamma + E_{\mathrm{T}}^{\mathrm{miss}}$ (and two forward jets with opposite rapidity in the VBF channel). The SM backgrounds for this process are dominated by $pp \to \gamma + jets$ and QCD multi-jet background $pp \to jets$, where the missing transverse momentum can arise from several sources, e.g., (a) jet energy mismeasurement, (b) invisible neutrinos arising from decays of heavy-flavour jets, and (c) very forward particles escaping the detector. The latter process contributes to the $\gamma + E_{\mathrm{T}}^{\mathrm{miss}}$ final state whenever one of the jets is misidentified as a photon. The main electroweak background consists of $pp \to W \to e\nu$, where the

electron is misidentified as a photon, $pp \to W(\to \ell\nu)\gamma$, for $\ell$ outside charged-lepton acceptance, and $pp \to Z(\to \nu\nu)\gamma$.

The signal and the background signatures could be distinguished thanks to some kinematic observable, such as the missing transverse energy ($E_{\mathrm{T}}^{\mathrm{miss}}$), the transverse momentum of the photon ($p_{\mathrm{T}}^{\gamma}$), and the transverse mass of the photon-invisible system ($m_{\mathrm{T}}(\gamma, \gamma_d)$). The latter carries the typical signature of the $H \to \gamma\gamma_d$ decay and is defined in Equation 9.1, where $\Delta\phi$ is the azimuthal distance between the photon transverse momentum $p_{\mathrm{T}}^{\gamma}$and the missing transverse momentum $E_{\mathrm{T}}^{\mathrm{miss}}$. The $E_{\mathrm{T}}^{\mathrm{miss}}$ is defined as the unbalanced momentum in the transverse plane due to the presence of invisible particles. The expected $m_{\mathrm{T}}(\gamma, \gamma_d)$ distribution for the signal is to peak at around the Higgs boson mass as shown in Figure 5.1.

$$m_{\mathrm{T}} = \sqrt{2E_{\mathrm{T}}^{\mathrm{miss}} p_{\mathrm{T}}^{\gamma}[1 - \cos[\Delta\phi(\vec{E}_{\mathrm{T}}^{\mathrm{miss}}, \vec{p}_{\mathrm{T}}^{\gamma})]]} \tag{5.1}$$

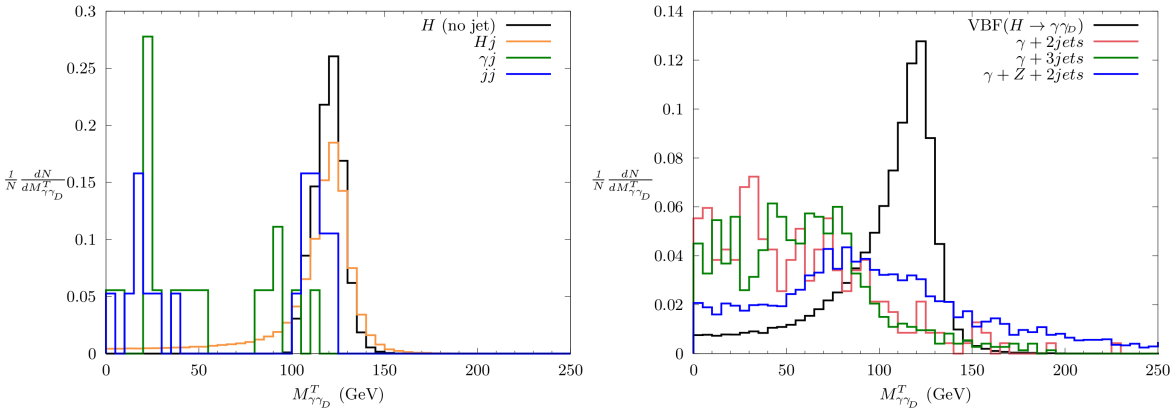


FIGURE 5.1: Transverse-mass distributions for the $H \to \gamma\gamma_d$ signal in the ggF (left), and VBF (right) processes. Corresponding distributions for SM backgrounds for inclusive $\gamma + E_{\mathrm{T}}^{\mathrm{miss}}$ (ggF) and $\gamma + E_{\mathrm{T}}^{\mathrm{miss}} + two forward jets$ (VBF) final states (with no isolated leptons), respectively, have also been shown. All distributions are normalized to unity.

This phenomenological study resulted in extracting the reach in BR($H \to \gamma\gamma_d$) for a 95% C.L ($2\sigma$) exclusion limit or a ($5\sigma$) discovery potential at $\sqrt{s}$ =14 TeV LHC for different integrated luminosities. For the ggF processes, at an integrated luminosity of 100 (300) fb$^{-1}$the $2\sigma$ exclusion limit on BR($H \to \gamma\gamma_d$) is found to be $6.41 \times 10^{-4}(3.71 \times 10^{-4})$, whereas the $5\sigma$ discovery reach is $1.61 \times 10^{-3}(9.21 \times 10^{-4})$. The corresponding $5\sigma$ reach can be improved down to $2.91 \times 10^{-4}$ at the High-Luminosity LHC (HL–LHC), with an integrated luminosity of 3000 fb$^{-1}$. For the VBF process, at an integrated luminosity of 100 (3000) fb$^{-1}$, the $5\sigma$ reach in the branching ratio is about BR($H \to \gamma\gamma_d$)$\simeq$ 2% $(3.41 \times 10^{-3})$. A comparison of significances for both of these Higgs production channels is presented in Table 5.2.

TABLE 5.2: 95% C.L. ($2\sigma$) exclusion or a $5\sigma$ discovery at $\sqrt{s}$ =14 TeV, in the ggF and VBF channels, for different integrated luminosities L.

| BR($H \to \gamma\gamma_d$)(%) | L= 100fb$^{-1}$ | | L= 300fb$^{-1}$ | | L= 3000fb$^{-1}$ | |
|---|---|---|---|---|---|---|
| Significance | $2\sigma$ | $5\sigma$ | $2\sigma$ | $5\sigma$ | $2\sigma$ | $5\sigma$ |
| BR($H \to \gamma\gamma_d$)(ggF) | 0.064 | 0.16 | 0.037 | 0.092 | 0.012 | 0.029 |
| BR($H \to \gamma\gamma_d$)(VBF) | 0.76 | 1.9 | 0.43 | 1.1 | 0.14 | 0.34 |

### 5.2.2 Experimental Searches at the LHC

The LHC experiments, ATLAS and CMS have searched for the dark photons from the Higgs boson decay in two different production channels, namely, VBF and ZH.

**VBF production:** Both the ATLAS and CMS experiments studied the $\gamma + E_{\mathrm{T}}^{\mathrm{miss}} + jets$ final state via the VBF Higgs boson production channel. The data collected in this channel has been interpreted in the context of Higgs boson decay to a photon and massless dark photon which goes undetected, $\gamma + \gamma_d + jets$. The SM backgrounds for this process are $V\gamma + jets$, where V = Z, W and $\gamma + jets$. In the case of $Z\gamma + jets$, the Z boson decays to a pair of $\nu\bar{\nu}$ and gives rise to an isolated photon, missing transverse momentum, and jets. $W\gamma + jets$ contribute to the same final state when the $W$ boson decays to a lepton and a neutrino, and the lepton goes missing as it may not satisfy the required identification criteria. The ATLAS search for $H \to \gamma\gamma_d$ in the VBF channel utilised 139 fb$^{-1}$data collected by the ATLAS experiment during 2015–2018 at $\sqrt{s}$ =13 TeV LHC collision energy. The search resulted in setting exclusion limits BR($H \to \gamma\gamma_d$) as a function of the hypothetical neutral Higgs boson in the mass range 60 GeV $< m_H <$ 2 TeV (Figure 5.2). The corresponding bound obtained by the ATLAS experiment is 0.19 pb. Assuming a SM-like Higgs production cross section in the VBF channel in this mass range, the results can be interpreted as a bound on BR($H \to \gamma\gamma_d$) for the SM Higgs boson ($m_H = 125$ GeV), the 95% C.L. upper corresponds to 0.014.

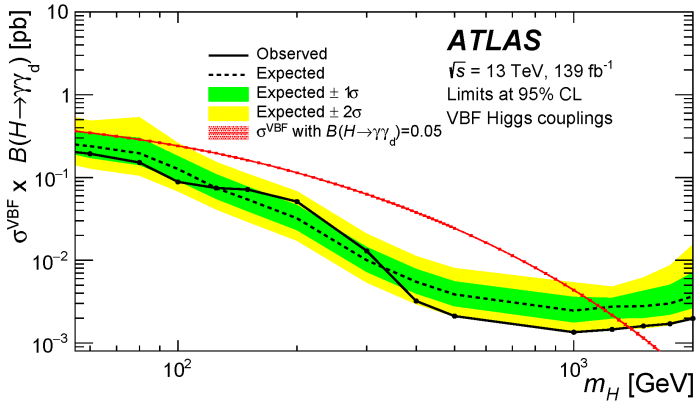


FIGURE 5.2: Observed and expected 95% C.L. upper limit on the Higgs production cross-section times BR($H \to \gamma\gamma_d$), for various scalar mass hypotheses. The red line corresponds to the theoretical SM-like Higgs production cross section in VBF channel times BR($H \to \gamma\gamma_d$)=5%..

The results of the corresponding CMS analysis in the VBF channel are shown in Figure 5.3 which corresponds to 130 fb$^{-1}$of data collected by the CMS experiment during 2016–2018 at $\sqrt{s}$

=13 TeV LHC collision energy. The observed 95% C.L. on the BR($H \to \gamma\gamma_d$) obtained by the CMS collaboration is 3.5% for the SM Higgs boson with $m_H = 125$ GeV.

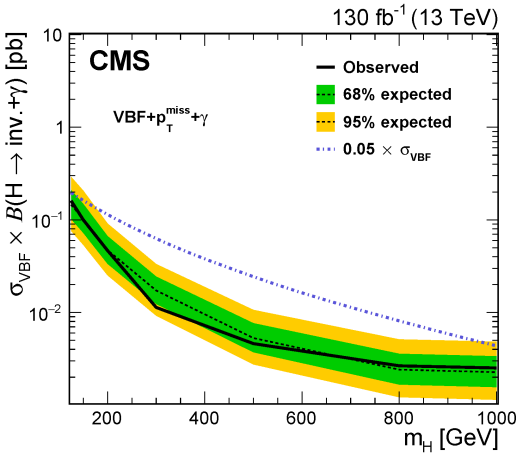


FIGURE 5.3: CMS bound on the cross-section ($\sigma_{VBF}$) times BR($H \to \gamma\gamma_d$) in the VBF channel as a function of the scalar mass ($m_H$ ). A solid black line corresponds to the observed limit, while the the black dashed line corresponds to the expected limit at 95% C.L. The dotted dashed line represents the signal corresponding to a SM $\sigma_{VBF}$ value and BR($H \to \gamma\gamma_d$)=5%

**ZH production:** The Higgs production in association with a Z-boson is another way to search for the dark photon, this channel benefits from a clean final state $pp \to Z(\to \ell^+\ell^-)H(\to \gamma\gamma_d)$ as presented later in Chapter 9. The thesis includes the full strategy and the results of the ATLAS search for the dark photon in the ZH production mode. In the same context, the CMS collaboration has searched for the dark photon in the ZH channel using the pp collisions with subsequent decay of the Higgs into a photon plus an undetected particle using the 137 fb$^{-1}$of data collected at $\sqrt{s}$ =13 TeV. In the absence of any significant excess over the SM backgrounds, an exclusion limit can be set on theoretical models predicting such exotic decay of the Higgs boson. The results of the CMS study have been interpreted in the context of models predicting the $H \to \gamma\gamma_d$ decay as presented in Chapter 10

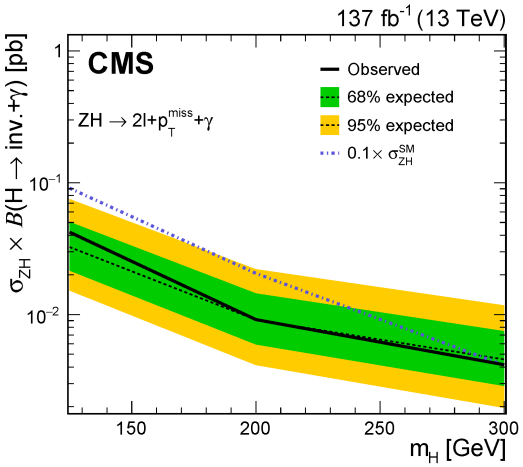


FIGURE 5.4: CMS bound on the cross-section ($\sigma_{ZH}$) times BR($H \to \gamma\gamma_d$) in the ZH channel as a function of the scalar mass ($m_H$ ). A solid black line corresponds to the observed limit while the the black dashed line corresponds to the expected limit, at 95% C.L. The dotted dashed line represents the signal corresponding to a SM $\sigma_{ZH}$ value and BR($H \to \gamma\gamma_d$) = 10%

# Part II

# EXPERIMENTAL SETUP

# 6 The Large Hadron Collider

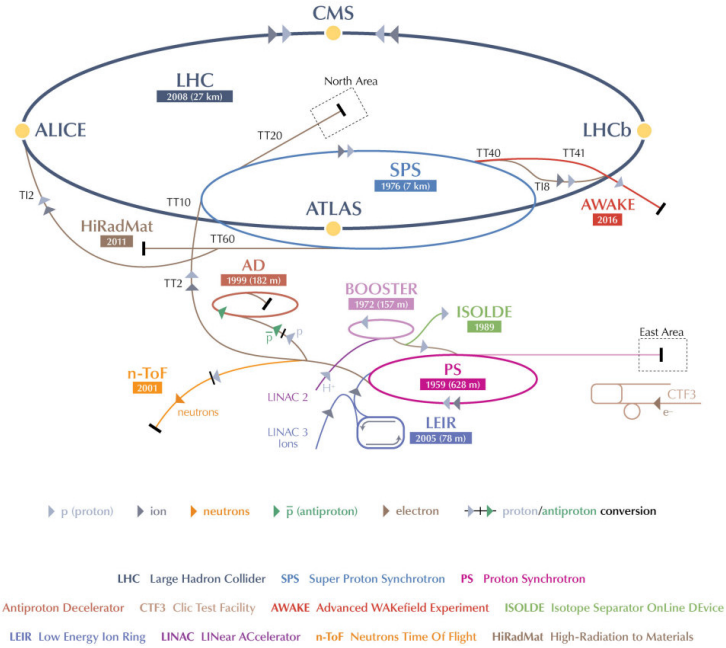


FIGURE 6.1: Sketch of the accelerator complex situated at CERN[123]. The acceleration of particles is done in consecutive steps, with the particles passing through different accelerators with different final energy.

The Large Hadron Collider (LHC) [124, 125] is an accelerator situated at the CERN laboratory, on the border between France and Switzerland. The accelerator is placed in a circular underground tunnel, at a depth of roughly 100 m and a circumference of 27 km, that previously hosted the Large Electron-Positron (LEP) collider. It is designed for proton-proton collisions at a maximum centre-of-mass energy $\sqrt{s}$ of up to 14 TeV, reaching a design instantaneous luminosity of $10^{34}\,\mathrm{cm}^{-2}\,\mathrm{s}^{-1}$. The LHC can also be configured to collide heavy ions. Making great use of a full chain of several previously built accelerator facilities (see 6.1) available at CERN to gradually accelerate particles to higher and higher energies, the injected particles go through various steps before being injected into the LHC itself. In the first step, hydrogen atoms are ionised and the bare protons are accelerated up to 50 MeV by the linear accelerator LINAC2. They are further injected into the proton synchrotron booster (PSB) and accelerated to 1.4 GeV before entering the proton synchrotron (PS). They leave the PS with an energy of 26 GeV and get injected into the Super Proton Synchrotron (SPS) which is the

last step before the LHC. They leave the SPS with an energy of 450 GeV and get injected into the LHC ring to increase the energy to the TeV scale. For the final acceleration in the LHC, superconducting radio frequency (RF) cavities [126] are utilised. Over the complete ring 16 RF cavities housed in four *cryomodules* are installed, bringing the 450 GeV energy of the protons to 6.5 TeV per beam. To bend the particles along their path within the beam pipe, 1232 superconducting dipole magnets are used. To avoid a spread of protons within the beam, they are additionally focused with quadrupole magnets. The particle beam within the LHC consists of separate bunches, each of which is made up of about $1.15 \times 10^{11}$ protons. During full-intensity operation, 2808 bunches per each beam are circulating within the LHC and brought to collision every 25 ns in the interaction points. To reach a high instantaneous luminosity, which is desirable to achieve large data sets, the beam bunches are tailored to lead to, on average, more than one $pp$ collision during a bunch crossing. That means that after triggering a high momentum hard scattering interaction, additional lower momentum $pp$ collisions will act as a background noise within the chosen events. This background is commonly referred to as *pileup*. Two different forms of pileup are differentiated, in-time pileup and out-of-time pileup. While additional $pp$ collisions within the same bunch crossing are called in-time pileup, out-of-time pileup is background signals found in the detector originating from previous or following bunch crossings. During the *Run 2* data taking, which denotes the period of operations between 2015 and 2018, the LHC delivered an integrated luminosity of 156 $\text{fb}^{-1}$, as can be seen from 6.2a. The pileup configuration changed between the years and lead to an average pileup of $\langle\mu\rangle = 33.7$ when integrating over the whole *Run 2* data set. The profile of $\langle\mu\rangle$ is displayed in 6.2b.

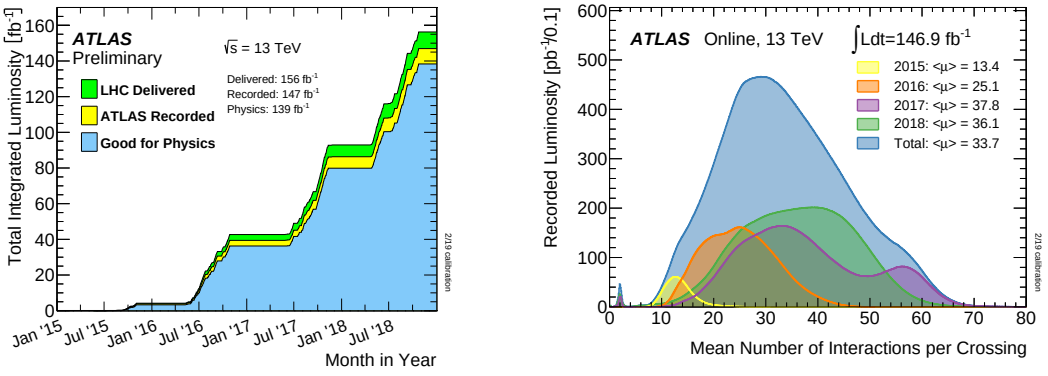


(a) (b)

FIGURE 6.2: (a): The cumulative integrated luminosity delivered by LHC and the fraction recorded by ATLAS and categorised as good for physics analysis. (b): Distribution of the average pileup $\langle\mu\rangle$. The average pileup during the full *Run 2* amounts to $\langle\mu\rangle = 33.7$ [127].

# 7 The ATLAS Experiment

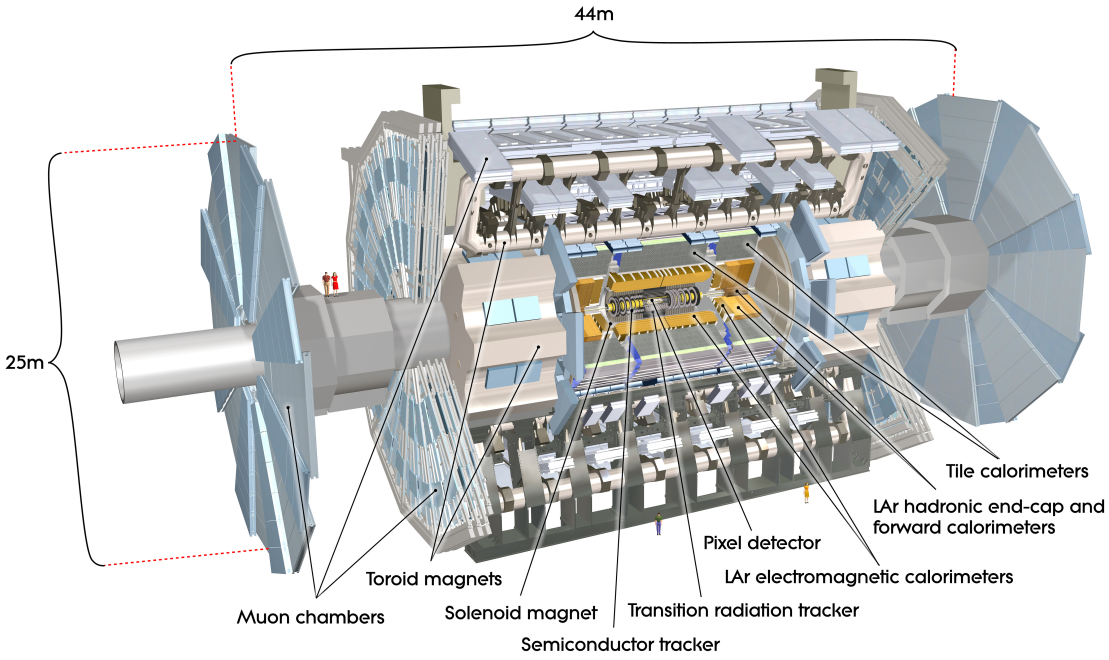


FIGURE 7.1: Overview of the ATLAS detector in cutaway style [128].

The ATLAS detector is a general-purpose particle detector which is designed [129] to cover a large field of physics including the search for potential new physics at the Large Hadron Collider (LHC). These range from Higgs physics over standard model measurements in the top quark and b-physics sectors to beyond standard model searches like searches for supersymmetric particles or heavy gauges bosons [130]. Its layout is optimised to provide excellent reconstruction efficiency and resolution for electron, photon, muon, tau-lepton and jet and missing transverse energy measurements and to perform under high luminosity conditions at the LHC for extended runtime.

This chapter describes the different subsystems of ATLAS, an overview of which can be seen in 7.1. The detector is built up in layers that each serves a specific task in the process of reconstructing the collision events. 7.1 discusses the Inner Tracker, which is responsible for reconstructing the trajectories of charged particles, called tracks. The electromagnetic and hadronic calorimeters, which have the purpose of stopping particles to measure their energy, are covered in 7.2. The muon system,

typically located outside of calorimeter systems due to the high penetration power of muons, is described in 7.3. 7.4 finally discusses the magnet system producing the magnetic field that ATLAS is immersed in.

For physics analysis, good knowledge of the luminosity delivered by the accelerator facilities is necessary, for which dedicated systems are deployed. These are briefly presented in 7.5. The trigger, allowing to bring down the event rate from the 40 MHz delivered by the LHC to a manageable rate for the data acquisition system and the storage facilities is discussed in 7.6. ATLAS uses a detailed computer simulation of its detector, implemented in the GEANT4 toolkit [131]. An overview of the available simulation structures is given in 7.7.

The ATLAS detector has – during its lifetime – undergone updates and configuration changes. The descriptions within this chapter apply to the *Run 2* configuration. In the following a stronger focus will be placed on the parts of the detector that are of more relevance to the studies performed within the scope of this work. For a full description of ATLAS, the reader is referred to [128].

## 7.1 Inner Detector

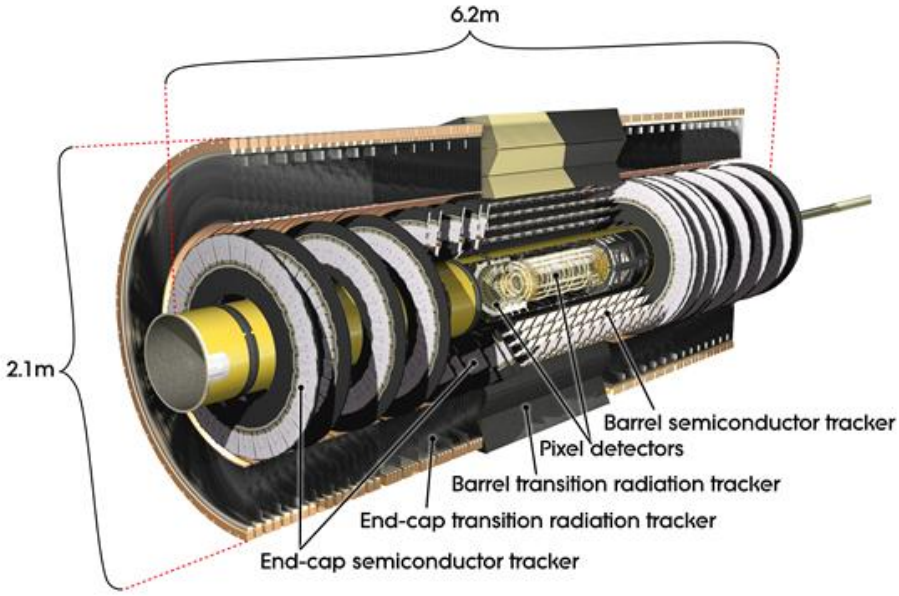


FIGURE 7.2: The Inner Detector of ATLAS [128], showing the different tracking sub-detectors in both the barrel and the end-cap region.

The basic task of a tracking detector is to provide measurements of charged tracks that allow for precise reconstruction of their trajectories. Using these it is possible to infer the particles' momenta as well as reconstruct the position of $pp$ collisions, called vertices, with high resolution. The ATLAS Inner Detector (ID) uses a combination of different technologies to meet the set requirements necessary to enable the physics program [132, 133]. Concentric layers of particle detectors with decreasing granularity for larger radii are deployed, allowing for full tracking coverage over the pseudorapidity [1] range $|\eta| \leq 2.5$. The concept followed by the Inner Detector design is to provide high precision

[1] ATLAS uses a right-handed coordinate system with its origin at the nominal interaction point, corresponding to the centre of the detector. The $x$ axis direction points towards the centre of the LHC ring, the $y$ axis vertically upwards, and the $z$ axis lies along the beam line. Pseudorapidity is defined in terms of the polar angle $\theta$ as $\eta = -\ln\tan\theta/2$, and transverse momentum and energy are defined relative to the beamline as $p_T = p\sin\theta$ and $E_T = E\sin\theta$.

measurements needed for track finding in the innermost parts of the tracking detector and follow with continuous tracking elements that add further measurements and improve the momentum resolution of the identified tracks in the outer parts of the tracker. This combination of technologies allows for reaching the design targets while keeping the total material budget low as well as limiting the cost of the detector system. A cutaway view of the Inner detector is shown in 7.2.

Closest to the interaction point, where high resolution is needed for vertex reconstruction and at the same time the track density is highest, four layers of silicon pixel sensors are utilised in the *Pixel Detector*, which will be described in 7.1.1. It is surrounded by further four precision layers of silicon micro-strip sensors. This so-called *Semiconductor Tracker* (SCT) is presented in 7.1.2. In the outer part of the Inner Detector, called *Transition Radiation Tracker* (TRT), track extensions using the high number of measurements provided by a large number of straw tubes allow for improved momentum measurement capabilities. Additionally, the TRT plays an important role in electron identification and photon conversion detection through the measurement of transition radiation photons. Details are provided in 7.1.3.

The whole Inner Detector is immersed in a 2 T magnetic field (see 7.4) which bends the trajectories of charged particles produced in the proton-proton collisions under the Lorentz force, allowing to infer the momentum from the particles' path as well as their electric charge.

### 7.1.1 The Pixel Detector

The pixel detector [134] provides high-precision measurements in the area closest to the interaction point. At the high luminosity environment of the LHC, the large density of charged tracks requires fine granularity to maintain occupancies low enough for performant pattern recognition that fulfils the requirements on vertex and momentum resolution. For this purpose, n-type silicon pixel sensors are deployed [135].

The individual sensors have a thickness of 250 µm and external dimensions of 19 mm × 63 mm. The nominal pixel pitch size on these sensors is 50 µm × 400 µm and 50 µm × 250 µm in the innermost layer in $R-\phi$ and $z$. Each sensor contains 47 232 pixels that are read out by ASICs bump bonded to the pixel elements. In total, the pixel detector has about 140 million read-out channels.

The pixel detector is separated into two parts, the barrel ($|\eta| < 1.5$) and the end-caps ($1.5 \leq |\eta| \leq 2.5$). In the barrel, the sensors are arranged on four concentric cylindrical layers around the beam pipe, where the innermost layer – the Insertable B-Layer (IBL) – was installed for the LHC Run 2 together with a beam pipe of reduced inner radius [136]. The four-barrel layers are located at nominal radii of 33 mm, 50.5 mm, 88.5 mm and 122.5 mm from the beam axis. The end-caps are made up of rings, with the sensor modules placed perpendicular to the beam axis. An overlap of the sensor modules guarantees hermetic coverage, providing typically four measurements per track.

While the pixel detector offers the best intrinsic resolution of 14 µm × 115 µm per space point, due to the necessity of on-sensor read-out chips for the roughly 80 million readout channels it contributes strongly to the total material budget of the ID, as can be seen from 7.3.

### 7.1.2 The Semiconductor Tracker

The Semiconductor Tracker (SCT) surrounds the Pixel Detector and forms the second component of the precision tracking part of the Inner Detector. Instead of pixel sensors, the SCT uses micro-strip sensors [137]. The detector is partitioned into a barrel and an end-cap part. The barrel consists of four concentric layers at average radii of 300 mm, 373 mm, 447 mm and 520 mm. The end caps are made up of nine disks, complementing the coverage of the SCT to $|\eta| < 2.5$.

Individual modules consist of double-sided silicon micro-strip sensors that are mounted parallel to the beam pipe in the barrel region and radially on the SCT disks. Each individual strip has nominal dimensions of 80 µm in $R - \phi$ and 126 mm in $z$. The detector's $z$ resolution is achieved by mounting strips on the two sides of a module under a small stereo angle of 40 mrad.

On average four measurements per track are provided by the SCT, which have an intrinsic resolution of 17 µm $\times$ 580 µm per space point in $R - \phi$ and $z$ respectively.

### 7.1.3 The Transition Radiation Tracker

The Transition Radiation Tracker (TRT) sits outside the Pixel Detector and SCT volumes. The basic detecting elements in the barrel are 150 cm long polyimide drift tubes (straws) of 4 mm thickness, that contain gold-plated tungsten anode wires of 31 µm diameter. To lower the overall occupancy, each straw is divided into two parts at the centre, both read out at the respective ends. The TRT allows tracking algorithms to extend tracks that are seeded and built in the inner part of the tracker and add additional measurements, improving the momentum resolution.

In total 50000 straws are installed in the barrel part of the TRT [138] and additional 320000 radial straws in the end-caps [139], allowing for an average of 36 measurements per track. This large number of measurements significantly improves the momentum resolution of tracks. Due to the drift-time measurement possible at each channel, enhancing the intrinsic spatial resolution due to the straw dimensions, an excellent spatial resolution of 170 µm in $R - \phi$ is reached.

The TRT plays also an important role in the identification of electrons in ATLAS. Electrons, being light particles, exhibit a higher probability to emit photons as transition radiation while passing the TRT materials. The gaps between the straws are filled with a transition radiator, either a polypropylene film or polypropylene fibres. By filling the straws with a gas mixture consisting mainly of Xenon that has a large cross-section for the emitted photons to deposit energy via the photoelectric effect, this effect is enhanced. Compared to minimum-ionising charged particles, the transition radiation signals yield a much larger signal amplitude. Using separate low and high thresholds in the read-out allows for applying distinction criteria between hadrons and electrons that can be taken into consideration during the electron reconstruction procedure. In addition, a systematic study was performed as a qualification task to identify sources of discrepancies between the TRTxAOD and the calibration formats. This work resulted in identifying and fixing the issue in the TRT reconstruction software after being validated in both data and MC simulation samples, this work is documented in Appendix A of this thesis.

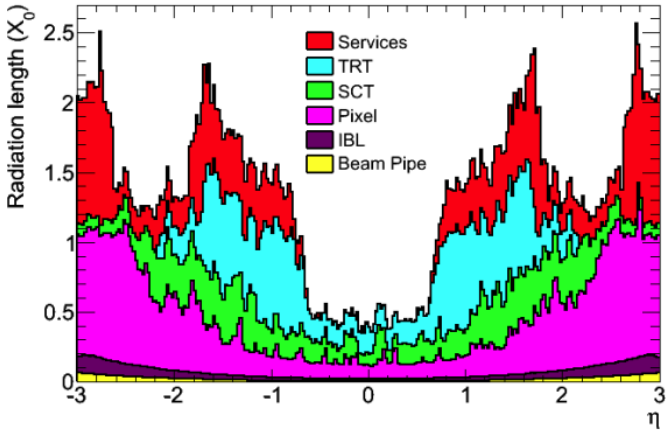


FIGURE 7.3: Cumulative material budget of the Inner Detector, given in radiation length units [136]. The sizeable contribution coming from the pixel detector alone which is strongly increasing over $|\eta|$ is visible in pink.

## 7.2 Calorimeter system

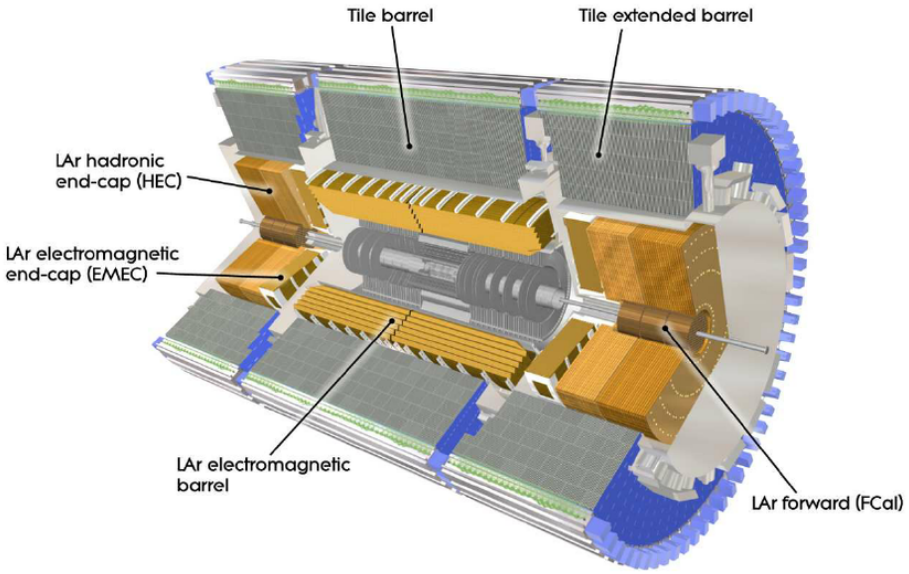


FIGURE 7.4: Cutaway view of the ATLAS calorimetric system [128]. The EM calorimeter sits inside the hadronic calorimeter. The split into the barrel and the end-cap partitions is visible.

The calorimeter system of ATLAS, presented in 7.4, is separated into two subsystems, the electromagnetic and the hadronic calorimeter, which combined cover the pseudo-rapidity range of $|\eta| < 4.9$. Its purpose is to provide high-resolution kinematics measurements for photons, electrons, jets and missing transverse energy ($E_{\mathrm{T}}^{\mathrm{miss}}$). The basic principle for calorimetric measurements is to stop particles coming from the interaction point (except for muons and neutrinos) within the detector volume and measure the charge deposited in the active material, which allows inferring the energy of a particle. The high granularity of the detector systems additionally gives excellent directional measurements as well as the capability of strong particle identification. The main requirement for a good $E_{\mathrm{T}}^{\mathrm{miss}}$

measurement is hermeticity, meaning both a large pseudo-rapidity coverage as well as the ability to fully contain electromagnetic and hadronic showers in their lateral extension. The combination of both calorimetric systems fulfils these constraints.

### 7.2.1 Electromagnetic calorimeter

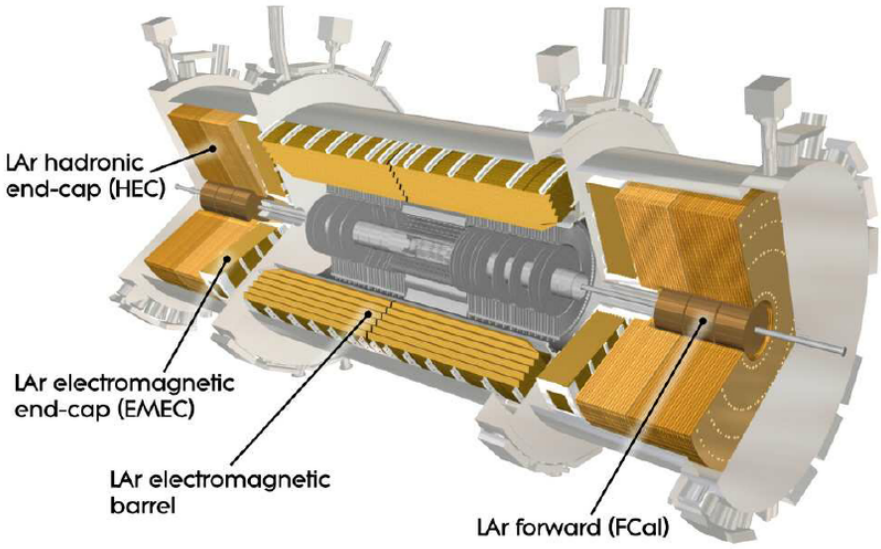


FIGURE 7.5: Cutaway view of the LAr calorimeter subdetectors [140].

The main energy loss mechanisms relevant for photons and electrons are bremsstrahlung, pair-production and ionisation. Electrons of energies $> 1\,\text{GeV}$ produce secondary photons by bremsstrahlung, and photons produce secondary electron-positron pairs via pair production. These secondaries in turn produce more particles via the same mechanism, causing a cascade of particles with progressively lower energies, called an EM *shower*. At low enough energies, the particles ionise the detector medium, which generates a signal that can be read out. The purpose of the electromagnetic (EM) calorimeter is to determine the energy of the electromagnetic part of particle showers by measuring the charge deposited in the active material. ATLAS uses a lead-liquid argon (LAr) sampling calorimeter [141] with accordion-shaped absorbers and electrodes (see 7.6b). The EM calorimeter is used for both triggering and precision measurements and operates in an energy range from several GeVto the TeVscale.

The EM calorimeter consists of a barrel part (EMB) covering the pseudo-rapidity range of $|\eta| < 1.475$ and two end-cap calorimeters (EMEC) extending the range to $1.375 < |\eta| < 3.2$, both of which are highlighted in 7.5. The EMB has a length of 6.4 m, an inner radius of 1.4 m and an outer radius of 2 m. It is split into two half barrels, each of which consists of 1024 absorbers. The thickness in terms of radiation lengths is at least 22 $X_0$ and is increasing with $\eta$. Each of the two EMEC calorimeters consists of two co-axial wheels that are 63 cm thick and sit between an inner radius of 33 cm and an outer radius of 210 cm. It has a thickness of least 22 $X_0$, increasing with $\eta$.

In the longitudinal dimension that describes the depth of the detector, the EMB is separated into three sampling layers with different granularity in each layer as can be seen in the sketch shown in 7.6a. Also, a presampler consisting of a 1 cm liquid argon layer is installed to correct for energy loss

in front of the calorimeter. An optimal choice of granularity is of high importance for the photon and electron identification capabilities as well as the positional and directional resolution. Longitudinal and transversal segmentations allow measuring the shape of an electromagnetic shower which provides important information for the discrimination between electromagnetic and hadronic showers. In the $\eta$ direction the segmentation is obtained by etching the respective patterns on the individual electrodes, while in the $\phi$ direction the adequate number of electrodes is grouped. The first layer possesses a very fine granularity of $0.003 \times 0.1$ in $\Delta\eta \times \Delta\phi$., which is instrumental to correctly reconstructing the direction of detected photon candidates. It also plays an important role in the rejection of neutral pions when decaying via $\pi^0 \rightarrow \gamma\gamma$, which forms a dominant background for photon identification. The second sampling, where electromagnetic showers deposit the majority of their energy, has a granularity of $0.025 \times 0.0245$ in $\Delta\eta \times \Delta\phi$. A coarser granularity of $0.05 \times 0.025$ in $\Delta\eta \times \Delta\phi$ has been chosen for the last sampling layer, which registers only the tails of showers and does not need the same fine segmentation.

The accordion shape geometry of absorbers and electrodes has the great benefit of naturally providing full $\phi$ coverage of the detector, without any cracks. The absorbers made out of lead are mechanically strengthened by steel sheets glued to them using a resin-impregnated glass-fibre fabric. In between these, copper layers are located that act as the readout electrodes. The space between the absorber and electrode is filled by the liquid argon as active material which is ionised by charged particles passing through the medium. Three copper layers insulated by polyimide sheets make up one electrode, where the outer two are at high-voltage potential and the inner one acts as the readout via capacitive coupling.

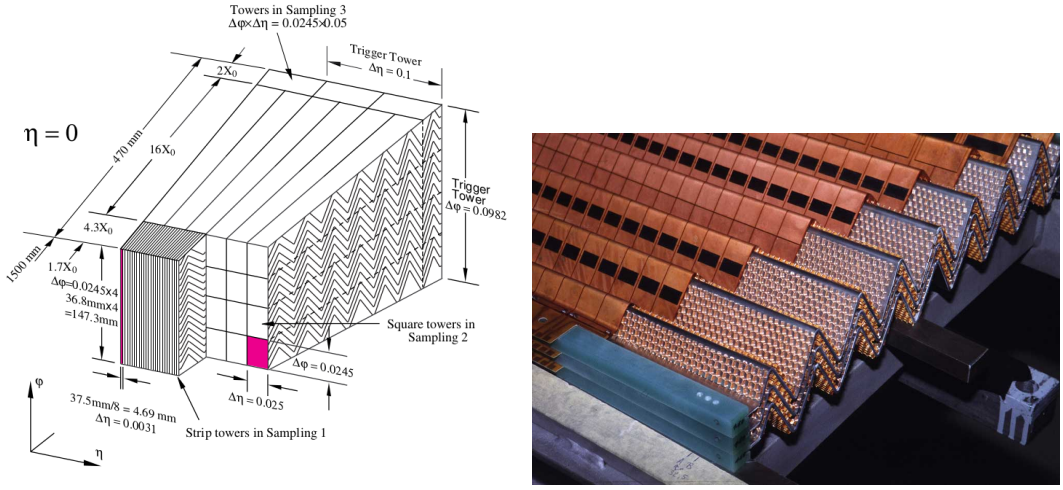


(a) (b)

FIGURE 7.6: (a): Sketch of the cell structure in the different sampling layers of the EM calorimeter [141]. Layers closer to the interaction point exhibit a finer granularity in $\eta$. (b): Photograph of the accordion-shaped electrodes of the EM barrel calorimeter, assuring full $\phi$ coverage of the detector [142].

The energy resolution provided by the EM calorimeter depends on the energy and can be described by [143]

$$\frac{\sigma_E}{E} = \frac{a}{\sqrt{E}} \oplus \frac{b}{E} \oplus c. \tag{7.1}$$

The first term is called the stochastic term which depends on fluctuations in the shower developments. The second term in 7.1 stems from electronic noise in the readout chain and decreases for increasing energies, where the signal-to-background ratio becomes larger. The last term, the constant term, does

not depend on the particle's energy and is caused by non-uniformities or imperfections in the detector system or readout system.

### 7.2.2 Hadronic calorimeter

The hadronic calorimeter system sits outside of the electromagnetic calorimeters. Hadronic showers develop through (mostly) strong interactions with the matter they pass, where hadronic and nuclear processes contribute to shower development. Hadrons typically shower later, so more material is needed to fully contain them. For the barrel, end-cap and forward region three different subsystems are deployed that will be described in this section.

The barrel and extended barrel of the *Tile calorimeter* [144] cover the pseudorapidity range $|\eta| < 1.0$ and $0.8 < |\eta| < 1.7$ respectively (see 7.4). Their radial extension ranges from 2.28 m to 4.25 m, segmented into three layers with a total thickness of 7.4 interaction lengths ($\lambda$) along the full coverage. It provides a granularity of $0.1 \times 0.1$ in $\Delta\eta \times \Delta\phi$ in the first two layers and $0.2 \times 0.1$ in the last layer. Both barrel parts utilise steel as the passive absorber and scintillators as the active material. Ionising particles produce ultraviolet light while passing the scintillators, which is converted to visible light by wavelength-shifting floors and read out in photomultiplier tubes. The steel-scintillator structure can be seen in 7.7a, which displays the periodical arrangement of the assembled parts. They are grouped into modules of size $\Delta\phi \sim 0.1$, 64 of which make up each barrel.

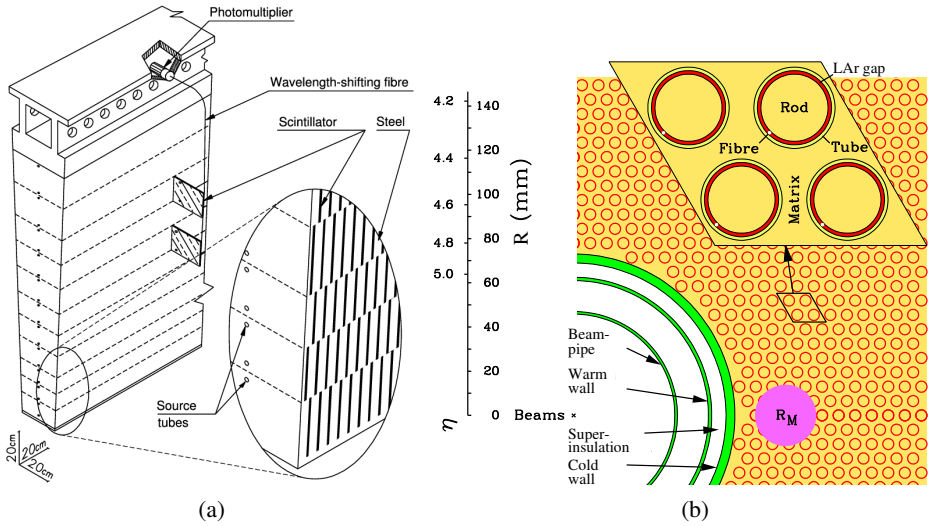


(a) (b)

FIGURE 7.7: Sketch of a tile calorimeter wedge depicting the alternating placement of steel absorbers and scintillators (a) and the electrode structure of the FCal (b) depicting the matrix of copper plates holding the copper tubes and rods with the LAr gap [128].

After the barrel sections, the hadronic end-cap calorimeter (HEC) complements the hadronic calorimeter system to pseudorapidities of up to $1.5 < |\eta| < 3.2$. It shares the same LAr cryostat as the EM end-cap calorimeter and uses a copper-liquid argon sampling technology. The HEC consists of two wheels per end-cap, each of which is divided into two segments in depth. These in total four layers have a granularity of $0.1 \times 0.1$ for $1.5 < |\eta| < 2.5$ and $0.2 \times 0.2$ for $2.5 < |\eta| < 3.2$ in $\Delta\eta \times \Delta\phi$.

The Forward Calorimeter (FCal) completes the calorimeter system in the very forward region between $|\eta| = 3.1$ and $|\eta| = 4.9$. To reduce the effect of the high neutron flux in the forward region the front surface of the FCal is placed 1.2 m further away from the interaction point with respect to the EMEC. To still provide the necessary depth in terms of interaction lengths a high-density design is chosen. A metal matrix consisting of copper in the first layer and tungsten in the second and third layers that contains longitudinal channels filled with concentric rods and a tube-shaped electrode

structure is deployed. A small gap between the rod and the tube is filled with liquid argon, acting as the sensitive medium. A cross-section of this structure is shown in 7.7b.

The overall energy resolution $\sigma_E$ provided by the hadronic calorimeter depends on the energy of the incoming particles and behaves as expressed in 7.1.

## 7.3 Muon Spectrometer

Muons typically penetrate very deeply into the matter, which means they cross both the inner detector as well as the calorimeter system with only minimal energy loss. This is due to their high mass, which makes them less susceptible to emitting bremsstrahlung while being accelerated in electromagnetic fields than electrons. At the same time, they don't interact strongly, meaning no hadronic interaction with the detector material takes place. The Muon Spectrometer [145] is a dedicated detector system for measuring charged particle tracks outside of the calorimeters, where the vast majority of other particles (except neutrinos) have already been absorbed. Several different chamber types are deployed, fulfilling both requirements on precision measurements and the potential for triggering. The performance goal of standalone reconstruction capabilities in terms of good momentum resolution of $\sigma_{p_T}/p_T = 10\,\%$ and charge identification provided by the Muon system range from momenta of $\sim$3 GeV to $\sim$3 TeV [128].

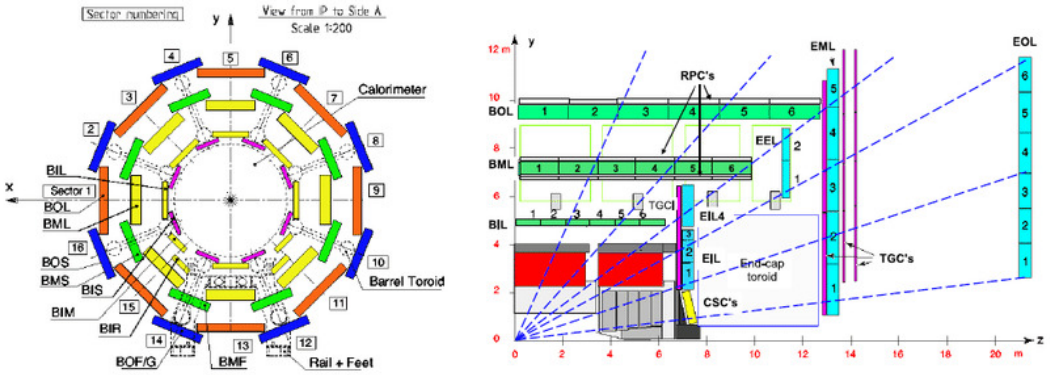


FIGURE 7.8: Left: Cross-section of the muon system in the transverse plane. The overlap of muon chambers to provide full coverage in the $\phi$ direction is visible. The location of the eight-barrel toroid magnets is traced out by dashed lines. Right: Quadrant cross-section of the ATLAS detector in a lateral plane. The placement of the muon chambers in the forward region, encompassing the end-cap toroid magnet, is highlighted here [128].

Cross sections of the muon system in the transverse as well as in the lateral plane are shown in 7.8. Like the other detector subsystems, the Muon Spectrometer is separated into a barrel and two end-cap parts. The barrel consists of three concentric cylindrical layers positioned outside of the calorimeters and between the mechanical structures of the barrel toroid magnets. The three layers have average radii of 5 m, 7.5 m and 10 m respectively. Neighbouring chambers are placed with a slight overlap (see 7.8, left) to ensure full coverage of the detector. In the end-caps, the muon chambers form wheels that are oriented perpendicular to the beam axis, with one wheel located upstream of the end-cap toroid magnet and the remaining two downstream. They are located at distances in $z$ of 7.4 m, 10.8 m, 14 m and 21.5 m from the interaction point. The full system is arranged so that a single muon typically crosses three muon stations.

As initially mentioned, the muon system consists of different detector types, that have different purposes. High precision measurements are provided by Monitored Drift Tube (MDT) chambers that are utilised in a pseudorapidity range $|\eta| < 2.7$. Each chamber consists of three to eight layers of drift

tubes that allow for an average resolution of 80 µm per tube or 35 µm per chamber. To deal with high rates in the forward region, the range of $2 < |\eta| < 2.7$ is covered by Cathode-Strip Chambers (CSC), which are multi-wire proportional chambers equipped with strip-segmented cathode planes arranged in orthogonal directions. A resolution of 40 µm per chamber is reached. To provide fast signals usable in the trigger, the Muon Spectrometer is complemented by additional tracking chambers. In the barrel region ($|\eta| < 1.05$) Resistive Plate Chambers provide tracking information with an intrinsic time resolution of about 1.5 ns. The end-caps ($1.05 < |\eta| < 2.4$) are instrumented with Thin Gap Chambers. Together they allow for a beam-crossing identification of $\geq 99\,\%$.

## 7.4 Magnet System

The ATLAS detector is immersed in a magnetic field that bends the trajectories of charged particles, necessary for the determination of momentum and charge in both the inner detector and the muon detector system. The magnet system [146] consists of a solenoid surrounding the inner detector and toroids in both the barrel and the end-caps that provide a magnetic field to the muon system.

The central solenoid shares its vacuum vessel with the LAr calorimeter. It has a length of 5.8 m and fills the radial range from 2.46 m to 2.56 m, providing a 2 T axial field in the volume of the inner tracker. The coils are made of superconducting NbTi, developed to provide a high magnetic field while keeping the material budget as low as possible. It contributes with a total of ∼0.66 radiation lengths to the total material.

A magnetic field with sufficient bending power for the muon system is realised by the barrel and end-cap toroid magnets. In the barrel, surrounding the calorimeter volume (see 7.9), eight symmetrically distributed coils are located around the beam axis. Overall, this system covers a length of 25.3 m and has inner and outer radii of 4.7 m and 10.05 m respectively. In the forward region, eight square coil units on each side make up the end-cap toroids. The bending power supplied by the toroid system ranges from 1.5 T m to 5.5 T m in the pseudorapidity range $0 < |\eta| < 1.4$ and from 1 T m to 7.5 T m in the end-cap ($1.6 < |\eta| < 2.7$). It is slightly lower in the transition region.

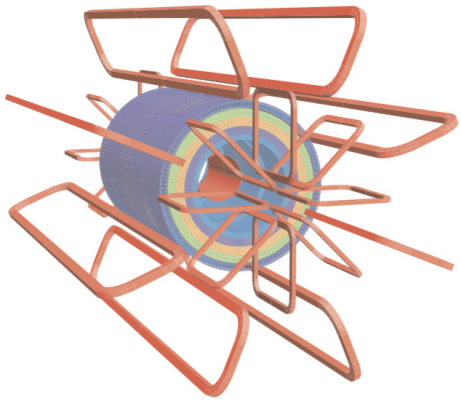

FIGURE 7.9: Overview of the superconducting coils installed in the toroidal magnet system [128]. The solenoid is located inside the calorimeter system. The tube around the solenoid models the layers of the Tile calorimeter with different magnetic properties and the return yoke at the outside. Eight toroid coils are arranged around the barrel as well as in the end-cap regions.

## 7.5 Luminosity measurement

During the *Run 2* data-taking period ATLAS has amassed a dataset corresponding to an integrated luminosity of $\mathcal{L}_{\text{int}} = 139\,\text{fb}^{-1} \pm 2.4$ taking into account the error of 1.7 % on the luminosity measurements. For physics analyses, good precision knowledge of this parameter is of high importance and it is often among the leading systematic uncertainties. Dedicated detector systems are installed in the very forward region for luminosity measurements, which are further supported by quantities proportional to instantaneous luminosity like the multiplicity of charged particles measured in the ID and particle fluxes through the calorimeters [147, 148].

The primary luminometers used in ATLAS are LUCID (Luminosity Cherenkov Integrating Detector) [149, 150] and BCM (Beam Conditions Monitor) [151]. LUCID consists of a total of sixteen Cherenkov detectors in each forward arm of ATLAS that use thin quartz windows of photomultipliers (PMTs) as Cherenkov medium. They sit at a distance of 17 m at either side of the interaction point, covering the pseudorapidity $5.6 < |\eta| < 6.0$. BCM consists of diamond sensors placed around the beampipe at $z = \pm 1.84\,\text{m}$ from the interaction point, corresponding to $|\eta| = 4.2$.

Luminosity measurements are obtained from different subsystems and even different algorithms. To obtain the final result on the integrated luminosity all available information is combined. The number of hits in the luminometers is typically proportional to the number of $pp$ interactions during a bunch crossing. The per-bunch instantaneous luminosity $\mathcal{L}_b$ is given by

$$\mathcal{L}_b = \frac{\mu_{\text{vis}} f_r}{\sigma_{\text{vis}}}, \tag{7.2}$$

where $\mu_{\text{vis}}$ is the visible interaction rate per bunch crossing, $\sigma_{\text{vis}}$ is the visible cross-section and $f_r$ is the LHC revolution frequency. While $\mu_{\text{vis}}$ is directly measurable, calculated e.g. from the hit counts in the PMTs from LUCID, the visible cross-section $\sigma_{\text{vis}}$ is derived from dedicated beam separation scans, called *van der Meer* scans, for each system and algorithm separately as detailed in [147].

## 7.6 Trigger and TDAQ

Proton proton collisions at the LHC occur at a rate of 40 MHz. Storing data at this rate is technically not feasible and with an event size of approximately 1.4 MB permanent storage of all recorded events would also not be possible. Additionally, the large majority of pp collisions are soft and not of high interest to the LHC physics program. A dedicated triggering system is used to select collision events that are written to disk and finally bring the rate of saved events down to ∼1 kHz. There are two different trigger levels implemented in ATLAS: Level 1 (L1) and the high-level trigger (HLT). The general aim of the trigger system is to pre-select events based on the detection of high-momentum muons, electrons, photons, jets and $\tau$-leptons. Also, large missing transverse energy and large total transverse energy are used. An overview of the data flow in the ATLAS TDAQ system is shown in 7.10.

For the L1 trigger, information based on a reduced granularity of the calorimeter and the dedicated muon trigger chambers is used. This reduced information is centrally processed by fast electronics and events selected to pass to the next levels are chosen based on a *trigger menu*, which combines the implemented selection criteria. At this stage, the event rate is already reduced to 100 kHz. Regions of interest in $\eta$ and $\phi$ are specified by the L1 trigger which gets passed to the software-based HLT. Within those regions the HLT accesses the full granularity detector information to further refine the trigger decision, reducing the event rate to approximately 1 kHz.

During the L1 decision, the event data is buffered on the individual front-end electronics of the sub-detectors. After passing the L1 selection, the data gets sent to the Readout System (ROS) which

is accessible for the HLT. It buffers the data for the time interval necessary for the HLT processing. HLT decides if a given event passes and is sent to permanent storage or gets registered for deletion.

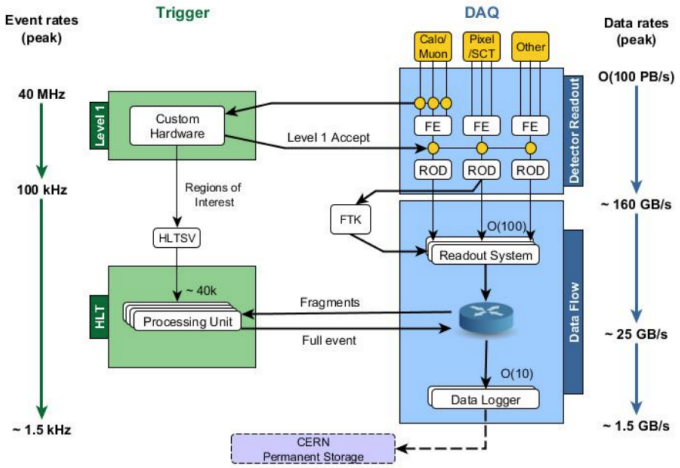


FIGURE 7.10: Schematic overview of the ATLAS TDAQ System used in *Run 2*. Events passing the L1 decision (top left) are passed to the HLT (bottom left). In parallel, event data from the detector front-end (FE) electronics are sent to the Readout System (ROS) in response to a L1 trigger accepting the signal. The data is buffered in the ROS and made available for algorithms running in the HLT. Once the HLT accepts an event it is sent to permanent storage via the Data Logger. [152].

## 7.7 MC simulation

The ATLAS experiment has a highly detailed computer simulation of the full detector system at its disposal [153]. A simulation is necessary to study the detector response and quantify the performance of the large range of reconstruction algorithms but plays also an essential role in the blinded experiment strategy deployed by the majority of physics analyses.

The full offline software allows going through the complete chain from event generation to detector simulation and digitisation. The final output of the simulation is equivalent to the detector output which means that for both the same reconstruction software can be used. A flow diagram of the full chain to produce Monte Carlo simulation samples is highlighted in 7.11.

In the *generation* step the set of particles considered as stable after the decays of the promptly produced particles coming from the hard proton-proton interaction are defined. For this, a whole suite of different third-party generators is included in the ATLAS software [154, 155]. The retained stable particles are in the following propagated through the detector geometry to simulate the particles' interaction with the material. This is made possible by a detailed implementation of the full detector within the GEANT4 [131] toolkit. The ATLAS simulation contains hundreds of different materials and hundreds of thousands of individual volumes are modelled in the simulation, which is constantly refined and further developed to come as close to reality as possible. In the *simulation* step the magnitude and time of energy deposits left by particles passing the active sensor materials are stored for further processing. Also, a "truth" record is stored, which allows to connect the detector response with the initially generated particles. This truth information is of high importance for reconstruction performance checks. To test, for example, if measurements that have been assembled to a track by the tracking reconstruction reconstruct a truth-generated particle and if the measured parameters like momentum or impact parameters have been determined correctly, this truth record is needed. The output of the simulation is further used as input for the *digitisation*. The task of the digitisation

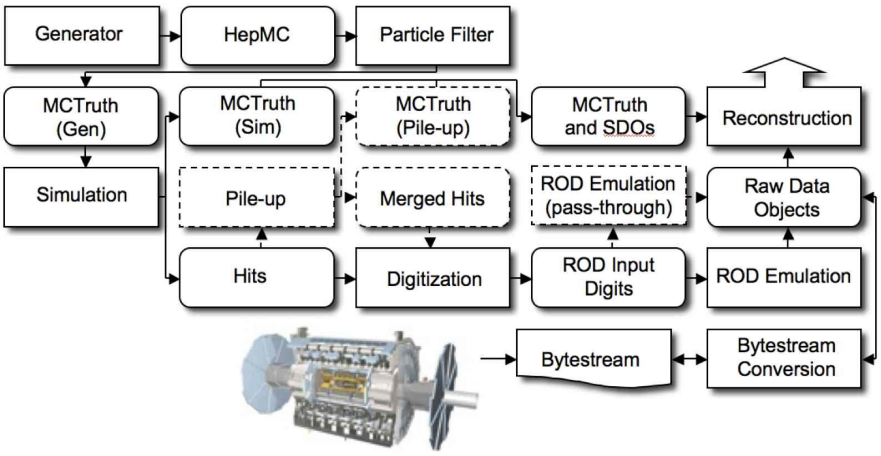


FIGURE 7.11: Flow diagram of the ATLAS simulation. Starting at the top left with the *generation*, the defined truth particles are fed into the *simulation* part and the individual particles propagated through the detector model. The Hits are overlaid with pileup and *digitised* to resemble detector signals. These simulated signals are equivalent to the bytestream coming from the real detector and are both input to the *reconstruction*.

step is to emulate the detector electronics response, modelling the read-out chain as realistically as possible to produce signals that correspond to those read from the real detector. This includes noise coming from the electronics. In this step, in addition to the generated hard scattering process of interest, additional sources of detector signals are overlaid, the so-called pileup (see 7). These include minimum bias events from simultaneous soft $pp$ collisions. Also, detector signals coming from the beam halo, beam gas and cavern backgrounds are added. After digitisation, the simulation data has a format equivalent to the detector output except for the truth record, which of course is only available in simulated events and not in recorded data. Both can be passed through the *reconstruction* that builds the final objects used as inputs for physics analyses.

# 8 Object reconstruction

Once the raw data corresponding to the readout signals registered by the different sensors of the various subdetectors inside of ATLAS is available, the underlying physical objects ($\gamma$, $e$, $\mu$, jets and $\tau$) have to be reconstructed in order to be used in physics analyses. For this, a variety of different algorithms is deployed. Their primary objective is to collect raw signals that belong to the same particle and then reconstruct its kinematic properties from those signals. Within this chapter, the approaches used in the ATLAS reconstruction software are presented.

The construction of objects can be split into two steps. First, low-level objects are formed, including *tracks* (8.1) built from measurements in the Inner Detector (ID) and *clusters* (8.2), which are constructed from energy deposits in the calorimeters. Then follows the construction of objects based on these basic components. The reconstruction of jets is described in 8.3. The approach used to identify possible photon and electron candidates are detailed in 8.4. Muon reconstruction utilises additional input from measurements in the muon system, as described in 8.5. The reconstruction of missing transverse momentum in collision events relies on the previously mentioned objects, as explained in 8.6.

## 8.1 Tracks

Tracks [156, 157] are built from measurements in the inner detector (ID) system of ATLAS (see 7.1), provided by its subsystems: the Pixel Detector, the Semiconductor Tracker (SCT), and the Transition Radiation Tracker (TRT). Tracks reconstruct the trajectory of electrically charged particles that allow inferring the kinematic variables and impact parameters of each particle. The reconstruction procedure can be split into several staged steps, which will be explained in the following.

The reconstruction chain starts by combining the raw measurements in the Pixel Detector and the SCT into clusters of connected cells [158]. This is done due to the possibility that charge deposited from a passing particle is shared between neighbouring pixel or strip sensors that have a common edge or corner due to crosstalk. Using the clusters as inputs, three-dimensional representations of these, so-called *space-points*, are built that represent the positions of the intersection of charged particles crossing the active detector material, accounting also for the uncertainty of the measurement position.

These pre-processed measurements are then assembled to *track seeds* consisting of sets of three space points each, which allows for a first estimation of track parameters. Both the Pixel Detector and the SCT are used in the seeding stage. Starting from the seeds, a combinatorial Kalman filter [159] is used to append additional space points. A window search given by the seed direction is applied, and space points compatible with the predicted trajectory are added or rejected by the Kalman filtering. These tracks form the initial candidates. Since at this stage, the creation of multiple tracks from

the same seed and a sharing of space points between candidates is possible, these ambiguities have to be resolved in an additional step. For this purpose scores are assigned to all tracks to quantify their respective quality, allowing an ordering of the candidates. These scores include expected cluster multiplicities in the reconstructed trajectory –, the $\chi^2$ of the track fit as well as the track momentum. Iteratively multiple associations of the same clusters to different tracks can thus be resolved.

The tracks that survive the resolving of ambiguities are fit with a high precision least square fit. After this, an extension to the TRT is performed, combining the track with compatible measurements in the straws through track extrapolation. Including these added hits, the global fit is repeated. In general, the TRT extension has large importance for an improved momentum resolution of tracks in ATLAS.

To further improve the track reconstruction efficiency, a second tracking sequence is carried out, starting with TRT measurements. Within this *outside-in* approach, calorimeter clusters (see 8.2) are used to identify regions of interest in the TRT within which seeds are formed from TRT measurements alone. Equivalent to the inside-out approach explained above, track candidates are built by a combinatorial Kalman filter. Those candidates are then extended to the SCT and Pixel surfaces, where hits not used by the first track finding sequence and compatible with the track are added. After the removal of possible shared hits and duplicates, a least square fit is performed again to obtain the track parameters. The outside-in reconstruction helps to recover tracks that originate from secondary vertices or photon conversions, where no seeds within the silicon detectors are found. They play an important role in the reconstruction of electrons and photons (see 8.4). The overall track reconstruction efficiency as a function of $\eta$ and $p_{\mathrm{T}}$ can be seen in 8.1a and 8.1b, respectively.

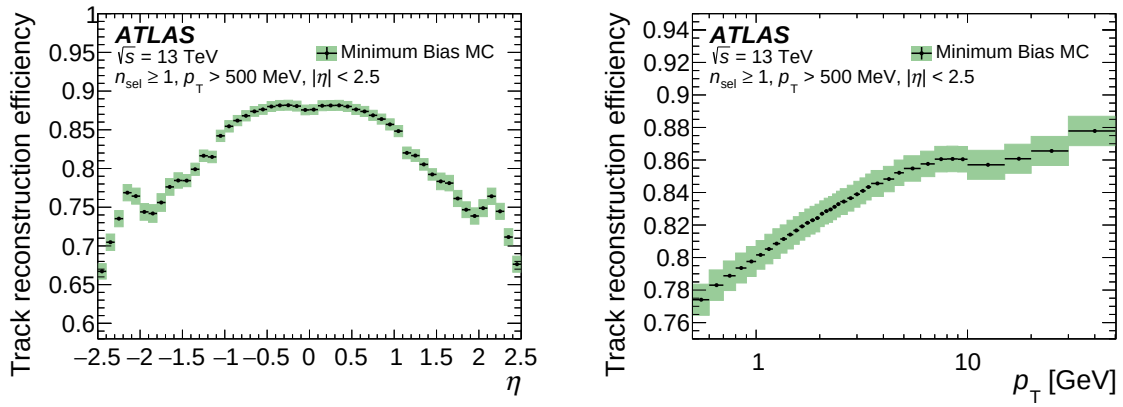


(a) (b)

FIGURE 8.1: Track reconstruction efficiency after application of a data-driven efficiency correction, shown as a function of $\eta$ in (a) and as a function of $p_{\mathrm{T}}$ in (b) [160].

## 8.2 Calorimeter clusters

Clustering of topologically connected cells [161] is a well-suited approach to reconstruct energy deposits in highly granular calorimeter systems, such as the ones deployed in ATLAS. The fine lateral and longitudinal segmentation of cells allows the resolution of the signal patterns generated by showering particles and effectively suppresses electronic noise or other backgrounds, like pileup. These *topo-clusters* form the basis of calorimetric input for higher-level reconstruction algorithms, for example in jets, photons and electrons.

Clusters are built by following patterns of signal significance $\zeta_{\text{cell}}^{\text{EM}}$ in each cell, defined as

$$\zeta_{\text{cell}}^{\text{EM}} = \frac{E_{\text{cell}}^{\text{EM}}}{\sigma_{\text{noise,cell}}^{\text{EM}}}, \tag{8.1}$$

where $E_{\text{cell}}^{\text{EM}}$ is the cell signal energy and $\sigma_{\text{noise,cell}}^{\text{EM}}$ is the average expected noise of the same cell. Both of these are measured on the electromagnetic (EM) scale, a scale that reconstructs energies deposited by photons or electrons correctly, but would need corrections to recover signals originating from hadronic showers [161]. This is due to the non-compensating response of the calorimeter technology used, which reacts differently to hadronic and electromagnetic showers coming from particles of the same energy.

To control the seeding, growth and boundary properties of the topo-clusters, three different requirements on cells in terms of signal significance are defined, that denote the significance requirement for a cell to either act as a seed, to be accounted as a cell neighbouring a seed cell or to be included into an outer perimeter. The algorithm collects cells into clusters by starting at the most energetic *seed* cells that pass a threshold $S$, $|\zeta_{\text{cell}}^{\text{EM}}| > S$. The neighbouring – which means directly adjacent – cells are added to the seed if they pass $|\zeta_{\text{cell}}^{\text{EM}}| > N$ or $|\zeta_{\text{cell}}^{\text{EM}}| > P$. If they pass $|\zeta_{\text{cell}}^{\text{EM}}| > N$, the procedure is iteratively continued to further neighbours, allowing the cluster to grow. If a neighbouring cell passes $|\zeta_{\text{cell}}^{\text{EM}}| > P$ but not $|\zeta_{\text{cell}}^{\text{EM}}| > N$, it is added to the cluster and the algorithm stopped. The default settings for the ATLAS reconstruction are $S = 4$, $N = 2$ and $P = 0$. Clusters can be merged in case the neighbouring cells are both seeds or if seed cells share a common neighbour that passes $|\zeta_{\text{cell}}^{\text{EM}}| > N$.

In all of the above-mentioned clustering requirements, the absolute value of $\zeta_{\text{cell}}^{\text{EM}}$ is used. This means that cells with negative measured energy are included, which are typically the result of random noise fluctuations. Nevertheless, including negative value cells into a cluster has the advantage of cancelling random upward noise fluctuations and thus improves the overall resilience against noise.

To further improve the quality of the topo-clusters, a splitting is performed. This can help to improve the reconstruction performance in case two or more close-by particles deposit energy in the calorimeter. The applied splitting algorithm consists of finding local maxima within clusters of $E_{\text{cell}}^{\text{EM}} > 500\,\text{MeV}$ that is surrounded by at least four neighbours, none of which are identified as a local maximum themselves. After splitting, a sharing of cells that are neighbouring two identified maxima is possible. The energy is then distributed according to a weight computed from the energies of the respective clusters and the distance of the shared cell to the centre of gravity of the clusters. The weight is defined as

$$w_{\text{cell,i}}^{\text{geo}} = \frac{E_{\text{cluster,i}}^{\text{EM}}}{E_{\text{cluster,i}}^{\text{EM}} + r E_{\text{cluster,j}}^{\text{EM}}}, \quad r = e^{d_i - d_j} \tag{8.2}$$

where $d_i$ and $d_j$ are the distances from the cell to the centre of gravity of the two clusters $i$ and $j$ respectively, and $E_{\text{cluster,i}}^{\text{EM}}$ is the energy measured in cluster $i$. The weight assigned to cluster $j$ is consequently $w_{\text{cell,j}}^{\text{geo}} = 1 - w_{\text{cell,i}}^{\text{geo}}$. This splitting is the last step in the topo-cluster building and the resulting clusters form the input for further final state reconstruction.

Combining the energies and directions of all cells within a cluster, cluster-level kinematics can be computed. The cluster energy $E_{\text{cluster}}^{\text{EM}}$ is obtained by computing

$$E_{\text{cluster}}^{\text{EM}} = \sum_{i}^{N_{\text{cell}}} w_{\text{cell,i}}^{\text{geo}} E_{\text{cell,i}}^{\text{EM}}. \tag{8.3}$$

The directional variables $\eta_{\text{clus}}$ and $\phi_{\text{clus}}$ are computed as

$$\eta_{\text{clus}} = \frac{\sum_i^{N_{\text{cell}}} w_{\text{cell,i}}^{\text{geo}} |E_{\text{cell,i}}^{\text{EM}}| \eta_{\text{cell,i}}}{\sum_i^{N_{\text{cell}}} w_{\text{cell,i}}^{\text{geo}} |E_{\text{cell,i}}^{\text{EM}}|} \tag{8.4}$$

$$\phi_{\text{clus}} = \frac{\sum_i^{N_{\text{cell}}} w_{\text{cell,i}}^{\text{geo}} |E_{\text{cell,i}}^{\text{EM}}| \phi_{\text{cell,i}}}{\sum_i^{N_{\text{cell}}} w_{\text{cell,i}}^{\text{geo}} |E_{\text{cell,i}}^{\text{EM}}|}, \tag{8.5}$$

where $\eta_{\text{cell,i}}$ and $\phi_{\text{cell,i}}$ are the directions of each cell computed from its position within the calorimeter with respect to the origin of the coordinate system defined in ATLAS.

## 8.3 Jets

A jet describes a stream of particles resulting from the hadronisation of an initial quark or gluon, produced during a proton-proton collision. Given the phenomenon of confinement in QCD, colour-charged particles can't exist freely. They then produce additional particles that allow them to form an overall colourless state. Finding and combining these individual objects originating from the same parton is the task of jet reconstruction algorithms, for which several different methods have been developed in the past. ATLAS reconstructs jets with the anti-$k_T$ algorithm [162], an infrared and collinear safe clustering algorithm widely used in particle physics. Infrared safety refers to the independence of jet definitions under the inclusion of soft radiation, while collinear safe algorithms have the property of reliably including a split parton within the given jet. This sequential algorithm uses the distance $d_{i,j}$ between the sub-components $i$ and $j$

$$d_{i,j} = \min\left(\frac{1}{p_{\text{T},1}^2}, \frac{1}{p_{\text{T},2}^2}\right) \frac{\Delta_{i,j}^2}{R^2}, \tag{8.6}$$

and the distance to the beam $d_{i,B}$ defined as

$$d_{i,B} = \frac{1}{p_{\text{T},i}^2}, \tag{8.7}$$

where $\Delta_{i,j}^2 = (\eta_i - \eta_j)^2 + (\phi_i - \phi_j)^2$ is the separation between two input candidates, $R$ is a free parameter related to the jet opening and $p_{\text{T},i}$ is the transverse momentum of $i$-th the sub-compontent. If for a given input object $i$ $d_{i,B} < d_{i,j}$, $i$ is considered a jet candidate. Otherwise, it is merged with object $j$. This is repeated until no clusters are left, such that the hard particles include the softer components in a cone around them.

A calibration is applied to jets in the form of a jet energy scale (JES) [163, 164] factor, that corrects the jet four-momentum to the particle-level energy scale. The jet energy resolution (JER) is derived as the width of a Gaussian fit to the jet response function.

The inputs to the anti-$k_T$ algorithm are four vectors, that can be differently defined. During *Run 2*, ATLAS has changed the inputs for the jet definition from a calorimeter-only based approach (see 8.3) to one that mixes calorimeter and tracker information and takes advantage of the better $p_{\text{T}}$ resolution of tracks at low momenta (see 8.3). Both are briefly introduced in the following.

### Jets based on calorimeter information

The basis for calorimeter jets are topological clusters (see 8.2), formed from connected cells in the calorimeter containing significant energy above a noise threshold. The identified positive-energy topological clusters found in an event are used as input to the anti-$k_T$ algorithm with a radius parameter of $R = 0.4$, assuming a massless particle hypothesis for each and using the reconstructed cluster energy at the electromagnetic scale.

### Jets combining tracker and calorimeter information

The most recent jet reconstruction algorithm that is used in physics analyses within ATLAS is the so-called *particle flow* (PFlow) algorithm, an idea that was pioneered in the ALEPH experiment at LEP [165]. The main consideration for using PFlow jets, instead of those based on calorimeter information alone, is an improved performance in higher pile-up environments.

Within this approach, [166], measurements from both the calorimeter and the tracking system are combined. This means that a combination of topological clusters and tracks are used as input for the anti-$k_T$ algorithm. To avoid double counting of calorimeter-based energy measurements by already well-measured charged tracks, the expected energy deposited in the calorimeter by charged particles is removed. For this, tracks are matched spatially to a topological cluster by extrapolating the track to the second layer in the LAr Calorimeter. Before the matching of a given track to a cluster, a preselection of topological clusters is performed by requiring $E^{\text{clus}}/p^{\text{trk}} > 0.1$. The cluster closest to the track is then chosen, using a distance metric defined as $\Delta R' < \sqrt{(\frac{\Delta\phi}{\sigma_\phi})^2 + (\frac{\Delta\eta}{\sigma_\eta})^2}$. The removal of the double-counted energy is done iteratively cell by cell until an amount corresponding to the track's energy is removed from the cluster.

## 8.3.1 Pileup jet rejection

In addition to the hard-scatter event within a bunch crossing, additional soft $pp$ collisions occur, denoted as pileup. The rejection of jets originating from pileup interactions is essential to many physics analyses. The method followed in ATLAS is described in the following. Two variables are defined for the pileup jet suppression that is finally used in a multivariate combination, which is called the jet-vertex-tagger (JVT) [167].

The first variable used is the so-called corrected jet vertex fraction (corrJVF), defined as

$$\text{corrJVF} = \frac{\sum_k p_T^{\text{trk}_k}(PV_0)}{\sum_l p_T^{\text{trk}_l}(PV_0) + \frac{\sum_{n\geq 1}\sum_l p_T^{\text{trk}_l}(PV_n)}{k\cdot n_{\text{trk}}^{\text{PU}}}}, \tag{8.8}$$

where $\sum_k p_T^{\text{trk}_k}(PV_0)$ is the scalar sum of the transverse momenta of the tracks associated with the jet and the originate from the hard-scatter vertex. The term $\sum_{n\geq 1}\sum_l p_T^{\text{trk}_l}(PV_n)$ computes the scalar sum of the transverse momenta of tracks associated with the jets that originate from the individual pileup vertices reconstructed in the event. Since this last term would introduce a dependence of the variable on the number of reconstructed vertices, it is divided by $k \cdot n_{\text{trk}}^{\text{PU}}$, where $n_{\text{trk}}^{\text{PU}}$ is the number of pileup tracks identified in the event and $k$ is a scale factor and set to $k = 0.01$.

The second variable used for pileup rejection is the charged fraction $R_{pT}$, defined as

$$R_{pT} = \frac{\sum_i p_{\text{T}}^{\text{track}_i}(PV)}{p_{\text{T}}^{\text{jet}}}, \tag{8.9}$$

where $\sum_i p_{\text{T}}^{\text{track}_i}(PV)$ is defined as above and $p_{\text{T}}^{\text{jet}}$ is the calibrated transverse momentum of the jet.

The distributions for corrJVT and $R_{pT}$ are shown in 8.2a and 8.2b, respectively, split into jets originating from the hard-scatter (HS) interaction and those coming from pileup (PU). Since pileup jets typically don't contain tracks originating from the hard scatter vertex, the value assumed by pileup jets for both variables is generally close to zero. The final JVT discriminant uses both before mentioned variables as input to build a two-dimensional likelihood based on the k-nearest neighbour algorithm [168]. Its distribution for HS and PU jets is shown in 8.2c. Jets with no associated tracks get the value JVT $= -0.1$ assigned. Depending on the cut applied to this variable, different HS efficiency and PU rejection working points can be selected. The ROC curve for the different discriminators is presented in 8.2d.

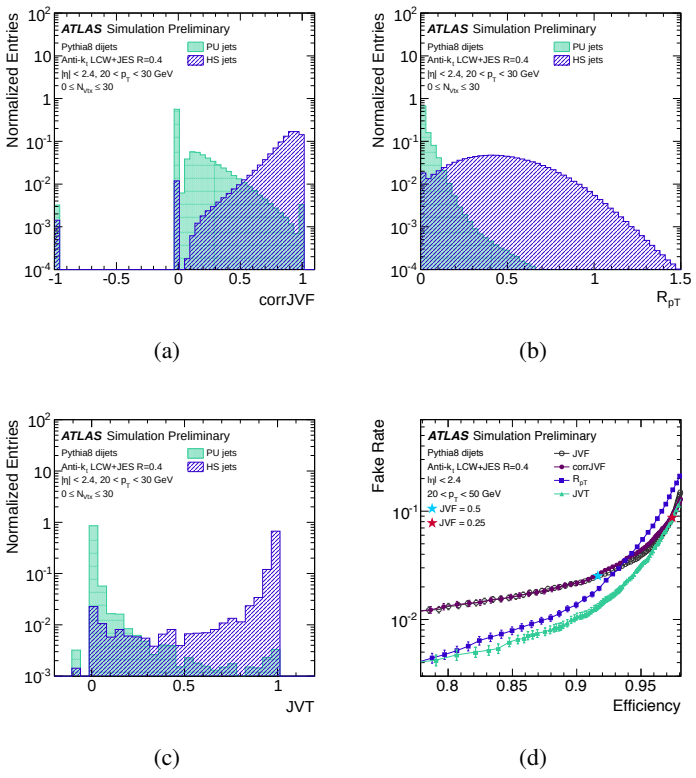


FIGURE 8.2: Distribution for corrJVT (a) and $R_{pT}$ (b) shown for hard-scatter and pileup jets in the transverse momentum range between 20 GeV $< p_{\mathrm{T}} <$ 30 GeV. The final JVT distribution and the ROC curves when applying the different discriminants are shown in (c) and (d) [167].

## 8.4 Photons and electrons

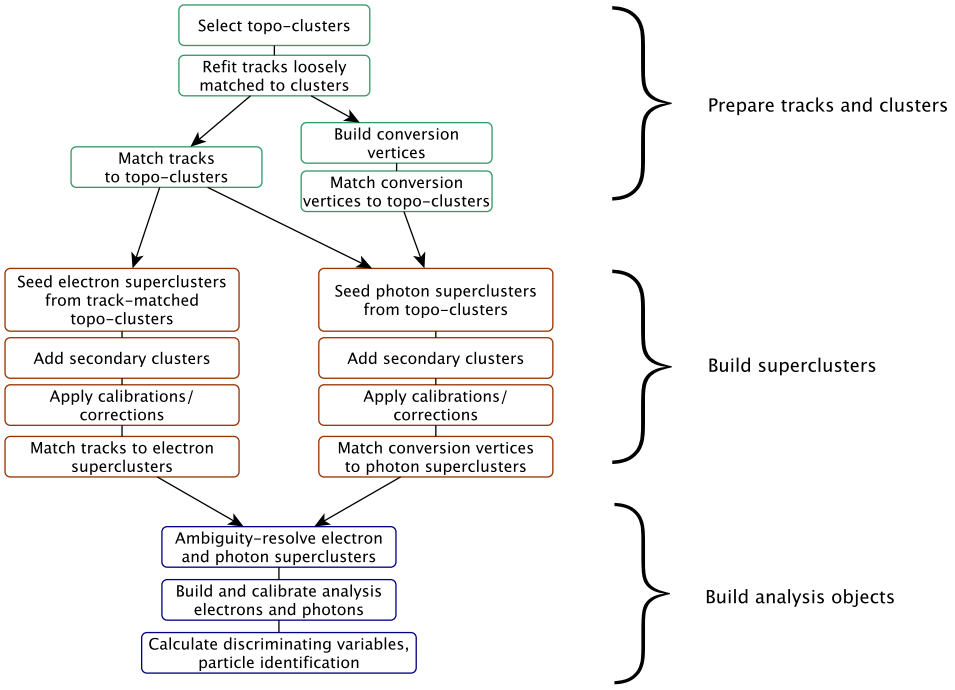


FIGURE 8.3: Flow diagram of the algorithm used for electron and photon reconstruction [169].

Photons ($\gamma$) and electrons ($e^{\pm}$) are reconstructed in ATLAS using both, calorimeter and tracker information. In a naive picture, photons – being electrically neutral – don't interact with the inner detector and deposit their energy only in the EM calorimeter in the form of an EM shower. The charged electrons on the other hand leave hits in the inner detector that form a track before showering electromagnetically in the calorimeter. Due to the sizeable amount of material sitting before the calorimeter, see 7.3, this simple description is complicated by the conversion of photons and also the emission of bremsstrahlung by electrons. To reach highly performant reconstruction of photons and electrons, these effects need to be accounted for. The necessity to be able to reconstruct a photon from an electron-positron pair coming from a conversion vertex as well as recovering energy lost by an electron emitting a bremsstrahlung photon introduces a certain codependence between these two object reconstructions, which is why they are covered simultaneously in this chapter. An overview of the deployed algorithm is shown in 8.3. The description follows the ATLAS documentation of $e^{\pm}/\gamma$ reconstruction with so-called *superclusters*, provided in [169].

### 8.4.1 Photon and electron reconstruction

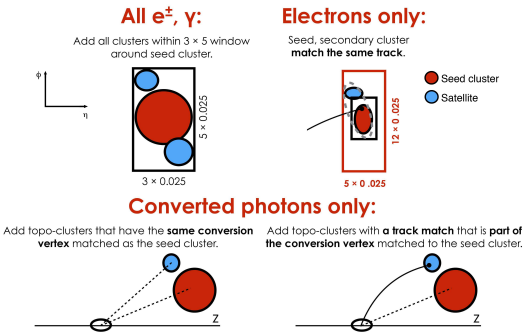


FIGURE 8.4: Visualisation of the inclusion of satellite clusters in the supercluster reconstruction chain [169].

For both photons and electrons, the energy deposited in the calorimeters is reconstructed using topological clusters equivalent to those described in 8.2, using the same $\{4,2,0\}$ thresholds. The difference in the $e^{\pm}/\gamma$ reconstruction compared to the jet reconstruction is that for the former only the electromagnetic part of topo-clusters is considered, meaning that only energy from cells in the EM calorimeter is used. Clusters need to pass a minimum EM energy threshold of 400 MeV. By requiring the EM fraction of the cluster energy to be $f_{\text{EM}} > 0.5$, an initial pile-up cluster rejection can be achieved at this early stage.

For the reconstruction of electrons and converted photons, ID tracks within a region of interest defined by the calorimeter clusters are used, following a two-step reprocessing of the ID information. Firstly, given that the standard tracking applied in the ID assumes a pion hypothesis, the track parameters of the considered tracks are refit, taking the considerably higher expected energy loss of electrons as well as the electron mass hypothesis into account. Secondly, standard tracking may fail altogether in producing track candidates due to the mentioned higher energy loss that is not considered in the standard track-finding procedure. In this case, silicon detector-based track seeds found within the region of interest that did not create tracks in the tracking sequence are used to find electron tracks, allowing for a higher energy loss at material intersections.

The obtained tracks are matched to EM topo-clusters, where a track is considered matched if $|\Delta\eta| < 0.05$ and $-0.1 < q(\phi_{\text{track}} - \phi_{\text{cluster}}) < 0.05$, where $q$ denotes the charge of the particle inferred from the trajectory. The $\phi$ cut is asymmetric to account for energy loss from radiated photons. In case of several tracks passing the matching requirements, a ranking of the tracks based on track quality and matching using $\Delta R = \sqrt{\Delta\phi^2 + \Delta\eta^2}$ as a distance metric is performed and the best track chosen.

At low pseudorapidity values, roughly 20 % of photons undergo conversion before reaching the calorimeter, increasing to ∼65 % for $|\eta| \approx 2.3$. For the reconstruction of these converted photons, the conversion vertex needs to be identified. Both, tracks that include silicon sensor measurements and those reconstructed from the TRT alone, are included in the procedure. Two kinds of conversion vertices are considered, two-track vertices and single-track vertices where the second track could not be reconstructed. For two-track vertices, the tracks need to be of opposite charge. Single-track vertices are built from tracks containing only TRT measurements. To limit the number of unconverted photons incorrectly matched to a conversion vertex built by TRT tracks, a high probability for the TRT tracks to be electrons [170] is required.

To build the final supercluster object, $E_{\text{T}}$-sorted topo-clusters are used as seeds to which so-called *satellite* clusters are added. For photons, a cluster must have $E_{\text{T}} > 1.5\,\text{GeV}$ to form a seed. For electrons, the seed cluster must match a track with at least four silicon hits and pass a minimum transverse energy requirement of $E_{\text{T}} > 1\,\text{GeV}$. Starting from seed clusters that fulfil the above

requirements, satellite clusters are added. These denote neighbouring clusters within a $\Delta\eta \times \Delta\phi = 0.075 \times 0.125$ window. They are added to the supercluster to recover secondary EM showers that originate from the same $e^{\pm}/\gamma$ object. This window is extended to $\Delta\eta \times \Delta\phi = 0.125 \times 0.300$ for electron seeds if the track matched to the seed cluster is also matched to the satellite cluster. For photon seeds that have a conversion vertex matched, clusters matched to the same conversion vertex are added as satellites as well. The method is visualised in 8.4.

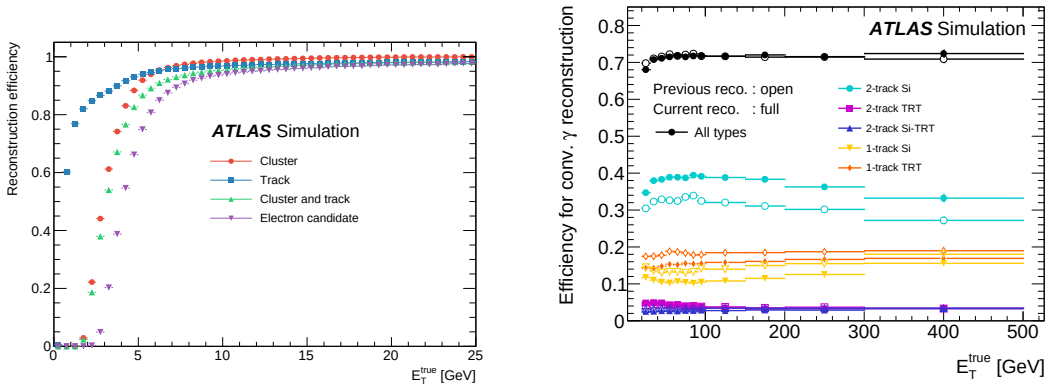


(a) (b)

FIGURE 8.5: Reconstruction efficiency for electrons (a) and converted photons (b) as a function of the transverse energy $E_T$ [169]. Only converted photons are highlighted here since the reconstruction efficiency of unconverted photons is close to 100 %.

Since electron and photon reconstruction is done in parallel (see 8.3), a given cluster can seed both an electron and a photon. In simply identifiable cases, like electrons matched to a good quality track or photons without a conversion vertex, the supercluster is transformed into an electron or photon object directly for usage in physics analyses. The remaining objects are flagged as ambiguous and it is left to the individual analyses to decide how to classify the object based on their specific needs. The reconstruction efficiency of the supercluster algorithm for electrons is shown in 8.5a as a function of the truth transverse energy $E_T$, reaching ∼98 %. The efficiency for reconstructing converted photons is shown in 8.5b, which levels off at ∼70 % for high truth transverse energy.

### 8.4.2 Photon identification

Photon identification aims to differentiate promptly produced photons from hadronic jets. Especially neutral pions decaying to two collimated photons present a significant background for the photon reconstruction. So-called *shower shape* variables are used for identification, which characterises longitudinal and transversal shower developments. An overview of these variables and their definitions

| Working point name | Utilised variables |
|---|---|
| Loose | $R_{\text{had}}$, $R_{\text{had}_1}$, $R_\eta$ and $w_{\eta_2}$ |
| Medium | Loose + $E_{\text{ratio}}$ |
| Tight | Loose + $R_\phi$, $w_{s\,3}$, $f_{\text{side}}$, $\Delta E_s$, $E_{\text{ratio}}$, $w_{s\,\text{tot}}$, $f_1$ |
| Loose′-2 | Tight, removing $w_{s3}$, $F_{\text{side}}$ |
| Loose′-3 | Tight, removing $w_{s3}$, $F_{\text{side}}$, $\Delta E$ |
| Loose′-4 | Tight, removing $w_{s3}$, $F_{\text{side}}$, $\Delta E$, $w_{s1,tot}$ |

TABLE 8.1: List of variables used to define the Loose, Tight, and Loose′ photon selections.

is given in 8.2. Due to the difference in the evolution of electromagnetic and hadronic showers, the shower shapes provide a strong separation power and allow the definition of selection cuts.

Three basic working points are provided for photons: *Loose*, *Medium* and *Tight*. Loose and Medium photons are primarily used in the trigger. Loose selection makes use of the variables $R_{\text{had}}$, $R_{\text{had}_1}$, $R_\eta$ and $w_{\eta_2}$. Medium selection adds a cut on $E_{\text{ratio}}$. The primary working point used for offline analyses is the Tight photon definition, incorporating cuts on the variables defined in 8.1. The identification cuts are tuned separately for high and low $E_{\text{T}}$ photons and are also optimised in bins of $|\eta|$ since shower shapes vary due to the slightly changing geometry of the calorimeter. 8.6 shows the identification efficiency obtained for unconverted and converted photons respectively as a function of $E_{\text{T}}$. The identification efficiency reaches $\sim$93 % for unconverted photons and $\sim$98 % for converted photons.

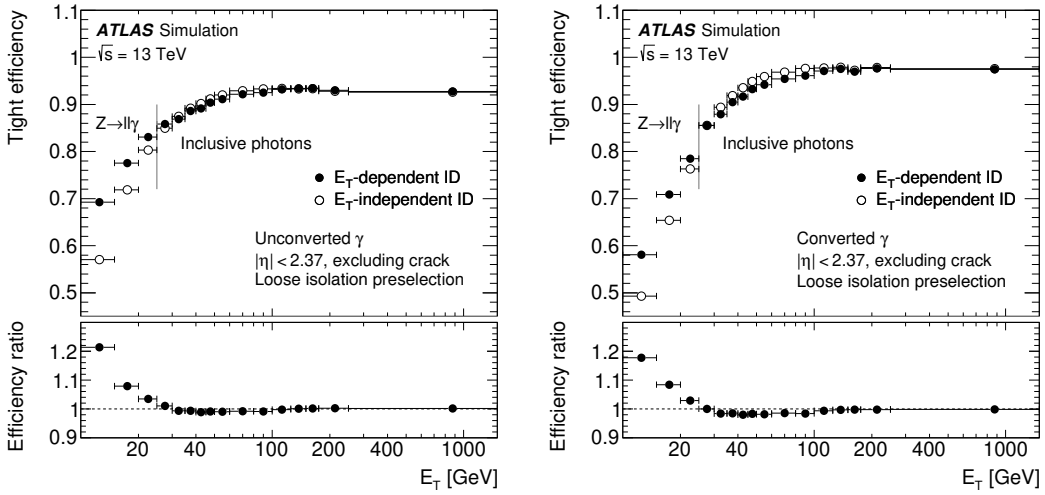


(a) (b)

FIGURE 8.6: Efficiency of the Tight photon identification as a function of $E_{\text{T}}$, split into unconverted (a) and converted (b) photons [169].

### 8.4.3 Photon isolation

To further suppress non-prompt photons originating from hadronic activities, isolation cuts are applied. The activity close to photon candidates can be quantified by searching for tracks or calorimetric energy deposits close to the object of interest. Since prompt photons are expected to appear isolated in the calorimeter, requiring this activity not to surpass a given threshold gives a powerful handle on background suppression.

The calorimeter isolation uses the $E_{\text{T}}^{\text{cone0.2}}\text{XX}$ variable, which is defined as

$$E_{\text{T}}^{\text{cone0.2}}XX = E_{\text{T,raw}}^{\text{isolXX}} - E_{\text{T,core}} - E_{\text{T,leakage}}(E_{\text{T}}, \eta, \Delta R) - E_{\text{T,pile-up}}(\eta, \Delta R),$$

where $XX$ encodes the size of the searched cone, $\Delta R = XX/100$. This means that for example in the $E_{\text{T}}^{\text{cone0.2}}40$ definition, the cone size is $\Delta R = 40/100 = 0.4$. $E_{\text{T,raw}}^{\text{isolXX}}$ sums the transverse energy of positive-energy topological clusters that fall within the chosen cone. From this value, the isolation variable is computed by subtracting the raw particle energy $E_{\text{T,core}}$ in a window of $\Delta\eta \times \Delta\phi = 0.125 \times 0.175$ around the barycentre of the cluster, a parametrised leakage correction $E_{\text{T,leakage}}(E_{\text{T}}, \eta, \Delta R)$ accounting for wider showers as well as a parametrised average contribution from pile-up $E_{\text{T,pile-up}}(\eta, \Delta R)$.

| Category | Description | Name | Usage |
|---|---|---|---|
| Hadronic leakage | Ratio of $E_{\mathrm{T}}$ in the first layer of the hadronic calorimeter to $E_{\mathrm{T}}$ of the EM cluster (used over the ranges $\lvert\eta\rvert < 0.8$ and $\lvert\eta\rvert > 1.37$) | $R_{\mathrm{had}_1}$ | $e/\gamma$ |
| | Ratio of $E_{\mathrm{T}}$ in the hadronic calorimeter to $E_{\mathrm{T}}$ of the EM cluster (used over the range $0.8 < \lvert\eta\rvert < 1.37$) | $R_{\mathrm{had}}$ | $e/\gamma$ |
| EM third layer | Ratio of the energy in the third layer to the total energy in the EM calorimeter | $f_3$ | $e$ |
| EM second layer | Ratio of the sum of the energies of the cells contained in a $3 \times 7$ $\eta \times \phi$ rectangle (measured in cell units) to the sum of the cell energies in a $7 \times 7$ rectangle, both centred around the most energetic cell | $R_\eta$ | $e/\gamma$ |
| | Lateral shower width, $\sqrt{(\Sigma E_i \eta_i^2)/(\Sigma E_i) - ((\Sigma E_i \eta_i)/(\Sigma E_i))^2}$, where $E_i$ is the energy and $\eta_i$ is the pseudorapidity of cell $i$ and the sum is calculated within a window of $3 \times 5$ cells | $w_{\eta_2}$ | $e/\gamma$ |
| | Ratio of the sum of the energies of the cells contained in a $3 \times 3$ $\eta \times \phi$ rectangle (measured in cell units) to the sum of the cell energies in a $3 \times 7$ rectangle, both centred around the most energetic cell | $R_\phi$ | $e/\gamma$ |
| EM first layer | Total lateral shower width, $\sqrt{(\Sigma E_i (i - i_{\mathrm{max}})^2)/(\Sigma E_i)}$, where $i$ runs overall cells in a window of $\Delta\eta \approx 0.0625$ and $i_{\mathrm{max}}$ is the index of the highest-energy cell | $w_{s\,\mathrm{tot}}$ | $e/\gamma$ |
| | Lateral shower width, $\sqrt{(\Sigma E_i (i - i_{\mathrm{max}})^2)/(\Sigma E_i)}$, where $i$ runs over all cells in a window of 3 cells around the highest-energy cell | $w_{s\,3}$ | $\gamma$ |
| | Energy fraction outside the core of three central cells, within seven cells | $f_{\mathrm{side}}$ | $\gamma$ |
| | Difference between the energy of the cell associated with the second maximum and the energy reconstructed in the cell with the smallest value found between the first and second maxima | $\Delta E_s$ | $\gamma$ |
| | Ratio of the energy difference between the maximum energy deposit and the energy deposit in a secondary maximum in the cluster to the sum of these energies | $E_{\mathrm{ratio}}$ | $e/\gamma$ |
| | Ratio of the energy measured in the first layer of the electromagnetic calorimeter to the total energy of the EM cluster | $f_1$ | $e/\gamma$ |

TABLE 8.2: Definition and description of the shower shape variables used to differentiate electromagnetic from hadronic showers [169].

| Working point | Calorimeter isolation | Track isolation |
|---|---|---|
| Loose | $E_{\mathrm{T}}^{\mathrm{cone20}} < 0.065 \times E_{\mathrm{T}}$ | $p_{\mathrm{T}}^{\mathrm{cone20}} / E_{\mathrm{T}} < 0.05$ |
| Tight | $E_{\mathrm{T}}^{\mathrm{cone40}} < 0.022 \times E_{\mathrm{T}} + 2.45\,\mathrm{GeV}$ | $p_{\mathrm{T}}^{\mathrm{cone20}} / E_{\mathrm{T}} < 0.05$ |

TABLE 8.3: Definition of the Loose and Tight photon isolation working points.

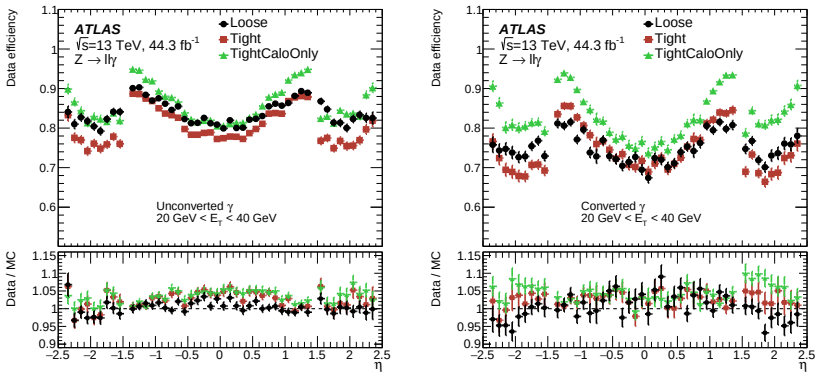


(a) (b)

FIGURE 8.7: Efficiency of the respective isolation working points as a function of $\eta$, split into converted photons ((a)) and unconverted photons ((b)) [169].

The track isolation variable $p_T^{\mathrm{coneXX}}$ uses tracking information. It is defined as the sum of the transverse momenta of all tracks within a given cone around the photon cluster direction, given as

$$p_T^{\mathrm{coneXX}} = \sum p_{T,\mathrm{track}}(\Delta R_{\mathrm{cone}}, PV)$$

The tracks in the sum have to pass a minimum transverse momentum cut of $p_{\mathrm{T}} > 1.5\,\mathrm{GeV}$ and need to be associated with the selected vertex (PV) of the event. Since for boosted topologies, the surrounding objects are less spread, the cone radius is $p_{\mathrm{T}}$ dependently defined as

$$\Delta R_{\mathrm{cone}} = \min\left(\frac{10\,\mathrm{GeV}}{p_{\mathrm{T}}[\mathrm{GeV}]}, 0.2\right).$$

The efficiency of the isolation is shown in 8.7 as a function of $\eta$. The working points shown in the Looses and Tight curves follow the definition given in 8.3.

## 8.5 Muons

Muons are reconstructed from measurements both in the Inner Detector (ID) as well as the Muon System (MS) [171]. Pattern recognition algorithms are applied in both systems independently and the resulting tracks from the ID and *segments* from the MS are then combined to form muon candidates.

For each chamber, a so-called track segment is built from hits aligned on a trajectory that is loosely compatible with the interaction point (IP). Muon track candidates are constructed by combining the segments from different chambers. Starting from seeds, which are defined as the segments built in the middle layer of the detector, a combinatorial search is performed. For the muon reconstruction accepted combinations of segments are selected based on hit multiplicity and overall fit quality requirements. Next, the tracks found in the inner detector and the muon candidates are combined.

Depending on which specific detector information is used to reconstruct a muon candidate, four distinct muon types are discerned, which are defined in the following. The first type, so-called *combined muons*, is obtained by extrapolating MS-only candidates consisting of combined segments inward, towards the IP, and searching for matching tracks in the ID. A complimentary inside-out extrapolation is used as well. After finding a match, the combined measurements are refit into one final muon track object using a global fit. These form the muon type of the highest purity. To regain efficiency in the reconstruction, additional reconstruction chains are deployed. *Segment-tagged muons* are reconstructed from ID tracks that are associated with at least one track segment after extrapolation to the MS. These segments need to be built either in the CSC or the MDT for segment-tagged muons to be accepted as muon candidates. Further, in regions where the MS is only partially instrumented due to gaps needed for services ($|\eta| < 0.1$), calorimeter information can also be used to build muon candidates. ID tracks matched to energy deposits in the calorimeter that is compatible with a minimum-ionising particle are then also identified as muons. These are called *calorimeter-tagged muons* and have the lowest purity of all muon types, but allow to recover acceptance. Outside of the ID acceptance ($2.5 < |\eta| < 2.7$), *extrapolated muons* can be reconstructed from MS measurements alone that are compatible with the IP. As a minimum requirement, muon segments need to be found in at least two out of three MS layers in the forward region.

## 8.6 Missing transverse momentum

For particles that either interact only weakly or possibly don't interact at all with the matter, no signals are registered in the active sensor elements of the ATLAS detector. The *missing transverse momentum* ($E_{\mathrm{T}}^{\mathrm{miss}}$) gives an experimental handle on signatures with undetected particles. Due to momentum conservation, the vectorial sum of the transverse momenta $\boldsymbol{p}_{\mathrm{T}}$ of all particles produced in a $pp$ collision has to add up to zero. A deviation in this sum from the expectation allows inferring the momentum carried away by particles that don't interact with the detector.

The basic task of the $E_{\mathrm{T}}^{\mathrm{miss}}$ reconstruction is thus to collect all objects originating from the hard scatter interaction and sum up the transverse components of their momenta. These objects can logically be separated in the *hard* event signals made up of reconstructed electrons, photons, muons, $\tau$-leptons as well as jets on one side and the *soft* event signals on the other. Soft signals are the remnant detector signals that did not get associated with any of the hard objects, like single tracks that still can be matched to the primary vertex, which need to be included in the $E_{\mathrm{T}}^{\mathrm{miss}}$ calculation to avoid – or minimise – reconstruction biases.

Missing transverse momentum is defined [172] using the negative sum of the transverse $x$ and $y$ components of the hard and soft signals

$$E_{x(y)}^{\mathrm{miss}} = -\sum_{i\in\{\text{hard objects}\}} p_{x(y),i} - \sum_{j\in\{\text{soft signals}\}} p_{x(y),j}, \tag{8.10}$$

that can be associated with the primarily selected vertex. $E_{\mathrm{T}}^{\mathrm{miss}}$ captures – as its name suggests – the momentum missing from the event to balance the vector sum to zero. From these components the following observables can be constructed:

$$\boldsymbol{E}_T^{\mathrm{miss}} = (E_x^{\mathrm{miss}}, E_y^{\mathrm{miss}}) \tag{8.11}$$

$$E_{\mathrm{T}}^{\mathrm{miss}} = |\boldsymbol{E}_T^{\mathrm{miss}}| = \sqrt{(E_x^{\mathrm{miss}})^2 + (E_y^{\mathrm{miss}})^2} \tag{8.12}$$

$$\phi^{\mathrm{miss}} = \tan^{-1}(E_y^{\mathrm{miss}} / E_x^{\mathrm{miss}}) \tag{8.13}$$

The vector $\boldsymbol{E}_T^{\mathrm{miss}}$ has a magnitude $E_{\mathrm{T}}^{\mathrm{miss}}$ and an azimuthal orientation $\phi^{\mathrm{miss}}$. By construction, $E_{\mathrm{T}}^{\mathrm{miss}}$ has a positive value. It has to be noted here that due to the finite detector acceptance and

limited reconstruction and selection efficiencies, not all four momenta of a hard interaction can be reconstructed. Also, neutral particles not included in any reconstructed objects are not accounted for, since the inclusion of these signals from the calorimeter would suffer unacceptable contributions from the pile-up. Thus the missing transverse momentum exhibits an observational bias towards positive values which is then also expected in events without a genuine transverse momentum loss from not detected particles. Resolution effects of the individual reconstructed objects play a role here as well since, for example, a shift in a jet momentum from its true value due to the resolution will cause a shift in the missing transverse momentum calculation.

### 8.6.1 $E_{\mathrm{T}}^{\mathrm{miss}}$ reconstruction

In the calculation of $E_{\mathrm{T}}^{\mathrm{miss}}$ only mutually exclusive detector signals should be used, leading to the necessity to define an overlap removal strategy to avoid any double counting. At the same time, different analyses prioritising different objects might not interpret a given event the same way. Both of these issues are addressed by defining a sequence of selected objects that are used for the $E_{\mathrm{T}}^{\mathrm{miss}}$ calculation. The $E_{\mathrm{T}}^{\mathrm{miss}}$ is split into one contribution for each hard object type ($e$, $\gamma$, $\tau_{\mathrm{had}}$, jet) as well as the soft term:

$$\boldsymbol{E}_T^{\mathrm{miss}} = \underbrace{-\sum_{\substack{\text{selected}\\ \text{electrons}}} \boldsymbol{p}_T^{e} - \sum_{\substack{\text{selected}\\ \text{photons}}} \boldsymbol{p}_T^{\gamma} - \sum_{\substack{\text{selected}\\ \tau-\text{hadrons}}} \boldsymbol{p}_T^{\tau_{\mathrm{had}}} - \sum_{\substack{\text{selected}\\ \text{muons}}} \boldsymbol{p}_T^{\mu} - \sum_{\substack{\text{selected}\\ \text{jets}}} \boldsymbol{p}_T^{\mathrm{jet}}}_{\text{hard term}} \underbrace{- \sum_{\substack{\text{unused}\\ \text{tracks}}} \boldsymbol{p}_T^{\mathrm{track}}}_{\text{soft term}}, \tag{8.14}$$

thus allowing for a flexible recalculation of the missing transverse momentum depending on an individual analysis selection. The soft term includes ID tracks that can not be associated with any of the hard objects but passes basic quality selections (for details see [173]) and can be associated with the selected primary vertex. The matching to the vertex applies cuts on the transverse and longitudinal impact parameters, namely $|d_0| < 1.5\,\mathrm{mm}$ and $|z_0 \sin(\theta)| < 1.5\,\mathrm{mm}$. Especially in events with a low multiplicity of hard objects, this term plays an important role in improving both the $E_{\mathrm{T}}^{\mathrm{miss}}$ scale and resolution.

### 8.6.2 $E_{\mathrm{T}}^{\mathrm{miss}}$ response and resolution

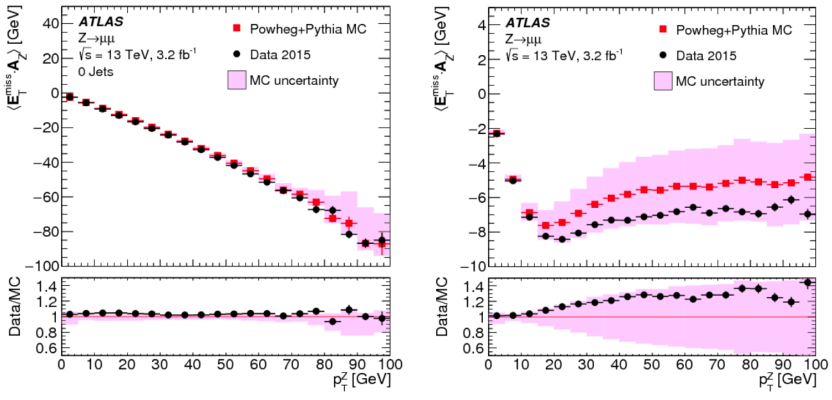


(a) (b)

FIGURE 8.8: Distribution of the mean missing transverse momentum projected on the transverse momentum vector of the $Z$ boson in $Z \to \mu\mu$ events [172]. A selection requiring no jets in the events is shown in (a), while (b) gives the inclusive selection.

The performance evaluation uses two basic characteristics to quantify the reconstruction quality, the $E_{\mathrm{T}}^{\mathrm{miss}}$ response and resolution. In this context, the response is the deviation of the measured $E_{\mathrm{T}}^{\mathrm{miss}}$ from the expected value $E_{\mathrm{T}}^{\mathrm{miss,\,true}}$ for a specific final state. The response is called linear if it does not depend on the truth $E_{\mathrm{T}}^{\mathrm{miss}}$ or the hardness of the interaction. To test the case of $\langle E_{\mathrm{T}}^{\mathrm{miss}} \rangle = 0$, the final state of $Z \to \mu\mu$ is chosen, which can be used both in MC as well as data due to the low backgrounds. Production of neutrinos in the hadronic recoil of the $Z$ is strongly suppressed and thus this channel can be seen as free from $E_{\mathrm{T}}^{\mathrm{miss}}$. In $Z \to \mu\mu$ events, one can use the $p_{\mathrm{T}}$ of the $Z$ boson as a reference for the hardness of the interaction, with respect to which one can evaluate the $E_{\mathrm{T}}^{\mathrm{miss}}$ response. To be sensitive to limitations in the $E_{\mathrm{T}}^{\mathrm{miss}}$ reconstruction, the magnitude of the $E_{\mathrm{T}}^{\mathrm{miss}}$ component parallel to the axis defined by the $Z$'s momentum, $P_{\parallel}^{Z^0}$, is used

$$P_{\parallel}^{Z^0} = \boldsymbol{E}_T^{\mathrm{miss}} \cdot \boldsymbol{A}_{\boldsymbol{Z^0}}, \quad \boldsymbol{A}_{\boldsymbol{Z^0}} = \frac{\boldsymbol{p}_T^{Z^0}}{p_T^{Z^0}}, \tag{8.15}$$

where $\boldsymbol{p}_T^{Z^0}$ is the two dimensional vector of the $Z$ boson's momentum in the transverse plane and $p_T^{Z^0}$ is its magnitude. The expectation value for $P_{\parallel}^{Z^0}$ is zero and any deviation from it represents a bias in the $E_{\mathrm{T}}^{\mathrm{miss}}$ reconstruction. 8.8 shows the mean value of $P_{\parallel}^{Z^0}$ as a function of the transverse momentum of the $Z$ boson. 8.8a shows the distribution for a selection of events that don't contain additional jets, while 8.8b displays the inclusive case. Without jets, $E_{\mathrm{T}}^{\mathrm{miss}}$ is reconstructed from the two muons and the soft term alone. One can see that without other hard objects in the event, the $E_{\mathrm{T}}^{\mathrm{miss}}$ depends strongly on the hard scatter activity. Neutral particles that are not included in the soft term but also charged particles that either did not get reconstructed or are not considered in the soft term due to failing the track selection cause this behaviour. In the inclusive case (8.8b), where the $Z$ recoils against reconstructed jets, the $p_T^{Z^0}$ dependence can be recovered above $p_T^{Z^0} > 20\,\mathrm{GeV}$. Still, a bias due to acceptance and reconstruction efficiency limitations is also expected in the inclusive selection.

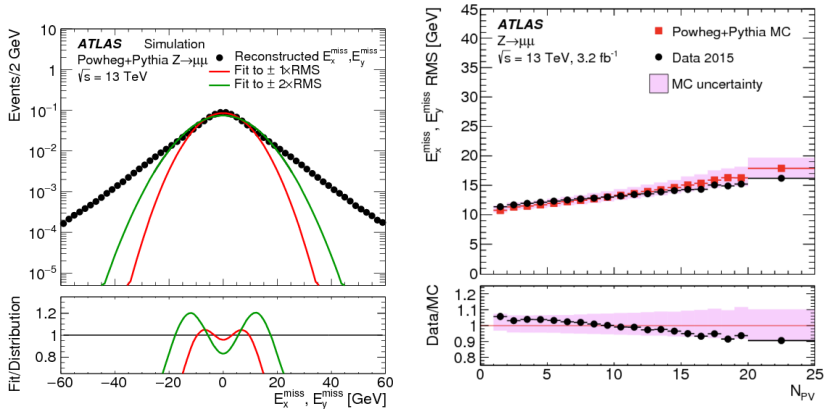


(a) (b)

FIGURE 8.9: The combined distribution of $E_x^{\mathrm{miss}}$ and $E_y^{\mathrm{miss}}$ from $Z \to \mu\mu$ simulation is shown in (a), while (b) displays the RMS of the $x$ and $y$ component of missing transverse energy as a function of the number of primary vertices [172].

The resolution is defined as the root mean square (RMS) of the differences between the $x(y)$ component of the $E_{\mathrm{T}}^{\mathrm{miss}}$ in reconstruction and at the truth level. One can see from the combined distribution of $E_x^{\mathrm{miss}}$ and $E_y^{\mathrm{miss}}$ in 8.9a that the shape exhibits non-gaussian tails, making the definition of the resolution via the RMS an appropriate measure of the variability between the reconstructed value and the true value compared to fitting a Gaussian function to the distribution and taking its width as the uncertainty.

# Part III

# EXPLORING DARK PHOTON PRODUCTION FROM HIGGS BOSON AND HEAVY BOSON DECAYS

# 9 Dark photon from SM Higgs boson decay in $ZH$ production mode

This analysis is based on the $ZH$ production mode where $Z \to \ell^+\ell^-$ ($\ell = e, \mu$) and $H \to \gamma\gamma_d$, which proceeds at leading order through the Feynman diagrams shown in Figure 9.1. The study is performed using a final state consisting of two same-flavour, opposite-charge electrons or muons, an isolated photon and missing transverse momentum. The requirements applied to the photon and the $E_{\mathrm{T}}^{\mathrm{miss}}$, originating from a potential SM Higgs boson decay, are optimised to maximise the signal acceptance. On the other hand, the leptons are used for triggering the event and provide a $Z$ boson mass constraint. The transverse mass $m_{\mathrm{T}}$ of the $\gamma - E_{\mathrm{T}}^{\mathrm{miss}}$ system presents a kinematic edge at the Higgs boson mass and is included as a variable of interest in the boosted decision tree (BDT) score that is exploited to search for a dark photon signal. The kinematics of these events allow the search for low-mass ($\neq 0$) $\gamma_d$. Hence, the analysis is optimised for dark photon searches in the [0-40] GeV mass range.

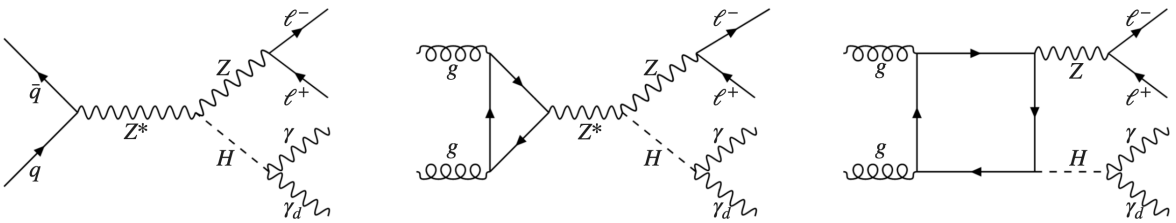


FIGURE 9.1: Feynman diagrams for H$\to \gamma\gamma_d$ in $q\bar{q} \to ZH$ and $gg \to ZH$ production modes.

## 9.1 Data samples

The data used in this search were collected by the ATLAS experiment from the LHC $pp$ collisions at $\sqrt{s} = 13$ TeV during stable beam conditions, with all subdetectors operational [174]. The corresponding total integrated luminosity is 139 fb$^{-1}$. The data were recorded with high efficiency using unprescaled trigger algorithms based on the presence of single leptons or di-leptons, where electrons and muons are considered as leptons [175, 176].

The trigger thresholds as summarised in Table 9.1 are based on the transverse momentum $p_{\mathrm{T}}$ of the leptons and are determined by the data-taking conditions during the different periods [177], particularly by the number of multiple $pp$ interactions in the same or neighbouring bunch crossings, referred to as pileup. The number of pileup interactions ranges from about 8 to 70, with an average of 34. Single-lepton triggers with low $p_{\mathrm{T}}$ threshold and lepton isolation requirements are combined in a logical OR with higher-threshold triggers without isolation requirements to give maximum efficiency.

The di-lepton triggers require two leptons that satisfy loose identification criteria, with symmetric (symmetric or asymmetric) $p_{\mathrm{T}}$ thresholds for electrons (muons). The di-lepton trigger complements the single-lepton trigger to recover between 3% and 3.6% signal efficiency depending on the dark photon mass points for combined $Z \to ee$ and $Z \to \mu\mu$ final states.

TABLE 9.1: List of single-lepton and di-lepton triggers.

| Period | Electron | Muon |
|---|---|---|
| | Single-lepton | |
| 2015 | $p_{\mathrm{T}} > 24$, 60, 120 GeV | $p_{\mathrm{T}} > 20$, 50 GeV |
| 2016-2018 | $p_{\mathrm{T}} > 26$, 60, 140 GeV | $p_{\mathrm{T}} > 26$, 50 GeV |
| | Di-lepton | |
| 2015 | $p_T^1, p_T^2 > 12$ GeV | $p_T^1 > 18$ GeV, $p_T^2 > 8$ GeV<br>$p_T^1, p_T^2 > 10$ GeV |
| 2016, 2018 | $p_T^1, p_T^2 > 17$ GeV | $p_T^1 > 22$ GeV, $p_T^2 > 8$ GeV<br>$p_T^1, p_T^2 > 14$ GeV |
| 2017, 2018 | $p_T^1, p_T^2 > 24$ GeV | $p_T^1 > 22$ GeV, $p_T^2 > 8$ GeV<br>$p_T^1, p_T^2 > 14$ GeV |

## 9.2 Simulated event samples

Monte Carlo (MC) simulated samples are used to model both the signal and the different background processes using the configurations shown in Table 10.4. All the samples were generated at a centre-of-mass energy of 13 TeV. The generated events were processed through a simulation [178] of the ATLAS detector geometry and response using GEANT [131], and through the same reconstruction software as the collected $pp$ collision data. Corrections were applied to the simulated events so that the particle candidates' selection efficiencies, energy scales and energy resolutions match those determined from data control samples. In addition, appropriate scale factors corresponding to the fired triggers are applied [175, 176]. The simulated samples are normalised to the total integrated luminosity, using the corresponding cross-sections computed to the highest order available in perturbation theory. The pileup effects were modelled using events from minimum-bias interactions generated using PYTHIA8.186 [179] with the A3 set of tuned parameters [180]. They were overlaid onto the simulated hard-scatter events according to the luminosity profile of the recorded data (reweighting procedure). For massive $\gamma_d$ signal samples and the $tW\gamma$ background process, the detector response was simulated using a fast parameterized simulation of the ATLAS calorimeters [181]. For the massless signal samples and all remaining background samples, the full GEANT simulation was used. All simulated samples, except those produced with the SHERPA2.2.1 [182] event generator, used EVTGEN 1.2.0 [183] to model the decays of heavy-flavour hadrons.

TABLE 9.2: The configurations used for event generation of signal and background processes. $V$ refers to an electroweak boson ($W$ or $Z/\gamma^*$). The matrix element (ME) order refers to the order in the strong coupling constant of the perturbative calculation in the MC event generation. PDF refers to the parton density libraries used with the generator. The tune refers to the underlying-event tune of the parton shower model.

| Process | Generator | ME Order | PDF | Parton Shower | Tune |
|---|---|---|---|---|---|
| | | Signal samples | | | |
| $ZH, H \to \gamma\gamma_d$ | POWHEG-BOX [v2] | NLO | NNPDF [3.0nlo] | PYTHIA [8.245] | AZNLO |
| | | SM background samples | | | |
| $V\gamma^{QCD}$ | SHERPA v2.2.8 | NLO (up to 2 jets), LO (up to 3 jets) | NNPDF [3.0nnlo] | SHERPA MEPS@NLO | SHERPA |
| $V\gamma^{EWK}$ | MADGRAPH5_aMC@NLO [v2.6.5] | LO | NNPDF [2.3lo] | PYTHIA [8.240] | A14 |
| $Z^{QCD}$ | SHERPA v2.2.1 | NLO (up to 2 jets), LO (up to 4 jets) | NNPDF [3.0nnlo] | SHERPA MEPS@NLO | SHERPA |
| $Z^{EWK}$ | SHERPA v2.2.1 | NLO (up to 2 jets), LO (up to 4 jets) | NNPDF [3.0nnlo] | SHERPA MEPS@NLO | SHERPA |
| Single $t$-quark/$t\bar{t}$ | POWHEG-BOX [v2] | NLO | NNPDF [2.3lo] | PYTHIA [8.230] | A14 |
| $t\bar{t}$ $(V, VV)$, $Wt\gamma$ | MADGRAPH5_aMC@NLO [v2.2.3] | NLO | NNPDF [2.3lo] | PYTHIA [8.210] | A14 |
| SM Higgs | POWHEG-BOX [v2] | NNLO (ggF), NLO (VBF, $VH, t\bar{t}H$) | PDF4LHC15 | PYTHIA [8.230] | AZNLO |
| $VV\gamma$ | SHERPA v2.2.11 | NLO (0 jets), LO (up to 3 jets) | NNPDF [3.0nnlo] | SHERPA MEPS@NLO | SHERPA |
| $VV/VVV$ | SHERPA v2.2.2 | NLO (0 jets), LO (up to 3 jets) | NNPDF [3.0nnlo] | SHERPA MEPS@NLO | SHERPA |
| | | Samples for evaluating systematic uncertainties | | | |
| $ZH, H \to \gamma\gamma_d$ | POWHEG-BOX [v2] | NLO | NNPDF [3.0nlo] | Herwig [v7.1.3] | H7-UE-MMHT |
| $Z\gamma^{QCD}$ | MADGRAPH5_aMC@NLO [v2.3.3] | NLO | NNPDF [2.3lo] | PYTHIA [8.212] | A14 |
| $W\gamma^{QCD}$ | MADGRAPH [v2.8.1] | NLO | NNPDF [2.3lo] | PYTHIA [8.244] | A14 |
| $W\gamma^{EWK}$ | MADGRAPH [v2.8.1] | NLO | NNPDF [3.0nlo] | Herwig [v7.1.3] | H7-UE-MMHT |
| $Z^{QCD}$ | MADGRAPH5_aMC@NLO [v2.2.3] | NLO | NNPDF [2.3lo] | PYTHIA [8.210] | A14 |
| $Z^{EWK}$ | Herwig [v7.1.3] | NLO | NNPDF [3.0nlo] | Herwig [v7.1.3] | H7-UE-MMHT |
| $V\gamma\gamma$ | MADGRAPH5_aMC@NLO [v2.7.3] | NLO | NNPDF [2.3lo] | PYTHIA [8.244] | A14 |
| $t\bar{t}$ | POWHEG-BOX [v2] | NLO | NNPDF [3.0nlo] | Herwig [v7.0.4] | H7-UE-MMHT |
| $t\bar{t}\,V$ | MADGRAPH5_aMC@NLO [v2.3.3] | NLO | NNPDF [3.0nlo] | Herwig [v7.2.1] | H7-UE-MMHT |

### 9.2.1 Signal samples

The signal process of a Higgs boson decaying to a photon and an invisible dark photon ($\gamma_d$) was generated in the $ZH$ production mode as shown in Figure 9.1. Both $q\bar{q} \to ZH$ and $gg \to ZH$ production modes were considered in order to have the full $ZH$ cross-section of 0.884 pb [184]. Matrix elements were estimatd using POWHEGv2 [185, 186] with the NNPDF3.0 parton density libraries [187]. Events from the $q\bar{q} \to ZH$ process were generated at the next-to-leading order (NLO) while the ones corresponding to $gg \to ZH$ were generated at the leading order (LO). PYTHIA8.245 was used to perform the Higgs boson decay as well as the hadronisation and showering with the CTEQ6L1 PDF set and the AZNLO tune [188]. The samples were generated at a Higgs boson mass of 125 GeV, a width set to the SM value of 4 MeV [184] and the complex pole scheme [189] turned off. The Hidden Valley scenario [190] for BSM Higgs boson decay as implemented in PYTHIA8.150 was used to produce $H \to \gamma\gamma_d$ signal events. In order to extend the reach of the analysis while keeping a similar approach and optimisation, several samples with higher $\gamma_\mathrm{d}$ masses were simulated. The aim is to perform searches for relatively massive $\gamma_\mathrm{d}$ in $H \to \gamma\gamma_\mathrm{d}$ decay channel using the same experimental data and analysis procedure. Samples with $m_{\gamma_\mathrm{d}}$ up to 40 GeV were compared to the nominal (massless) one as presented in Figure 9.2, and they present small variations in the considered kinematics variables. These small differences would be partially mitigated at the reconstruction level after taking into account the different detector effects and resolutions. In addition, signal-to-background optimisation will be performed for all $m_{\gamma_\mathrm{d}}$ masses and the same analysis procedure can be extended to the search for "low-mass" dark photons and extract the corresponding sensitivity. It was decided to limit the scope of this search to $m_{\gamma_\mathrm{d}} = 40$ GeV because of the limited phase-space above this value due to constraints from the Higgs boson mass. A total of six Monte Carlo samples were generated with dark photon masses equal to 0, 1, 10, 20, 30, 40 GeV. Finally, to increase the generation efficiency, a generator-level lepton filter was applied, requiring two electrons or muons with $p_\mathrm{T} > 10$ GeV and $|\eta| < 2.7$.

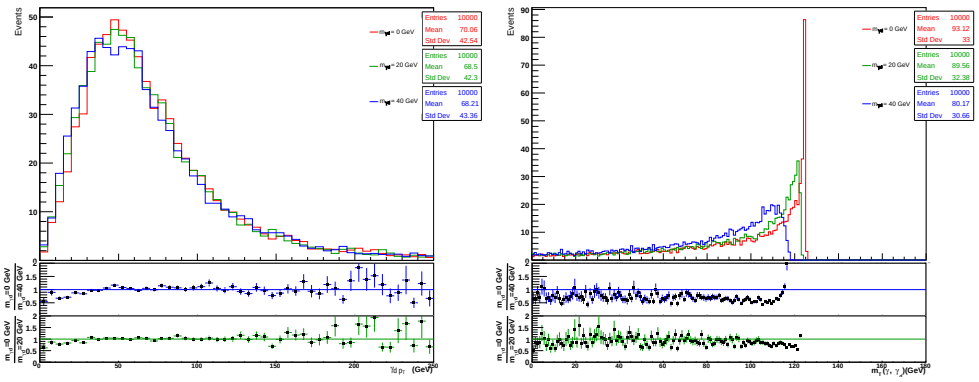

(a) (b)

FIGURE 9.2: Comparison of truth level kinematics variables: $p_\mathrm{T}\gamma_\mathrm{d}$ (a) and $m_\mathrm{T}$ (b) for several hidden valley dark photon masses (0, 20, 40 GeV) in qqZH, $H \to \gamma\gamma_\mathrm{d}$. The ratio is calculated with respect to the massless point (0 GeV).

### 9.2.2 Background samples

The analysis is affected by a large variety of background processes. The irreducible background comes from $VV\gamma$ final states ($V$ being any of $W, Z$) with both $V$ bosons decaying leptonically. The reducible background, which is dominant, comes from biased $E_{\mathrm{T}}^{\mathrm{miss}}$ measurement (fake $E_{\mathrm{T}}^{\mathrm{miss}}$) — typically due to undetected particles or hadronic jets not fully contained in the detector acceptance — or from particle misidentification. For instance, an electron can wrongly be identified as a photon (electron faking photon, $e \rightsquigarrow \gamma$), or an energetic neutral pion ($\pi^0 \rightarrow \gamma\gamma$) contained in a hadronic jet can wrongly be identified as a photon (jet faking photon, $j \rightsquigarrow \gamma$). Moreover, a track in a jet may also be wrongly identified as a lepton, or a lepton from a heavy-flavour quark decay may appear as an isolated lepton (jet faking lepton, $j \rightsquigarrow \ell$). Finally, events from top-quark production, with subsequent semi-leptonic $t \rightarrow W(\rightarrow \ell\nu)b$ decay, contain genuine $E_{\mathrm{T}}^{\mathrm{miss}}$, one or two leptons, and one or two $b$-jets that may fail a $b$-jet veto.

Whenever higher-order cross-section computations are available [191, 192, 193], they are used to rescale the cross-section of the generator. Finally, a specific treatment was applied to processes with possible overlapping events in $Z\gamma$ and $Z$+jets, $VV$ and $VV\gamma$ or in $t\bar{t}$ and $t\bar{t}\gamma$. To avoid duplicated events, the overlap removal algorithm gives preference to photons produced in matrix elements (ME) over the ones from initial/final state radiations or decays. As an example, overlapping events were removed from $Z$+jets and kept in the $Z\gamma$ process. Finally, $\ell\ell$ final states consist of $ee$ and $\mu^+\mu^-$ channels and include the leptonic decay of $\tau$-leptons.

**Irreducible background:** These processes were generated according to the number of leptons in their final states as $\ell\ell\nu\nu\gamma$, $\ell\ell\ell\nu\gamma$ and $\ell\ell\ell\ell\gamma$ using the SHERPA v2.2.11 [194] event generator at NLO with up to three jets at the leading order (LO). In addition, contributions from off-shell bosons were also included. The full event was generated using NNPDF30_nnlo_as_0118 libraries and tuning developed by the Sherpa authors [187].

**$Z\gamma$+jets and $W\gamma$+jets productions:** The $Z(\rightarrow \ell\ell)\gamma$+jets and $W(\rightarrow \ell\nu)\gamma$+jets processes are split into two components based on the order in the electroweak coupling constant $\alpha_{\mathrm{EWK}}$. The strongly-produced component is of order $\alpha_{\mathrm{EWK}}^3$ and the electroweak component is of order $\alpha_{\mathrm{EWK}}^5$. The strong background processes of $Z(\rightarrow \ell\ell)\gamma$+jets are modelled using filtered SHERPA 2.2.8 [182] samples. These samples are filtered by requiring a vector boson $p_{\mathrm{T}} > 90$ GeV and are merged with SHERPA 2.2.8 $V\gamma$+jets samples produced with a biased phase space enhancing $p_{\mathrm{T}}(V)$ and $p_{\mathrm{T}}(\gamma)$ at high values. A photon filter was applied, with $p_{\mathrm{T}} > 7$ GeV, for all the merged $Z(\rightarrow \ell\ell)\gamma$+jets samples. These calculations use the Comix [195] and Open-Loops [196] matrix element generators, and merging is done with the SHERPA parton shower [197] using the ME+PS@NLO prescription [198]. The NNPDF30_nnlo_as_0118 PDF and tuning [187] is used. Matrix elements for the strongly-produced contribution are calculated at NLO in $\alpha_{\mathrm{S}}$ for up to two additional final-state partons, and at LO for up to three additional partons with NLO EWK+QCD corrections used as the central value for SHERPA. Matrix elements for the electroweak VBF contribution are calculated at LO in $\alpha_{\mathrm{S}}$ with five final-state partons (e.g. $\ell^+\ell^-\gamma jj$ QCD=0) in MADGRAPH 2.6.5. The LO interference between this electroweak and strong production samples was generated, and its cross-section is about 5% of the electroweak sample. This value is taken into account as uncertainty on the electroweak background contribution. The showering is done using PYTHIA8.240 [199] and merged in the CKKW-L scheme [200]. The photon $p_{\mathrm{T}}$ is required to be larger than 10 GeV, and the Frixione isolation [201] is applied to remove overlap with charged partons.

**$Z$ + jets production:** The modelling of $Z$+jets is crucial in this analysis. This background has significant systematic uncertainties, as the modelling of the $E_{\mathrm{T}}^{\mathrm{miss}}$ depends on the modelling of pile-up interactions and the jet energy response. The $Z$+jets samples used are simulated using the SHERPA 2.2.1 event generator and the NNPDF3.0 NNLO libraries and the SHERPA tuning, with the invariant $\ell\ell$ mass $m_{\ell\ell} > 40$ GeV.

**Top-quark pair and single top-quark productions:** Background samples for top-quark pair production, as well as single top-quark, including $Wt$ production, were simulated using POWHEG-BOX [v2] interfaced with PYTHIA8.230 with the NNPDF2.3LO libraries and the A14 tuning was used. Both $s$-channel and $t$-channel productions are included in the single top-quark samples. The diagram removal scheme (DR) [202] is used to remove interferences and overlap between the $tW$ and $t\bar{t}$ productions.

**$t\bar{t}$ ($V$, $VV$), $t\bar{t}\gamma$ and $Wt\gamma$ production:** Background samples for top-quark pair production in association with one or two vector bosons ($W$ or $Z$) or a photon, as well as a single top-quark with an additional $W$ and $\gamma$, were simulated with the MADGRAPH5_aMC@NLO 2.3.3 generator [154] interfaced with PYTHIA8.210 with the NNPDF2.3LO libraries and the A14 tune.

**SM Higgs boson production:** Different production modes are considered as backgrounds as they can produce final states with $\ell^+\ell^- + \gamma + E_{\mathrm{T}}^{\mathrm{miss}}$. Higgs bosons produced in association with a $W$ or $Z$ boson as well as Higgs bosons produced via gluon-gluon fusion (ggF), vector boson fusion (VBF) and $ttH$ productions were all considered. These samples were generated using POWHEG-BOX [v2] with the NNPDF3.0 libraries and then showered with PYTHIA8.230 and AZNLO tuning.

**Di-boson production:** $ZZ \to \ell^+\ell^-\ell'^+\ell'^-$, $ZZ \to \ell^+\ell^-\nu\bar{\nu}$, $WZ \to \ell\nu\ell^+\ell^-$ and $WW \to \ell^+\nu\ell^-\bar{\nu}$ ($\ell = e, \mu$) processes are simulated using the SHERPA2.2.2 [194] event generator with NNPFD3.0NNLO libraries in the case of $qq$ and $gg$-initiated production. The $gg \to ZZ$ processes include a QCD k-factor of 1.7 which was calculated from the ratio NLO/LO of the corresponding cross-sections at 13 TeV [184]. The $qq \to \ell^+\ell^-\nu\bar{\nu}$ samples include both $ZZ$ and $WW$ events.

**Tri-boson production:** The expected contribution from this background is very minor as it is suppressed by the requirement of no more than two leptons in the final state. Tri-boson production, $VVV$, with $V$ = $W$ or $Z$, is simulated by the SHERPA2.2.2 event generator at NLO with NNPDF3.0 NNLO PDF libraries and tuning.

## 9.3 Event reconstruction and selection

### 9.3.1 Event reconstruction

Candidate events are required to have a reconstructed vertex with at least two associated tracks, originating from the beam collision region in the $x-y$ plane, with $p_{\mathrm{T}} > 0.5$ GeV. The primary vertex in the event is selected as the vertex with the highest scalar sum of the squared $p_{\mathrm{T}}$ of associated tracks [203].

Electrons are reconstructed by matching clustered energy deposits in the EM calorimeters to tracks in the ID [204]. Candidates falling within the transition regions between the barrel and endcap EM calorimeters ($1.37 < |\eta| < 1.52$) are also included. All electrons must fulfill $p_{\mathrm{T}} > 4.5$ GeV and $|\eta| < 2.47$ as well as loose identification criteria [204]. A longitudinal impact parameter requirement of $|z_0 \sin(\theta)| < 5$ mm as well as a transverse impact parameter satisfying $|d_0|/\sigma(d_0) < 5$ are required to ensure that electrons originate from the primary vertex.

Muons are reconstructed by matching ID tracks to MS tracks or track segments, by matching ID tracks to a calorimeter energy deposit compatible with a minimum-ionizing particle, or by identifying MS tracks passing the loose requirement and compatible with the primary vertex [205]. Muon candidates are required to fulfil $p_{\mathrm{T}} > 4$ GeV, $|\eta| < 2.7$ and a very loose isolation criterion. A longitudinal impact parameter requirement of $|z_0 \sin(\theta)| < 5$ mm as well as a transverse impact parameter satisfying $|d_0|/\sigma(d_0) < 3$ are required to ensure that muons originate from the primary vertex as well.

Photon candidates are reconstructed from clustered energy deposits in the EM calorimeter [204]. They must fulfill $p_{\mathrm{T}} > 15$ GeV, $|\eta| < 2.37$ and tight identification and isolation criteria [204]. They are also required to be outside the transition region ($1.37 < |\eta| < 1.52$) between barrel and endcap EM calorimeters.

Particle flow (PFlow) jets are reconstructed using the anti-$k_t$ algorithm [162, 206] with a radius parameter of $R = 0.4$, using charged constituents associated with the primary vertex and neutral PFlow constituents as inputs [207]. A complete energy calibration procedure, which recovers the initial parton energies after removing pile-up effects, is then applied [208]. Jet candidates are required to have $p_{\mathrm{T}} > 20$ GeV and $|\eta| < 4.5$. A jet vertex tagger (JVT) discriminant [209] is used to identify jets within $|\eta| < 2.5$ originating from the hard scattered (HS) interaction through the use of tracking and vertexing. For jets with $|\eta| > 2.5$, a forward jet vertex tagging algorithm (fJVT) [210, 211] is used to reject pile-up jets. The working points used for JVT (fJVT) provide an HS selection efficiency of about 97% (93% for $p_{\mathrm{T}} > 50$ GeV). In the case of $b$-jets, a multivariate discriminant output is used for the identification [212]. The used working point provides a 77% $b$-jet tagging efficiency in simulated inclusive $t\bar{t}$ events, with rejection factors of 6 and 134 for charm-hadron jets and light-flavour quark- or gluon-initiated jets, respectively.

The missing transverse momentum $\vec{E}_{\mathrm{T}}^{\mathrm{miss}}$, originating from the unbalanced momentum in the transverse plane, is defined as the negative vectorial sum of the transverse momenta of all selected (hard objects) electrons, muons, photons, PFlow jets, as well as the "soft term", which is estimated from tracks compatible with the primary vertex, but not matched to any of those objects [213]. Jets are only included in the $\vec{E}_{\mathrm{T}}^{\mathrm{miss}}$ definition if they have $p_{\mathrm{T}} > 20$ GeV and satisfy the tight JVT and fJVT selections to mitigate pile-up effects. Moreover, an $E_{\mathrm{T}}^{\mathrm{miss}}$ significance $S$ is defined to reduce the effects on $E_{\mathrm{T}}^{\mathrm{miss}}$ from resolution fluctuations.$S$ is a powerful quantity to discriminate between events with fake $\vec{E}_{\mathrm{T}}^{\mathrm{miss}}$, arising from instrumental sources or poorly reconstructed physics objects and events with genuine $\vec{E}_{\mathrm{T}}^{\mathrm{miss}}$ originating from weakly interacting particles, like neutrinos. The variable $S$ is calculated as $|\vec{E}_{\mathrm{T}}^{\mathrm{miss}}|/\left[\sigma_{\mathrm{L}}^2\left(1-\rho_{\mathrm{LT}}^2\right)\right]^{1/2}$, where $\sigma_{\mathrm{L}}$ is the total standard deviation in the direction longitudinal to the $\vec{E}_{\mathrm{T}}^{\mathrm{miss}}$ corresponding to the summation of the covariance matrices from resolution effects of physics objects and soft term entering the $\vec{E}_{\mathrm{T}}^{\mathrm{miss}}$ calculation and $\rho_{\mathrm{LT}}$ is the correlation factor of the longitudinal (L) and transverse (T) measurements [214].

To resolve ambiguities in the reconstruction of physics objects and to avoid double counting of energy deposits and momentum measurements, a $\Delta R$ separation is required as detailed in Table 9.3.

Finally, several cleaning requirements are applied to suppress non-collision backgrounds [215]. Misreconstructed (bad quality) jets can be caused by electronic noise, and jets from collisions are identified by requiring a good fit to the expected pulse shape for each constituent calorimeter cell. Cosmic-ray showers and beam-halo interactions with the LHC collimators are other sources of misreconstructed jets. Those jets are identified by requirements on their energy distribution in the calorimeter and the fraction of their constituent tracks that originate from the primary vertex. Events are rejected if they contain a bad quality jet with $p_{\mathrm{T}} > 20$ GeV as they tend to give rise to fake $E_{\mathrm{T}}^{\mathrm{miss}}$ and a poor description of its distribution in the tail region.

TABLE 9.3: Overview of the overlap removal between reconstructed physics objects and the corresponding matching criteria in order of priority.

| Remove | Keep | Matching criteria |
|---|---|---|
| jet | electron | $\Delta R < 0.2$ |
| jet | muon | number of tracks $< 3$ and $\Delta R < 0.2$ |
| jet | photon | $\Delta R < 0.4$ |
| electron | jet | $0.2 < \Delta R < 0.4$ |
| electron | muon | shared same ID track |
| electron | electron | shared same ID track, electron with lower $p_{\mathrm{T}}$ removed |
| muon | jet | $0.2 < \Delta R < 0.4$ |
| muon | electron | muon with calorimeter deposits and shared ID track |
| photon | electron | $\Delta R < 0.4$ |
| photon | muon | $\Delta R < 0.4$ |

### 9.3.2 Signal region selection

The signal region (SR) targets the $\ell^+\ell^-$+$\gamma$+$E_{\mathrm{T}}^{\mathrm{miss}}$ final state, where the two same-flavour, oppositely charged leptons come from a $Z$ boson decay, the photon comes from the Higgs boson decay and the $E_{\mathrm{T}}^{\mathrm{miss}}$ arises from the potential undetected dark photon. Accepted leptons are required to match the corresponding online trigger candidates, and trigger scale factors and their uncertainties are applied. Table 9.4 lists the event selections in the SR, optimised using a multivariate approach to maximize the signal over background acceptance. A BR($H \to \gamma\gamma_d$) = 5% was assumed for all dark photon masses. The resulting acceptance times efficiency for combined $qqZH$ and $ggZH$ signal events amounts to 10.5% for all considered $\gamma_d$ masses.

TABLE 9.4: Optimised kinematic selections defining the signal region for $\ell^+\ell^-$+$\gamma$+$E_{\mathrm{T}}^{\mathrm{miss}}$.

| |
|---|
| Two same flavour, opposite sign, medium ID and loose isolated leptons, with leading $p_{\mathrm{T}} > 27$ GeV, sub-leading $p_{\mathrm{T}} > 20$ GeV |
| Veto events with additional lepton(s) with loose ID and $p_{\mathrm{T}} > 10$ GeV |
| 76 GeV $< m_{\ell\ell} <$ 116 GeV |
| Only one tight ID, tight isolation photon with $E_{\mathrm{T}}^{\gamma} > 25$ GeV |
| $E_{\mathrm{T}}^{\mathrm{miss}} > 60$ GeV with $\Delta\phi(\vec{E}_{\mathrm{T}}^{\mathrm{miss}}, \vec{p}_{\mathrm{T}}^{\ell\ell\gamma}) > 2.4$ rad |
| $m_{\ell\ell\gamma} > 100$ GeV |
| $\mathrm{N_{jet}} \leq 2$, with $p_{\mathrm{T}}^{\mathrm{jet}} > 30$ GeV, $\lvert\eta\rvert < 4.5$ |
| Veto events with $b$-jet(s) |

Accepted signal electrons, reconstructed using a likelihood-based identification algorithm, must fulfil a 'Medium' criteria [204], while 'Loose' criteria are used to veto additional electrons in the SR. The likelihood relies on the shape of the EM shower measured in the calorimeter, the quality of the track reconstruction, and the quality of the match between the track and the cluster. Similarly, selected

muons are also required to have 'Medium' quality identification [205] while 'Loose' criteria are used to veto additional muons. To suppress hadronic and non-prompt lepton backgrounds, electron and muon candidates are required to satisfy the particle-flow 'Loose' isolation criteria, which are based on tracking and calorimeter measurements [205]. The veto on events with a third loose lepton is used to reduce $ZZ \to \ell^+\ell^-\ell'^+\ell'^-$ and $WZ \to \ell\nu\ell^+\ell^-$ contributions. The invariant mass of the selected lepton pairs $m_{\ell\ell}$ is required to be within the $Z$ boson peak ($[76-116]$ GeV) to reject processes such as $t\bar{t}$ and $WW \to \ell^+\nu\ell^-\bar{\nu}$.

Exactly one 'Tight' photon, satisfying the tight isolation criteria [204] is required. The isolation section requires that the sum of the transverse energies (at the electromagnetic scale) of positive-energy topological clusters located within a distance $\Delta R = 0.4$ of the photon candidate $\gamma$ must be less than $0.24 \times E_{\mathrm{T}}^{\gamma} + 2.45$ [GeV], where $E_{\mathrm{T}}^{\gamma}$ is the transverse energy of the photon. In addition, the scalar sum of the $p_{\mathrm{T}}$ of all tracks located within a distance $\Delta R = 0.2$ of the photon candidate must be less than $0.05 \times E_{\mathrm{T}}^{\gamma}$ [GeV].

Other selections are applied, which exploit the topology and kinematics of the signal events. A threshold on $E_{\mathrm{T}}^{\mathrm{miss}}$ was optimised to select signal events while rejecting the inclusive $Z$ production. In addition, $\vec{E}_{\mathrm{T}}^{\mathrm{miss}}$ is expected to be back-to-back with the $(Z-\gamma)$ system, leading to a requirement on the azimuthal separation $\Delta\phi(\vec{E}_{\mathrm{T}}^{\mathrm{miss}}, \vec{p}_{\mathrm{T}}^{\,\ell\ell\gamma})$ applied in the SR. Furthermore, events with more than 2 jets (with $p_{\mathrm{T}}^{jet} > 30$ GeV, $|\eta| < 4.5$) are rejected to reduce contributions from $V$+jets processes. Finally, a veto on any $b$-tagged jet is also applied to reduce processes with a top quark. Moreover, a cut flow is presented in Table 9.5 showing the effect and the efficiency times acceptance of each optimised SR selection.

Events are categorised into two sub-regions called, respectively, $e^+e^-$- and $\mu^+\mu^-$-channel. The expected signal and background composition in each SR, as predicted from MC simulation, after all the optimisations, is shown in Table 9.6. It should be noticed that the $VV$ background is dominated by the $WZ$ process where the photon is the result of an electron misidentification while contributions from $WW, ZZ$ are found to be negligible due to the very low probability of jets being misidentified as photons. The $VV\gamma$ background is dominated by $ZZ\gamma$ and $WW\gamma$ contributions from the $\ell\ell\nu\nu\gamma$ final state.

To enhance the sensitivity of the search for the $\gamma_d$ signal, a boosted decision tree (BDT) algorithm was implemented using the XGBoost classifier [216]. For training and testing, all events entering the SR are used. All signal events are assigned to the positive class (y = 1) and all background events are assigned to the negative class (y = 0) in the training data. The model has been trained using a feature set consisting of the following 6 variables, according to their ranking: $S$ ($E_{\mathrm{T}}^{\mathrm{miss}}$ significance), $m_{\mathrm{T}}$ (Equation 9.1), $m_{\ell\ell}$, $p_{\mathrm{T}}^{\gamma}$, $m_{\ell\ell\gamma}$, and $p_{\mathrm{T}}^{ratio}$ (Equation 9.2), with:

$$m_{\mathrm{T}} = \sqrt{2E_{\mathrm{T}}^{\mathrm{miss}} p_{\mathrm{T}}^{\gamma}[1 - \cos[\Delta\phi(\vec{E}_{\mathrm{T}}^{\mathrm{miss}}, \vec{p}_{\mathrm{T}}^{\gamma})]]} \tag{9.1}$$

$$p_{\mathrm{T}}^{ratio} = \frac{|\vec{E}_{\mathrm{T}}^{\mathrm{miss}} + \vec{p}_{\mathrm{T}}^{\gamma}| - p_{\mathrm{T}}^{\ell\ell}}{p_{\mathrm{T}}^{\ell\ell}} \tag{9.2}$$

The distributions of the first three more important input variables are presented in Figure 9.3. To train the BDT, the simulated samples introduced in section 9.2 for the signal and the background processes are used. The signal samples for all considered $\gamma_d$ masses were merged and the same weight was assigned to their events. To enhance the statistical power of the training sample, a five-fold cross-validation strategy was adopted. The simulation samples were divided into five equal subsets. Five BDT classifiers with the same input variables were trained. In each BDT training, four subsets of simulation samples were used as the training sample, and the remaining subset was used as the testing sample. The five BDT training correspond to the five possible permutations of such training-testing setups. The five trained BDT models were used to calculate the BDT score of data that were divided

TABLE 9.5: Number of events after each cut in SR for 139 fb$^{-1}$ for $ZH$, $H \to \gamma\gamma_d$ considering BR=5% and $m\gamma_d = 0$ GeV. Generator-level filters are applied to the total events. Only the statistical uncertainty is shown.

| Channel | $ee$ | | $\mu\mu$ | |
|---|---|---|---|---|
| Selection | Yields | $\epsilon \times A$ [%] | Yields | $\epsilon \times A$ [%] |
| Filter efficiency | 396.3 | 100 | 396.3 | 100 |
| Preselections | $101.1 \pm 0.5$ | 25.5 | $101.1 \pm 0.5$ | 25.5 |
| Trigger | $100.7 \pm 0.5$ | 25.4 | $100.7 \pm 0.5$ | 25.4 |
| $ee$ or $\mu\mu$ channel | $38.0 \pm 0.3$ | 9.6 | $45.3 \pm 0.3$ | 11.4 |
| Veto extra photons | $37.9 \pm 0.3$ | 9.6 | $45.2 \pm 0.3$ | 11.4 |
| Veto extra leptons | $37.8 \pm 0.3$ | 9.5 | $45.2 \pm 0.3$ | 11.4 |
| Leading lepton $p_T$ | $37.8 \pm 0.3$ | 9.5 | $45.2 \pm 0.3$ | 11.4 |
| Photon $p_T$ | $36.8 \pm 0.3$ | 9.3 | $44.1 \pm 0.3$ | 11.1 |
| $E_T^{miss}$ | $22.6 \pm 0.2$ | 5.7 | $26.5 \pm 0.3$ | 6.7 |
| $m_{ll}$ | $21.7 \pm 0.2$ | 5.5 | $25.2 \pm 0.2$ | 6.3 |
| $m_{ll\gamma}$ | $21.7 \pm 0.2$ | 5.5 | $25.1 \pm 0.2$ | 6.3 |
| $\Delta\phi(\vec{E}_{\mathrm{T}}^{\mathrm{miss}}, \vec{p}_{\mathrm{T}}^{\ell\ell\gamma})$ | $19.3 \pm 0.2$ | 4.9 | $22.4 \pm 0.2$ | 5.7 |

TABLE 9.6: Expected event yields for signal and background in the SR corresponding to $\mathcal{L} = 139$ fb$^{-1}$. Signal events are for massless $\gamma_d$, assuming BR$(H \to \gamma\gamma_d) = 5\%$. Events for background processes are categorised as $Z\gamma$ (QCD+EWK $Z\gamma$), $Z$+jets (QCD+EWK $Z$+jets), Top (single top-quark, $Wt$), $t\bar{t}$ ($t\bar{t}, t\bar{t}V, t\bar{t}VV$), Top$\gamma$ ($Wt\gamma$), $VV\gamma$ ($WW\gamma, WZ\gamma, ZZ\gamma$), $VV$ ($WW, WZ, ZZ$), SM Higgs ($ggH, VH$, VBF $H$) and $W\gamma$ (QCD+EWK $W\gamma$). Only statistical uncertainties on the simulated samples are shown.

| Channel | Signal | $Z\gamma$ | $Z$+jets | $Top$ | $t\bar{t}$ | Top$\gamma$ | $VV\gamma$ | $VV$ | SM Higgs | $W\gamma$ | Total background |
|---|---|---|---|---|---|---|---|---|---|---|---|
| $ee$ | $19.3 \pm 0.2$ | $155 \pm 15$ | $274 \pm 55$ | $3.5 \pm 0.7$ | $25 \pm 1$ | $1.9 \pm 0.1$ | $26 \pm 1$ | $27 \pm 1$ | $0.41 \pm 0.01$ | $3.5 \pm 1.5$ | $517 \pm 57$ |
| $\mu\mu$ | $22.4 \pm 0.2$ | $283 \pm 18$ | $380 \pm 63$ | $4.6 \pm 0.8$ | $26 \pm 1$ | $2.4 \pm 0.1$ | $35 \pm 1$ | $24 \pm 1$ | $0.54 \pm 0.01$ | $1.6 \pm 1.1$ | $758 \pm 66$ |

into five subsets in the same manner. The BDT classifier output is then used as an observable for the final statistical analysis as discussed in Section 9.6.

## 9.4 Treatment of the background processes

The different background sources, described in Section 9.2.2, are classified into disjoint categories, described below, according to their treatment in the analysis. In what follows, weak bosons $W$, $Z$ are always meant to decay leptonically: $W \to \ell\nu$ and $Z \to \ell^+\ell^-$, unless stated otherwise.

- **Irreducible background from $VV\gamma$ final states**: $Z(\to \ell^+\ell^-)Z(\to \nu\bar{\nu})\gamma$ and $W^+(\to \ell^+\nu)W^-(\to \ell^-\bar{\nu})\gamma$ .
- **Background from electrons faking photons** ($e \rightsquigarrow \gamma$): the involved final states are mostly $Z(\to \ell^+\ell^-)W(\to e\nu)$, and to a lesser extent also $Z(\to \ell^+\ell^-)Z(\to e^+e^-)$ with an undetected electron, $VVV$ with undetected leptons, and finally $\ell^+\ell^- Vt$ and $VVt\bar{t}$ that were not rejected by the $b$-veto.
- **Background from fake $E_{\mathrm{T}}^{\mathrm{miss}}$**: the largest contribution comes from $Z\gamma$ + jets and $Z$ + jets, where the $E_{\mathrm{T}}^{\mathrm{miss}}$ mismeasurement is mostly due to jet energy mismeasurement. For the $Z$ + jets to mimic the signal sought, one jet must be misreconstructed as a photon; this source

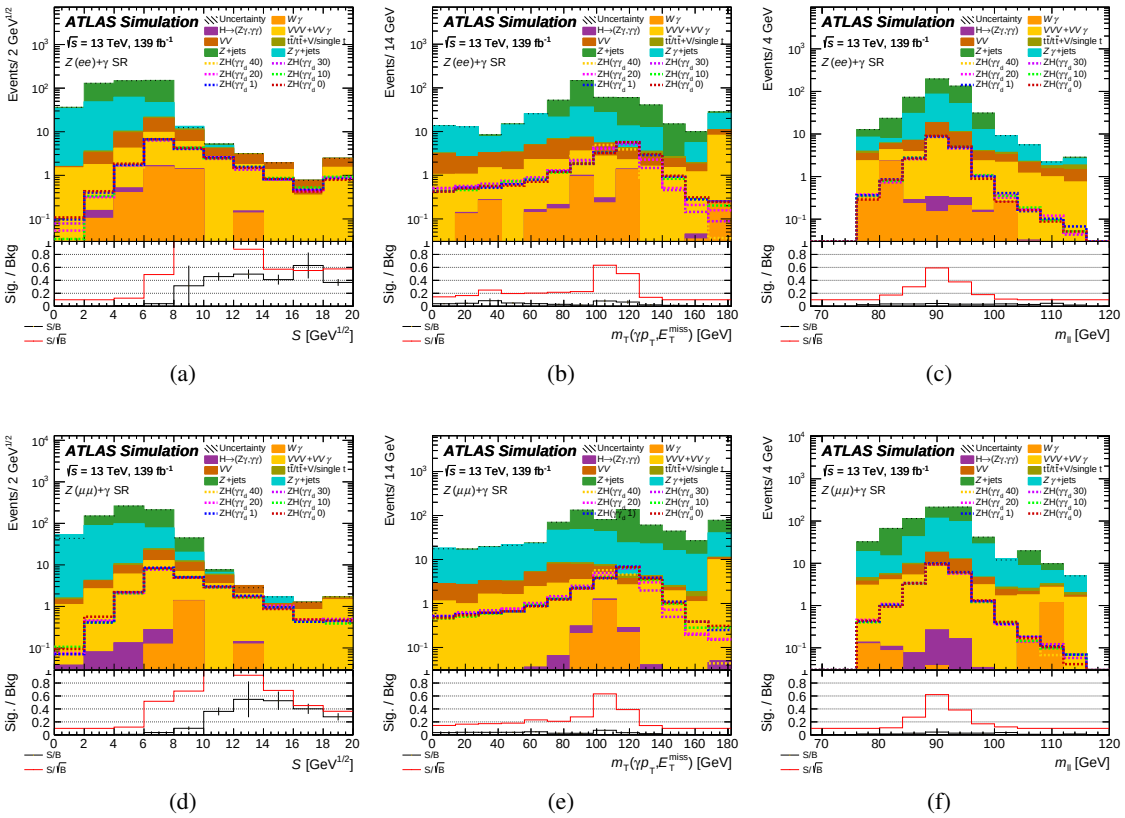


FIGURE 9.3: Signal and MC backgrounds distributions of the most important input variables $S$ $(a,d)$, $m_T$ $(b,e)$ and $m_{\ell\ell}$ $(c,f)$ used in the BDT training and testing for the $(ee,\ \mu\mu)$ SR respectively. The $S/B$ (black) and $S/\sqrt{B}$ (red) ratios are also shown where the signal is considered for $m\gamma_d = 0$ GeV and assuming BR$(H \to \gamma\gamma_d) = 5\%$.

of background is therefore included in the fake $E_{\mathrm{T}}^{\mathrm{miss}}$ estimation. Minor contributions to this category come from $Z\gamma\gamma$ and $ZH(\to \gamma\gamma)$ with an undetected photon, and from $gg \to H$ and VBF Higgs production with subsequent $H \to Z\gamma$ decay. The $ZZ$ and $VVV$ final states are not included in this category, as they are already accounted for in the $e \rightsquigarrow \gamma$ case.

- **Background from top quark production**: the main final states are $tW\gamma$, $t\bar{t}\gamma$, $t\bar{t}$ and single top-quark production — in the last two cases, the identified photon comes from $j \rightsquigarrow \gamma$. The $\ell^+\ell^- Vt$ and $VVt\bar{t}$ events are not included in this category, as they already enter the $e \rightsquigarrow \gamma$ category.

- **Background from** $W\gamma$: enters the SR due to a jet faking a lepton.

- **Other background from Higgs:** $t\bar{t}H(\to Z\gamma)$ **and** $VH(\to Z\gamma)$: this category can be divided into $t\bar{t}H(\to Z\gamma)$, $ZH(\to Z\gamma)$ and $W(\to \ell\nu)H(\to Z\gamma)$. Their experimental effects differ: the first one fails the $b$-veto; the second is irreducible if one of the two $Z$s decays to $\nu\bar{\nu}$ and the other to $\ell^+\ell^-$; the third has genuine $E_{\mathrm{T}}^{\mathrm{miss}}$ and an undetected lepton. However, their contributions are so tiny (by 3 or 4 orders of magnitude) with respect to any other concurrent process that it is more convenient to treat them all in a dedicated category. Note that this category does not include all processes involving the Higgs boson, as some are already accounted for in previously described categories.

The background contributions coming from the fake $E_{\mathrm{T}}^{\mathrm{miss}}$ category (which is dominant) and from the $e \rightsquigarrow \gamma$ category are estimated with data-driven techniques. The other categories are estimated from MC simulation. The normalization for the top-quark background is checked in a dedicated validation region (VR), while the normalization of $VV\gamma$ irreducible background is adjusted in a dedicated control region (CR), as described in Section 9.4.3.

### 9.4.1 Evaluation of the background from electrons faking photons

This background occurs because electrons and photons produce similar shower shapes in the EM calorimeter, and photons may convert early in the tracker into an asymmetric $e^+e^-$ pair where one track may not be reconstructed; to keep the photon detection efficient, such cases must be considered, at the price of having a background from electrons wrongly identified as photons.

As this background cannot be perfectly modelled in simulation, a two-step data-driven approach has been performed. First, the "electron-to-photon fake rate", $f_{e\rightsquigarrow\gamma}$ is estimated. This rate is then applied to a "probe-electron" CR, whose events are selected with the same criteria as for the SR, but requiring an extra electron instead of the photon — called "probe electron", $e_p$, in the following.

To estimate $f_{e\rightsquigarrow\gamma}$, two sets of data events are selected, respectively with $e^+e^-$ and $e^\pm\gamma$ final states, with no additional leptons or photons. The distributions of the invariant masses, $m_{ee}$ and $m_{e\gamma}$, for the two final states, both exhibit a peak around the $Z$ mass, on top of a continuous background. The $Z$ contribution is extracted using a functional fit, where the peak is modelled as a double-sided Crystal Ball function, while the continuum is described by an exponential of a polynomial function. The quantity $f_{e\rightsquigarrow\gamma}$is computed from the results of this fit as the ratio of the number of events from $Z \rightarrow e^+e^-$ and from $Z \rightsquigarrow e^\pm\gamma$ where the second category counts the $e^\pm\gamma$ misidentification.

The estimate is done in several bins of photon $p_{\mathrm{T}}$ and $\eta$, as $f_{e\rightsquigarrow\gamma}$ exhibits a strong dependence on these two variables. The values of $f_{e\rightsquigarrow\gamma}$ increase both as a function of $\eta$ and $p_{\mathrm{T}}$, ranging from 1.3–3% in the barrel, to about 7% at high $p_{\mathrm{T}}$ in the endcap as shown in Figure 9.4. The overall uncertainty on each value is evaluated by combining in quadrature the statistical uncertainties of the data samples, a systematic uncertainty quantifying the deviation between the actual and fitted peak, and an additional systematic uncertainty from a non-closure of the whole procedure carried out on MC simulation. The overall relative uncertainty on $f_{e\rightsquigarrow\gamma}$ ranges from 7% to 11%.

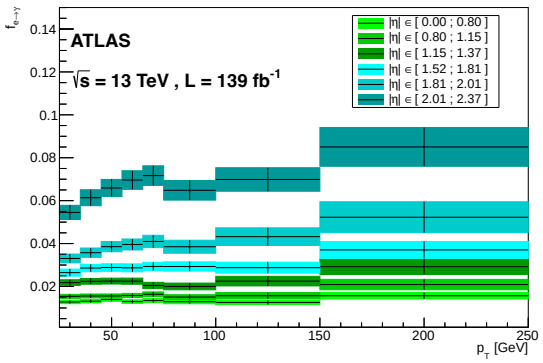


FIGURE 9.4: Values of $f_{e\rightsquigarrow\gamma}$ as a function of $p_{\mathrm{T}}$, for different regions of $\eta$.

The probe-electron CR ($e_p$-CR) is populated with $\ell^+\ell^- e_p + E_{\mathrm{T}}^{\mathrm{miss}}$ events, where the probe electron must satisfy the same kinematic requirements as the photon: in particular $p_{\mathrm{T}}^{e_p} > 25$ GeV, $|\eta^{e_p}| < 1.37$ or $|\eta^{e_p}| \in [1.52, 2.37]$, $m_{\ell\ell e_p} > 100$ GeV, and $\Delta\phi(\vec{E}_{\mathrm{T}}^{\mathrm{miss}}; \vec{p}_{\mathrm{T}}^{\,\ell\ell e_p}) > 2.4$ rad. The rest of the event satisfies the same requirements as for the SR. Each event in the $e_p$-CR is then scaled by the respective $f_{e\rightsquigarrow\gamma}$, computed as a function of $\eta^{e_p}$ and $p_{\mathrm{T}}^{e_p}$; the number of the scaled events gives the estimate of the

$e \rightsquigarrow \gamma$ background in the SR. Since this procedure is done per event, it also allows for the estimation of the distributions of all kinematic variables for this background.

For the $\mu^+\mu^-$ channel and the $e^+e^-$ channel, the final states of the $e_p$-CRs are respectively $\mu^+\mu^- e_p + E_{\mathrm{T}}^{\mathrm{miss}}$ and $e^+e^- e_p + E_{\mathrm{T}}^{\mathrm{miss}}$; in the latter case, there is an ambiguity about which of the three electrons to be considered as the $e_p$. In principle, any of the three could be misidentified as a photon; however, the opposite-charge requirement on the remaining $e^+e^-$ pair always rules out one of the 3 possibilities.

In the $e_p$-CR, there is a contamination of jets faking electrons, occurring at a rate $f_{j\rightsquigarrow e}$, which is estimated from the simulation at the level of 6%–7%. This is accounted for by rescaling all events in the $e_p$-CR by a quantity $1 - f_{j\rightsquigarrow e}$; a systematic uncertainty equal to $f_{j\rightsquigarrow e}$ is assigned to this correction.

The data-driven estimates of the background from $e \rightsquigarrow \gamma$ in the $e^+e^-$ channel and $\mu^+\mu^-$ channel are, respectively, $21.0 \pm 2.4$ and $20.4 \pm 2.1$ events. The errors are evaluated by combining in quadrature the statistical uncertainty of the $e_p$-CR, the uncertainty on $f_{e\rightsquigarrow\gamma}$ and $f_{j\rightsquigarrow e}$.

### 9.4.2 Evaluation of the background from fake $E_{\mathrm{T}}^{\mathrm{miss}}$

The data-driven estimate of the background from fake $E_{\mathrm{T}}^{\mathrm{miss}}$ is achieved by means of an "ABCD method"; besides the SR (here labelled region $A$), three CRs ($B$, $C$, $D$) are defined by inverting the selection cuts on the $E_{\mathrm{T}}^{\mathrm{miss}}$ and $\Delta\phi(\vec{E}_{\mathrm{T}}^{\mathrm{miss}}; \vec{p}_{\mathrm{T}}^{\,\ell\ell\gamma})$ variables:

- **region** $A$: $E_{\mathrm{T}}^{\mathrm{miss}} > 60$ GeV and $\Delta\phi(\vec{E}_{\mathrm{T}}^{\mathrm{miss}}; \vec{p}_{\mathrm{T}}^{\,\ell\ell\gamma}) > 2.4$ rad;
- **region** $B$: $E_{\mathrm{T}}^{\mathrm{miss}} \in [30, 40]$ GeV and $\Delta\phi(\vec{E}_{\mathrm{T}}^{\mathrm{miss}}; \vec{p}_{\mathrm{T}}^{\,\ell\ell\gamma}) > 2.4$ rad;
- **region** $C$: $E_{\mathrm{T}}^{\mathrm{miss}} > 60$ GeV and $\Delta\phi(\vec{E}_{\mathrm{T}}^{\mathrm{miss}}; \vec{p}_{\mathrm{T}}^{\,\ell\ell\gamma}) < 2.4$ rad;
- **region** $D$: $E_{\mathrm{T}}^{\mathrm{miss}} \in [30, 40]$ GeV and $\Delta\phi(\vec{E}_{\mathrm{T}}^{\mathrm{miss}}; \vec{p}_{\mathrm{T}}^{\,\ell\ell\gamma}) < 2.4$ rad.

Two more validation regions (VR) are introduced:

- **region** $A'$: $E_{\mathrm{T}}^{\mathrm{miss}} \in [40, 60]$ GeV and $\Delta\phi(\vec{E}_{\mathrm{T}}^{\mathrm{miss}}; \vec{p}_{\mathrm{T}}^{\,\ell\ell\gamma}) > 2.4$ rad;
- **region** $C'$: $E_{\mathrm{T}}^{\mathrm{miss}} \in [40, 60]$ GeV and $\Delta\phi(\vec{E}_{\mathrm{T}}^{\mathrm{miss}}; \vec{p}_{\mathrm{T}}^{\,\ell\ell\gamma}) < 2.4$ rad.

as illustrated in Figure 9.5.

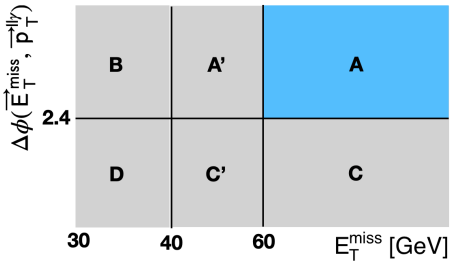


FIGURE 9.5: Regions involved in the "ABCD" method for estimation of the background from fake $E_{\mathrm{T}}^{\mathrm{miss}}$; region $A$ is the signal region.

The regions $B$, $C$, $D$ are built such to be enriched in events with fake $E_{\mathrm{T}}^{\mathrm{miss}}$. The residual contribution of events with genuine $E_{\mathrm{T}}^{\mathrm{miss}}$ is subtracted; a large portion of them come from the $e \rightsquigarrow \gamma$ background and therefore can be evaluated and subtracted by applying the data-driven procedure described in Section 9.4.1 to the specific regions. The other processes ($VV\gamma$, top, $W\gamma$, and $t\bar{t}H + VH$)

are estimated from simulation and subtracted. Then, the fake $E_{\mathrm{T}}^{\mathrm{miss}}$ background in region $A$ can be computed as:

$$N_A^{\text{fake } E_{\mathrm{T}}^{\mathrm{miss}}} = R \cdot \frac{N_B^{\text{fake } E_{\mathrm{T}}^{\mathrm{miss}}} \cdot N_C^{\text{fake } E_{\mathrm{T}}^{\mathrm{miss}}}}{N_D^{\text{fake } E_{\mathrm{T}}^{\mathrm{miss}}}} \tag{9.3}$$

where $R$ is a parameter that accounts for the correlation between the variables $E_{\mathrm{T}}^{\mathrm{miss}}$ and $\Delta\phi(\vec{E}_{\mathrm{T}}^{\mathrm{miss}}; \vec{p}_{\mathrm{T}}^{\ell\ell\gamma})$ in the fake $E_{\mathrm{T}}^{\mathrm{miss}}$ processes — if the two variables were independent, $R = 1$. The variables were chosen to have $R$ close to 1 and to be stable when varying the requirements on each of the variables used.

The value of $R$ is estimated from MC simulation; the dominant processes to the fake $E_{\mathrm{T}}^{\mathrm{miss}}$ background are $Z\gamma$ + jets and $Z$ + jets. In these processes, only a few events enter the $A$, $C$ regions, causing the statistical uncertainty on $R$ to be large; to overcome this, regions $(A + A')$ and $(C + C')$ are used instead, exploiting the stability of $R$ with respect to the value of the $E_{\mathrm{T}}^{\mathrm{miss}}$ cut. Moreover, the compatibility of the $R$-value obtained with this approach with that from $A$, $C$ regions has been checked. The extracted value for:

$$R_{\mathrm{MC}} = \frac{N_{A+A'}^{Z(\gamma)+\text{jets}} \cdot N_D^{Z(\gamma)+\text{jets}}}{N_B^{Z(\gamma)+\text{jets}} \cdot N_{C+C'}^{Z(\gamma)+\text{jets}}} \tag{9.4}$$

is displayed in Table 9.7, for the $ee$ and $\mu\mu$ channels; the quoted uncertainties are due to the statistical uncertainties on the MC simulation. The relative contribution of $Z\gamma$ + jets and $Z$ + jets processes, and the $j \rightsquigarrow \gamma$ fake rate occurring in the second case, are known not to be precisely modelled by MC simulation; for this reason, the contribution of the $Z$ + jets process has been changed by $\pm 50\%$ of the MC prediction, to check its impact on $R_{\mathrm{MC}}$. The result is also shown in Table 9.7; the small variations are well covered by the statistical uncertainties, therefore there is no evidence that the amount of $Z$ + jets has an impact on $R_{\mathrm{MC}}$.

A further check on the reliability of $R_{\mathrm{MC}}$ has been carried out exploiting the two VRs $A'$, $C'$, where a similar factor:

$$R' = \frac{N_{A'}^{\text{fake } E_{\mathrm{T}}^{\mathrm{miss}}} \cdot N_D^{\text{fake } E_{\mathrm{T}}^{\mathrm{miss}}}}{N_B^{\text{fake } E_{\mathrm{T}}^{\mathrm{miss}}} \cdot N_{C'}^{\text{fake } E_{\mathrm{T}}^{\mathrm{miss}}}} \tag{9.5}$$

is introduced, and computed from MC simulation and data. $R'_{\mathrm{MC}}$ is computed using $Z\gamma$ + jets and $Z$ + jets processes, while $R'_{\mathrm{data}}$ uses event counts after the subtraction of $e \rightsquigarrow \gamma$, $VV\gamma$, top, $W\gamma$ and $VH$ background processes. The results are shown in Table 9.7; the comparison of $R'_{\mathrm{MC}}$ and $R'_{\mathrm{data}}$ shows no significant discrepancy. In a conclusion, the evaluation of $R_{\mathrm{MC}}$ is considered reliable and is used in Equation (9.3).

TABLE 9.7: Values of $R$ for the $ee$ and $\mu\mu$ channels. $R_{\mathrm{MC}}$ is computed from simulation, assuming a relative amount of $Z$ + jets with respect to $Z\gamma$ + jets processes as predicted by the simulation (nominal) or changed by factors 0.5 or 1.5. $R'$ is computed using regions $A', C'$ instead of $(A + A')$ and $(C + C')$, to allow a comparison between simulation and data in a sample enriched by fake $E_{\mathrm{T}}^{\mathrm{miss}}$. Statistical uncertainties on the simulated samples are reported.

| channel | $R_{\mathrm{MC}}$ | | | $R'$ | |
|---|---|---|---|---|---|
| | nominal | $0.5 \times (Z + \text{jets})$ | $1.5 \times (Z + \text{jets})$ | $R'_{\mathrm{MC}}$ | $R'_{\mathrm{data}}$ |
| $ee$ | $1.12 \pm 0.11$ | $1.15 \pm 0.13$ | $1.06 \pm 0.08$ | $1.09 \pm 0.11$ | $1.16 \pm 0.06$ |
| $\mu\mu$ | $1.24 \pm 0.11$ | $1.25 \pm 0.14$ | $1.23 \pm 0.09$ | $1.15 \pm 0.11$ | $1.18 \pm 0.05$ |

The data-driven estimates of the fake $E_{\mathrm{T}}^{\mathrm{miss}}$ background in the $ee$ and $\mu\mu$ channels are, respectively, $413 \pm 50$ and $581 \pm 64$ events. The errors are evaluated from the propagation of the statistical uncertainties of $R_{\mathrm{MC}}$ and of data in the ABCD regions.

### 9.4.3 Treatment of the irreducible background and the top-quark background

The irreducible $VV\gamma$ background plays an important role at high values of the BDT score, which drives the sensitivity of the search; for this reason, a dedicated "$VV\gamma$-CR" is introduced, to correct the normalisation of this background (see Section 9.6). Recalling that such a background is a pure electroweak process, to which $Z(\to \ell^+\ell^-)Z(\to \nu\bar{\nu})\gamma$ and $W^+(\to \ell^+\nu)W^-(\to \ell^-\bar{\nu})\gamma$ contribute, the "$VV\gamma$-CR" has been built to be enriched in $Z(\to \mu^+\mu^-)W(\to \mu\nu)\gamma$, thus requiring exactly three muons, one photon and no electrons. The opposite-charge $\mu^+\mu^-$-pair whose invariant mass is closest to the $Z$ mass must fulfil all $\ell^+\ell^-$ kinematic cuts of the SR; to reduce the statistical uncertainty, no requirements are applied on $E_{\mathrm{T}}^{\mathrm{miss}}$ and $\Delta\phi(\vec{E}_{\mathrm{T}}^{\mathrm{miss}}; \vec{p}_{\mathrm{T}}^{\,\ell\ell\gamma})$. The purity of $ZW\gamma$ events in such a CR is estimated to be 83% from simulation.

To check the normalization of the top-induced background predicted by simulation, a "top-VR" has been used, enriched by such processes; it is defined starting from the selection of the SR, removing the requirements on $m_{\ell\ell}$ and $\Delta\phi(\vec{E}_{\mathrm{T}}^{\mathrm{miss}}; \vec{p}_{\mathrm{T}}^{\,\ell\ell\gamma})$, and requiring at least one $b$-tagged jet. The purity of events with top-quark production is estimated to be 92% from simulation in such a VR.

### 9.4.4 Background proportion in the signal region

Following the background estimation using data-driven techniques as presented above, the background proportion in the signal region is presented in Figure 9.6, for the $\mu^+\mu^-$ (left) and $e^+e^-$ (right) channels.

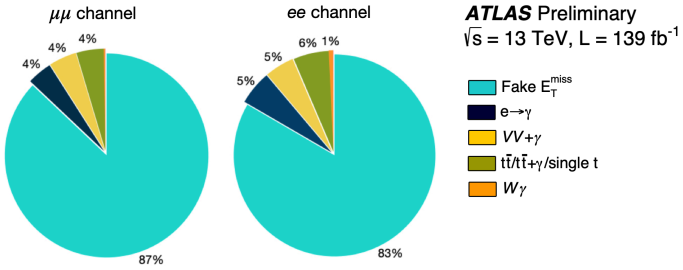


FIGURE 9.6: Expected relative proportions of different background categories in the signal region, for the $\mu^+\mu^-$ (left) and $e^+e^-$ (right) channels. Fake $E_{\mathrm{T}}^{\mathrm{miss}}$ and $e \rightsquigarrow \gamma$ yields are evaluated data-driven, as explained in the text, while other backgrounds are from MC simulation.

### 9.4.5 Background checks in validation region

As an overall check of the background estimates, the data-driven techniques described in Section 9.4.2 and Section 9.4.1 are applied in the VR $A'$ (Figure 9.5). The comparison between the expected background and data is displayed in Figures 9.7 and 9.8, showing good agreement.

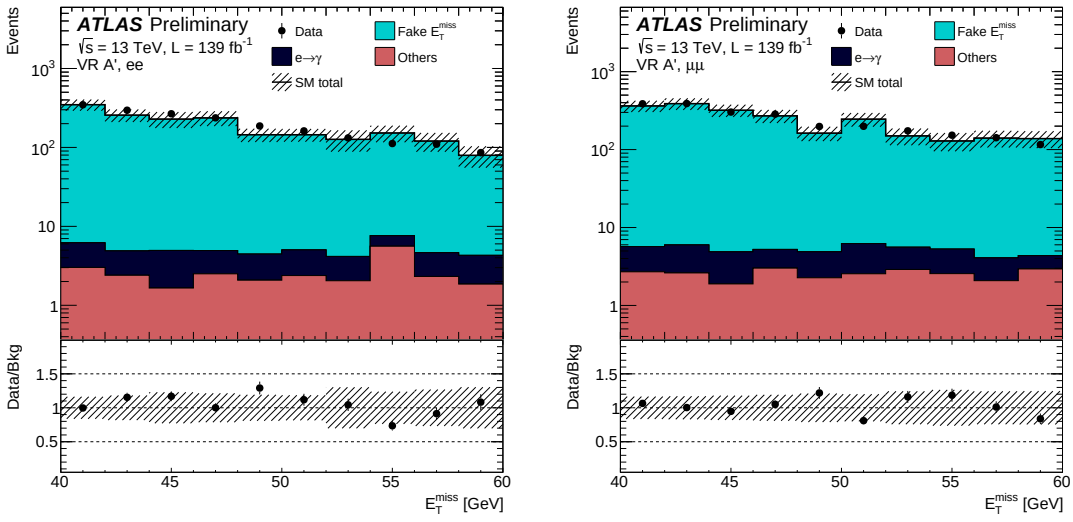


(a) (b)

FIGURE 9.7: Comparison between the expected background and data in the validation region $A'$, as a function of $E_{\mathrm{T}}^{\mathrm{miss}}$, for the $ee$ (a) and $\mu\mu$ (b) channels. The background yields from "fake $E_{\mathrm{T}}^{\mathrm{miss}}$" and "$e \rightsquigarrow \gamma$" are estimated with data-driven techniques. The other backgrounds are obtained from simulation and have been merged. Uncertainties shown are statistical, both for data and for simulated backgrounds, while for the data-driven backgrounds, the systematic uncertainties related to the method are also included.

## 9.5 Systematic uncertainties

This section presents the various sources of systematic uncertainties affecting all levels of the analysis. They are categorised according to their origin, effects and the way they have been estimated.

### 9.5.1 Experimental systematic uncertainties

The analysis is impacted by several uncertainties related to the detector resolution, inefficiencies and mis-measurements. They are grouped into the following categories: uncertainties in the luminosity, uncertainties in the trigger efficiencies and uncertainties related to the reconstruction of physics objects such as electrons, muons, jets, and $E_{\mathrm{T}}^{\mathrm{miss}}$. The estimations of these uncertainties require a particular treatment as they affect the search via potential biases to the modelling of the signal and background processes in the MC simulation. These systematic uncertainties can affect both the yield and the shape of the final observable (BDT classifier response) and are included in the statistical evaluation.

The uncertainty in the luminosity is 1.7% [217] and impacts the simulated yields of both the signal and backgrounds. This uncertainty was obtained using the LUCID-2 detector [218] for the primary luminosity measurements. In addition, systematic uncertainties resulting from the effects of pile-up modelling, due to the reweighting procedure, are also considered.

Systematic uncertainties are estimated for lepton reconstruction and isolation efficiencies [204, 205] and for the energy scale and resolution, [204]. Additional uncertainties on lepton trigger efficiencies are also considered to take into account differences between data and simulation [175, 176].

For the photons, uncertainties in the reconstruction, isolation, energy scale and resolution are considered [204, 219].

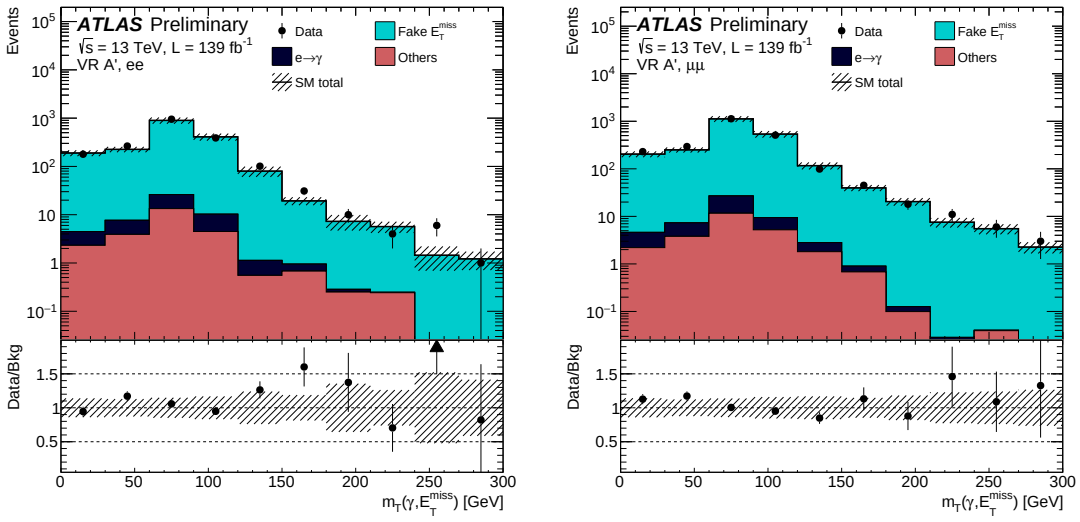


(a) (b)

FIGURE 9.8: Comparison between the expected background and data in the validation region $A'$, as a function of $m_{\mathrm{T}}$, for the $ee$ (a) and $\mu\mu$ (b) channels. The background yields from "fake $E_{\mathrm{T}}^{\mathrm{miss}}$" and "$e \rightsquigarrow \gamma$" are estimated with data-driven techniques. The other backgrounds are obtained from simulation and have been merged. Uncertainties shown are statistical, both for data and for simulated backgrounds, while for the data-driven backgrounds, the systematic uncertainties related to the method are also included.

For jets, uncertainties related to the energy and resolution [208] as well as pile-up jet tagging [220] are all taken into account. Specific systematic uncertainties are considered for heavy flavour tagging to correct for identification efficiencies of the bottom, charm and light tagged jets [221, 222].

For $E_{\mathrm{T}}^{\mathrm{miss}}$, uncertainties associated with reconstructed objects are propagated and included in its calculation. Additional uncertainties associated with the $E_{\mathrm{T}}^{\mathrm{miss}}$ soft term scale and resolution are independently evaluated [213].

An additional uncertainty on the shape of the BDT classifier response for the fake $E_{\mathrm{T}}^{\mathrm{miss}}$-induced background (Section 9.4) is considered. It is meant to account for inaccuracies in the shape of the $Z$+jets MC events characterized by high bin-to-bin fluctuations. To reduce these fluctuations a Gaussian smoothing algorithm is applied to the $Z$+jets distribution and the uncertainty is obtained from the difference between this varied shape and the one corresponding to the nominal $Z$+jets MC distribution together with the other MC simulated processes entering the fake $E_{\mathrm{T}}^{\mathrm{miss}}$ category.

Finally, the comparison between data and MC predictions in the "top-VR" shows a discrepancy at the level of 20% for top-induced background (Section 9.4.3). For this reason, in the treatment of such a background, a relative systematic uncertainty of $\pm$20% is considered.

### 9.5.2 Theoretical systematic uncertainties

Theoretical uncertainties affect all simulated signal and background processes. They originate from the limited order in $\alpha_s$ or $\alpha_{EWK}$ at which the matrix elements are calculated, the matching of those calculations to parton showers and the uncertainty of the proton PDFs. The uncertainties from the variation of the QCD scale and the variation of PDFs are considered for the signal and simulated background processes. Uncertainties for backgrounds entering different control (CR) and validation (VR) regions were also estimated.

For the $H \to \gamma\gamma_d$ signal, the total $ZH$ cross-section is calculated up to NLO precision and is provided by the LHC Higgs Cross-Section Working Group [184]. NLO electroweak corrections reduce the cross section by 5.3%.

This correction has been propagated to the BDT classifier response. The corresponding systematic uncertainties are extracted from the maximum and minimum variations of the NLO corrections and amount to 0.2-0.3%. The parton shower (PS) model effects on signal processes were estimated through a comparison between PYTHIA8 and HERWIG7 showering models. The difference between the two algorithms in each BDT classifier response bin is taken as a systematic uncertainty on the PS model and amounts to 0.4-6.0% (0.2-36%) for $qq \to ZH$ ($gg \to ZH$).

For the QCD renormalisation $\mu_R$ and factorisation $\mu_F$ scales, a seven-point scale variation is considered, which amounts to varying the renormalisation and factorisation scales independently by a factor of 1/2 and 2 around $\mu$ to the combinations of ($\mu_R$, $\mu_F$ ) = ($\mu$/2, $\mu$/2), (2$\mu$, 2$\mu$), ($\mu$, 2$\mu$), (2$\mu$, $\mu$), ($\mu$, $\mu$/2) and ($\mu$/2,$\mu$). The effect of these variations was propagated to the BDT classifier distributions. An envelope covering differences with respect to the nominal values is taken as the systematic uncertainty.

Depending on the $\gamma_d$ mass and the BDT bin, the uncertainties from PS vary from [-4,+5]% ($qqZH$) to [-19,+25]% ($ggZH$). Finally, uncertainties related to the choice of the PDF are computed by considering the yield predictions with a full ensemble of 100 PDFs within the NNPDF set. The standard deviation of this set of yields is taken as the corresponding PDF uncertainty. The uncertainties related to the $\alpha_s$ variations are computed by considering the difference in the yield from two $\alpha_s$ variations (0.1195 and 0.1165). The $\alpha_s$ and PDF uncertainties are quadratically added and their impact varies from $\pm$0.4% to $\pm$1.1%.

Similar approaches have also been applied to estimate theoretical uncertainties for background processes that were evaluated using MC predictions. Up and down variations with respect to nominal values for QCD ($\mu_R, \mu_F$) scales, PDF+$\alpha_s$ and PS algorithms were considered as systematic uncertainties for $VH, t\bar{t}H(H \to Z\gamma), t\bar{t}, t\bar{t}V, Wt\gamma$, single top-quark, $W\gamma^{QCD,EWK}$ and $VV\gamma$. Uncertainties from PDF+$\alpha_s$ amount to a maximum up to $\pm$10% ($W\gamma$, single top-quark), QCD scale up to $\pm$30% ($t\bar{t}V$) and PS up to $\pm$40% ($W\gamma, t\bar{t}$). Finally, theoretical uncertainties associated with $Z\gamma$ and $Z$+jets were also evaluated as contributions from these processes need to be known in data-driven background estimation.

## 9.6 Results and Interpretation

To estimate the compatibility of the data with the SM expectations, as well as to extract upper limits at 95% confidence level (CL) on the branching ratio of $H \to \gamma\gamma_d$ a binned maximum likelihood fit is performed in the SR to the distribution of the BDT classifier response merging the $ee$ and $\mu\mu$ channels to obtain the best sensitivity.

The chosen binning in the SR is optimised to obtain the best-expected sensitivity to the signal model, while also keeping low statistical uncertainties in each bin.

The likelihood function is built as a product of Poisson probability functions based on the expected signal and background yields in each BDT bin of the SR and the single-bin $VV\gamma$ CR. Two

free parameters are included in the simultaneous likelihood fit: the branching ratio BR($H \to \gamma\gamma_d$), which consists in the parameter of interest (POI) and multiplies the signal yield and the floating normalization factor for the $VV\gamma$ irreducible background $k_{VV\gamma}$, which is constrained by the $VV\gamma$ CR. The systematic uncertainties are included as nuisance parameters, which are constrained by Gaussian distributions centred at zero with a width equal to the corresponding uncertainty:

$$\mathcal{L}(data|\mu_{sig},\boldsymbol{\theta}) = \prod_{i\in\{\text{BDT bins}\}} \text{Pois}(N_i^{data}|N_i(\mu_{sig},\boldsymbol{\theta})) \times \prod_{j\in\{\text{syst}\}} G(\theta_j|0,1) \tag{9.6}$$

where:

- $N_i(\mu_{sig},\boldsymbol{\theta}) \propto \mu_{sig} N_i^{sig}(\boldsymbol{\theta}) + \sum_{bkg} N_i^{bkg}(\boldsymbol{\theta})$
- $G(x|0,1)$ is a Gaussian with mean $\mu = 0$ and $\sigma = 1$
- $N_i^{sig/bkg}(\theta_j) = n_i^{sig/bkg} \times (1 + \theta_j\Delta_j)$, with $\Delta_j$ the value of the $j^{th}$ systematic uncertainty and $n_i^{sig/bkg}$ the central values from MC of from data-driven estimates.

The dominant backgrounds, fake $E_{\text{T}}^{\text{miss}}$ and electron faking photons are included in the fit taking the normalization from data-driven estimates described in Section 9.4. To model the BDT shape in the fit, simulated events are used for fake $E_{\text{T}}^{\text{miss}}$, while for the background with an electron faking a photon data from the probe-electron CR ($e_p$-CR) is considered after re-scaling each event by the appropriate fake rate $f_{e\rightsquigarrow\gamma}$. The systematic uncertainties from data-driven methods are included in the fit as correlated among different BDT bins, as well as other experimental and theoretical systematic variations.

Two different fits are performed. The first corresponds to the background-only fit, in which the background predictions are determined in a fit to data assuming the presence of no signal. The second configuration instead allows for the presence of a specific signal and it is referred to as the model-dependent fit.

The results of the background-only fit are shown in Table 9.8, where observed and expected event yields are shown for all of the background processes considered in this analysis. The normalisation $k_{VV\gamma}$ factor is found to be $1.35 \pm 0.38$. The pre-fit and post-fit distributions of the BDT classifier response are shown in Figure 9.9 for the combined $ee + \mu\mu$ channels. Post-fit uncertainties are reduced thanks to the constraints on nuisance parameters, in particular the ones related to the fake $E_{\text{T}}^{\text{miss}}$-induced background. Post-fit distributions of the BDT classifier response for the separate channels are shown in Figure 9.10. Pre-fit distribution of $m_T$ is also shown in Figure 9.11, being one of the most discriminant variables entering the BDT classifier.

The relative impact of each source of systematic uncertainty on the SM background estimates is summarised in Table 10.3. The purely statistical uncertainty of simulated samples is dominant, except in the last BDT bin, varying from about 3% to 16%. The largest systematic uncertainties in the last BDT bin are related to the shape of fake $E_{\text{T}}^{\text{miss}}$ and to the jet energy scale and resolution corresponding respectively to 18% and 13%; uncertainty due to energy scale and resolution of electrons and photons corresponds to 5.6%, while the same uncertainty for muons corresponds to 4.1%. The other experimental and theoretical systematic uncertainties have a relative impact below about 3.5% in all BDT bins.

The event yields in data are consistent with the predicted SM background event yields, as shown in Table 9.8. The model-dependent fit is therefore performed to extract upper limits at 95% CL on the branching ratio of the sought decay mode of the Higgs boson. These limits are based on the profile-likelihood-ratio test statistic [223] and $\text{CL}_\text{s}$ prescriptions [224], evaluated using the asymptotic approximation [225]. The fit is performed including the signal component of the Higgs boson production in $ZH$ with subsequent Higgs boson decays into $\gamma$ and $\gamma_d$. The results are provided for the massless dark photon, as well as for low dark photon mass values up to 40 GeV, as shown in Figure

TABLE 9.8: Observed event yields in 139 fb$^{-1}$ of data compared to expected yields from SM backgrounds obtained from the background-only fit for the $ee + \mu\mu$ channel in the SR and the $VV\gamma$ CR. The total expected yields before the fit are also shown. The expected yields for the massless $\gamma_d$ signal are shown assuming BR$(H \to \gamma\gamma_d)$ = 5%. The uncertainty includes both statistical and systematic sources. The individual uncertainties can be correlated and do not necessarily add in quadrature to equal the total background uncertainty.

| BDT bin | SR 0 - 0.50 | SR 0.50 - 0.64 | SR 0.64 - 0.77 | SR 0.77 - 0.88 | SR 0.88 - 0.96 | SR 0.96 - 1 | $VV\gamma$ CR |
|---|---|---|---|---|---|---|---|
| Observed | 910 | 84 | 59 | 72 | 42 | 6 | 32 |
| Post-fit SM background | $910 \pm 29$ | $85.5 \pm 8.7$ | $59.9 \pm 7.3$ | $69.7 \pm 7.8$ | $41.6 \pm 6.1$ | $7.3 \pm 2.0$ | $31.4 \pm 5.4$ |
| Fake $E_T^{miss}$ | $800 \pm 34$ | $72.1 \pm 8.3$ | $45.7 \pm 6.5$ | $53.2 \pm 7.1$ | $27.9 \pm 6.1$ | $2.0 \pm 1.9$ | $2.1^{+3.5}_{-2.1}$ |
| $e \rightsquigarrow \gamma$ | $21.5 \pm 2.0$ | $3.33 \pm 0.62$ | $3.75 \pm 0.74$ | $6.4 \pm 1.1$ | $5.7 \pm 1.4$ | $1.47 \pm 0.25$ | $1.24 \pm 0.07$ |
| $VV\gamma$ | $44 \pm 12$ | $5.3 \pm 1.6$ | $5.8 \pm 1.7$ | $6.4 \pm 1.8$ | $5.7 \pm 1.9$ | $3.30 \pm 0.97$ | $27.3 \pm 6.4$ |
| $t\bar{t}$, $t\bar{t}\gamma$, single $t$ | $42 \pm 15$ | $4.3 \pm 1.5$ | $3.4 \pm 1.2$ | $3.6 \pm 1.2$ | $2.13 \pm 0.80$ | $0.50 \pm 0.18$ | $0.63 \pm 0.22$ |
| $W\gamma$ | $3.3 \pm 1.5$ | $0.39 \pm 0.18$ | $1.18 \pm 0.55$ | – | $0.04 \pm 0.02$ | – | – |
| $t\bar{t}H$, $VH$ | $0.15 \pm 0.02$ | $0.03 \pm 0.01$ | $0.04 \pm 0.01$ | $0.06 \pm 0.01$ | $0.09 \pm 0.03$ | $0.02 \pm 0.01$ | $0.17^{+0.18}_{-0.17}$ |
| Pre-fit SM background | $900 \pm 120$ | $90 \pm 35$ | $65 \pm 27$ | $53 \pm 24$ | $35 \pm 22$ | $7.8 \pm 4.4$ | $24 \pm 4.7$ |
| Signal ($ZH \to \gamma\gamma_d$) | $5.1 \pm 1.3$ | $1.98 \pm 0.51$ | $3.2 \pm 1.0$ | $5.5 \pm 1.6$ | $11.1 \pm 3.1$ | $14.9 \pm 1.9$ | – |

TABLE 9.9: Summary of the relative uncertainties in the background estimate for the BDT bins after the background-only fit. The individual uncertainties can be correlated and do not necessarily add in quadrature to equal the total background uncertainty.

| BDT bin | 0 - 0.50 | 0.50 - 0.64 | 0.64 - 0.77 | 0.77- 0.88 | 0.88 - 0.96 | 0.96 - 1 |
|---|---|---|---|---|---|---|
| | [%] | [%] | [%] | [%] | [%] | [%] |
| Total (statistical+systematic) uncertainty | 3.1 | 10 | 12 | 11 | 15 | 28 |
| Statistical uncertainty | 3.1 | 9.9 | 12 | 11 | 14 | 16 |
| Fake $E_{\mathrm{T}}^{\mathrm{miss}}$ shape | 0.17 | 0.97 | 0.40 | 0.55 | 2.8 | 18 |
| Jet $E$ scale and resolution | 0.02 | 3.3 | 2.1 | 0.47 | 2.1 | 13 |
| Electron, photon $E$ scale and resolution | 0.04 | 0.45 | 0.75 | 0.46 | 1.7 | 5.6 |
| Muon $E$ scale and resolution | 0.08 | 0.17 | 0.15 | 0.91 | 1.2 | 4.1 |
| Fake $E_{\mathrm{T}}^{\mathrm{miss}}$ data-driven | 0.50 | 0.28 | 0.18 | 0.04 | 0.40 | 3.5 |
| $E_{\mathrm{T}}^{\mathrm{miss}}$ soft term scale and resolution | 0.26 | 0.16 | 0.59 | 0.49 | 0.20 | 2.8 |
| Electron trigger/ID/ iso/reco eff. | 0.01 | 0.10 | 0.10 | 0.01 | 0.17 | 1.0 |
| Muon trigger/ID/ iso/reco eff. | 0.01 | 0.07 | 0.08 | 0.06 | 0.03 | 0.84 |
| Flavour tagging eff. | $< 0.01$ | 0.08 | 0.10 | 0.04 | 0.02 | 0.82 |
| Electrons faking photons data-driven | 0.02 | 0.08 | 0.06 | 0.06 | 0.07 | 0.73 |
| Photon ID/iso/reco eff. | 0.01 | 0.07 | 0.08 | 0.04 | 0.09 | 0.61 |
| Reweighting of $\langle\mu\rangle$ in MC simulation | 0.08 | 0.10 | 0.32 | 0.46 | 0.09 | 0.48 |
| Top normalization | 0.08 | 0.06 | 0.06 | 0.02 | 0.09 | 0.13 |
| Theoretical $VV\gamma$ | 0.04 | 0.02 | 0.16 | 0.04 | 0.13 | 0.49 |
| Theoretical fake $E_{\mathrm{T}}^{\mathrm{miss}}$ | 0.05 | 0.11 | 0.12 | 0.22 | 0.29 | 0.45 |
| Theoretical top | 0.09 | 0.05 | 0.17 | 0.10 | 0.04 | 0.28 |
| Theoretical $W\gamma$ | 0.04 | 0.10 | 0.18 | 0.05 | 0.13 | 0.24 |
| Theoretical Higgs | 0.01 | 0.05 | 0.04 | 0.02 | 0.08 | 0.05 |

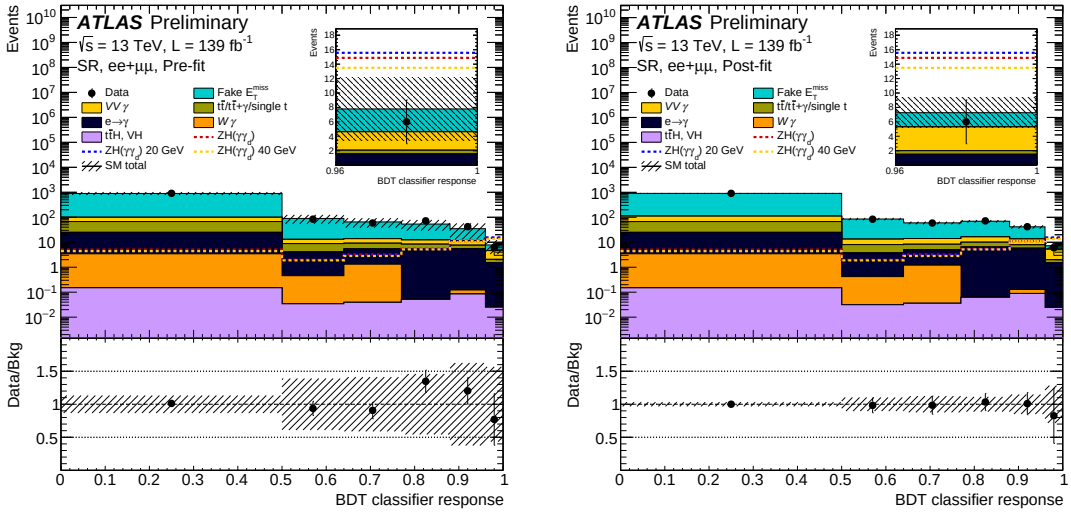


(a) (b)

FIGURE 9.9: Distribution of the BDT classifier response in data and for the expected SM background before (a) and after (b) the background-only fit. The expectations for $ZH$, $H \to \gamma\gamma_d$ are also shown for the massless dark photon (red dashed line) and for dark photon mass values of 20 GeV (blue dashed line) and 40 GeV (yellow dashed line), assuming BR$(H \to \gamma\gamma_d)$ = 5%. A zoomed view of the last BDT bin with a linear y-axis scale is also shown. Uncertainties shown are statistical for data, while backgrounds include statistical and systematic sources determined by the multiple-bin fit. The lower panel shows the ratio of data to expected background event yields.

9.12. The corresponding values are also reported in Table 9.10. The observed (expected) upper limits on BR(H$\to \gamma\gamma_d$) are at the level of 2.3% (2.8%), for massless $\gamma_d$ and vary slightly until mass values of 20 GeV. The mass dependence of the limits becomes stronger beyond that value and the observed (expected) upper limit increases to about 2.5% (3.1%) at 40 GeV.

TABLE 9.10: Observed and expected limits at 95% CL on BR$(H \to \gamma\gamma_d)$ for different values of the $\gamma_d$ mass for the $ee + \mu\mu$ channel. The asymmetric error corresponds to the $\pm 1\sigma$

| $m_{\gamma_d}$ | BR$(H \to \gamma\gamma_d)^{95\%\,\mathrm{CL}}_{\mathrm{obs}}$ | BR$(H \to \gamma\gamma_d)^{95\%\,\mathrm{CL}}_{\mathrm{exp}}$ |
|---|---|---|
| [GeV] | [%] | [%] |
| 0 | 2.28 | $2.82^{+1.33}_{-0.84}$ |
| 1 | 2.19 | $2.71^{+1.28}_{-0.81}$ |
| 10 | 2.21 | $2.73^{+1.31}_{-0.82}$ |
| 20 | 2.17 | $2.69^{+1.29}_{-0.81}$ |
| 30 | 2.32 | $2.87^{+1.36}_{-0.86}$ |
| 40 | 2.52 | $3.11^{+1.48}_{-0.93}$ |

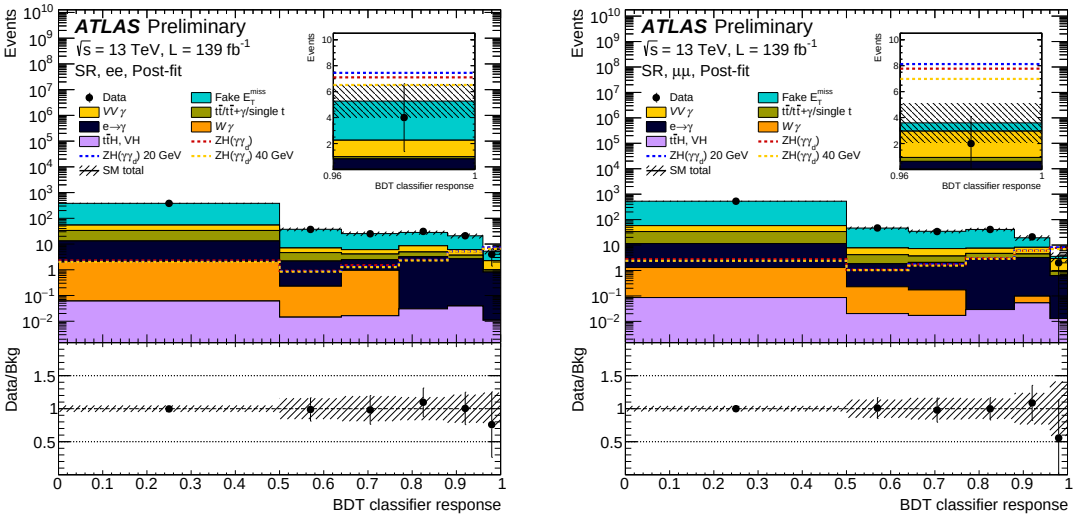


FIGURE 9.10: Distribution of the BDT classifier response in data and for the expected SM background after the background-only fit in the $ee$-SR (left) and $\mu\mu$-SR (right). The expectations for $ZH$, $H \to \gamma\gamma_d$ are also shown for the massless dark photon and for dark photon mass values of 20 and 40 GeV, assuming BR$(H \to \gamma\gamma_d)$=5%. A zoomed view of the last BDT bin with a linear y-axis scale is also shown. The error bars are statistical, and the dashed band includes statistical and systematic uncertainties determined by the multiple-bin fit. The lower panel shows the ratio of data to expected background event yields.

## 9.7 Summary

A search for dark photon candidates arising from semi-visible Standard Model Higgs boson decay $H \to \gamma\gamma_d$ is performed. The Higgs boson production in association with a $Z(\to \ell^+\ell^-)$ boson is exploited, which benefits from a relatively clean signal and high-efficiency lepton triggers. The search uses $pp$ collision data collected by the ATLAS experiment at a centre-of-mass energy of $\sqrt{s} = 13$ TeV between 2015 and 2018 and corresponding to an integrated luminosity of 139 fb$^{-1}$. A rectangular cut optimisation method is used to optimize the signal region where data events are shown in the event display shown in Figure 9.13. Moreover, Data-driven techniques are optimized to estimate the main backgrounds from processes characterized by fake $E_{\mathrm{T}}^{\mathrm{miss}}$ and electrons misidentified as photons, while the normalization of the irreducible background is obtained using MC simulations constrained by data in a dedicated control region.

The sensitivity of the search is enhanced thanks to a Boosted Decision Tree algorithm that permits the construction of the discriminant kinematic observable. No excess of events above the SM expectation is found. Therefore, limits on the branching ratio of a SM Higgs boson decaying to a photon and a dark photon can be set. For massless $\gamma_d$, an observed (expected) upper limit on BR$(H \to \gamma\gamma_d)$ of 2.28% ($2.82^{+1.33}_{-0.84}$%) is set at 95% CL. For massive $\gamma_d$, the observed (expected) upper limits are found to be within the [2.19,2.52]% ([2.71,3.11]%) range for masses spanning from 1 GeV to 40 GeV.

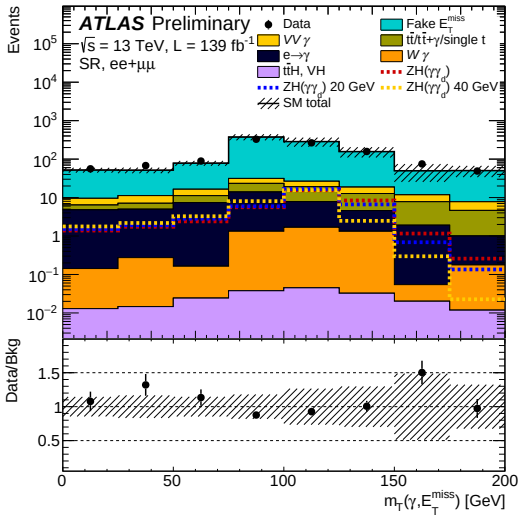


FIGURE 9.11: Distribution of $m_{\mathrm{T}}$ in data and for the expected SM background before the background-only fit. The expectations for $ZH$, $H \to \gamma\gamma_d$ are also shown for the massless dark photon (red dashed line) and for dark photon mass values of 20 GeV (blue dashed line) and 40 GeV (yellow dashed line), assuming $\mathrm{BR}(H \to \gamma\gamma_d) = 5\%$. Uncertainties shown are statistical for data, while backgrounds include statistical and systematic sources determined by the multiple-bin fit. The lower panel shows the ratio of data to expected background event yields.

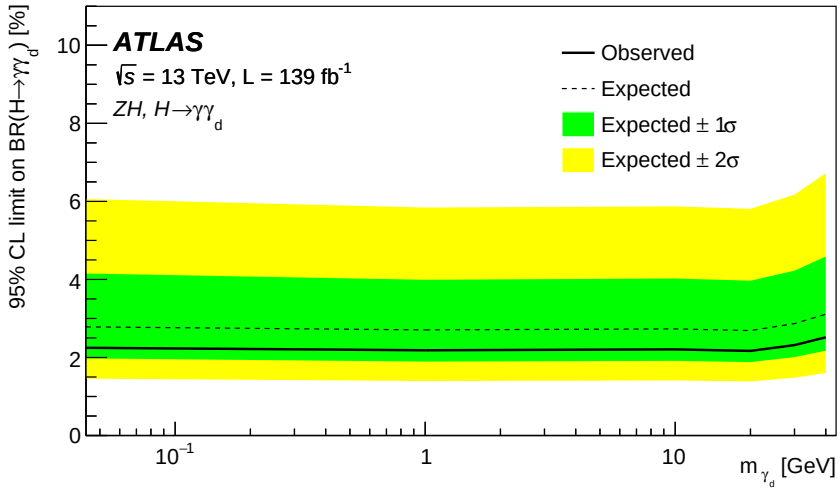


FIGURE 9.12: Observed and expected exclusion limits at 95% CL on $\mathrm{BR}(H \to \gamma\gamma_d)$ as function of the $\gamma_d$ mass. The green and yellow bands show respectively the $\pm 1\sigma$ and $\pm 2\sigma$ uncertainties.

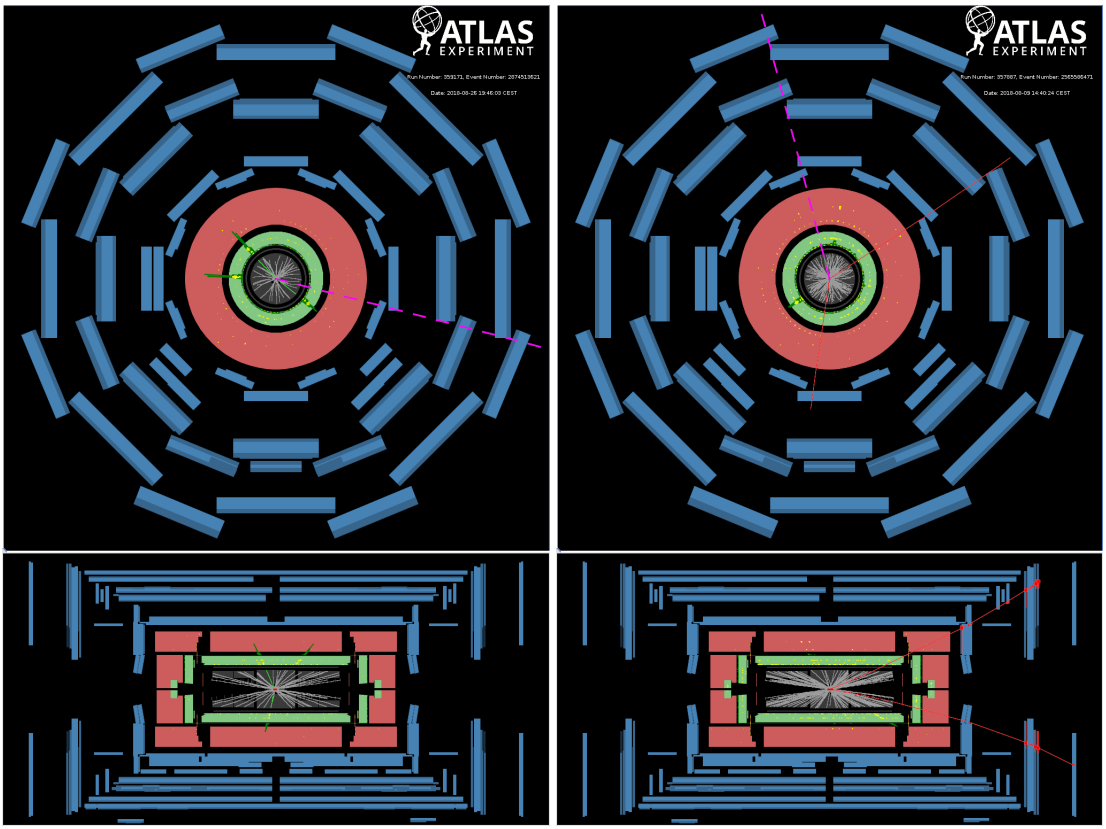


FIGURE 9.13: Display of a candidate event in the search for dark photons in $H \to \gamma\gamma_d$ produced through the $ZH$ production mode with $Z \to ee$ (left) and $Z \to \mu\mu$ (right) from proton-proton collisions at 13 TeV centre-of-mass energy at the LHC. Starting from the centre of the ATLAS detector, the hits and reconstructed tracks of the charged particles in the Inner Detector (ID) are shown as grey-coloured dots and lines, respectively. The energy deposits in the electromagnetic (the green layer) and hadronic (the red layer) calorimeters are shown as yellow boxes. The associated green histograms show the amount of energy in the EM calorimeter. Identified electrons are shown with their reconstructed track (green line) and their energy in the EM calorimeter. Identified muons are shown with their reconstructed track (red line) from the ID track and the muon spectrometer (outer blue layer) hits (in red dots). The $p_{\mathrm{T}}$ values of the leading and subleading electrons (green) and muons (red lines) are 57 (91) GeV and 34 (23) GeV, respectively. The $p_{\mathrm{T}}$ of the identified photon (yellow cluster and green histogram without an associated track) is 62 (37) GeV. The value of $E_{\mathrm{T}}^{\mathrm{miss}}$ (purple dashed line) from a potential non-interacting $\gamma_d$ is 63, (91) GeV for $ee(\mu\mu)$ channels. The invariant mass of the $ee(\mu\mu)$ pair is 92 (91) GeV while the transverse mass of the $\gamma - E_{\mathrm{T}}^{\mathrm{miss}}$ system is (123 GeV, 105 GeV) for ($Z \to ee$, $Z \to \mu\mu$). The figure at the top shows the transverse plane, while the one at the bottom shows the side projection.

# 10 Dark photon from BSM Higgs boson decay in $ggF$ and $VBF$ production modes

This search is based on the reinterpretation of the ATLAS mono-photon results [18] using the RECAST strategy (Request Efficiency Computation for Alternative Signal Theories) [226], a framework designed to preserve the same topology of the original mono-photon analysis, reusing the same phase-space and background estimates as well as systematic uncertainties, in the context of searching for dark matter production from heavy Higgs bosons decay to a photon and a massless dark photon. The introduced signal model includes both the gluon-gluon Fusion ($ggF$) and the $VBF$ production modes of the heavy Higgs bosons as presented in the Feynman diagrams shown in Figure 10.1. To improve the sensitivity of this search, different signal regions (SR) are considered based on the missing transverse momentum $E_{\mathrm{T}}^{\mathrm{miss}}$ selections ranging from 200 GeV to 375 GeV, being the primary observable of this search. The results of this reinterpretation are presented in terms of 95% CL exclusion limits on the $\sigma \times BR(H \rightarrow \gamma\gamma_d)$, considering separate $ggF$ and $VBF$ production modes as well as the combined $ggF + VBF$ production for different heavy Higgs boson masses: 400, 600, 800, 1000, 1500, 2000, 2500 and 3000 GeV.

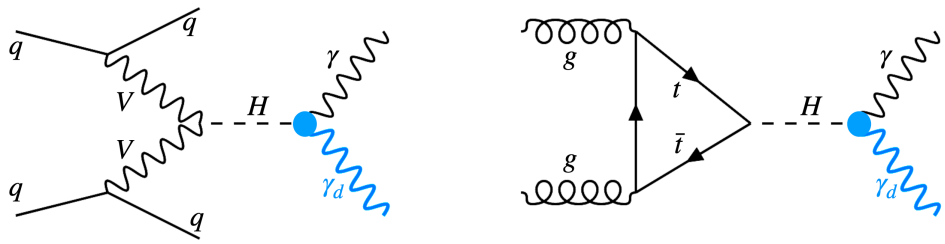


FIGURE 10.1: Feynman diagrams for H$\rightarrow \gamma\gamma_d$ in $ggF$ (right) and $VBF$ (left) production modes.

## 10.1 The $\gamma + E_{\mathrm{T}}^{\mathrm{miss}}$ search

An overview of the $\gamma + E_{\mathrm{T}}^{\mathrm{miss}}$ search [227] based on the full Run-2 dataset collected with the ATLAS experiment is presented in this section. The aim is to look for an excess of events with a $\gamma + E_{\mathrm{T}}^{\mathrm{miss}}$ final state over the SM prediction, which offers a clean signature to search for new physics processes that include extremely weekly- or non-interacting particles, leading to $E_{\mathrm{T}}^{\mathrm{miss}}$ in the final states.

### 10.1.1 Event selection

All the events in the analysis must satisfy beam, detector and data-quality criteria. They are selected by a trigger requiring at least one photon candidate with transverse energy $E_{\mathrm{T}}^{\gamma}$ above a threshold of 140 GeV and passing 'loose' identification requirements. Events are required to satisfy the selection reported in Table 10.1, more details concerning these criteria can be found in [227]. To improve the sensitivity of the analysis, seven SRs are defined corresponding to different $E_{\mathrm{T}}^{\mathrm{miss}}$ ranges: four inclusive (SRI1–SRI4) and three exclusive (SRE1–SRE3).

TABLE 10.1: Selection criteria for the SRs.

| | | | | | | | |
|---|---|---|---|---|---|---|---|
| Event cleaning | Detector quality conditions and primary vertex | | | | | | |
| Leading $\gamma$ | $E_{\mathrm{T}}^{\gamma} > 150$ GeV, $\lvert\eta\rvert < 1.37$ or $1.52 < \lvert\eta\rvert < 2.37$, tight, isolated, $\lvert\Delta z_{\gamma}\rvert < 250$ mm, $\Delta\phi(\gamma, \boldsymbol{E}_{\mathrm{T}}^{\mathrm{miss}}) > 0.4$ | | | | | | |
| $E_{\mathrm{T}}^{\mathrm{miss}}$ significance | $> 8.5$ | | | | | | |
| Jets | 0 or 1 with $p_{\mathrm{T}} > 30$ GeV, $\lvert\eta\rvert < 4.5$ and $\Delta\phi(\text{jet}, \boldsymbol{E}_{\mathrm{T}}^{\mathrm{miss}}) > 0.4$ | | | | | | |
| Leptons | veto on $e$, $\mu$ and $\tau$ | | | | | | |
| | SRI1 | SRI2 | SRI3 | SRI4 | SRE1 | SRE2 | SRE3 |
| $E_{\mathrm{T}}^{\mathrm{miss}}$ [GeV] | $> 200$ | $> 250$ | $> 300$ | $> 375$ | 200–250 | 250–300 | 300–375 |

### 10.1.2 Background estimates and results

The SM background in the various SRs arises from several processes that generate real photons and from events in which one or more energetic jets or electrons are misidentified as photons. The latter are estimated through the use of control samples including jets or electrons, scaled by misidentification rates determined from data. The background with real photons is dominated by the $Z(\to \nu\nu)\gamma$ process, secondary contributions come from $W(\to l\nu)\gamma$ and $Z(\to ll)\gamma$ production with unidentified electrons, muons or with hadronically decaying $\tau$ leptons and from $\gamma$+jets events. These contributions are obtained using Monte Carlo (MC) simulations constrained by observed event counts in dedicated control regions (CRs) through the estimation of normalisation factors. Control regions are built by inverting one or more of the selection criteria used to define the SRs, allowing one of the background processes to become dominant but otherwise kinematically similar to the given SR. The contribution of these backgrounds is determined separately for each SR, as defined in Table 10.1, with a maximum-likelihood fit, referred to as the 'background-only fit'. This procedure constrains the normalisation of the dominant backgrounds to the observed event yields in the associated CRs, assuming that no signal is present in the CRs and including the background contribution from the misidentification of electrons and jets as photons estimated with data-driven techniques. The inputs to the fit

for each SR include the number of events observed in its associated CRs and the number of events predicted by simulation in the SR and CRs for each background process. The latter is described by Poisson statistics. The systematic uncertainties are included in the fit as nuisance parameters, modelled by Gaussian distributions with widths corresponding to the sizes of the associated uncertainties. Using a simultaneous fit technique allows a straightforward combination of multiple CRs and permits a coherent treatment of the correlation of the systematic uncertainties across the different regions. The product of the various probability distributions forms the likelihood, which the fit maximises by adjusting the background normalisation and the nuisance parameters.

Since the shape of BSM signal models over multiple $E_{\mathrm{T}}^{\mathrm{miss}}$ bins is different from the background prediction, a 'simplified shape fit' is applied in the CRs associated with the exclusive SRs plus the inclusive SR corresponding to the highest $E_{\mathrm{T}}^{\mathrm{miss}}$ range (SRI4) shown in Table 10.1. This allows normalisation factors for the background contributions in each $E_{\mathrm{T}}^{\mathrm{miss}}$ bin to be extracted by exploiting the $E_{\mathrm{T}}^{\mathrm{miss}}$ shape information and it is used to set exclusion limits on the considered models when no excess is found in the data.

The background-only simultaneous fit is performed to evaluate the SM background expectations in all regions of the analysis. The event yields in data are consistent with the SM expectations within uncertainties in all signal regions. The observed number of events and the expected SM background contribution resulting after performing the 'simplified shape fit' are reported in Table 10.2 [227]. The values of the normalisation factors for $W/Z+\gamma$ and $\gamma+$jets backgrounds are also shown.

TABLE 10.2: Observed and expected yields from SM backgrounds obtained from the 'simplified shape fit' [227]. The normalisation factors obtained from the fit are also shown at the bottom of the table. The uncertainty includes both statistical and systematic uncertainties. The individual uncertainties can be correlated and do not necessarily add in quadrature to equal the total background uncertainty.

| | SRE1 | SRE2 | SRE3 | SRI4 |
|---|---|---|---|---|
| Observed events | 3023 | 1164 | 679 | 427 |
| Expected SM events | $3070 \pm 130$ | $1182 \pm 75$ | $680 \pm 53$ | $448 \pm 42$ |
| $Z(\to \nu\nu)\gamma$ | $1910 \pm 110$ | $758 \pm 65$ | $468 \pm 49$ | $306 \pm 40$ |
| $W(\to \ell\nu)\gamma$ | $394 \pm 22$ | $159 \pm 15$ | $71.0 \pm 8.2$ | $56.7 \pm 7.1$ |
| $Z(\to \ell\ell)\gamma$ | $33.2 \pm 2.4$ | $9.32 \pm 0.89$ | $4.26 \pm 0.48$ | $2.69 \pm 0.37$ |
| $\gamma$ + jets | $87 \pm 35$ | $11.9 \pm 4.8$ | $2.7 \pm 1.1$ | $3.0 \pm 1.2$ |
| Fake photons from $e$ | $511 \pm 48$ | $188 \pm 18$ | $100.9 \pm 9.5$ | $59.7 \pm 5.6$ |
| Fake photons from jets | $136 \pm 28$ | $56 \pm 29$ | $33 \pm 16$ | $20 \pm 11$ |
| $k_{Z\gamma}$ | $0.99 \pm 0.08$ | $0.89 \pm 0.09$ | $0.90 \pm 0.11$ | $0.86 \pm 0.12$ |
| $k_{W\gamma}$ | $0.81 \pm 0.09$ | $0.84 \pm 0.11$ | $0.74 \pm 0.11$ | $0.85 \pm 0.13$ |
| $k_{\gamma+\mathrm{jets}}$ | | $0.82 \pm 0.21$ | | |

The total uncertainty ranges from 3.5% to 9.5% depending on the SR. The purely statistical uncertainty is dominant, varying from 2.4% to 8.5% and driven by the statistical precision from the CRs adopted to constrain the normalisation of the leading $Z(\to \nu\nu)\gamma$ background. The relative impact of each source of systematic uncertainty on the total SM background estimates is summarised in Table 10.3 [227]. A large experimental uncertainty is related to jets misidentified as photons and varies from 1.4% to 4.1%. The impact of the uncertainty in the jet energy scale and resolution varies from 1.6% to 2.7%. The uncertainty related to electrons misidentified as photons varies between about 2% and 2.3%. Other experimental systematic uncertainties related to electrons, photons, muons and the $E_{\mathrm{T}}^{\mathrm{miss}}$ 'soft term' have a relative impact below 1.5% in all SRs. Theoretical systematic uncertainties in the $W/Z+\gamma$ and $\gamma+$jets MC estimates have an impact of 0.5% in all SRs.

TABLE 10.3: Summary of the uncertainties (%) in the background estimate for inclusive SRs after the background-only fit and for exclusive SRs after the 'simplified shape fit' [227]. The individual uncertainties can be correlated and do not necessarily add in quadrature to equal the total background uncertainty.

| | SRI1 [%] | SRI2 [%] | SRI3 [%] | SRI4 [%] | SRE1 [%] | SRE2 [%] | SRE3 [%] |
|---|---|---|---|---|---|---|---|
| Total (statistical+systematic) uncertainty | 3.5 | 4.8 | 6.2 | 9.5 | 4.3 | 6.3 | 7.8 |
| Statistical uncertainty | 2.4 | 3.6 | 5.3 | 8.5 | 3.3 | 5.0 | 6.7 |
| Fake photons from jets | 1.4 | 2.5 | 2.8 | 4.1 | 1.4 | 3.6 | 3.7 |
| Jet energy scale/resol | 1.6 | 2.2 | 2.5 | 2.7 | 2.2 | 2.2 | 2.3 |
| Fake photons from electrons | 2.1 | 2.0 | 2.0 | 2.0 | 2.3 | 2.3 | 2.1 |
| Electrons reco/id/isolation eff. | 1.0 | 1.2 | 1.3 | 1.4 | 1.0 | 1.0 | 1.2 |
| Electron/photon energy scale/resol | 0.8 | 0.6 | 0.7 | 0.9 | 0.9 | 0.9 | 0.6 |
| Muon reco/id/isolation eff. | 0.7 | 0.8 | 0.9 | 1.0 | 0.6 | 0.7 | 0.9 |
| $E_{\mathrm{T}}^{\mathrm{miss}}$ soft term scale/resolution | 0.1 | 0.4 | 0.7 | 0.9 | 0.5 | 0.2 | 0.5 |
| Theoretical $W/Z+\gamma$, $\gamma+$jets | 0.5 | 0.5 | 0.5 | 0.5 | 0.5 | 0.5 | 0.5 |
| $\langle\mu\rangle$ reweighting in MC simulation | 0.3 | 0.2 | 0.2 | 0.2 | 0.3 | 0.2 | 0.2 |

## 10.2 Description of the signal model

In the search for high mass resonances from heavy Higgs bosons in $\gamma + E_{\mathrm{T}}^{\mathrm{miss}}$ final states carried out in this search, the phase-space defined by the reinterpreted mono-photon analysis leads to dominant contributions from both $ggF$ and $VBF$ production processes as shown in Figure 10.1. For both these processes, dedicated MC generators are used to simulate and model the signal events, at a centre-of-mass energy of 13 TeV following the configurations shown in Table 10.4. The heavy Higgs boson decay to a photon and a massless dark photon $H \to \gamma\gamma_d$ is handled assuming the Hidden-Valley dark photon scenario [190] implemented in PYTHIA since 8.150 version.

The signal events produced via $ggF$ are generated using POWHEG [v2 NNLOPS] [228, 229, 230, 231, 232] with the CT10 set of parton distribution functions (PDFs), calculated at NNLO accuracy in $\alpha_{\mathrm{S}}$. The simulation was interfaced with PYTHIA [8.306] using the CTEQ6L1 PDF set and the AZNLO underlying-event tune to handle the heavy Higgs boson decay, the parton shower and the non-perturbative hadronization effects. The $ggF$ prediction from the MC samples is normalised to the next-to-NNLO cross-section in QCD plus electroweak corrections at NLO [184, 233, 234, 235, 236, 237, 238, 239, 240, 241, 242]. In addition, a filter is applied at the generator level requiring events to contain one photon with a $p_{\mathrm{T}} > 120$ GeV and $|\eta| < 2.5$.

The other signal production process is through $VBF$. Signal events from this production mode were generated with matrix elements calculated using POWHEG [v2] [185, 186] at NLO accuracy in $\alpha_{\mathrm{S}}$, using the PDF4LHC15_nlo_30_pdfas set of PDFs [243]. In addition, PYTHIA [8.306] [244] was used with the dipole recoil shower variable [245] turned on, to perform the heavy Higgs boson decay as well as the parton shower and the non-perturbative hadronization effects with the CTEQ6L1 PDF set and the AZNLO underlying-event tune. Moreover, at the generator level, a filter is applied to require events with $E_{\mathrm{T}}^{\mathrm{miss}}$ higher than 75 GeV.

The samples of both $ggF$ and $VBF$ processes were generated with the width set to the SM value of 4 MeV [246] and the complex pole scheme [189] turned off. A total of eight MC samples per production process were generated with heavy Higgs boson masses equal to 400, 600, 800, 1000, 1500, 2000, 2500 and 3000 GeV.

The generated events were processed through a simulation [178] of the ATLAS detector geometry and response using GEANT [131], and through the same reconstruction software as the collected $pp$ collision data. Corrections were applied to the simulated events so that the particle candidates'

selection efficiencies, energy scales and energy resolutions match those determined from data control samples. The simulated samples are normalised to the total integrated luminosity assuming their cross-sections, computed to the highest order available in perturbation theory as given in Table 10.5 [246]. The detector response was simulated using a fast parameterised simulation of the ATLAS calorimeters [181] and the full GEANT simulation is used for the other sub-detectors.

TABLE 10.4: The configurations used for event generation of the signal processes. The matrix element (ME) order refers to the order in the strong coupling constant of the perturbative calculation. The tune refers to the underlying-event tune of the parton shower.

| Process | Generator | ME Order | Parton Shower | PDF | Tune |
|---|---|---|---|---|---|
| $ggF, H \to \gamma\gamma_d$ | POWHEG [v2 NNLOPS] | NNLO | PYTHIA [8.306] | CT10, CTEQ6L1 | AZNLO |
| $VBF, H \to \gamma\gamma_d$ | POWHEG [v2] | NLO | PYTHIA [8.306] | PDF4LHC15, CTEQ6L1 | AZNLO |

TABLE 10.5: Cross-section $\sigma$ values of heavy Higgs boson productions in $ggF$ and $VBF$ processes.

| $m_H$ (GeV) | 400 | 600 | 800 | 1000 | 1500 | 2000 | 2500 | 3000 |
|---|---|---|---|---|---|---|---|---|
| $\sigma_{ggF}$ (pb) | 9.516 | 2.006 | 0.449 | 0.123 | $8.91\times10^{-3}$ | $1.08\times10^{-3}$ | $1.78\times10^{-4}$ | $3.50\times10^{-5}$ |
| $\sigma_{VBF}$ (pb) | 0.758 | 0.327 | 0.162 | 0.087 | $2.28\times10^{-2}$ | $7.05\times10^{-3}$ | $2.36\times10^{-3}$ | $8.25\times10^{-4}$ |

TABLE 10.6: Theoretical uncertainties (%) for $ggF$ and $VBF$ production modes and different heavy Higgs masses computed in the most inclusive SRI1, with $E_T^{miss} > 200$ GeV.

| $m_H$ (GeV) | $ggF, H \to \gamma\gamma_d$ | | | $VBF, H \to \gamma\gamma_d$ | | |
|---|---|---|---|---|---|---|
| | PDF+scale (%) | | PS (%) | PDF+scale (%) | | PS (%) |
| 400 | (-14.6 | +16.9) | 2.20 | (-1.54 | +1.29) | 10.0 |
| 600 | (-14.7 | +16.1) | 2.20 | (-2.57 | +2.04) | 2.82 |
| 800 | (-15.0 | +16.2) | 6.49 | (-2.63 | +1.82) | 2.94 |
| 1000 | (-15.4 | +16.4) | 4.54 | (-4.21 | +3.41) | 3.43 |
| 1500 | (-16.3 | +17.2) | 3.01 | (-5.28 | +4.01) | 2.51 |
| 2000 | (-13.3 | +13.3) | 2.17 | (-6.46 | +5.05) | 1.46 |
| 2500 | (-22.1 | +23.1) | 2.36 | (-8.15 | +7.38) | 1.09 |
| 3000 | (-22.1 | +23.1) | 3.60 | (-9.03 | +7.52) | 2.28 |

**Theoretical uncertainties:** Signals from $ggF$ and $VBF$ are considered for the computation of the theoretical uncertainties in each SR bin of the analysis as shown in Table 10.1. As no dependence on $E_{\mathrm{T}}^{\mathrm{miss}}$ has been noticed, the estimates in the most inclusive SRI1 ($E_{\mathrm{T}}^{\mathrm{miss}} > 200$ GeV) have been considered. Theoretical uncertainties include uncertainties on the NLO cross-section due to the QCD factorisation and renormalisation scales [247] as well as the choice of parton distribution functions. Uncertainties on initial- and final-state radiations due to the choice of parton shower (PS) parameters used with PYTHIA [8.306] are estimated by generating MC samples with the alternative tunes described in Ref. [248]. The uncertainties for both production processes and for each mass point are summarised in Table 10.6. Because of technical reasons, some information was missing in the samples $m_H$ = 400 GeV, 2500 GeV, so the corresponding uncertainties related to samples $m_H$= 600 GeV, 3000 GeV are considered as a conservative estimate.

## 10.3 Reinterpretation results

The reinterpretation of the Run-2 $\gamma + E_{\mathrm{T}}^{\mathrm{miss}}$ search is performed including the heavy Higgs boson signal decaying to a photon and a massless dark photon into the simultaneous likelihood fit described in Section 10.1. The signal experimental and theoretical uncertainties are considered in the fit as nuisance parameters. The background estimation has been obtained providing to the fit the same inputs of the $\gamma + E_{\mathrm{T}}^{\mathrm{miss}}$ analysis. To illustrate the shape of the different $H \to \gamma\gamma_d$ signals in the SR, their $E_{\mathrm{T}}^{\mathrm{miss}}$ distributions have been superimposed to the expected SM background and data after performing the 'simplified shape fit' as shown in Figure 10.2. Signal acceptances for $ggF$ and $VBF$ processes in the SRs used in the 'simplified shape fit' are shown in Table 10.7.

TABLE 10.7: Signal acceptance (%) for $ggF$ and $VBF$ processes in all the exclusive and the last inclusive SRs used in the 'simplified shape fit'.

| | SRE1 | | SRE2 | | SRE3 | | SRI4 | |
|---|---|---|---|---|---|---|---|---|
| $m_H$ (GeV) | $ggF$ (%) | $VBF$ (%) | $ggF$ (%) | $VBF$ (%) | $ggF$ (%) | $VBF$ (%) | $ggF$ (%) | $VBF$ (%) |
| 400 | 8.15 | 4.30 | 0.35 | 0.49 | 0.04 | 0.05 | 0.00 | 0.01 |
| 600 | 9.05 | 4.95 | 18.9 | 9.10 | 7.74 | 5.44 | 0.35 | 0.53 |
| 800 | 3.21 | 1.96 | 5.33 | 3.27 | 15.4 | 9.39 | 15.6 | 10.5 |
| 1000 | 1.63 | 1.24 | 2.50 | 1.72 | 5.92 | 4.01 | 29.4 | 21.2 |
| 1500 | 0.50 | 0.38 | 0.73 | 0.69 | 1.65 | 1.33 | 33.3 | 30.0 |
| 2000 | 0.22 | 0.21 | 0.35 | 0.33 | 0.67 | 0.69 | 32.7 | 34.3 |
| 2500 | 0.10 | 0.09 | 0.16 | 0.18 | 0.35 | 0.41 | 29.6 | 38.0 |
| 3000 | 0.04 | 0.08 | 0.08 | 0.11 | 0.19 | 0.29 | 28.9 | 39.6 |

Exclusion upper limits at 95% CL on $\sigma \times BR(H \to \gamma\gamma_d)$ are obtained performing the 'simplified shape fit' including both the SRs and their associated CRs by means of the HistFitter package [249]. These limits are based on the profile-likelihood-ratio test statistic [223] and $\mathrm{CL_s}$ prescriptions [224], evaluated using the asymptotic approximation [250]. Results for the heavy Higgs boson signal produced via $ggF$ and $VBF$ separately as well as through a combination in which the two processes have been merged proportionally to their relative theoretical cross-sections [246] $ggF$+$VBF$ are shown in Figure 10.3 for the considered Higgs mass values. The theoretically predicted cross-section of a heavy Higgs boson produced via $ggF$ or $VBF$ is superimposed assuming

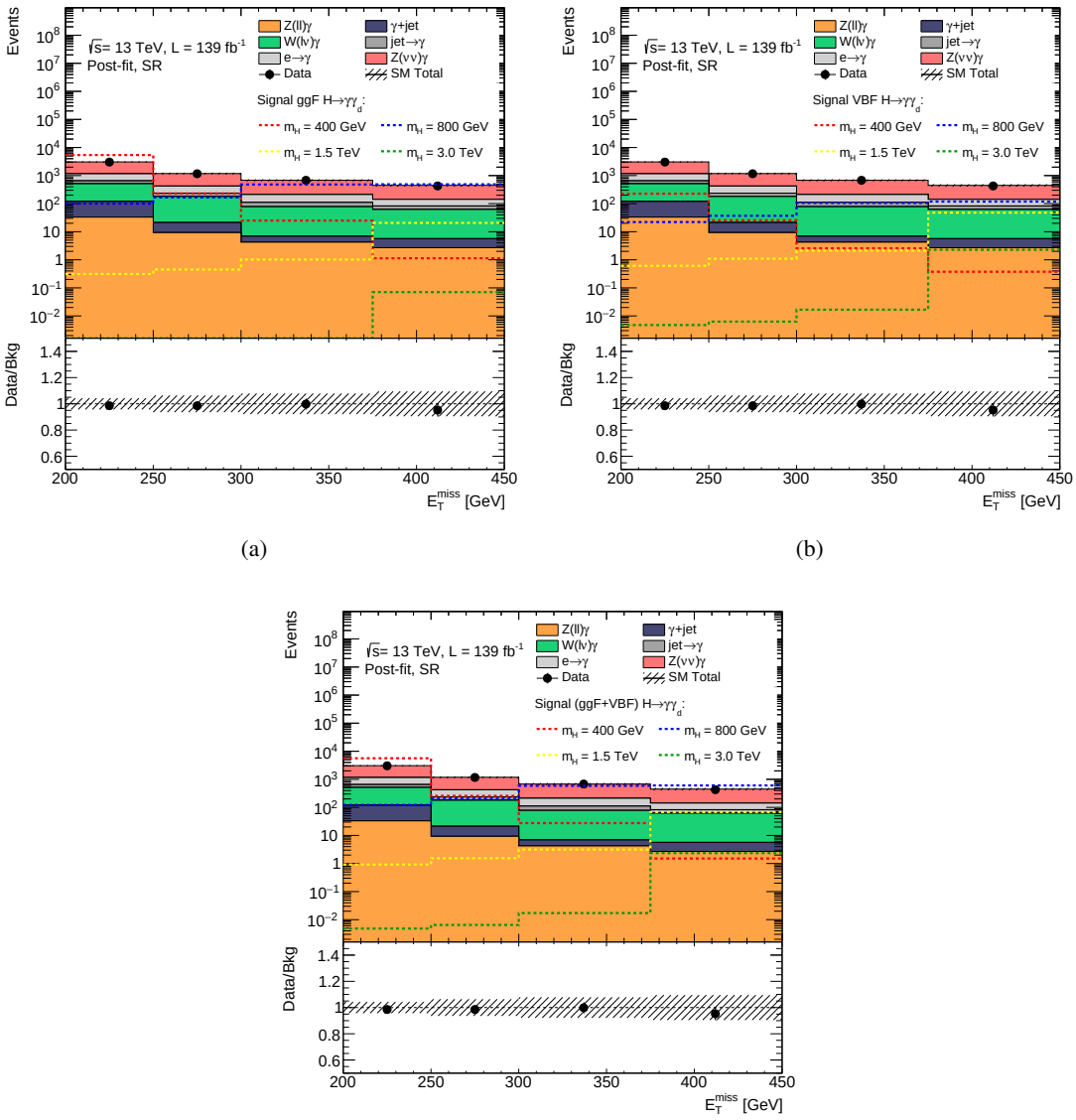


FIGURE 10.2: Distributions of $E_{\mathrm{T}}^{\mathrm{miss}}$ for (a) $ggF$, (b) $VBF$, and (c) $ggF$+$VBF$ production modes of $H \to \gamma\,\gamma_d$ assuming the BR($H \to \gamma\,\gamma_d$) = 0.05. The signals are superimposed to the expected SM background and data after performing the 'simplified shape fit'. The error bars are statistical, and the dashed band includes statistical and systematic uncertainties determined by the fit. The lower panel shows the ratio of data to expected background event yields.

a $BR(H \to \gamma\gamma_d) = 0.05$. Table 10.8 summarises the observed and the expected exclusion limits at 95% CL on $\sigma \times BR(H \to \gamma\gamma_d)$ for $ggF$ and $VBF$ separately as well as for the combined productions $ggF$+$VBF$. The relative impact of the signal theoretical uncertainties on the exclusion limits is below 11.5% for the $ggF$ process and below 2.5% for the $VBF$ process considering all mass samples, while the signal experimental uncertainties have an overall impact below 7% for both processes.

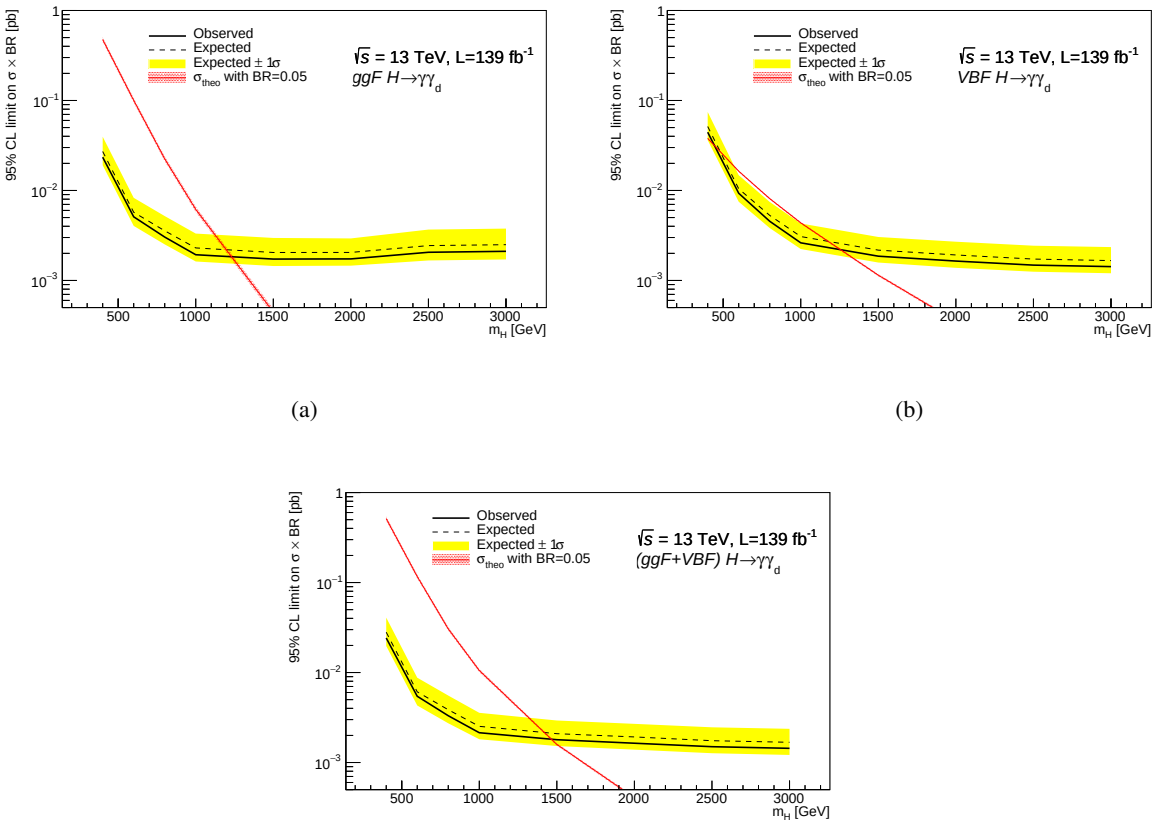


(a) (b)

(c)

FIGURE 10.3: Observed and expected exclusion limits at 95% CL on $\sigma\times$ BR($H \to \gamma\ \gamma_d$) as function of the heavy Higgs mass. The yellow band shows the $\pm 1\sigma$ uncertainties. The theoretically predicted cross-section of a heavy Higgs boson produced via (a) $ggF$, (b) $VBF$ and (c) $ggF$+$VBF$ is superimposed assuming a $BR(H \to \gamma\gamma_d) = 0.05$.

## 10.4 Summary

The reinterpretation of the ATLAS full Run-2 $\gamma + E_{\mathrm{T}}^{\mathrm{miss}}$ search using the RECAST framework is performed in the context of the production of a heavy Higgs boson decaying to a photon and a massless dark photon. Dominant contributions come from both gluon-gluon Fusion ($ggF$) and Vector-Boson Fusion ($VBF$) production modes and different mass hypotheses for the heavy Higgs boson have been considered spanning from 400 GeV to 3 TeV to probe the sensitivity of the $\gamma + E_{\mathrm{T}}^{\mathrm{miss}}$ search towards the $H \to \gamma\gamma_d$ signal. Exclusion upper limits on the cross-section times the branching ratio for $H \to \gamma\gamma_d$ are provided for both production modes $ggF$ and $VBF$ separately and for the combined $ggF + VBF$ processes for the considered Higgs masses. The exclusion limits at 95% confidence

TABLE 10.8: Observed and expected exclusion limits at 95% CL on $\sigma \times BR(H \to \gamma\gamma_d)$ obtained with the 'simplified shape-fit' for $ggF$, $VBF$ and combined $ggF$+$VBF$ channels.

| 95% CL Limits | $\sigma_{ggF} \times BR$ | | $\sigma_{VBF} \times BR$ | | $\sigma_{(ggF+VBF)} \times BR$ | |
|---|---|---|---|---|---|---|
| $m_H$ | Obs. (fb) | Exp.$^{+1\sigma}_{-1\sigma}$ (fb) | Obs. (fb) | Exp.$^{+1\sigma}_{-1\sigma}$ (fb) | Obs. (fb) | Exp.$^{+1\sigma}_{-1\sigma}$ (fb) |
| 400 GeV | 23.9 | $27.3\ ^{+12.7}_{-7.80}$ | 44.4 | $51.4\ ^{+23.1}_{-15.2}$ | 24.2 | $28.1\ ^{+12.7}_{-8.30}$ |
| 600 GeV | 5.08 | $5.72\ ^{+2.60}_{-1.65}$ | 9.30 | $10.43\ ^{+4.35}_{-2.94}$ | 5.45 | $6.10\ ^{+2.66}_{-1.80}$ |
| 800 GeV | 3.04 | $3.56\ ^{+1.63}_{-1.05}$ | 4.54 | $5.28\ ^{+2.17}_{-1.46}$ | 3.31 | $3.86\ ^{+1.69}_{-1.13}$ |
| 1 TeV | 1.93 | $2.30\ ^{+1.02}_{-0.67}$ | 2.62 | $3.08\ ^{+1.21}_{-0.85}$ | 2.14 | $2.52\ ^{+1.04}_{-0.71}$ |
| 1.5 TeV | 1.73 | $2.05\ ^{+0.92}_{-0.60}$ | 1.86 | $2.17\ ^{+0.87}_{-0.59}$ | 1.79 | $2.09\ ^{+0.84}_{-0.57}$ |
| 2 TeV | 1.74 | $2.05\ ^{+0.88}_{-0.59}$ | 1.64 | $1.92\ ^{+0.78}_{-0.52}$ | 1.64 | $1.93\ ^{+0.76}_{-0.54}$ |
| 2.5 TeV | 2.06 | $2.44\ ^{+1.24}_{-0.77}$ | 1.48 | $1.73\ ^{+0.70}_{-0.49}$ | 1.50 | $1.75\ ^{+0.71}_{-0.48}$ |
| 3 TeV | 2.11 | $2.50\ ^{+1.27}_{-0.79}$ | 1.42 | $1.66\ ^{+0.69}_{-0.46}$ | 1.44 | $1.68\ ^{+0.69}_{-0.46}$ |

level for the $ggF + VBF\ H \to \gamma\gamma_d$ are found to be in the range from 1.44 (1.68 fb) to 24.2 (28.1 fb) observed (expected) respectively, with the highest limit corresponding to a heavy Higgs boson with a mass of 400 GeV and the lowest limit corresponds to the heaviest considered mass of 3 TeV.

# Part IV

# THE HL-LHC ATLAS UPGRADE: PERFORMANCE EVALUATION OF LGAD SENSORS FOR THE HGTD

# 11 The High Granularity Timing Detector (HGTD)

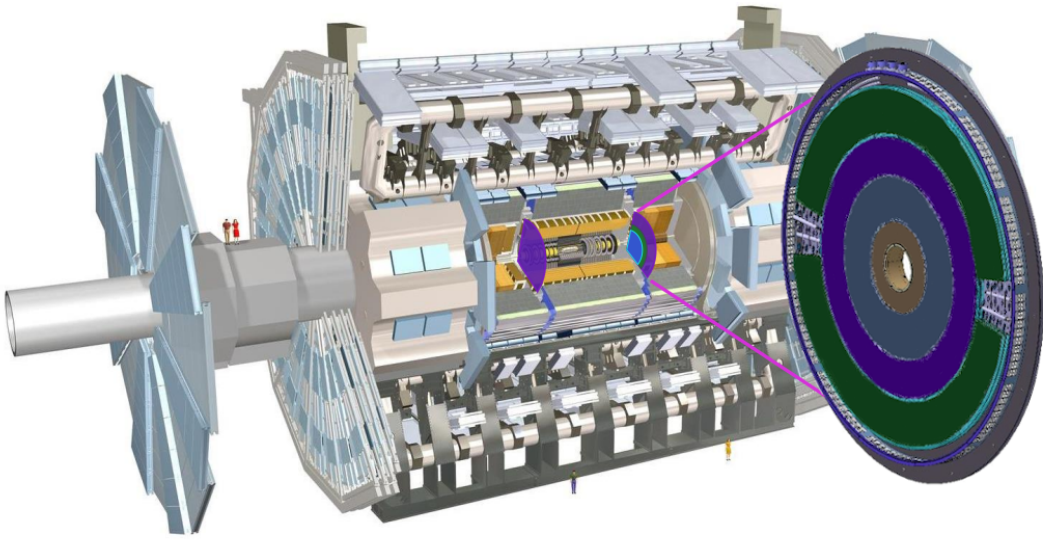

FIGURE 11.1: Position of the two HGTD disks within the ATLAS Detector, outside of the Inner Tracker and in front of the forward calorimeters. Each disk is equipped with two double-sided instrumented layers [251].

After *Run 3* of data taking at the LHC (between 2021 and 2024), the machine will be upgraded to deliver an increased instantaneous luminosity to amass $pp$ collision data at an even faster rate. The *High-Luminosity LHC* (HL-LHC) [252] is expected to start operations in 2027 at a centre of mass energy of 14 TeV and run at least until 2040, a period dubbed *Phase II*. It will achieve an instantaneous luminosity of $7.5 \times 10^{34}\,\mathrm{cm}^{-2}\,\mathrm{s}^{-1}$ and will provide a dataset of an integrated luminosity of up to $4000\,\mathrm{fb}^{-1}$. The expected running conditions will be an environment with an average number of interactions per collision of around 200, about one order of magnitude larger than during *Run 2*. Thus the successful physics program at the LHC can expand, improving precision measurements of the Standard Model [253], and continue probing the Higgs sector where studying the couplings to the SM to the per cent level will be possible [254], but also expanding the reach of searches for signatures of physics beyond the SM to higher mass ranges [255].

The ATLAS detector was constructed to operate at an instantaneous luminosity of $1 \times 10^{34}\,\mathrm{cm}^{-2}\,\mathrm{s}^{-1}$ withstand radiation damage during the collection of up to $1000\,\mathrm{fb}^{-1}$ of integrated luminosity. Substantial updates of the individual subsystems are thus necessary to cope with the

HL-LHC environment, which requires the capability to process much higher data rates as well as a radiation hardness to a fluence of $1 \times 10^{16}\,\mathrm{n_{eq}\,cm^{-2}}$ and an irradiation of 10 MGy.

The goal of the upgrades of ATLAS is a performance equal to or better than achievable with the current detector but in the much harsher environment of the HL-LHC. The trigger and data acquisition systems will improve their granularity and will have faster electronics, achieving an output rate of 10 kHz. The current tracking detector of ATLAS would in general not survive the expected radiation levels and the TRT would reach an occupancy of 100 %. The tracker will thus be completely replaced by a fully silicon-based tracking detector, the *Inner Tracker* (ITk) [256, 257]. Compared to the current tracker, ITk will have more pixel layers and feature a higher granularity. Its acceptance will be extended and allow reconstruction of charged particle tracks up to $|\eta| = 4$. The calorimeter system will also be upgraded. Both, the Liquid Argon Calorimeter [258], as well as the Tile Calorimeter [259], will receive new front end and back-end electronics to cope with the higher data rates. In the end-cap region, the electronics of the muon chambers will also be replaced to perform under the new conditions. Additionally, a new detector will be installed in the forward region, measuring the time of minimum ionising particles (MIPs) with high precision, the *High-Granularity Timing Detector* (HGTD) [260, 251].

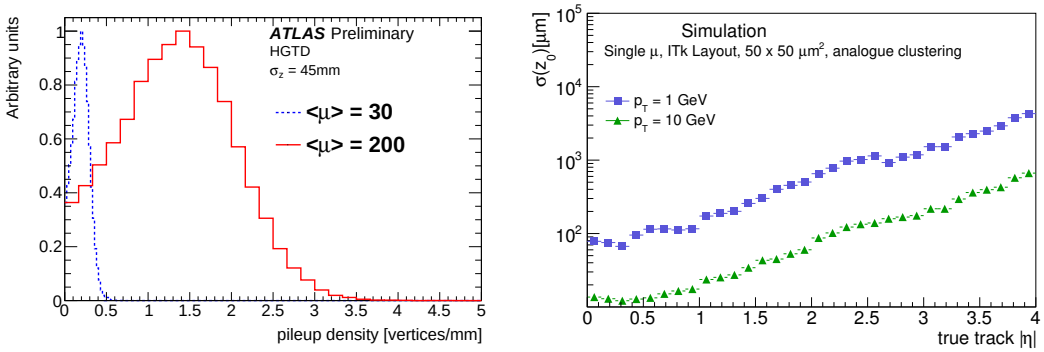


(a) (b)

FIGURE 11.2: The expected pile-up density at HL-LHC conditions is compared to the situation found during *Run 2* in (a) [260]. The expected resolution of the longitudinal track impact parameter $\sigma_{z_0}$ provided by ITk is shown as as a function of $|\eta|$ for muons of $p_\mathrm{T} = 1\,\mathrm{GeV}$ and $p_\mathrm{T} = 10\,\mathrm{GeV}$ in (b) [251].

HGTD aims to provide high precision time measurements for tracks in the forward region, with an average resolution of 30 ps per track at the beginning of the HL-LHC runtime, deteriorating not farther than 50 ps per track until the end of the HL-LHC due to the increasing radiation damage to the sensor. The detector consists of two disk-shaped vessels, one installed in each end-cap region, both containing two double-sided instrumented layers, that will be installed in the forward region of the ATLAS detector (see 11.1), covering the range $2.4 < |\eta| < 4.0$.

Contamination from additional pile-up interactions is one of the main challenges for the HL-LHC. In the nominal operation scenario [261], an average of 200 simultaneous $pp$ interactions ($\langle\mu\rangle = 200$) are expected to occur within each bunch crossing. The luminous region is expected to show a Gaussian spread of 45 mm along the beam axis ($z$) and a spread of 175 ps in time. The expected average pile-up vertex density (11.2a) at nominal conditions will be 1.8 vertices/mm. While the ITk can resolve the quoted vertex density in the central region, the degradation of the resolution of the longitudinal impact parameter $z_0$ in the forward region, as can be seen from 11.2b, leads to sizeable pile-up contaminations. Beyond a pseudorapidity value of $|\eta| \sim 2.2$ the $z_0$-resolution is already in the millimetre range for low $p_\mathrm{T}$ tracks. It is thus challenging to unambiguously associate tracks in the forward region to reconstructed vertices. The approach followed by HGTD to resolve this issue

is to take advantage of the time component provided by this new detector. Even though a forward track might be spatially compatible with a given vertex, by observing a large difference in the time associated with the track and that associated to the selected vertex, pile-up tracks can be identified and rejected. Using a back-of-the-envelope estimation, given a beam spread of 175 ps and a time resolution per track of 30 ps, the pile-up can be reduced by a factor 6 in the HGTD acceptance. The added time component will thus improve the object reconstruction performance in the forward region, which includes better object identification as well as enhanced pile-up rejection.

HGTD also provides luminosity measurement capabilities. HGTD shows a nearly perfectly linear detector response as a function of $\langle\mu\rangle$, using the proportionality between the number of hits in a limited acceptance range and the instantaneous luminosity. The time information also allows to reject backgrounds in the high-radiation environment, which makes HGTD more reliable than for example track counting techniques. Finally, occupancy data read out at 40 MHz makes the luminosity measurement available at a bunch-by-bunch level without limitations from a trigger bias.

# 12 Performance in beam tests of Low Gain Avalanche Detectors for the HGTD

## 12.1 Introduction

The High Luminosity upgrade of the Large Hadron Collider (HL-LHC) [262, 263] at CERN is expected to deliver an integrated luminosity of 4000 $\text{fb}^{-1}$ with an increase of the instantaneous luminosity from $10^{34}\text{cm}^{-2}s^{-1}$ to $7.5 \times 10^{34}\text{cm}^{-2}s^{-1}$ resulting in a nominal average of 200 simultaneous $pp$ interactions per bunch crossing. The correct assignment of particles originating from the hard-scattering process and the suppression of detector signals produced by the additional low-energy pp collisions (pile-up) are among the most difficult challenges in this busy environment.

A High Granularity Timing Detector (HGTD) [264, 251] installed at the end-cap/forward region of the ATLAS detector [265] with an $\eta$ coverage of 2.4 to 4.0 would provide additional capabilities to the foreseen new inner tracker [257, 256] to mitigate pile-up effects on physics final states containing forward jets/particles. Due to the high radiation levels expected in this region for an integrated luminosity of 4000 $\text{fb}^{-1}$, the detector sensors and front-end electronics must sustain a 1 MeV neutron equivalent fluence of up to $2.5\times10^{15}$ $\text{n}_{eq}/\text{cm}^2$ and 2 MGy of total ionising dose estimated at a distance of 120 mm from the beam pipe. Assuming a safety factor of 1.5, the inner (middle) ring of the detector should be replaced at every 1000 $\text{fb}^{-1}$ (2000 $\text{fb}^{-1}$) to keep its performances at an optimal level. The HGTD would be able to measure the time of a minimum ionising particle (MIP) with a resolution ranging from approximately 30 ps at the beginning of the HL-LHC operations to 50 ps towards the end, with an average time resolution per hit of 35 ps and 70 ps, respectively. Given the need for an accurate time measurement and a high radiation hardness, the Low Gain Avalanche Detector (LGAD) technology [266] was chosen for the sensors with an active thickness of 50 µm and a pad area of $1.3 \times 1.3\,\text{mm}^2$. The time resolution is strongly linked to the front-end analogue performance, which makes the read-out ASIC a very challenging circuit to design. The time jitter should be low enough to not deteriorate the sensor performance. The HGTD ASIC, ATLAS LGAD Time Read Out Chip (ALTIROC) [267], has a discriminator of $\sim$2 fC and should achieve a good time measurement for charges as low as 4 fC, to cope with the reduction of the sensor gain due to irradiation. This lower limit on charge collection of 4 fC should satisfy the HGTD requirements of a minimum hit efficiency of 95% taking into account the ALTIROC jitter. The final ALTIROC is under design, where early prototypes are being tested at both laboratory and beam lines to validate their performances and readiness for the HL-LHC requirements [268, 251].

This chapter presents the performance of LGAD sensors, mounted on custom electronic boards, using the data collected in 2018 and 2019. In 2018 the tests were carried out at CERN SPS [269] with a high-energy pion beam, while in 2019 they were carried out at the DESY II Test Beam Facility [270]

with an electron beam. Previous results for unirradiated and irradiated LGADs and first HGTD hybrid modules can be found in Refs. [271, 272, 268]. This chapter is organised as follows: in Section 12.2 the LGAD technology and the tested sensors are described, while the test beam set-up and the data acquisition system are presented in Section 12.3. The data processing and the analysis methods are detailed in Section 12.4, followed by the presentation and discussion of the results in Section 12.5. The conclusions are presented in Section A.5.

## 12.2 Sensors

This section describes the main features and properties of the tested sensors. Several irradiation campaigns were carried out and the different irradiation levels are indicated. The initial electrical characterization is also presented.

### 12.2.1 Low Gain Avalanche Detectors

The LGAD sensors are thin n-on-p silicon devices whose design [266, 273] has been originally developed by the Centro National de Microelectrónica (CNM) Barcelona within the CERN-RD50 collaboration [274]. Their geometry was later optimized for high-precision time measurements. LGADs are based on implanting a few micrometre-thick, highly doped p-type layer between the high-resistivity p-type bulk and the $n^+$ implant (Figure 12.1), which acts as a high-field charge multiplication layer providing a moderate gain of about 5 to 70.

The tested prototypes have been manufactured by CNM and Hamamatsu Photonics (HPK). Wafers (W) from both vendors contain a variety of pad structures, such as single-pad diodes and segmented arrays of pad diodes with various granularities. CNM sensors were produced on 4-inch silicon-on-silicon wafers with an active thickness of 50 µm and a resistivity of 12 kΩ cm on a 300 µm-thick support wafer and 1 µm buried oxide (see Figure 12.1). To improve the radiation hardness, CNM investigated different doping materials: Boron for wafer 4[1], Boron plus Carbon for wafer 5[1] and Gallium for wafer 6[2] [275]. Carbon-enriched LGADs aimed to obtain similar performances as Boron ones but at lower bias voltages. On the other hand, HPK sensors were produced on 6-inch silicon-on-insulator wafers with an active thickness of 45 µm and a resistivity of 3.4 kΩ cm to 4.6 kΩ cm. HPK used only Boron to manufacture two types of LGADs with different doping profiles, a gain layer depth of 1.6 µm for the type-3.1 and 2.2 µm for the type-3.2, edge sizes of 300 µm and 500 µm as well as different nominal inter-pad distances (from 30 µm to 95 µm) in the case of 2×2 arrays. The tests reported in this thesis were performed on CNM single-pad sensors with an overall active area of $1\times1$ mm$^2$ and a gain layer of about $0.7\times0.7$ mm$^2$ with a single guard ring (GR) structure of 0.135 mm and HPK single-pad and 2×2 array sensors with an overall active area of $1.3\times1.3$ mm$^2$. Figure 12.2 shows a schematic view of the CNM and HPK single-pad LGAD sensors.

[1] CNM production run 10478.
[2] CNM production run 10924.

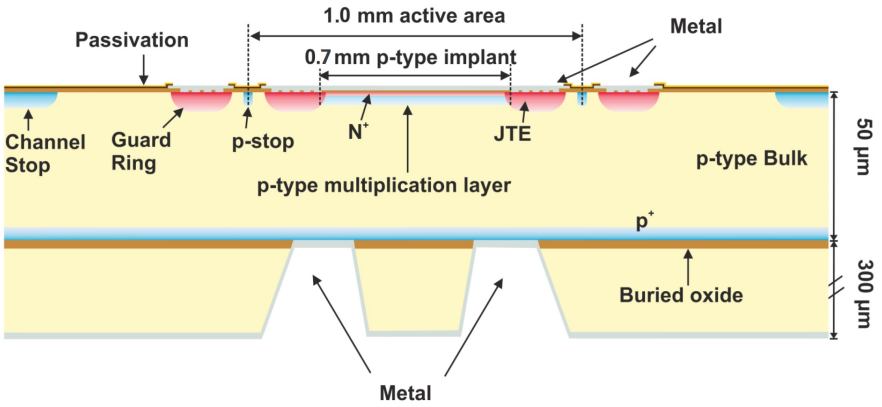


FIGURE 12.1: Cross section of a single-pad CNM LGAD sensor.

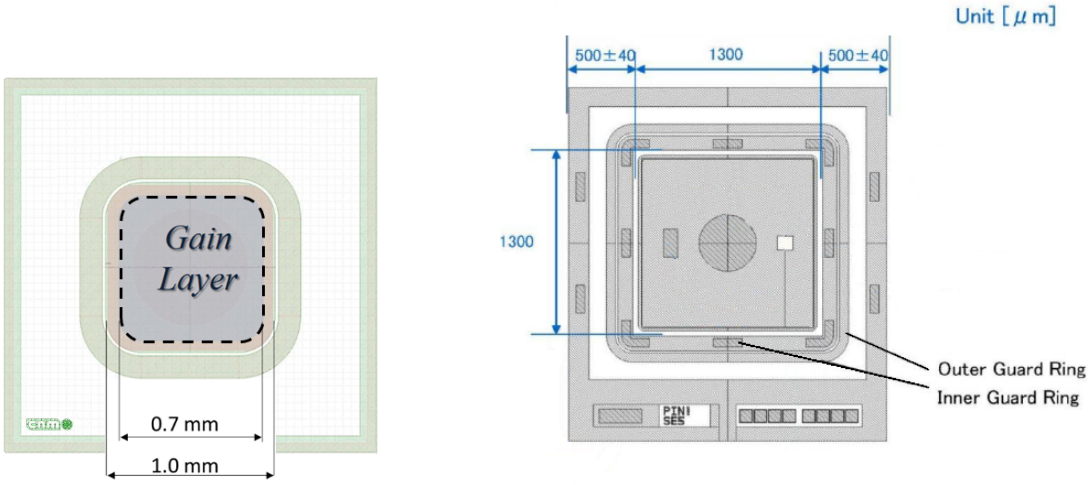


FIGURE 12.2: Geometry of CNM (left) and HPK 3.1 (right) single-pad LGAD sensors.

### 12.2.2 Irradiation

Radiation damage in silicon mainly results in the reduction of the effective doping concentration and the acceptor removal, by introducing trapping centres that reduce the mean free path of the charge carrier and increase the leakage current [274]. A surface effect is the accumulation of positive charge in the oxide ($SiO_2$) and the Si-$SiO_2$ interface which affects the interpixel capacitance. This has an impact on the detector's performance and charge collection efficiency. For LGADs, the radiation damage results in the degradation of the gain with fluence at a fixed voltage [276], which implies the need to increase the applied bias voltage after irradiation to at least partially compensate for this loss.

To study the LGAD performance after irradiation, the sensors were exposed to fluences up to $3\times10^{15}$ $n_{eq}/cm^2$ at various facilities with different particle types and energies. The main facilities are the TRIGA reactor in Ljubljana for 1 MeV neutrons, the CERN Proton Synchrotron (PS) IRRAD facility for 24 GeV protons and the CYRIC facility in Japan for 80 MeV protons. Table 12.1 lists the LGAD sensors measured in the beam tests, including the manufacturer, the sensor IDs, the implant of the multiplication layer as well as the irradiation type and fluence. It also includes the device name assigned to each sensor for easier reference in the text and contains several pieces of information: the sensor type (Boron, Carbon, Gallium, 3.1 or 3.2), the geometry (single-pad or array), the irradiation level in units of $10^{14}n_{eq}/cm^2$ and the type of particle that were exposed to.

TABLE 12.1: List of CNM and HPK LGAD sensors studied in the 2018-2019 beam test periods: single-pads ("S") and arrays ("A") including the information on the implant of the multiplication layer, the irradiation level and type.

| Device name | Manufacturer | Sensor ID | Implant | Irradiation type | Fluence [$n_{eq}/cm^2$] |
|---|---|---|---|---|---|
| LGA35 | CNM | W9LGA35 | Boron | unirradiated | |
| Boron S | CNM | W4S1030 | Boron | unirradiated | |
| Boron S1n | CNM | W4S1095 | Boron | n | $1\times10^{14}$ |
| Boron S6n | CNM | W4S1016 | Boron | n | $6\times10^{14}$ |
| Boron S1p | CNM | W4S1067 | Boron | p | $1\times10^{14}$ |
| Carbon S | CNM | W5S1013 | Boron+Carbon | unirradiated | |
| Carbon S1n | CNM | W5S1005 | Boron+Carbon | n | $1\times10^{14}$ |
| Carbon S1p | CNM | W5S1038 | Boron+Carbon | p | $1\times10^{14}$ |
| Gallium S | CNM | W6S1021 | Gallium | unirradiated | |
| Gallium S1n | CNM | W6S1007 | Gallium | n | $1\times10^{14}$ |
| Gallium S30n | CNM | W6S1006 | Gallium | n | $30\times10^{14}$ |
| Gallium S1p | CNM | W6S1028 | Gallium | p | $1\times10^{14}$ |
| 3.1 A | HPK | 3.1 W8 2x2 SE5IP3 | Boron | unirradiated | |
| 3.1 S8n | HPK | 3.1 W8 P2LGE5 | Boron | n | $8\times10^{14}$ |
| 3.1 S10p | HPK | 3.1 W8 LGE5 | Boron | p | $10\times10^{14}$ |
| 3.2 A | HPK | 3.2 W18 2x2 SE5IP3 | Boron | unirradiated | |
| 3.2 S8n | HPK | 3.2 W18 P4LGE5 | Boron | n | $8\times10^{14}$ |
| 3.2 A15n | HPK | 3.2 W18 2x2 SE5IP3 | Boron | n | $15\times10^{14}$ |
| 3.2 S15n | HPK | 3.2 SE3 (high gain) | Boron | n | $15\times10^{14}$ |

### 12.2.3 I-V and C-V measurements

Electrical measurements on the sensors were carried out before the beam test using a cooled probe station equipped with needle contacts. To study the gain layer $V_{gl}$, full depletion $V_{fd}$ and breakdown $V_{bd}$ voltages, the current-voltage (I-V) and the capacitance-voltage (C-V) scans were performed for each sensor with the guard ring grounded. Figure 12.3 shows the I-V characteristics for several tested sensors. The I-V measurements for both CNM and HPK sensors revealed a bulk leakage current of about 1 nA before irradiation. This value increases for irradiated sensors to about 0.1 µA and it is about two orders of magnitude higher for Gallium-type LGADs at lower fluences. For the unirradiated devices, $V_{bd}$ is below 100 V at −30 °C for the CNM sensors and $V_{bd}$ is 140 V for HPK-3.2 and 270 V for HPK-3.1 at 20 °C. For HPK sensors the I-V curve was later measured at −30 °C, and $V_{bd}$ was found to be 70 V for HPK-3.2 and 200 V for HPK-3.1 [251]. As expected, the breakdown voltage moves towards lower voltage values as the temperature decreases and it also moves towards higher voltage values as the fluence increases.

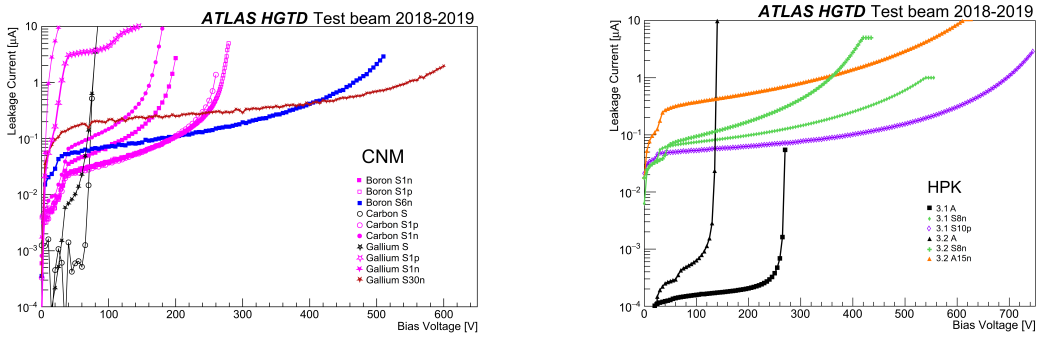


FIGURE 12.3: Leakage current-voltage dependence for CNM (left) and HPK (right) sensors. Note that all curves were performed at −30 °C except the two unirradiated HPK devices that were measured at 20 °C.

The C-V measurements in Figure 12.4 show the $V_{gl}$ and $V_{fd}$ for unirradiated HPK sensors. The $V_{gl}$ is 40 V for HPK-3.1 and 55 V for HPK-3.2 and the $V_{fd}$ is 50 V for HPK-3.1 and 65 V for HPK-3.2. This is explained by the difference in gain layer depth, as deeper the gain layer more bias is required for the sensor to be fully depleted, which is the case of HPK-3.2. Similar measurements for CNM sensors showed equivalent $V_{gl}$ and $V_{fd}$ values below 50 V [275]. The detector capacitance was measured to be C = 2.9 pF for both CNM and HPK sensors.

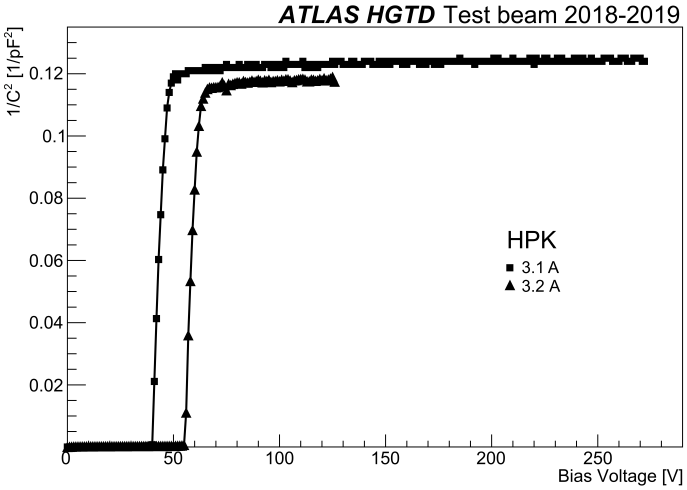


FIGURE 12.4: Capacitance-voltage dependence for unirradiated HPK sensors showing a full depletion voltage of 50 V for HPK-3.1 and 65 V for HPK-3.2.

## 12.3 Test beam set-up

The HGTD beam test campaigns were conducted at CERN SPS [269] H6A line using a high-momentum 120 GeV pion beam and at DESY [270] TB 22 line using a 5 GeV electron beam. The two set-ups are similar, but to reduce the multiple scattering at DESY the number of devices under test (DUTs) evaluated simultaneously was therefore reduced. At CERN, up to six DUTs were tested at the same time [271], placed in a thermally isolated enclosure where the temperature could reach $-40\,^{\circ}$C. Measurements were taken at $-30\,^{\circ}$C and $-20\,^{\circ}$C. At DESY, only three DUTs were tested simultaneously with a cooling system consisting of a styrofoam box with a separate compartment for the addition of dry ice packs [277]. The temperature was monitored with a Pt100 sensor and it was in the range of $-40\,^{\circ}$C to $-25\,^{\circ}$C. In both test beam infrastructures, for position-dependent measurements, a beam telescope [278] was used allowing the evaluation of sensor efficiency and charge uniformity as a function of the particle incident position. An independent time reference was provided to the data acquisition (DAQ) system by a Silicon Photomultiplier (SiPM) assembly [279].

### 12.3.1 Read-out electronics boards

LGAD sensors were assembled on 10 cm × 10 cm read-out and amplification boards using double-sided conductive tape. These boards were developed at the University of California Santa Cruz (UCSC) [280] in two versions: single-channel for single-pad LGADs and four-channel for 2 × 2 LGAD arrays. The LGAD front-side metal pad layer was coupled to the input of an onboard trans-impedance first-stage amplifier via multiple wire bonds to reduce the inductance, while the guard ring was grounded. The single-channel version (Figure 12.5 (left)) only includes this first amplification stage based on a single-transistor common emitter design that acts as an inverting trans-impedance amplifier. For further amplification, it uses an external second-stage amplifierwith hermetic E/B cover design from Mini-Circuits with a gain of about 10 and a 2 GHz bandwidth. The four-channel version (Figure 12.5 (right)) includes, in addition to the first amplification stage, two more amplifiers with a voltage divider between them resulting in a total gain of about 200 at a 1.6 GHz bandwidth. Both boards are equipped with SMA connectors providing low voltage input (2.25 V for the single-channel version, or 5 V for the four-channel version), one amplifier output (which goes to the external second-stage amplifier in the single-channel version) or four amplifier outputs (four-channel version), a calibration line input and a high-voltage input for reverse biasing the LGAD from the back of the sensor. The amplifier outputs were connected to the oscilloscope to record the LGAD signal. A third type of board developed at the University of Kansas (KU) was also used to test two 2×2 DUTs, 3.1 A and 3.2 A. This KU board [281, 282] is a two-channel version and is equipped with a 2-pin connector providing low voltage input, two SMA connectors providing two amplifier outputs and a LEMO connector serving as high-voltage input. It includes two identical two-stage trans-impedance amplifiers.

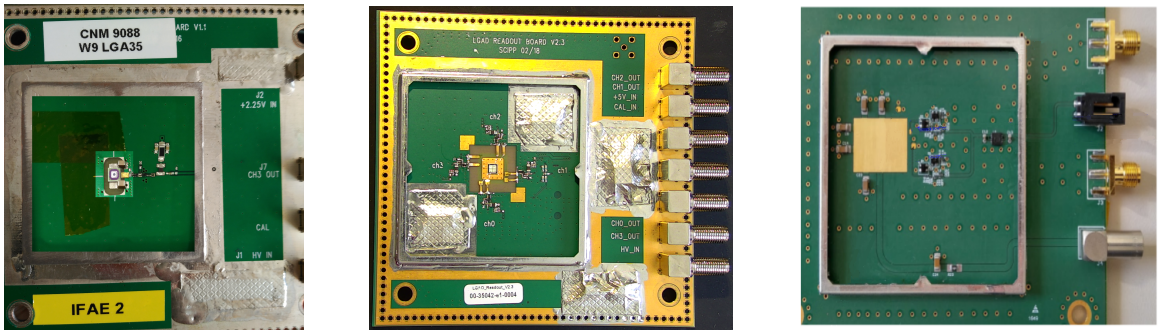


FIGURE 12.5: LGAD read-out boards: UCSC single-channel version (left), UCSC four-channel version (centre) and KU two-channel version.

### 12.3.2 Time reference system

To perform timing measurements with the DUTs, a time reference system with a resolution similar to or better than that of the DUT is needed. The chosen system [279] consists of a SiPM coupled to a quartz bar assembled in a light-tight housing. The full assembly is attached to a custom read-out board designed at Institut de Física d'Altes Energies (IFAE). The measured time resolution from this time reference system was found to be 39.0(22) ps for an operating voltage of 27.8 V. After hundreds of hours in operation and under beam exposure in several beam tests, an increase in the SIPM leakage current was observed. Thus, a reduced voltage of 27.6 V was applied and the corresponding time resolution was found to be 63.3(9) ps. This time reference system was tested together with the DUTs and with an additional unirradiated LGAD, LGA35 (see Table 12.1), which has a well-known performance and was also used as a reference in the evaluation of the time resolution performances (See Section 12.5).

### Quartz bar

A 6-side polished quartz bar of size $3 \times 3 \times 10$ mm$^3$ was used as a medium where the traversing charged particles generate photons through the Cherenkov effect. To maximize the photon transmission efficiency, the chosen quartz is suitable for ultraviolet (UV) light where the Cherenkov spectrum peaks. A transparent optical grease[3] was selected for the interface quartz-SiPM window which is also optimized for blue light detection [283].

### SiPM

A SiPM detector[4] was chosen due to its extremely high sensitivity, high efficiency and very low time jitter. It has an active area of $3\,\text{mm} \times 3\,\text{mm}$ made of $50\,\mu\text{m}$ micro-cells interconnected in a parallel manner [284], providing a 72% fill factor. The sensor is encapsulated on a $4\,\text{mm} \times 4\,\text{mm} \times 0.7\,\text{mm}$-thick SMT package [283] and is integrated into an evaluation board which can be easily mounted via pin headers (Figure 12.6) [285]. This design allows a fast replacement which is useful since after its use in several beam test campaigns its performance degrades due to the particle fluence.

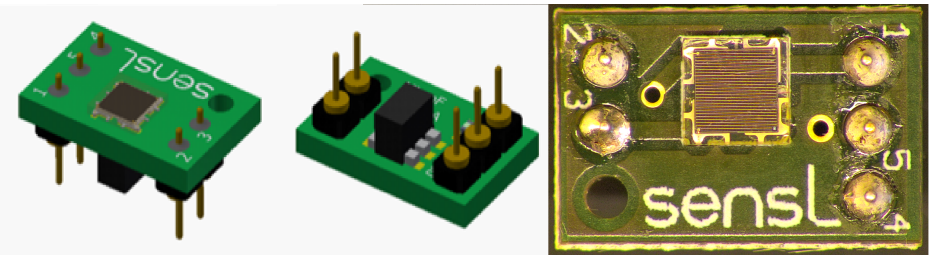


FIGURE 12.6: SiPM evaluation board (3D schematics and picture).

### Light-tight support

The SiPM and the quartz assembly needed both mechanical support and optical isolation from the environment to achieve efficient photon detection. A light-tight enclosure was designed at IFAE and 3D printed using black PLA plastic with a 90% fill factor at IJCLab. The support as shown in Figure 12.7 consists of two parts:

- a main cubic unit with a hole allowing the insertion of the quartz bar and the attachment via a screw of the SiPM evaluation board at the back face
- a cover for fixation via two screws and optical isolation of the quartz bar at the front face

[3] Bluesil Paste 7 from Silitech AG.
[4] MicroFC-30050-SMT model from SensL Technologies TM.

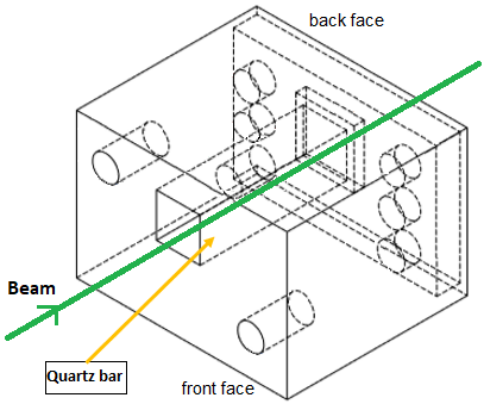


FIGURE 12.7: SiPM light-tight support design of the main unit.

### Read-out board

The SiPM evaluation board does not include any amplification stage. Therefore, a read-out board was designed at IFAE for this purpose using a commercial amplifier [286], providing a 2 GHz bandwidth with a gain of 10 at a nominal operating voltage (12 V). In addition, the position of the SiPM-quartz assembly in the board was chosen to be aligned with the LGADs on their respective read-out boards. To avoid high-frequency electromagnetic interference a metal shield encloses the amplifier and filtering circuitry (Figure 12.8 (left)).

## 12.3.3 Beam tracking system

The alignment of the DUTs was provided by custom-made L-shape supports where the LGAD read-out boards could be mounted back-to-back in pairs on a base plate. As explained earlier, at CERN, the set-up was placed in a thermally isolated enclosure whereas at DESY it was mounted on a light-tight cooling box. In both cases, the position of the assembly was remotely controlled by a micrometric $x - y$ motor stage in the perpendicular plane to the beam axis ($z$ direction). In this way, DUTs were precisely positioned inside the beam profile of a size of about $2 \times 2$ cm$^2$. Position-dependent measurements were possible to perform with the use of a EUDET-type telescope [278] consisting of two equidistant arms, each comprised of three MIMOSA pixel planes. Each MIMOSA plane has an area of $10.6 \times 21.2$ mm$^2$ and is composed of pixels with a size of $18.5 \times 18.5$ $\mu$m$^2$, providing particle track information with a resolution of a few micrometres. DUTs were placed in

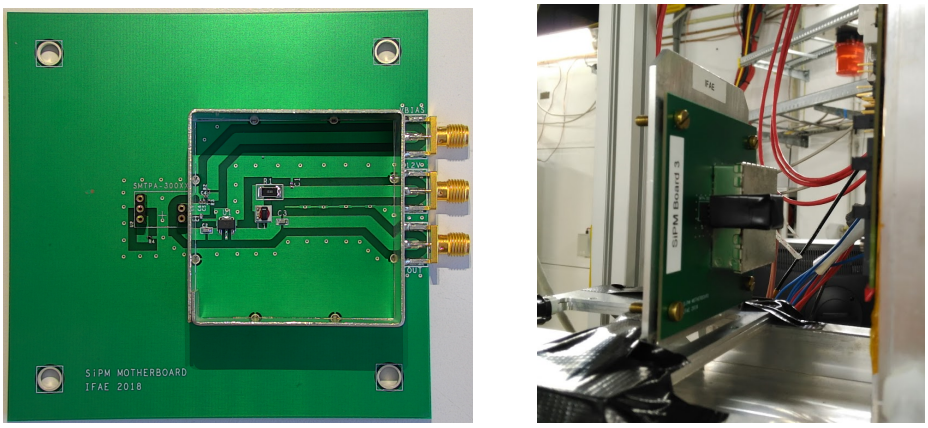


FIGURE 12.8: SiPM PCB without metal cover (left) and full assembly at the test beam (right).

the space available between the two telescope arms as shown in Figure 12.9. Two intersecting plastic scintillators coupled to photomultiplier tubes were also integrated at each extremity of the telescope and used in the trigger scheme. An additional pixel reference plane, using the FE-I4 [287] read-out chip, was also positioned at the end of the second telescope arm and served for DUT alignment as well as for triggering purposes. The dimension of the FE-I4 plane is $16.8 \times 20.0$ mm$^2$ with a pixel size of $50 \times 250$ $\mu$m$^2$. The time reference system described before was placed after the pixel reference plane. At CERN, this system was mounted outside the telescope structure and it was aligned with respect to the beam by using a remote control positioning stage[5] whereas at DESY it was mounted directly on the telescope structure, being already aligned with the MIMOSA and pixel reference planes.

### 12.3.4 Data acquisition and trigger scheme

Signals from DUTs were registered by a four-channel oscilloscope (the first 3 channels for DUTs and a fourth channel for the time reference signal coming from the SiPM assembly). In the case of data-taking at CERN, two identical $10\,\mathrm{GS\,s^{-1}}$ synchronized oscilloscopes with a 2 GHz bandwidth were used, each of them with an input of a time reference signal from two identical SiPM systems. For data-taking at DESY, only one oscilloscope was used since only three DUTs were tested simultaneously to reduce the multiple scattering.

The trigger and DAQ architecture are presented in Figure 12.10 (top). A region of interest (ROI) on the FE-I4 plane that contained the projected area of the different LGADs and SiPM was defined. It is critical to have an optimal alignment of all the LGADs and the SIPM to perform time measurements. The typical size of the ROI was about the SIPM size, $3\,\mathrm{mm} \times 3\,\mathrm{mm}$. Thus, the implementation of this ROI resulted in a reduced hit rate. The downstream intersecting scintillators in the telescope, the HitOR signal from the FE-I4 plane and the oscilloscope auxiliary output were the input to the EUDET Trigger Logic Unit (TLU) [288]. The oscilloscope needed to have a sufficient time offset to record the signal that arrived previous to the trigger. When the oscilloscope is triggered through the EXT signal coming from the TLU (event), it emits a TTL pulse that is sent back to the TLU module for synchronization of the telescope and FE-I4 DAQ system (NI-Crate using EUDAQ [289] and USBPix/MMC3 [290]) with the HGTD DAQ system (oscilloscope). The oscilloscope has a dead time of approximately 10 s caused by the buffer read-out, which at CERN SPS was granted by the time in between spills (about 4 s-long, every 16 s). At DESY, a NIM logic circuit was implemented to generate a busy signal (20 ns-long veto pulse) from the oscilloscope for the TLU. Figure 12.10 (bottom) shows the busy signal implementation scheme.

Two independent data streams were recorded, one containing particle position information from the telescope and the FE-I4 while the second containing waveform signals from the DUTs registered by the oscilloscope. These two data streams were merged offline for further analysis (See Sections 12.4 and 12.5.

[5] Stage system from Physik Instrumente (PI).

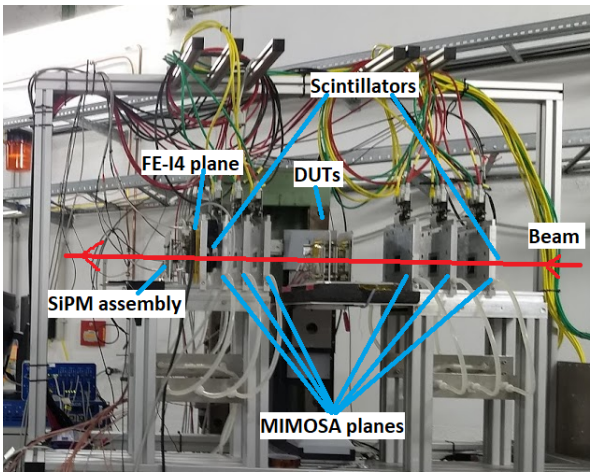


FIGURE 12.9: Beam telescope infrastructure at DESY including scintillators for triggering, a pixel reference plane, a time reference system based on a SiPM and LGAD sensors as DUTs.

## 12.4 Data analysis approach

As mentioned in the previous section, two independent systems were used to collect the data used in this analysis: the oscilloscope provided data on the LGAD and SIPM waveforms while the telescope on the particle track information. This section describes the general methodology used to reconstruct and process the information from these two chains, and how it was used to derive the physical quantities of interest for the analysis.

### 12.4.1 Waveform processing

This procedure is described in several steps as it is done in [291]. The first step was to convert the oscilloscope binary data into a ROOT ntuple containing the raw waveform information of each DUT which was sampled with a time bin of 25 ps. Figure 12.11 shows a typical LGAD signal. The second step was the determination of the pulse polarity, the maximum, the minimum, the start and the stop points of the signal. With this information, a check if the complete pulse was within the oscilloscope acquisition window was made. The third step was to compute the pedestal and the noise in the range from the 10 % to 90 % points before the start of the pulse. They were defined as the mean and the standard deviation of a Gaussian fit, respectively. Subsequently, the value obtained for the pedestal was subtracted from all the data points of the waveform, on an event-by-event basis. The minimum, maximum, start and stop points were then re-calculated. The maximum of the waveform was determined from the sample with the highest amplitude. The fourth step was the computation of several waveform properties such as the charge, the rise time, the jitter, the signal-to-noise ratio and the Time Of Arrival (TOA) at different thresholds.

For each event, the charge, $q$, was determined by dividing the integral of the pulse (see Figure 12.11) by the trans-impedance of the read-out board, $R_b$, and the gain of the voltage amplifier, $G_{ampl}$:

$$q = \frac{\int_{start}^{stop} A\, dt}{R_b \times G_{ampl}} \tag{12.1}$$

Several methods to reconstruct the TOA have been studied [271], the analysis presented in this thesis uses the Constant Fraction Discriminator (CFD) method: the TOA is defined as the point in which the signal crosses a predefined fraction, $f_{CFD}$, of its total amplitude. To obtain the time resolution, the TOA value at $f_{CFD}$=20% will be used for the time references and the unirradiated

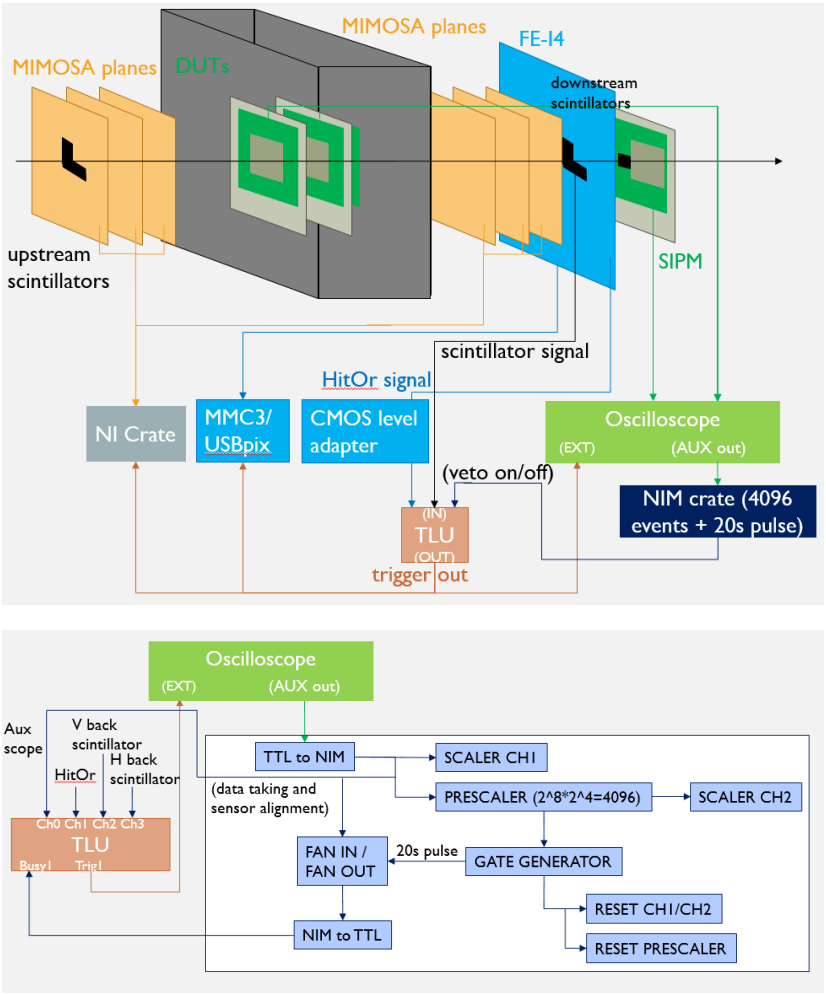


FIGURE 12.10: DAQ and trigger scheme (top) and busy signal scheme (bottom).

DUTs whereas for the irradiated DUTs the TOA value will be at $f_{CFD}$=50%. The impact of this choice on the time resolution estimate is discussed in Appendix 12.6.

The last step was to produce a merged file containing the oscilloscope data together with the telescope-reconstructed data (see next Section) for user analysis.

### 12.4.2 Track reconstruction

The telescope together with the FE-I4 provided the tracking information that allowed us to reconstruct the trajectory of the particles and to identify the specific position where the DUT has been hit. The tracking capability of the telescope was provided by six MIMOSA planes as explained in Section 12.3.3. The positions of the MIMOSA, FE-I4 and DUT planes were known with a precision of 1 mm in the $z$ direction along the beam line. The position of the hits from each MIMOSA plane, together with their respective $z$ coordinate, were used to reconstruct the particle trajectory and the ($x$,$y$) coordinates of the hit on the DUT planes.

After the removal of "hot" pixels from the MIMOSA planes, identified as the ones with an occupancy higher than ten times the average one, the remaining hits were grouped into clusters. Only clusters with a maximum of 6 hits were used for tracking. In the FE-I4 plane, a cluster was required to have a maximum of 2 neighbouring hits. The cluster coordinates were the centroid of the hit coordinates in $x$ and $y$. Only events with exactly one cluster in the FE-I4 were then considered. The MIMOSA planes were aligned by iteratively shifting the plane's coordinates in the $x$ and $y$ direction

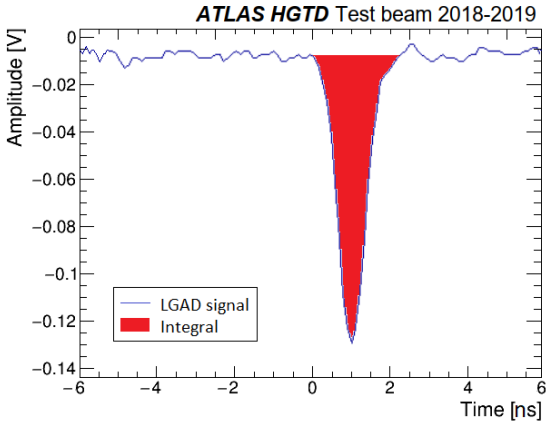


FIGURE 12.11: Recorded waveform from an LGAD. The integral of the signal is denoted by the red area.

with respect to a reference plane. This procedure aimed to minimize the difference between the reconstructed track position at the MIMOSA plane and the measured hit position in the same plane. The position resolution was taken as the resolution of the fit performed during the alignment procedure.

For data collected at CERN SPS, the following track-fitting procedure was applied. Given the $z$ position of the MIMOSA planes along the beam axis and the $x$ and $y$ positions of the hits in these planes, 3D tracks were built from the six planes of the telescope starting with the planes closest to the FE-I4 [271]. The reconstructed tracks must coincide with a hit in the FE-I4 plane and only events with a single reconstructed track through the six MIMOSA planes were considered. The track fitting procedure was slightly different for data collected at DESY in order to take into account the differences in the experimental set-up and the beam type. The tracking procedure was initialised in the upstream MIMOSA planes, and no matching requirement between the extrapolated track and the FE-I4 cluster was applied [292, 293]. Events with more than one candidate track were retained if the candidate tracks were compatible with kinks from multiple scattering from a single track.

Once the tracks have been reconstructed, their trajectory was evaluated at the $z$ coordinate of the DUTs, to determine the $(x,y)$ coordinates of the hit and this information was saved into a file. The precision on the position of the extrapolated reconstructed track in the DUT planes was about 3 µm in the $x$ and $y$ directions.

## 12.5 Sensors performance results

The study presented in this thesis aims to evaluate the LGAD sensor performances, before and after irradiation, with particle beams using the reconstructed position of the tracks. The following LGAD properties have been investigated: the collected charge, the time resolution and the hit reconstruction efficiency.

In the subsequent analyses, two types of cuts were applied to remove the background events (Figure 12.12). A geometrical cut based on the position where the DUT or the time references (LGA35, SIPM) were located inside the FE-I4 ROI, and a timing cut using a 2 ns window from the maximum point of the time difference distribution between the TOA of the DUT and SIPM read out by the same oscilloscope. As mentioned in Section 12.4, the TOA was determined for all of the devices with the CFD method, where the values at $f_{CFD}$ =20% for the unirradiated DUTs and the references and at $f_{CFD}$ =50% for the irradiated DUTs were considered. Figure 12.12 shows the reconstructed tracks inside the FE-I4 ROI at the DUT plane before (left) and after (right) the timing cut. After applying

the cleaning selections in geometry the retained events correspond to reconstructed tracks inside the FE-I4 ROI that are crossing the DUT.

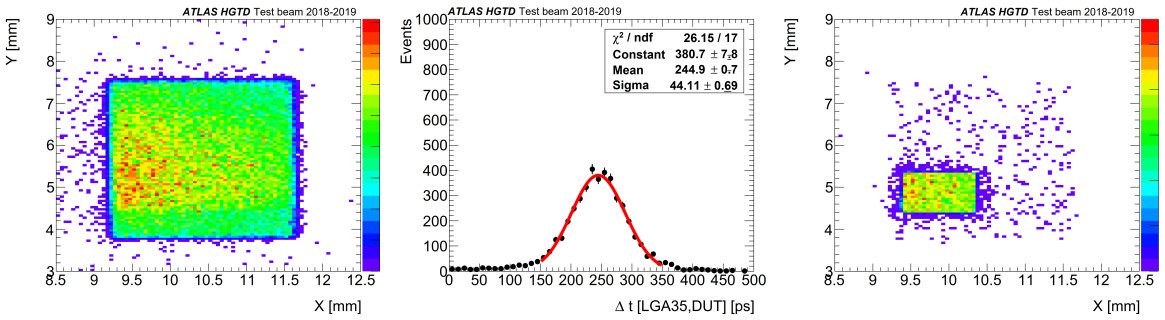


FIGURE 12.12: Reconstructed tracks inside the FE-I4 ROI at the DUT plane before (left) and after (right) a timing cut was applied. Time difference distributions between the DUT and LGA35 (centre).

To guide the interpretation in terms of irradiation fluence, in the presented figures points corresponding to the same fluence will be shown in the same colour. Solid markers correspond to neutron irradiation and empty markers correspond to proton irradiation. Black points either solid or empty markers correspond to unirradiated DUTs.

### 12.5.1 Collected charge

From the retained events after applying the cleaning cuts, a distribution using the charge derived from Equation 12.1 was obtained for each DUT and it was fitted with a Landau-Gaussian convoluted function. The collected charge reported for each sensor is defined as the Most Probable Value (MPV) from this fit and designated as Charge$_{MPV}$ for later calculations. As an example, Figure 12.13 shows a charge distribution of Carbon S1p operated at a bias voltage of 220 V, before (left) and after (right) the cleaning selections. Figure 12.13 (right) also includes the resulting fit function with an MPV of 9.8 fC. The negative charge remaining after the cleaning cuts results from noise events or fluctuating signals from particles hitting the edge of the sensor.

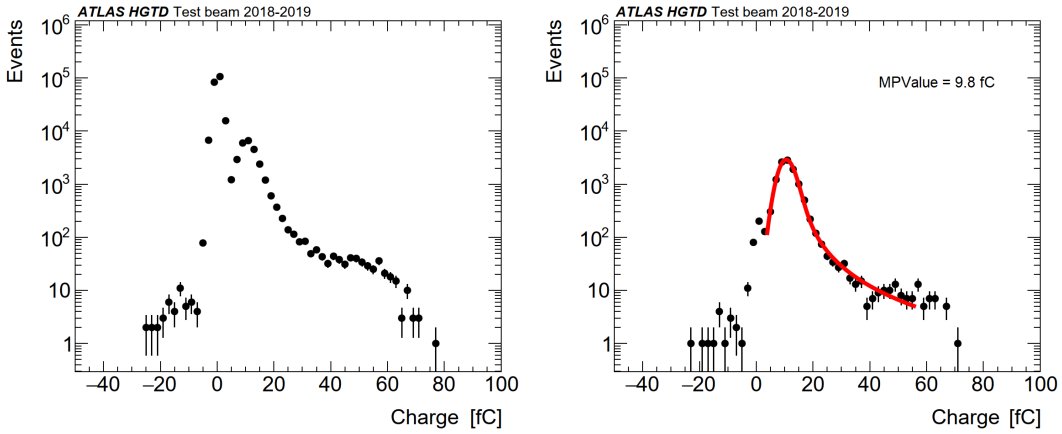


FIGURE 12.13: Charge distribution for Carbon S1p operated at a bias voltage of 220 V before (left) and after (right) cleaning cuts. The right figure also includes the Landau-Gaussian fit.

Figure 12.14 show the results for CNM and HPK sensors, respectively. Unirradiated sensors always have high collected charges, even if they are operated at low bias voltages. Irradiated sensors yield a lower collected charge than unirradiated devices at the same bias voltage and they require

a higher bias voltage to obtain similar performance. The gain of the sensors is reduced with the irradiation, the higher the fluence the higher the bias voltage needed to obtain the minimum required charge of 4 fC to provide a good timing. The three types of CNM sensors were irradiated at a fluence of $10^{14}$ $n_{eq}/cm^2$ with neutrons (S1n DUTs) and protons (S1p DUTs). By comparing them, neutron-irradiated DUTs show better performance at the same bias voltage. In particular, Carbon S1n collects more charge than Boron S1n whereas Gallium S1n need more voltage to get the same amount of charge. This is in agreement with laboratory data [294]. Unirradiated DUTs, Boron S6n and Gallium S30n were not operated at higher voltages to prevent the early death of the sensor. For HPK sensors, 3.2 A does not perform properly at low temperatures and could not be operated at voltages higher than $-70$ V because it presented self-triggering [251, 294]. However, after irradiation type-3.2 performs better than type-3.1 as is seen in the case of 3.2 S8n which requires less voltage to achieve the same performance as 3.1 S8n. Type-3.2 has a deep and high-dose multiplication layer, which leads to a reduced acceptor removal rate. Therefore, the gain is higher at the same voltage for the same irradiation level. Figure 12.14(right) for HPK 3.2 sensors is in agreement with Figure 5.8 (a) in [251].

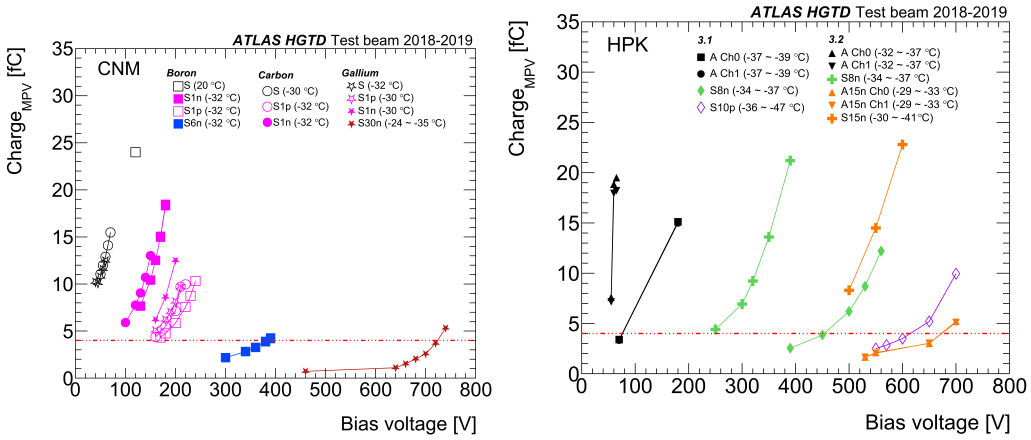


FIGURE 12.14: Collected charge as a function of the bias voltage for CNM Boron, Carbon and Gallium sensors (left) and HPK 3.1 and 3.2 sensors (right). The horizontal line represents the HGTD requirement of a minimum collected charge of 4 fC.

### 12.5.2 Uniformity

To study how uniform is the charge within the pad of the sensors, a two-dimensional (2D) map of the occupancy as a function of the reconstructed particle position in the DUT plane was built. To increase the number of events and provide a simpler interpretation of the results, the uniformity of the charge was evaluated in the $x$-axis while integrating over the $y$-axis. This was done by dividing the sensor active area into ten bins of $0.1 \times 1$ mm$^2$ as shown in Figure 12.15 (left). The collected charge in each bin $k$, $\text{Charge}_{MPV_k}$, was computed. As an example, Figure 12.15 (right) shows the charge distribution in one bin together with the Landau-Gaussian function fit for DUT Carbon S1p.

The uniformity of the charge was evaluated for each DUT at the maximum applied voltage. As shown in Figure 12.14, the collected charge varies with the bias voltage and with the irradiation level. To compare sensors with different collected charges, the value computed in each bin is normalized to the collected charge of the sensor. Thus, the uniformity of the charge along the $x$-axis is calculated as a relative charge defined as:

$$\text{Relative Charge} = \frac{Charge_{MPV_k}}{Charge_{MPV}} \tag{12.2}$$

Figure 12.16 shows the uniformity for the CNM sensors while Figure 12.17 shows for the HPK ones. The uniformity in the $y$-axis was also checked and was found to be similar. Small deviations are

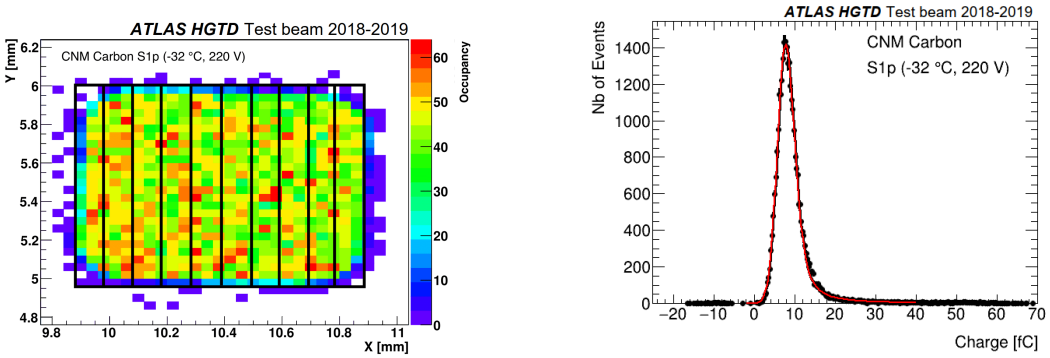


FIGURE 12.15: 2D map of the hit occupancy as a function of the reconstructed particle position in the DUT plane for Carbon S1p operated at a bias voltage of 220 V (left). The black boxes correspond to the bins along the $x$-axis. Charge distribution computed in a bin size of $0.1 \times 1$ mm$^2$ (right).

observed for the unirradiated and low-fluence CNM sensors. The uniformity of Carbon S1p shows larger deviations, which stay within 10% of the average and therefore are not considered significant. Similarly, the uniformity of Gallium S30n presents a spread within 5% on most of its surface. The tested HPK sensors show a very good uniformity at all fluences. At the highest fluence, for A15n-ch0 the relative charge decreases at the edges much more than for the other DUTs. In general, for both vendors, larger deviations can be appreciated in the periphery of the sensors due to edge effects.

### 12.5.3 Time resolution

The time resolution is one of the key parameters when assessing the sensor performance. It can be determined by:

$$\sigma^2_{LGAD} = \sigma^2_{Landau} + \sigma^2_{Timewalk} + \sigma^2_{Jitter} \tag{12.3}$$

The Landau fluctuations, $\sigma_{Landau}$, are caused by non-uniformities in energy deposition along the particle path inside the sensor. While this effect is reduced by decreasing the thickness of the sensor, thinner sensors suffer from large capacitance and low deposited charge. Therefore, a compromise must be made. The time walk effect, $\sigma_{Timewalk}$, is explained by the fact that signals with different amplitudes reach a fixed discriminator at different times. This effect can be mitigated by using specific reconstruction techniques. The jitter term, $\sigma_{Jitter}$, is instead proportional to the presence of electronic noise and to the rise time, while it is inversely proportional to the signal slope.

For all the combinations of DUTs and references tested simultaneously, a distribution of the TOA differences can be built and used to extract the DUT time resolution. The width of the time difference distribution between device $i$ and $j$ will be given by:

$$\sigma_{i,j} = \sigma_i \oplus \sigma_j, \tag{12.4}$$

where $\sigma_i$ and $\sigma_j$ are the individual time resolutions of the two devices, and $\sigma_{i,j}$ is estimated as the width of a Gaussian function fit.

When exactly three devices are considered, it is possible to solve the system of three equations and derive the individual time resolutions by measuring the resolution of several time differences. For example, considering two references and a DUT, the time resolution of the DUT can be extracted as:

$$\sigma_{DUT} = \sqrt{\frac{\sigma^2_{DUT-Ref1} + \sigma^2_{DUT-Ref2} - \sigma^2_{Ref2-Ref1}}{2}} \tag{12.5}$$

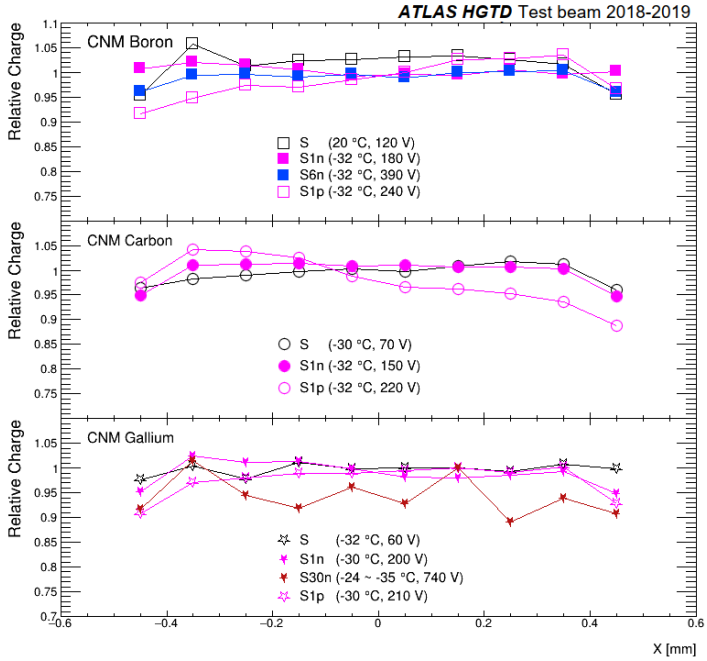


FIGURE 12.16: Relative charge along the $x$-axis for CNM Boron, Carbon and Gallium sensors, indicating the temperature and the bias voltage of operation.

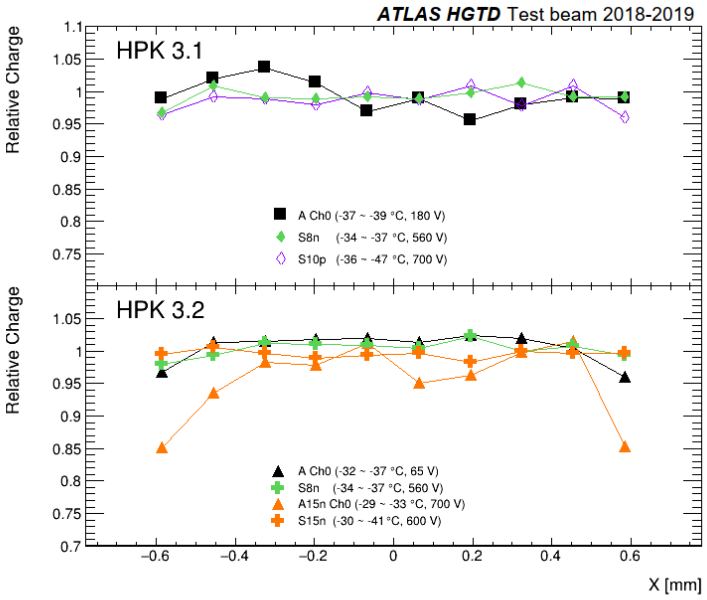


FIGURE 12.17: Relative charge along the $x$-axis for HPK 3.1 and 3.2 sensors, indicating the temperature and the bias voltage of operation.

When more than three devices are considered simultaneously, the system is over-constrained and one way to determine the value of the individual time resolutions is through a $\chi^2$ minimization:

$$\chi^2 = \sum_{i=1}^{N} \sum_{j=1}^{j<i} \frac{(\sigma_{ij}^2 - \sigma_i^2 - \sigma_j^2)^2}{\sigma_{\sigma_{ij}^2}^2} \tag{12.6}$$

For each DUT, the two references (LGA35 and SIPM) were used to compute its time resolution using Eq. 12.5. An example of a time difference distribution together with the Gaussian fit function used to extract the resolution was shown in Figure 12.12 (centre).

Figure 12.18 shows the time resolution as a function of the bias voltage for CNM and HPK sensors, respectively. Both figures show an improvement in the time resolution with higher bias voltages. For Gallium sensors in Figure 12.18 (left), at 200 V, both neutron- and proton-irradiated at a fluence $10^{14}$ $n_{eq}/cm^2$ were tested. DUT Gallium S1n achieves a time resolution of 27.4 ps, this type of radiation, therefore, causing less damage than the proton one, for which DUT Gallium S1p achieves a time resolution of 38.3 ps at the same bias voltage. The same conclusion can be obtained for Carbon sensors in the bias voltage range of 150 V to 160 V, where both neutron- and proton-irradiated sensors were tested and the neutron-irradiated one shows a better performance.

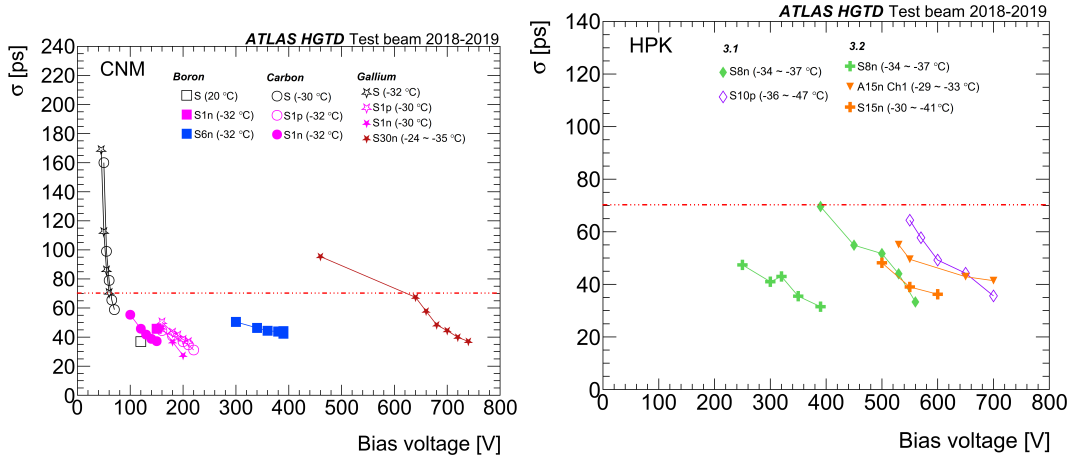


FIGURE 12.18: Time resolution as a function of the bias voltage for CNM Boron, Carbon and Gallium sensors (left) and HPK 3.1 and 3.2 sensors (right) .

Gallium S30n reaches the target time resolution at expense of being operated at a rather high voltage. Detailed studies on the uniformity of the time resolution within the pad for this sensor are included in [277].

Figure 12.18 (right) for HPK 3.2 sensors agrees with Figure 5.11 (a) in [251]. At $8\times10^{14}$ $n_{eq}/cm^2$, HPK 3.2 performs better than HPK 3.1. For HPK sensors, a conclusion on the impact of the irradiation type on the sensor performance cannot be made. DUT 3.2 S8n achieves the best resolution of about 30 ps at 400 V.

The time resolution together with the collected charge obtained in Section 12.5.1, allows for defining the best operating voltage point for each sensor and irradiation level. Looking at these two key parameters in Figure 12.19, only for irradiated DUTs from both vendors, all sensors follow the same trend. This figure is in agreement with Figure 5.8 (a) in [251] for HPK 3.2 sensors. The plot is divided into four regions where LGADs meeting the HGTD requirements in terms of collected charge $>4$ fC and time resolution $<70$ ps appear in the bottom right area.

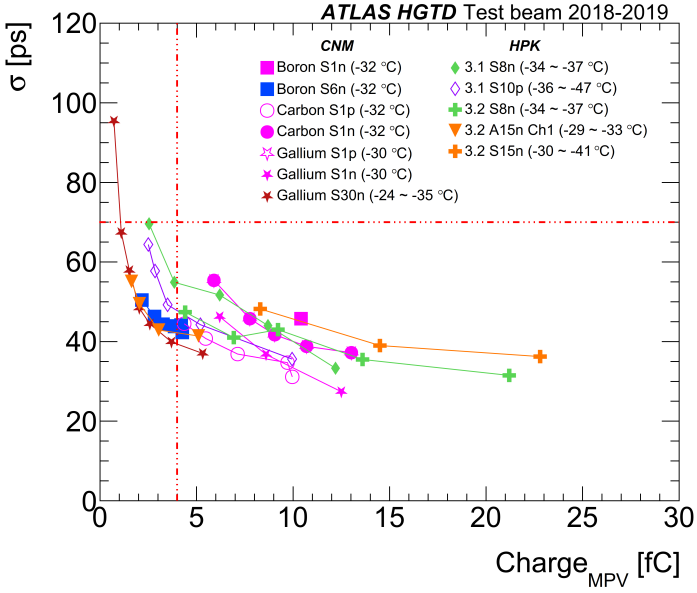


FIGURE 12.19: Time resolution as a function of the collected charge for irradiated CNM and HPK sensors.

### 12.5.4 Hit reconstruction efficiency

The hit reconstruction efficiency is defined as the reconstructed tracks giving a signal on the sensor for which the charge in the sensor is greater than a given threshold value, $Q_{cut}$, divided by the total number of reconstructed tracks crossing the sensor:

$$\text{Hit Efficiency} = \frac{\text{Reconstructed tracks with } q > Q_{cut}}{\text{Total reconstructed tracks}} \tag{12.7}$$

To avoid the effect of the edge of the sensor, the global efficiency values sensor are computed in the central $0.5 \times 0.5$ mm$^2$ region of the DUT, representing a quarter of its surface for the CNM sensors and less than a quarter of its surface for the HPK sensors.

The efficiency as a function of the charge threshold at the highest operating voltage is shown in Figure 12.20 for CNM and HPK sensors, respectively. All DUTs do not get the same amount of charge at their maximum operating voltage, thus, the charge threshold results in a more dramatic efficiency drop in the cases with low collected charge. This is the case of DUTs irradiated with a fluence greater than $6 \times 10^{14}$ $n_{eq}$/cm$^2$, where the efficiency decreases as the charge threshold increases. This can be seen in Figure 12.20 (left) for Boron S6n where the efficiency decreases from 99.7% to 52.4% at 390 V when the charge threshold varies from 0.5 fC to 5 fC. In this case, the sensor was operated at a moderate voltage and the collected charge was rather low (4.26 fC). Similarly, for Gallium S30n the efficiency decreases from 99.9% to 74.7% at 740 V when the charge threshold varies from 0.5 fC to 5 fC, where the collected charge is 5.31 fC. For less irradiated DUTs, the efficiency as a function of the collected charge threshold is more constant as can be seen for other DUTs represented in Figure 12.20 (left). In the case of HPK sensors in Figure 12.20 (right), the efficiency for both type-3.1 and type-3.2 remains constant as the charge threshold increases. At higher fluences, $1.5 \times 10^{15}$ $n_{eq}$/cm$^2$, for DUT 3.2 A15n the efficiency decreases as the charge threshold increases because of its low collected charge of about 5 fC whereas for DUT 3.2 S15n the efficiency remains constant as its collected charge is 22.76 fC.

An efficiency larger than 95% is reached for all the sensors up to a fluence of $3 \times 10^{15}$ $n_{eq}$/cm$^2$ for a charge threshold of 2 fC, corresponding to the discriminator of the ALTIROC.

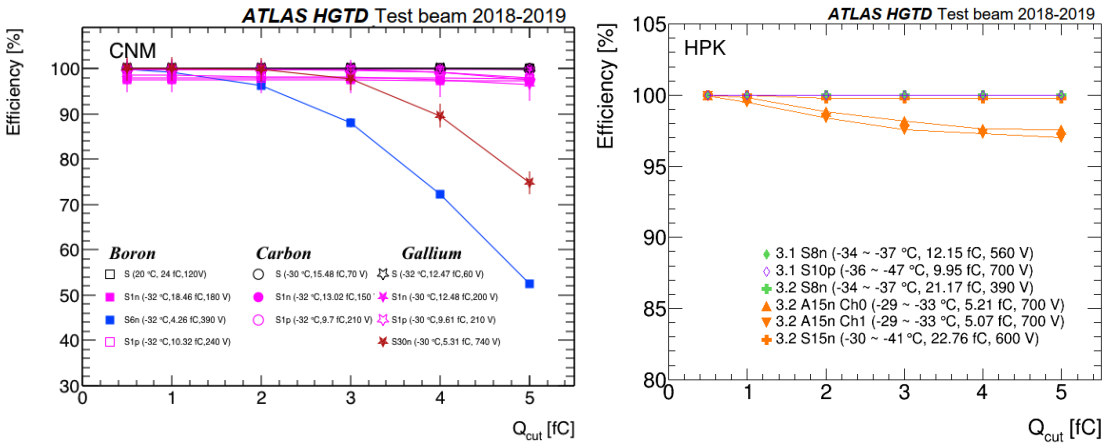


FIGURE 12.20: Efficiency as a function of the charge threshold for CNM Boron, Carbon and Gallium sensors (left) and HPK 3.1 and 3.2 sensors (right).

In order to study the uniformity of the efficiency within the sensor, the efficiency was determined as a function of the hit position of the track on the sensor. In the following studies, the charge threshold was set to 2 fC for all sensors. Figure 12.21 (left) shows the 2D map of the efficiency as a function of the hit position in DUT Carbon S1p and Figure 12.21 (right) in DUT 3.1S10p. On the left plot, the sensor was tested at CERN SPS with a 120 GeV pion beam and using a thermally isolated enclosure with a well-stabilized position in $x - y$ plane whereas the sensor on the right plot was tested at DESY with a 5 GeV electron beam and using a styrofoam box, filled with dry ice, which was moving upwards during data taking due to the evaporation of dry ice. The consequences of the movement/temperature variation and other different factors as the lower beam energy contributes to a more smeared plot.

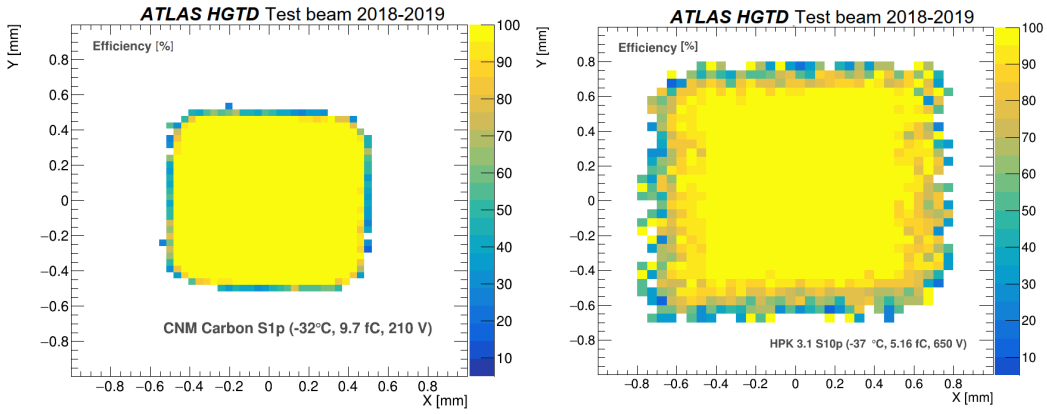


FIGURE 12.21: 2D efficiency map for CNM Carbon S1p (left) and for HPK sensor 3.1 S10n (right).

The effect of the bias voltage on the efficiency was also studied. Figure 12.22 show the efficiency as a function of the bias voltage for CNM and HPK sensors, respectively. To maintain equivalent efficiencies in highly irradiated sensors, the bias voltage has to be increased except in highly irradiated CNM sensors. For the HPK sensors, 3.2 S8n has higher efficiency at lower voltages compared to 3.1 S8n since the gain for type-3.2 is higher at the same voltage, thus achieving higher efficiency earlier.

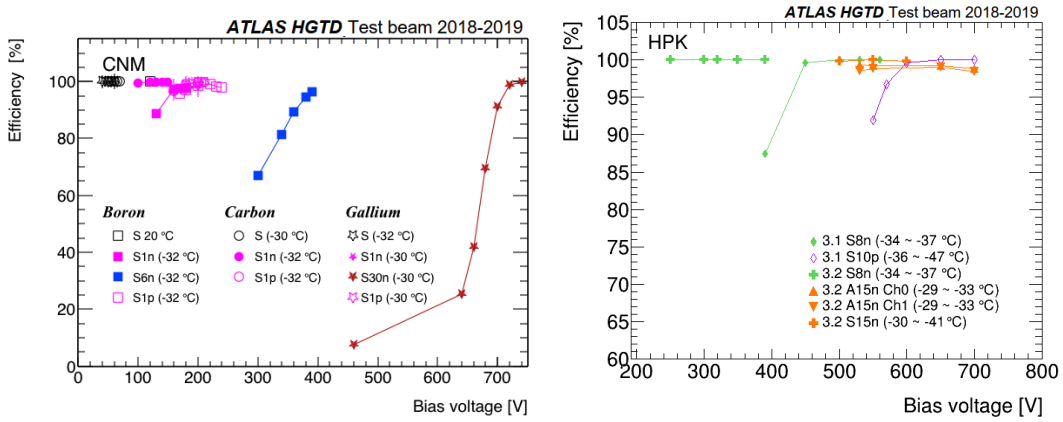


FIGURE 12.22: Efficiency as a function of the bias voltage for CNM Boron, Carbon and Gallium sensors (left) and HPK sensor 3.1 S10n (right). For each data point, the charge threshold is 2 fC.

## 12.6 Impact of the CFD fraction

A study of the time resolution variation for different CFD fractions is presented. The results of this study are used to determine if the CFD fractions, 20% for unirradiated DUTs and references and 50% for the irradiated DUTs, used to calculate the time resolutions in this study are indeed the optimal values achieving the best time resolution. The calculation is carried out by repeating the computation of the time resolution (following the same procedure as for the results in Section 12.5.3) changing each time the fraction used in the CFD method for the DUT and using 12.6.

Figure 12.23 and Figure 12.24 show the time resolution as a function of the DUT CFD fraction for CNM and HPK sensors, respectively. For the unirradiated sensors, the Landau term dominates the time resolution and a low CFD fraction is preferred. For DUT Carbon S1p and operated at a bias voltage of 150 V, the time resolution is significantly better compared to the DUT Gallium S. The Landau term still dominates the time resolution and a low CFD fraction is also preferred. HPK sensors were irradiated at a higher fluence up to $10^{15}$ $n_{eq}/cm^2$. Given the higher noise in these sensors, the effect on the time resolution of the jitter term becomes larger. The measured time resolutions varied from 1.20% to 11.99% for various HPK sensors with CFD fraction in the range from 30 % to 60 %. This interval is identified as the optimal range of CFD fraction for HPK sensors. The 50% CFD fraction used for the DUTs is within the optimal range of CFD fraction for HPK sensors. The fraction of 20% used for the SiPM and the LGA35 is the optimal fraction for the unirradiated devices. The unirradiated, or with low fluence, CNM sensors results in a 5 to 20% change of measured resolution when compared to resolution for the optimal CFD fraction.

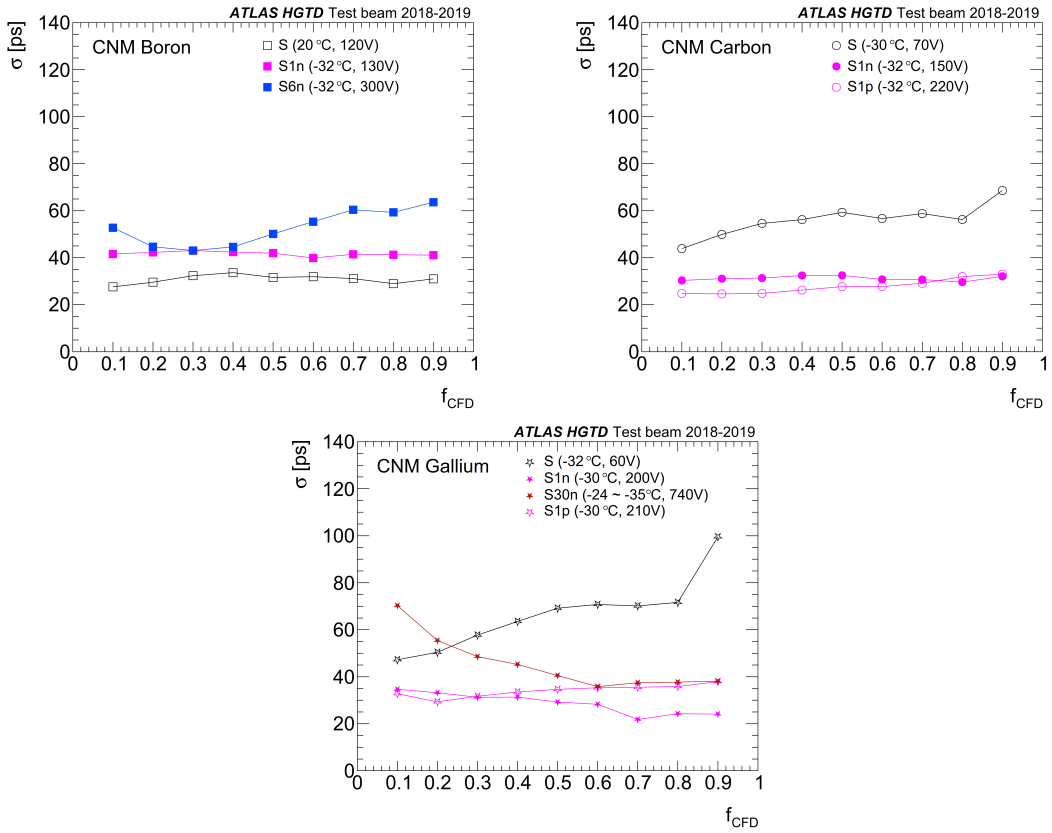


FIGURE 12.23: Time resolution as a function of the CFD fraction for CNM Boron (left), Carbon (right) and Gallium (bottom) sensors.

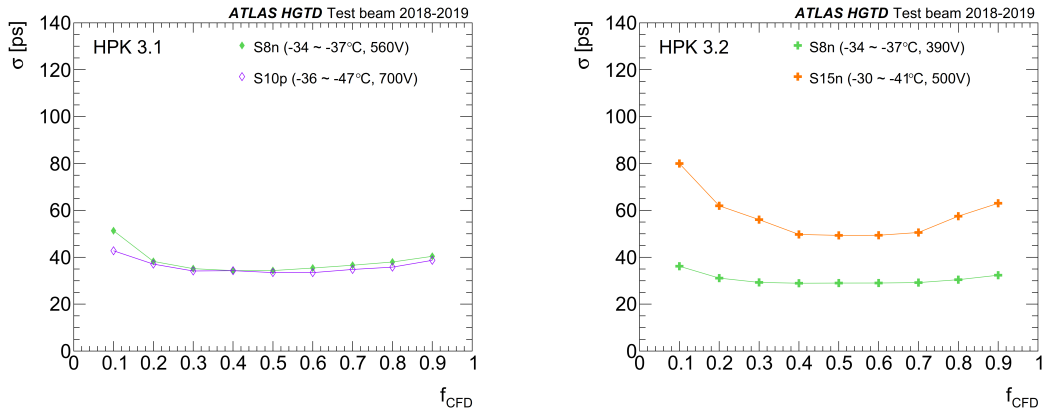


FIGURE 12.24: Time resolution as a function of the CFD fraction for HPK 3.1 (left) and 3.2 (right) sensors.

# Conclusion

This thesis presents two distinct subjects, the first one is related to the search for dark photons with the ATLAS detector at the LHC, and the second presents an upgrade study of the ATLAS detector for the HL-LHC run expected to start in 2029.

For the dark photon section, two different searches were performed at a centre-of-mass energy of $\sqrt{s} = 13$ TeV using the total LHC Run-2 integrated luminosity of 139 fb$^{-1}$ recorded by the ATLAS detector, the first one concerns a search for dark photon candidates arising from semi-visible SM Higgs boson decay $H \rightarrow \gamma\gamma_d$, produced together with a $Z$ boson with the $Z(\rightarrow \ell^+\ell^-)$ ensures a relatively clean signal and high-efficiency lepton triggers. Data-driven techniques are optimized to estimate the main backgrounds from processes characterized by fake $E_{\mathrm{T}}^{\mathrm{miss}}$ and electrons misidentified as photons, while the normalization of the irreducible background is obtained using MC simulations constrained by data in a dedicated control region. Moreover, the sensitivity of the search is enhanced thanks to a Boosted Decision Tree algorithm that permits to construct the optimal kinematic observable. No excess of events above the SM expectation is found. Therefore, limits on the branching ratio of a SM Higgs boson decaying to a photon and a dark photon can be set. For massless $\gamma_d$, an observed (expected) upper limit on BR(H$\rightarrow \gamma\gamma_d$) of 2.28% ($2.82^{+1.33}_{-0.84}$%) is set at 95% CL. For massive $\gamma_d$ the observed (expected) upper limits are found to be within the [2.19-2.52]% ([2.71-3.11]%) range for masses spanning from 1 GeV to 40 GeV.

To broaden the exploration of this predicted dark matter particle, a second search for massless dark photons was carried out considering some heavy Higgs bosons with masses ranging from 400 GeV to 3 TeV, produced either in gluon-gluon Fusion $ggF$ or in Vector-Boson-Fusion $VBF$ modes. The results of this search are presented in terms of exclusion limits on the cross-section times the branching ratio. For a massless dark photon, the exclusion limits at 95% confidence level on the $\sigma \times BR(H \rightarrow \gamma\gamma_d)$ obtained with a simplified shape-fit for the combined $ggF + VBF$ production of the heavy Higgs boson are found to be in the range from 1.44 (1.68 fb) to 24.2 (28.1 fb) observed (expected) respectively, with the highest limit corresponding to the lightest considered boson with a mass of 400 GeV and the lowest limit corresponding to the heaviest considered mass of 3 TeV. Limits for separate $ggF$ and $VBF$ productions as well as intermediate heavy boson masses are provided.

Concerning the upgrade section, after the ongoing *Run 3*, the LHC will be upgraded to provide an even higher instantaneous luminosity. To cope with the challenging environment, a new timing detector called the High Granularity Timing Detector (HGTD) that will be installed in the ATLAS detector to mitigate pile-up effects during the High Luminosity (HL) upgrade of the LHC. The design of the HGTD is based on the use of Low Gain Avalanche Detectors (LGADs), with an active thickness of 50 µm, that allow measuring with high-precision the time of arrival of particles. The HGTD will improve the particle-vertex assignment by measuring the track time with a resolution ranging from approximately 30 ps at the beginning of the HL-LHC operations to 70 ps at the end.

Before the assessment of the module performance, each component is studied separately. This thesis reports performance studies of several unirradiated, as well as neutron- and proton-irradiated, LGAD sensors with different structures, single-pads and $2\times2$ array of pads, from two vendors, CNM and HPK. Beam test measurement campaigns have been done during the years 2018 and 2019 at the CERN Super Proton Synchrotron (SPS) and the Deutsches Elektronen-Synchrotron (DESY). The results obtained with data recorded by an oscilloscope synchronised with a beam telescope which provides particle position information within a resolution of a few $\mu$m such as the collected charge, time resolution, hit efficiency as well as the charge uniformity as a function of the position of the incident particle inside the sensor pad are documented in this section.

For CNM LGADs, different doping materials aiming to have an improvement in radiation hardness are compared. At the same fluence, Boron plus Carbon sensors collect more charge than Boron at the same bias voltage, whereas Gallium sensors collect less charge. The addition of Carbon helps reduce the operating voltage to achieve the same amount of charge. This is extremely important at higher fluences where standard LGADs need a rather high voltage to get a good performance. The replacement of Boron with Gallium does not show clear benefits, thus, this research line is not pursued. This was also confirmed by laboratory measurements.

For HPK LGADs, two different doping profiles were investigated. Type-3.2 operate at a lower voltage and performs better than type-3.1 after irradiation and it was chosen as a baseline in HGTD TDR. The worse performance before irradiation was explained by the high Boron dose. All tested LGADs achieve the HGTD requirement of a collected charge greater than 4 fC for an ALTIROC optimal operation to perform good timing.

The tested sensors reach a time resolution below 40 ps. The hit reconstruction efficiency is greater than 95% at a threshold of 2 fC for all the sensors when operated at the highest voltage point. Test beam results are in agreement with laboratory measurements. Gallium S30n meets the HGTD requirements in terms of collected charge, time resolution and hit efficiency after a fluence of $3\times10^{15}$ $n_{eq}/cm^2$.

# Appendices

# A TRTxAOD Buggy variables

The Transition Radiation Tracker TRT is the outermost and largest of the three sub-systems of the ATLAS Inner Detector. It is designed to operate in the 2T solenoidal magnetic field at the LHC design luminosity ($L = 10^{34} cm^2 s^{-1}$). It is made of thin-walled straw drift tubes of 4 mm diameter with a single hit design resolution of $130 \mu m$ [295]. The TRT consists of about 50000 straws in the barrel region that are mounted in a 32-fold geometry, divided into three layers of modules. The end-cap regions, on the other hand, consist of 320000 straws divided into 14 layers of wheels [296]. The TRT was designed to provide many measurements aimed at increasing the momentum resolution and providing additional particle identification. Its geometry gives on average 30 two-dimensional space-points for charged particles with $|\eta| < 2$ and $p_T > 0.5 GeV/c$. In addition to a significant contribution to the precision of the momentum measurement due to the track length measured, the TRT provides particle identification through the collection of ionization electrons in the active gas and electron-pion discrimination through the production and detection of transition radiation (TR) photons [295].

The xAOD is part of the overall ATLAS EDM, thus the TRTxAOD is a special extended xAOD format used in the TRT system. During the past, several discrepancies have been observed when comparing similar information included in the xAOD data format and the calibration ntuples derived from ESD's. Among the known issues was the one related to the drift circle error variable which was not correctly filled in the xAOD. The systematic study presented in this appendix succeeded in identifying the origin of these differences and correcting the drift circle error variable in the xAOD. Hence the provided fix of deactivating track slimming in MC xAODs gives significantly better agreement for the variables in the xAOD and ESD ntuples that had disagreed.

TRTxAOD Buggy variables or TRT reconstruction software validation is a qualification task that was crucial for tracking studies as it essentially strives to prove compatibility when going from ESD to xAOD event data model formats. The aim was to first identify these TRTxAOD buggy variables by comparing all relevant ones in xAOD and ntuple data. The origin of the problem behind discrepancies in these variables needed to be fully understood through a systematic study. A fix was then provided and a full validation was performed using data and MC TRT samples.

## A.1 Run-2 Event Data Model

During the 2013–2014 shutdown of the Large Hadron Collider, ATLAS switched to a new event data model for analysis storing its data using xAOD format [297], which can be created and read in standalone ROOT. It is produced as the result of the Athena-based reconstruction, used as both input and output for physics group productions and allows reduction of content without changing the format [298]. The MC production requires going through several steps:

- Event generation: Creation of particle with a certain four-momentum, EVGEN.
- Simulation: Propagation of particles through the detector, HITS.
- Digitization: Calculation of detector response to particles, RDO.
- Reconstruction: Turning detector hits into tracks, energy deposits, particle hypotheses, ESD.
- Derivation: Adding and removing objects & variables, the output format generated in this step is (AOD, xAOD).

On the other hand, raw data is the equivalent of MC RDO, starting directly at reconstruction.
TRTxAOD production (MC and data) usually requires running Reconstruction and Derivation steps on MC, data production shown below (in special cases, Digitization might be needed as well).

## A.2 Track slimming

One important aspect of tracking EDM is the size that the written data takes when being stored on disks. This is far less trivial than it first sounds: on the one hand, small persistent representations of the tracking EDM are necessary to comply with the computing budget of the experiment, but on the other hand, as much information as possible should be accessible for the physicist to allow optimal event analysis techniques. In the context of tracking EDM, a major step towards achieving a good balance between disk size and usability was to identify all information that can be recreated when the track is read back from disk storage. In principle, this includes all fitted parameters and estimated covariances, but excludes the hit collection. A simple refit such as a slimmed track after it has been read from the persistent storage would recreate the full track information as achieved in the original event reconstruction. The flexible TSOS(TrackStateOnSurface) container design of the Track class was hereby a key feature since it allows the creation of a track collection of stripped hits and a Perigee representation that is then written to disk. The track collection size could be significantly reduced (depending on the track collection, the reduction factor varies between 6 to 10) [299].

## A.3 Samples, event and track selection

This study was done using TRTFramework,v1.6 and AnalysisBase,21.2.5, two ntuples (data&MC), four xAOD samples (data&MC) with and without Track slimming, produced by Philippe Calfayan.

- Data and MC ntuples:/eos/user/h/heljarra/Ntuple
  calibNtuple_data18_v2.root ; calibNtuple_mc_v2.root
- xAOD track slimming deactivated: /eos/user/h/heljarra/xAOD/notrkslimming
  TRTxAOD_data18_v2.pool.root; TRTxAOD_mc_noTrkSlim_v3.pool.root

- xAOD track slimming activated: /eos/user/h/heljarra/xAOD/trkslimming
  TRTxAOD_data18_trkSlim_v3.pool.root; TRTxAOD_mc_v2.pool.root

The Base configuration file of TRTFramework used for TRT analyses consisting of event and track selection was updated to become :

- TRTAnalysis - General setup
  GRL.UseGRL: NO
  RemoveEventOverlap: YES
  SkipTriggers: NO
  PixHits: 1
  SiliconHits: 7
  TRTHits: 15

- Lepton Requirements
  LepHandler.ElectronPtCutGeV: 10
  LepHandler.ElectronAbsEtaCut: 2.0
  LepHandler.MuonPtCutGeV: 10
  LepHandler.MuonAbsEtaCut: 2.0
  LepHandler.TrackPtCutGeV:0 #it was 10
  LepHandler.TrackAbsEtaCut: 2.0

## A.4 Results

### A.4.1 searches for TRTxAOD buggy variables

During this study, a systematic check was done for all TRTxAOD variables and the corresponding ones in ntuples. This comparison resulted in 3 classes of variables: non-problematic ones not needing any correction, variables with naming issues in the 2 data formats and finally variables which are different (buggy) and need to be corrected.

#### TRTxAOD non-problematic variables

Variables presenting a good agreement in xAOD-Ntuple comparison, both in data and MC, are non-problematic and don't need any correction. They are highly related to TRT geometry, like bec, layer, phi_module, strawlayer, strawnumber, TRTboard, TRTchip, t0, tot, isHTh, driftTimeToTCorrection, driftTimeHTCorrection, gasType. Figures[A.1, A.2, A.3, A.4, A.5, A.6, A.7, A.8, A.9, A.10, A.11, A.12, A.13] show the comparison for all these variables.

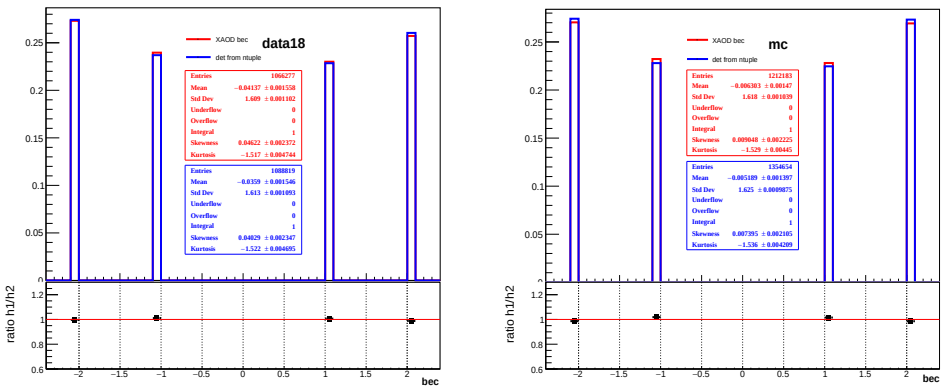


FIGURE A.1: bec(Barrel/EndCap) form xAOD which is det("Detector part") in ntuple and it takes -1,1 for Barrel, 2 for End-cap A and -2 for End-cap C.

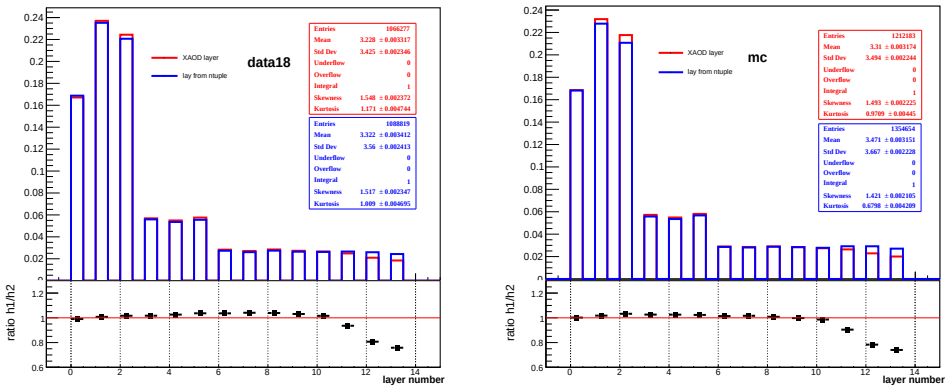


FIGURE A.2: Layer number (Barrel [0-2]; End-cap [0-13].

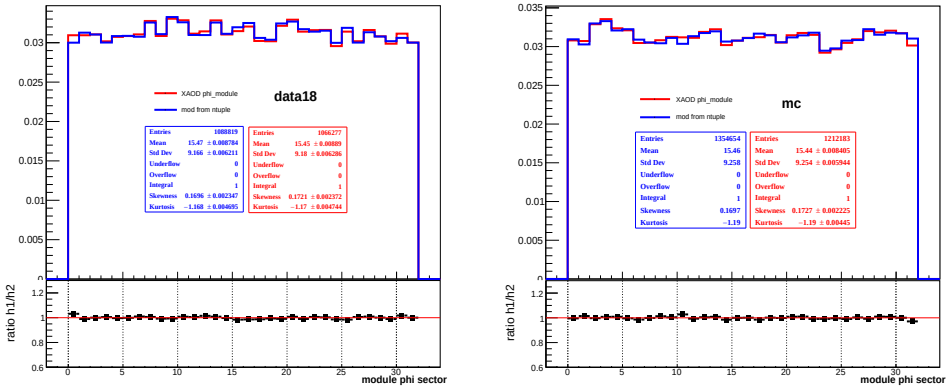


FIGURE A.3: phi_module from xAOD which is mod in ntuple, it is defined like Module phi sector [0-31].

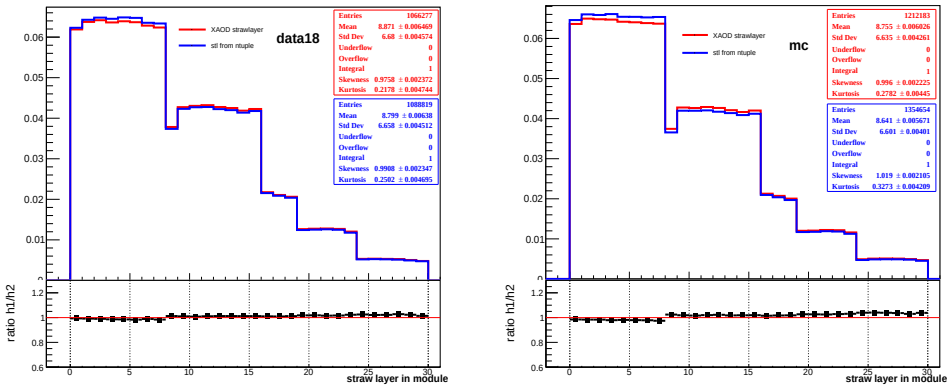


FIGURE A.4: straw layer from xAOD which is stl in ntuple. In xAOD it takes the values [19, 24, 30] in the Barrel and [6x16, 8x8] in Endcap. In ntuple it is defined in the Barrel: [0,18], [0,24],[0,30], Endcap: for lay 0-5 : [0,15] for lay 6-13 :[0,7]

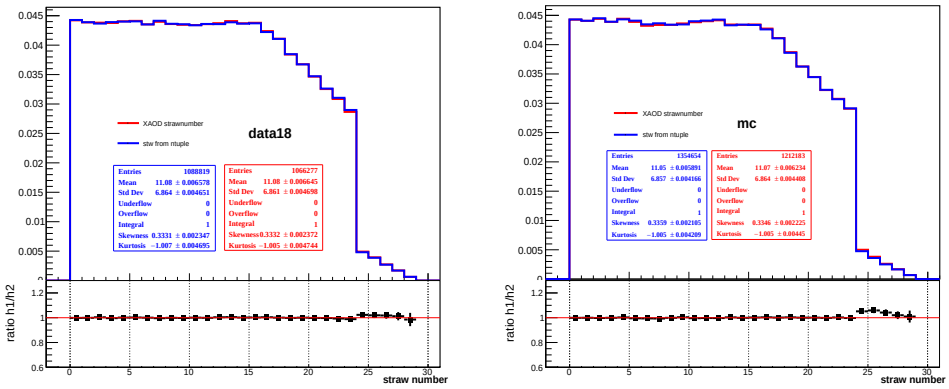


FIGURE A.5: straw number (xAOD) which is stw(Ntuple), it is defined like the straw number in the straw layer, Barrel: [0,14-17],[0,18-22],[0,22-27], Endcap: 6x[0,23], 8x[0,23].

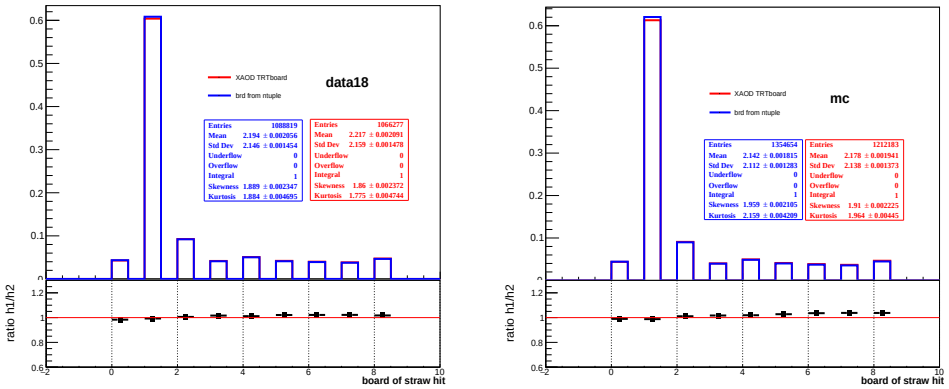


FIGURE A.6: TRTboard(xAOD) which is brd(Ntuple), it is defined like the Board of straw hit (Barrel: [0-1],[2-4],[5-8], Endcap: [1]).

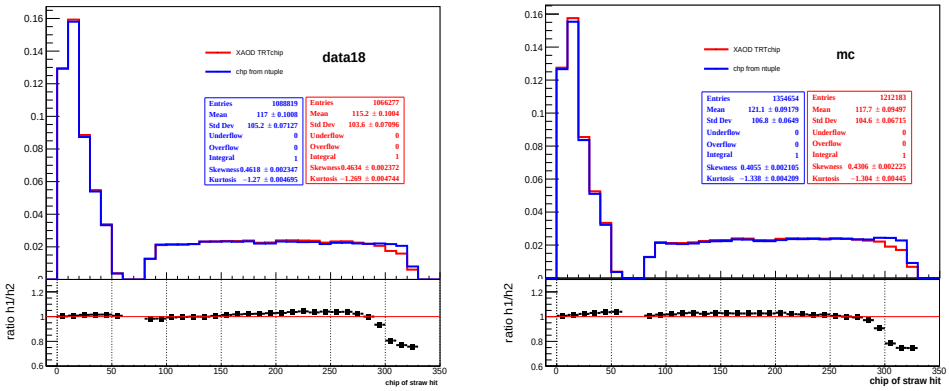


FIGURE A.7: TRTchip(xAOD) which is brd(Ntuple), it is defined like the chip of straw hit, (Barrel: [1-21],[1-34],[1-50], Endcap: [84-107]...[204-227], [228-239]...[312-323]).

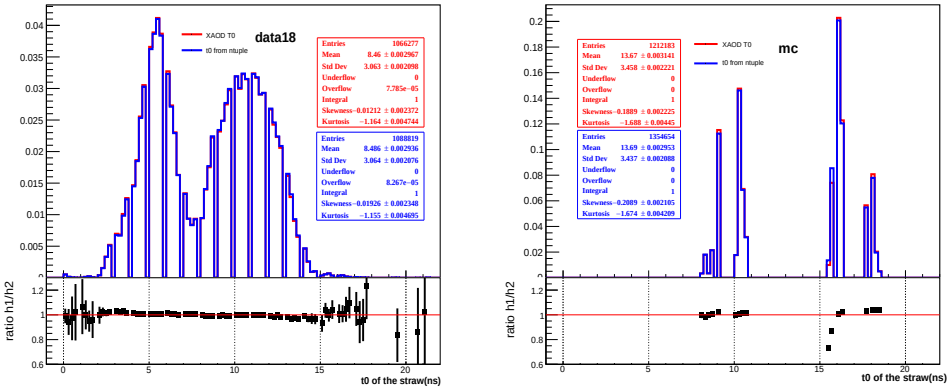


FIGURE A.8: t0, in xAOD it is defined to be the t0 of the straw (from calibration) [0-35 ns, mostly 6-12 ns], and in ntuple: [0, 19ns] roughly.

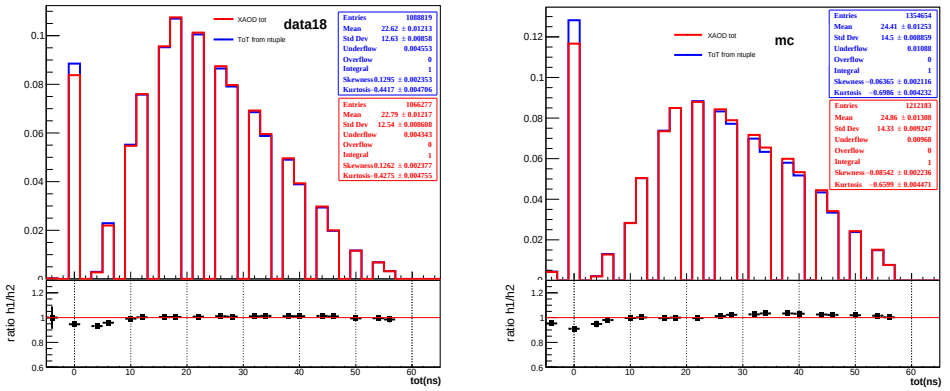


FIGURE A.9: tot, in xAOD it is the Time-Over-Threshold of the Low-Threshold bits [0-75 ns], and in ntuple: (0,56.7) discreet values.

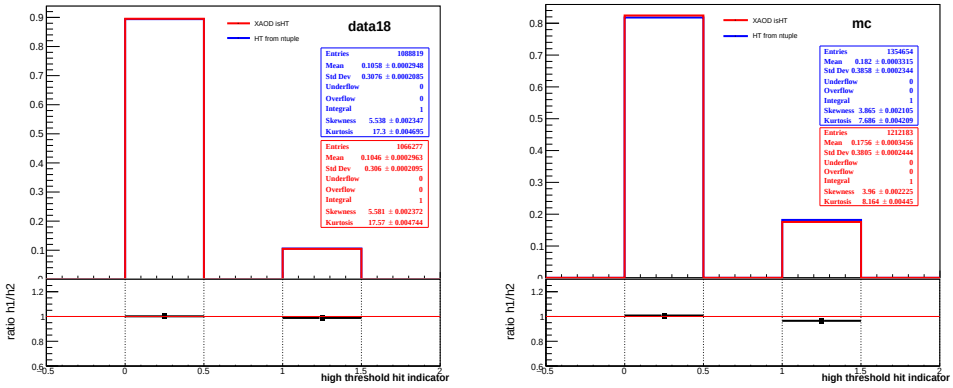


FIGURE A.10: isHTh(xAOD) which is HT(Ntuple), it is defined like the High-Threshold hit indicator [0/1].

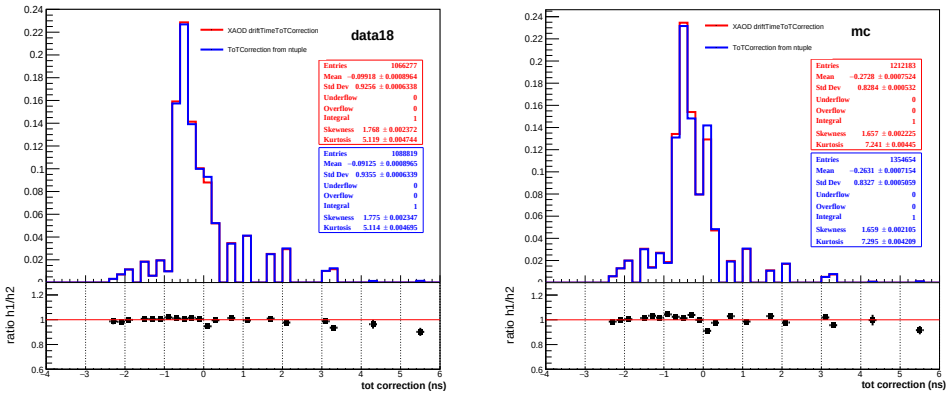


FIGURE A.11: driftTimeToTCorrection(xAOD) which is ToTCorrection(Ntuple), it is defined like the TOT correction to the drift time [-3-6 ns].

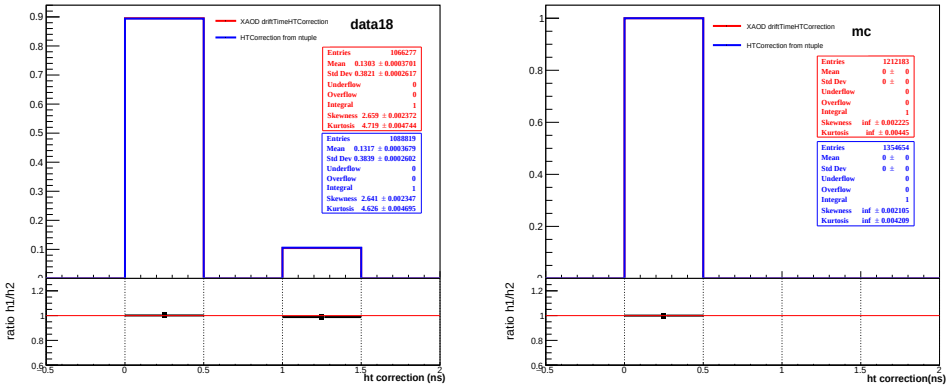


FIGURE A.12: driftTimeHTCorrection(xAOD) which is HTCorrection(Ntuple), it is defined like the HT correction to the drift time [0.0-1.5 ns], 0 (for MC).

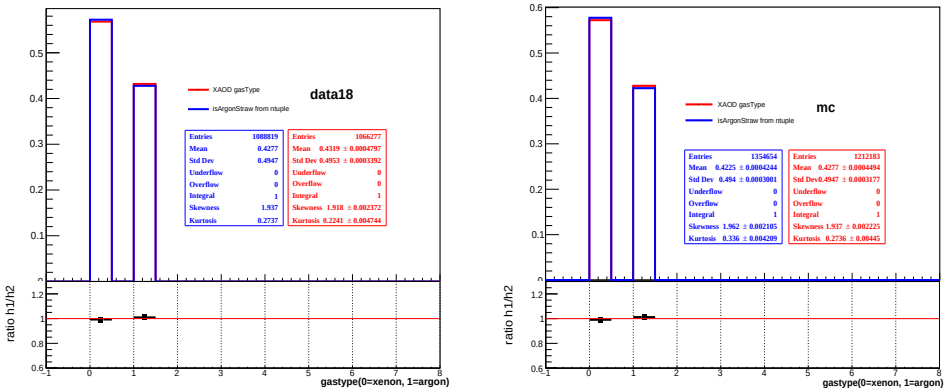


FIGURE A.13: gasType(xAOD) which is isArgonStraw(Ntuple), it takes 0 for Xenon and 1 for Argon.

### Nomenclature issue variables

Variables globalX and globalY from xAOD's are defined as the x(y)-position of the hit [-1050-1050 mm], In order to check whether they are problematic or not, a comparison to their equivalents in calibration formats is needed. In the latter, variables locx and locy are defined as the position x(y) (for the hit) [-1075,+1075]. In principle, the comparison should show a good agreement between globalX(Y) from xAOD and ntuple locx(y) variables. However, Figures A.14, A.15 show disagreements between

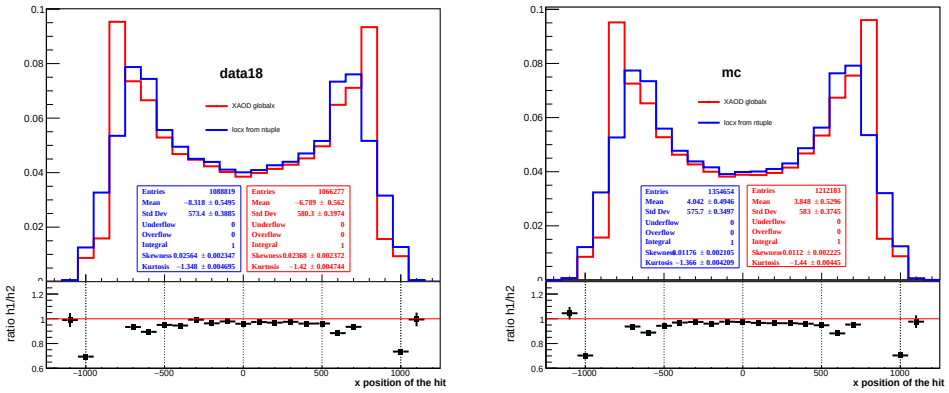


FIGURE A.14: Comparison of globalX and locx in DATA and MC

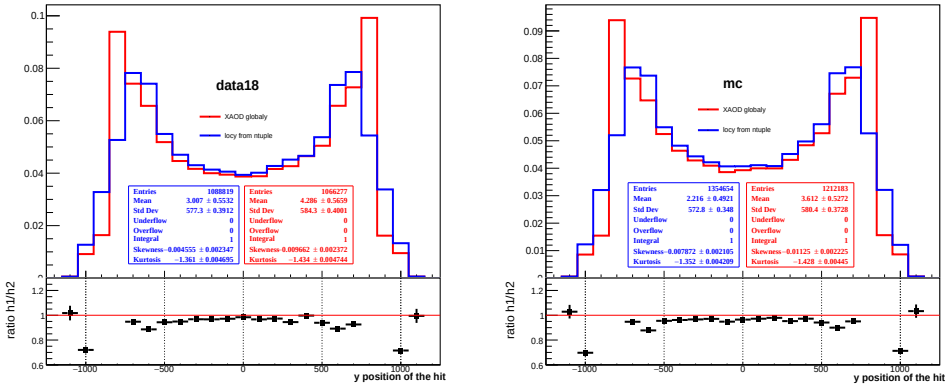


FIGURE A.15: Comparison of globalY and locy in DATA and MC

globalX(Y) and locx(y), meaning that locx and locy are not globalX and globalY. Furthermore, ntuple data include two other variables, x and y which are defined as the centre of the specific detector element in x (y) within the [-1075,+1075] range. These 2 variables show a good agreement when compared to globalX(Y)(Figures A.16, A.17). We can conclude and say that there is a nomenclature issue with globalX(Y), locX(Y) and X(Y). Variables x and y from ntuple should be defined like the x(y)-position of the hit not the centre of the specific detector element in x (y) [-1075,+1075] as it is in the TWiki page.

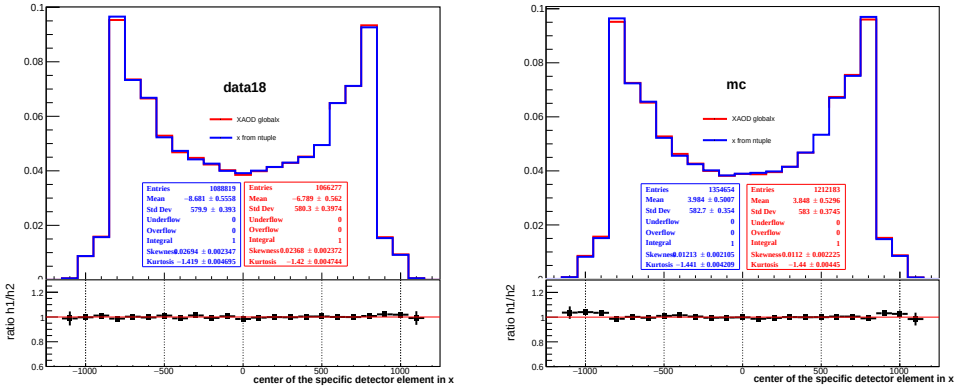


FIGURE A.16: Comparison of globalX and x in DATA and MC

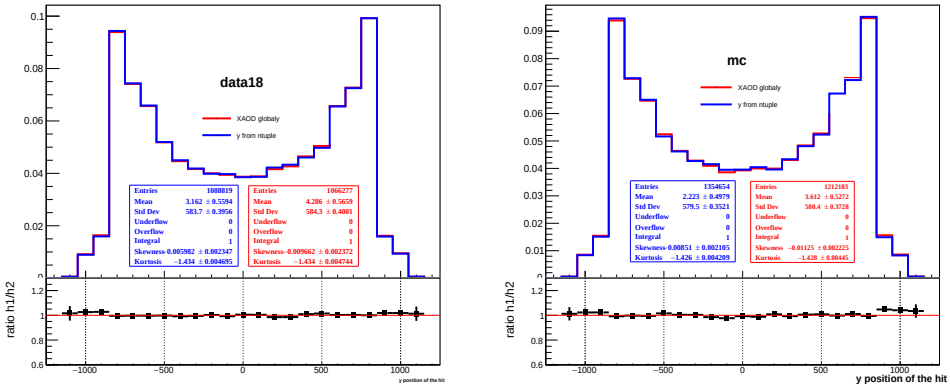


FIGURE A.17: Comparison of globalY and y in DATA and MC

### TRTxAOD problematic variables

Following a systematic comparison of xAODs and ntuples, a significant disagreement for some variables in DATA and MC is observed, while for some others the difference is visible only in MC. The list of these variables is shown below; localX, TrackError_(un)biased show a disagreement between TRTxAOD and ntuple in DATA and MC (Figures A.18, A.19, A.20). Variables localX and driftTime

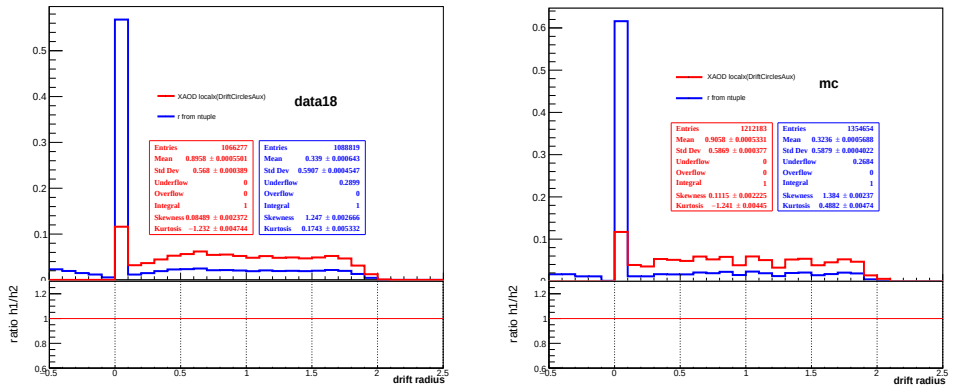


FIGURE A.18: localX from xAOD which is r from ntuple, in xAOD it is defined like the estimated drift radius in straw [-2.0-2.0 mm] and r in ntuple is the drift radius [0,2mm].

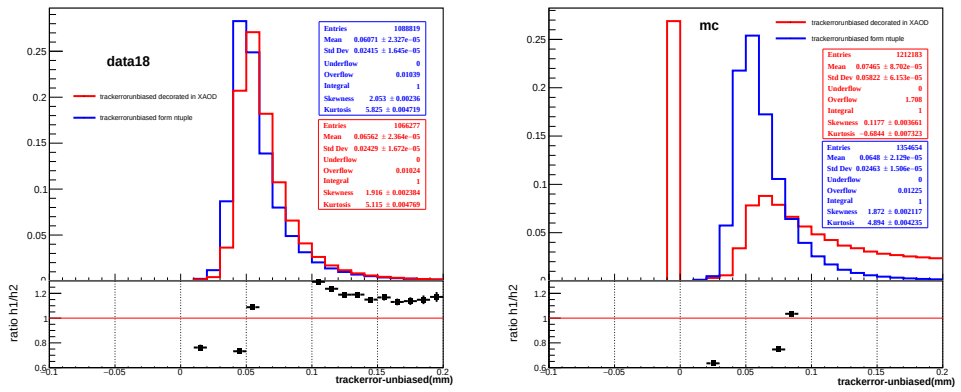


FIGURE A.19: TrackError_unbiased from xAOD is $drrtrackunbias^2$ in ntuple.

from msos, drifttime, (un)biasedResidualX, (un)biasedPullX, where pull, from ntuple, is defined as :

$$pull = \frac{drift\_radius - track\_unbiased}{\sqrt{drift\_radius\_error^2 + track\_unbiased\_error^2}} \tag{A.1}$$

and bpull defined as :

$$bpull = \frac{drift\_radius - track\_biased}{\sqrt{drift\_radius\_error^2 - track\_biased\_error^2}} \tag{A.2}$$

show an agreement in data but not in MC (Figures A.21, A.22, A.23, A.24, A.25, A.26, A.27). These particular variables need more detailed study in order to understand the origin of the observed discrepancies.

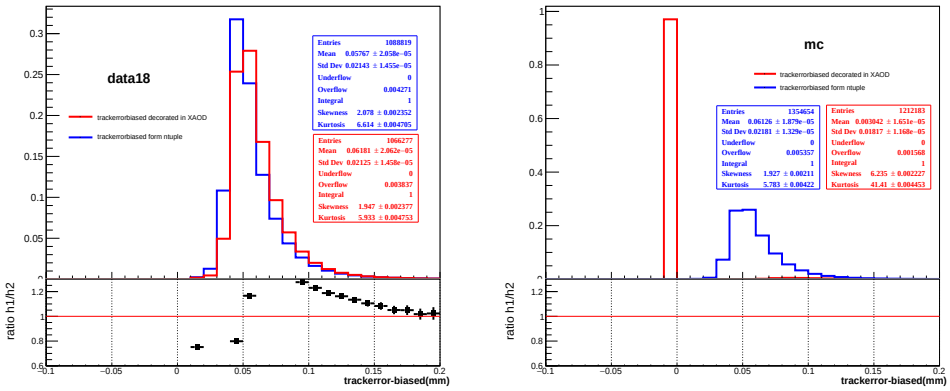


FIGURE A.20: TrackError_biased fron xAOD is $drrtrack^2$ in ntuple.

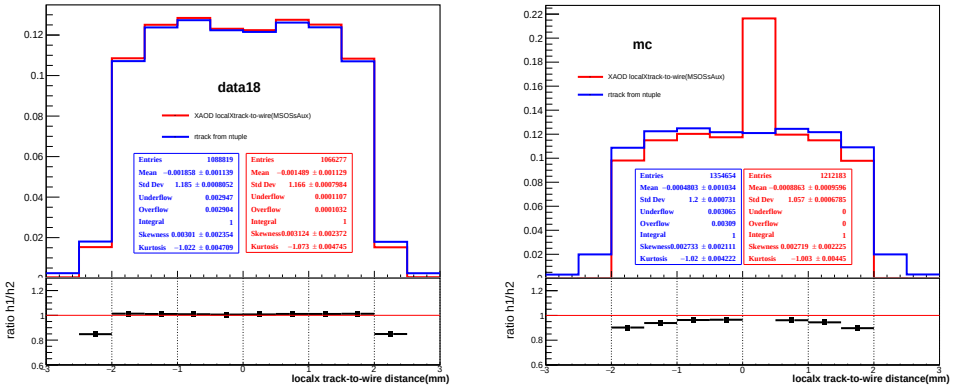


FIGURE A.21: localX from msos in xAOD and rtrack from ntuple, it is defined like the drift radius as obtained from the biased track ( track-to-wire distance), in xAOD takes the values [-2.2-2.2 mm] and in ntuple (-3,3mm).

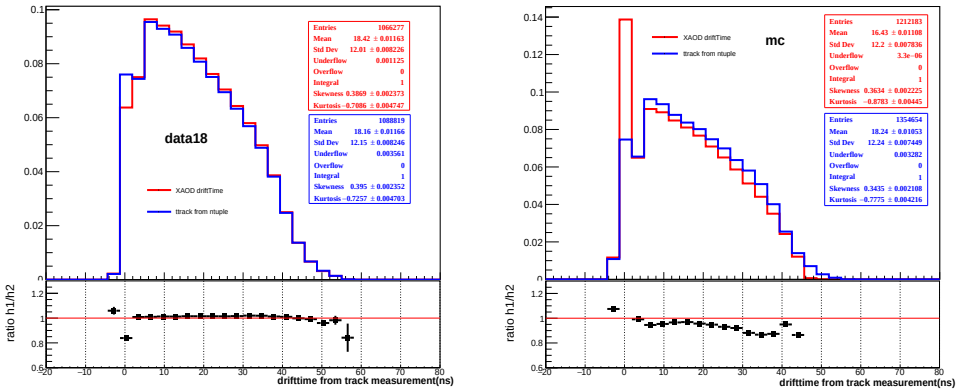


FIGURE A.22: driftTime from msos in xAOD and ttrack from ntuple, it is defined in xAOD like the drift time from track measurement and ntuple it is the expected drift time based on time to wire distance (-1,60ns).

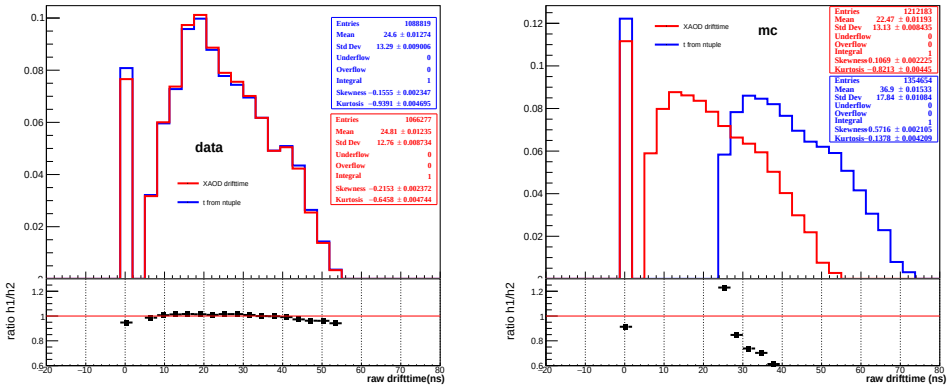


FIGURE A.23: The raw drift time which is drift time from xAOD and t from ntuple.

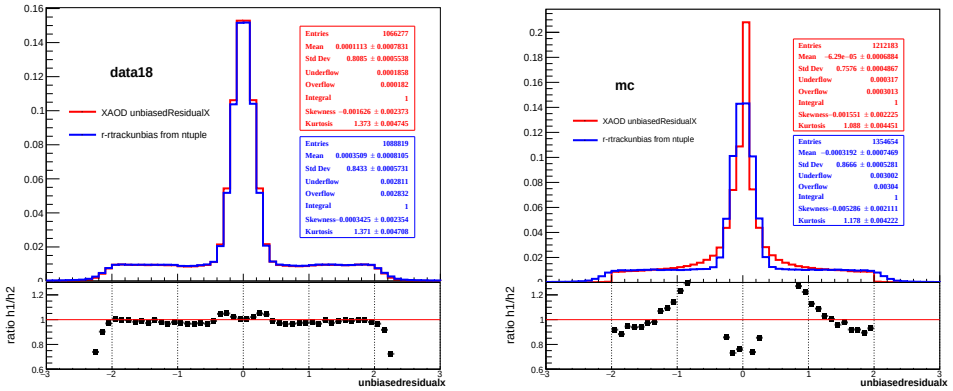


FIGURE A.24: The unbiased drift circle radius residual(i.e. NOT including the hit in track fit) which is unbiasedResidualX in xAOD and (r-rtrackunbias) in ntuple.

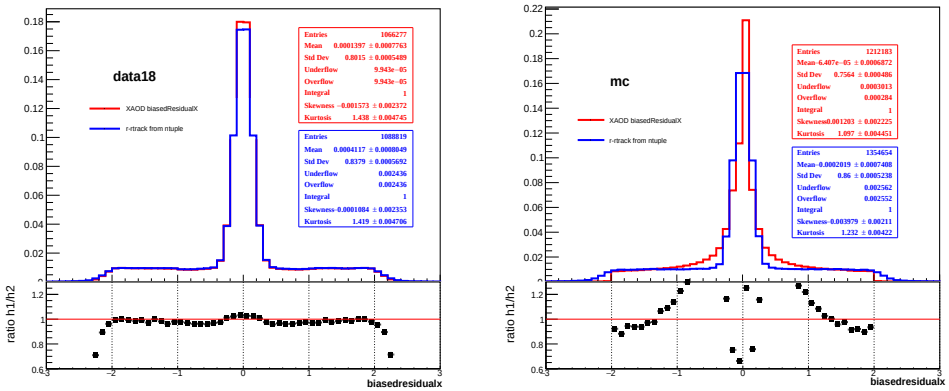


FIGURE A.25: The biased drift circle radius residual(i.e. including the hit in track fit) is biasedResidualX in xAOD and (r-track) in ntuple.

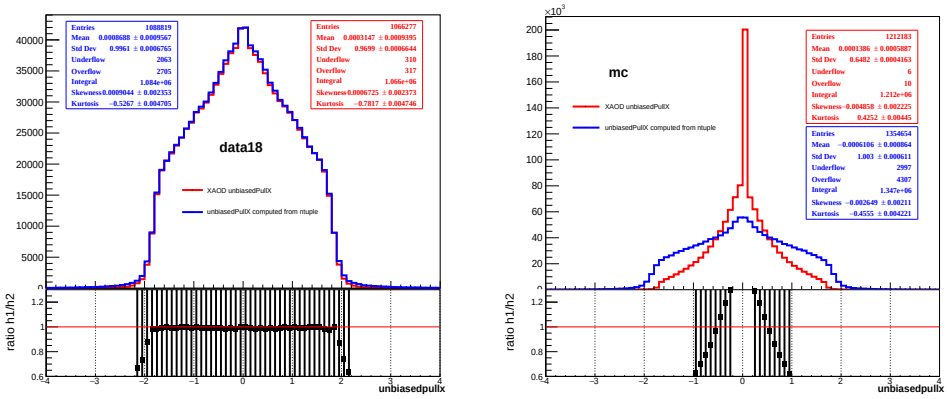


FIGURE A.26: The unbiased drift circle pull is unbiasedPullX from xAOD and pull A.1 from ntuple.

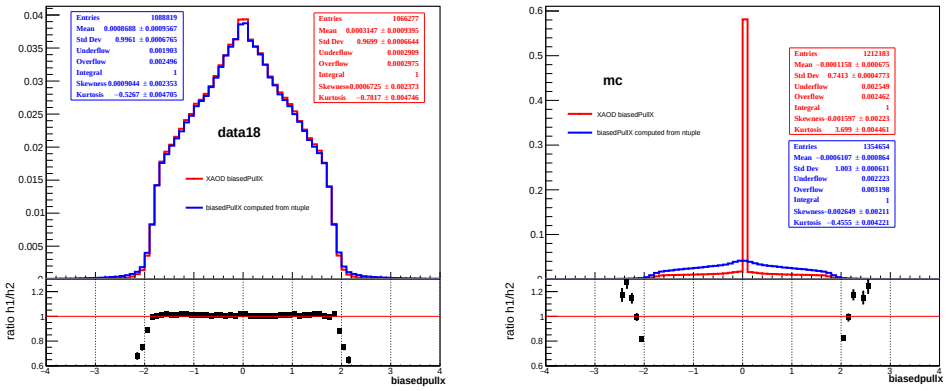


FIGURE A.27: The biased drift circle pull is biasedPullX from xAOD and bpull A.2 from ntuple.

### A.4.2 Understanding the source of TRTxAOD variables discrepancies

The second step of this study aims to understand the source of all the disagreements. It requires looking at possible correlations between multiple observables to identify the subset of hits/tracks/events that cause the problem and provide a fix to the TRT reconstruction software. Observations made in Paragraph A.4.1 point out to the following: Requiring trackError ==0 in xAOD MC and rejecting hits with Trackerror_unb (ttwd) ==0 while considering only TrackError_unbiased !=0 may help to reduce the number of problematic variables.

#### Problematic variables from xAOD for trackError ==0 (MC only)

Figures A.28, A.29, A.30, A.31, A.32 show the distributions of localX, driftTime, drifttime, (un)biasedResidualX, (un)biasedPulllX after rejecting hits with trackError ==0. The peak around 0 seems to appear only in MC events.

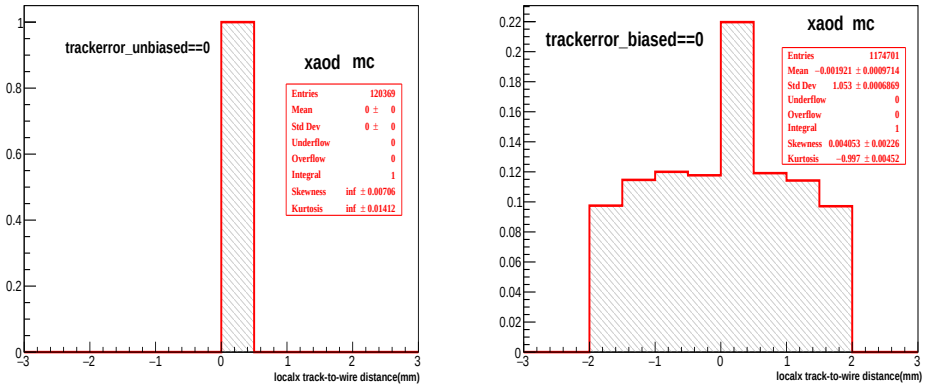


FIGURE A.28: localX for trackerror_(un)biased==0 in MC

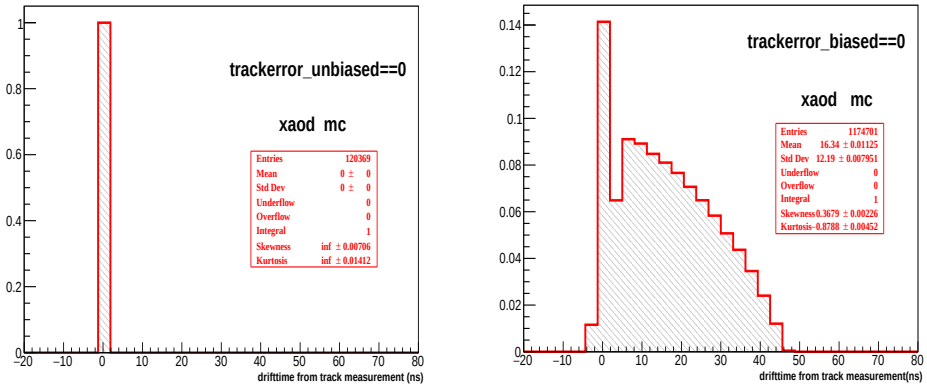


FIGURE A.29: driftTime for trackerror_(un)biased==0 in MC

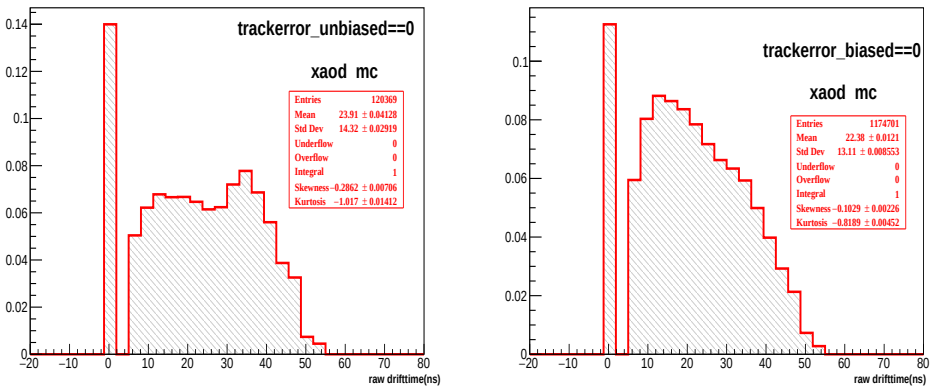


FIGURE A.30: drifttime for trackerror_(un)biased==0 in MC

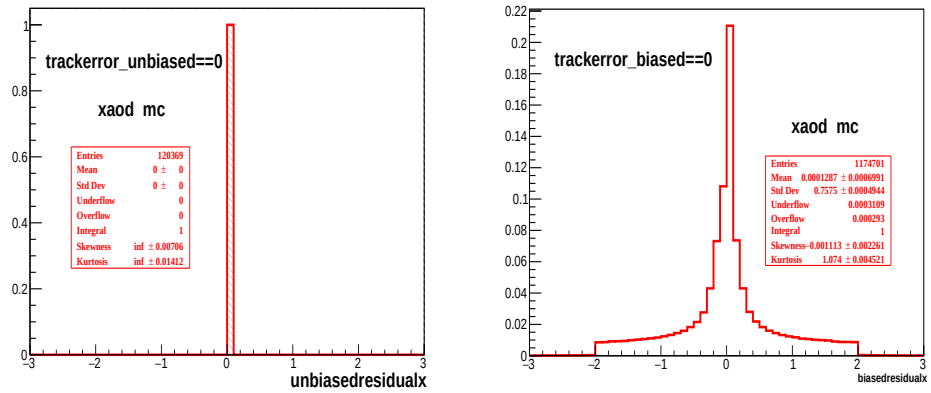


FIGURE A.31: (un)biasedResidualX for trackerror_(un)biased==0 in MC

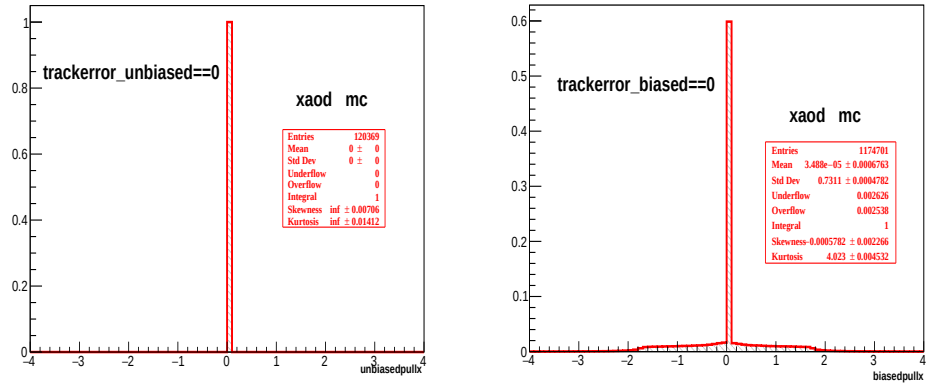


FIGURE A.32: (un)biasedPulllX for trackerror_(un)biased==0 in MC

**Problematic variables from xAOD for TrackError_unbiased !=0 (The same for ttwd != 0)**

Figures A.33, A.34, A.35, A.36, A.37, A.38, A.40, A.41, A.39 show the distributions of localX, driftTime, localx(r), (un)biasedResiduals, (un)biasedPull, trackError_unbiased after rejecting hits with Trackerror_unb ==0 ( or ttwd ==0) from DATA and MC.

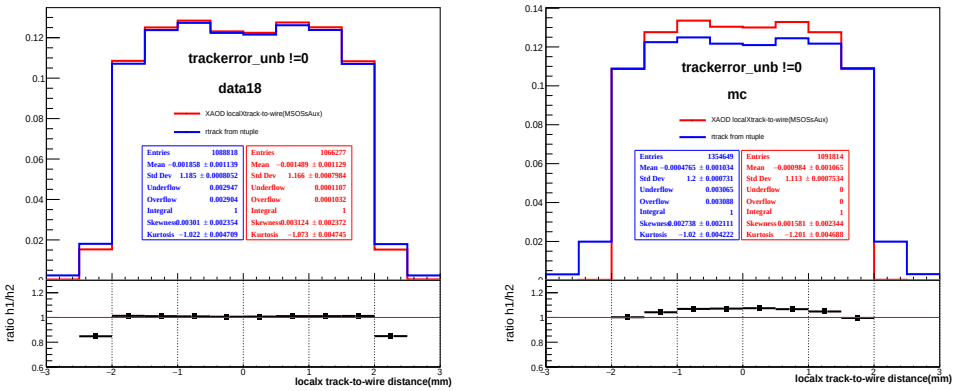


FIGURE A.33: localX track_to_wire(rtrack) for TrackError_unbiased !=0 in DATA and MC.

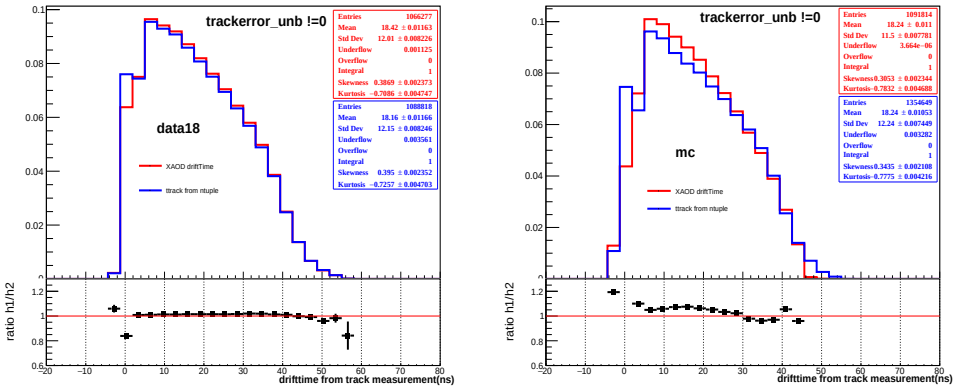


FIGURE A.34: driftTime(ttrack) for TrackError_unbiased !=0 in DATA and MC

These results show that for TrackError ==0, distributions of xAOD variables: localX, driftTime, localx(r), (un)biasedResiduals, (un)biasedPull, trackError_unbiased are affected by hits with ttwd ==0. The peak at 0, observed only in MC, means that some hits have TrackError ==0 and Trackerror_unb (ttwd !=0). Variables that are not affected by hits with ttwd ==0 are "r" in (data & MC) and trackError_biased, biasedPulls in MC. Based on these results, the remaining problems seem to point to an incorrect hit or track slimming procedure in xAOD production.

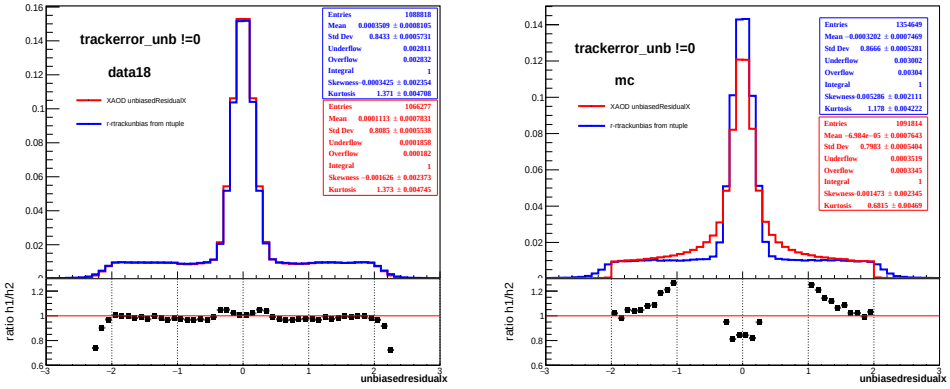


FIGURE A.35: unbiasedResidualX(r-rtrackunbias) for TrackError_unbiased !=0 in DATA and MC

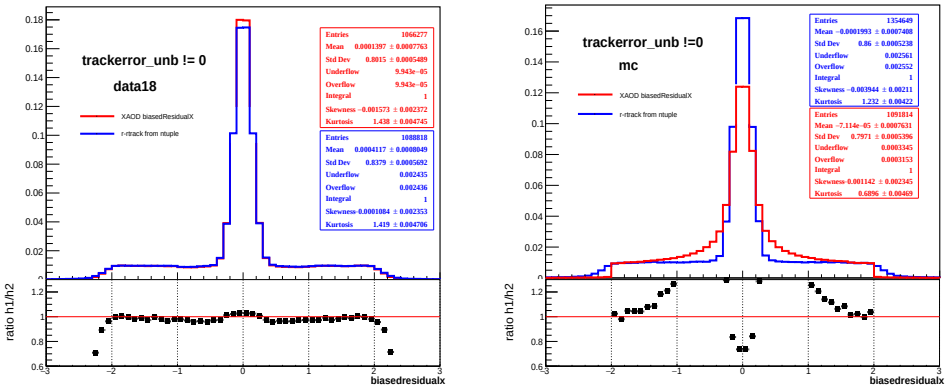


FIGURE A.36: biasedResidualX(r-rtrack) for TrackError_unbiased !=0 in DATA and MC

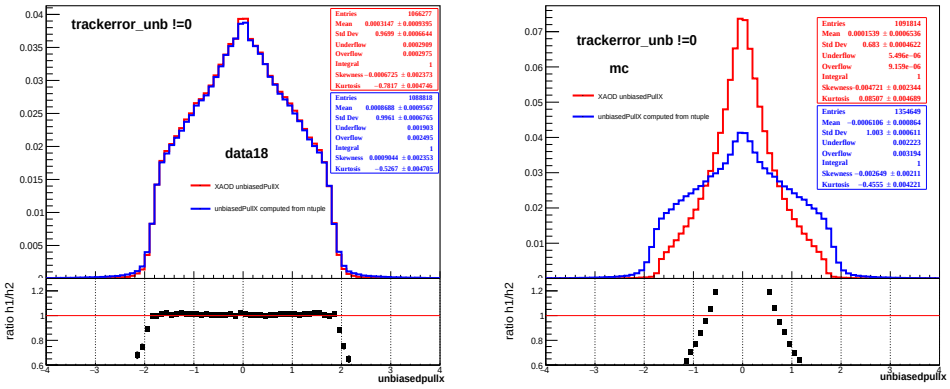


FIGURE A.37: unbiasedPullX(pull) for TrackError_unbiased !=0 in DATA and MC

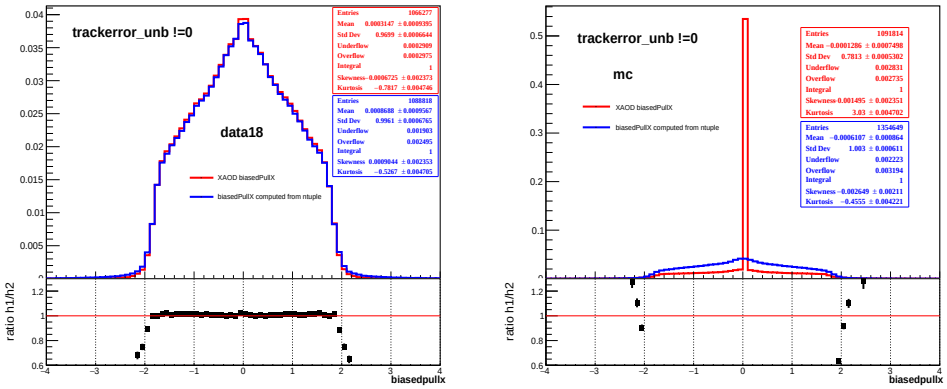


FIGURE A.38: biasedPullX(bpull) for TrackError_unbiased !=0 in DATA and MC

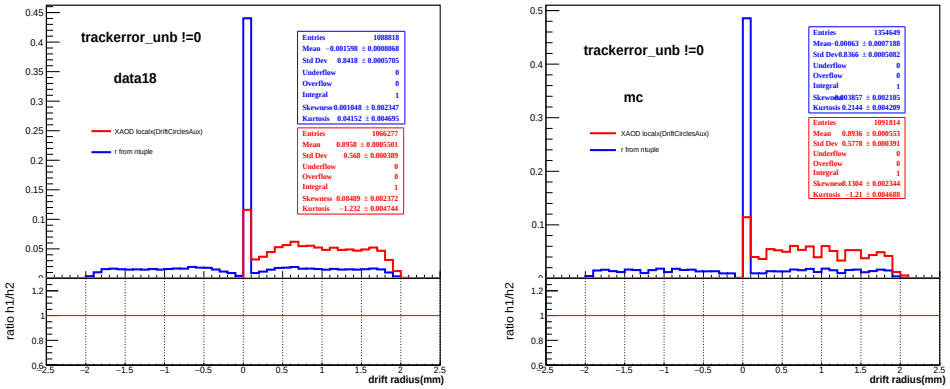


FIGURE A.39: localX(r) for TrackError_unbiased !=0 in DATA and MC

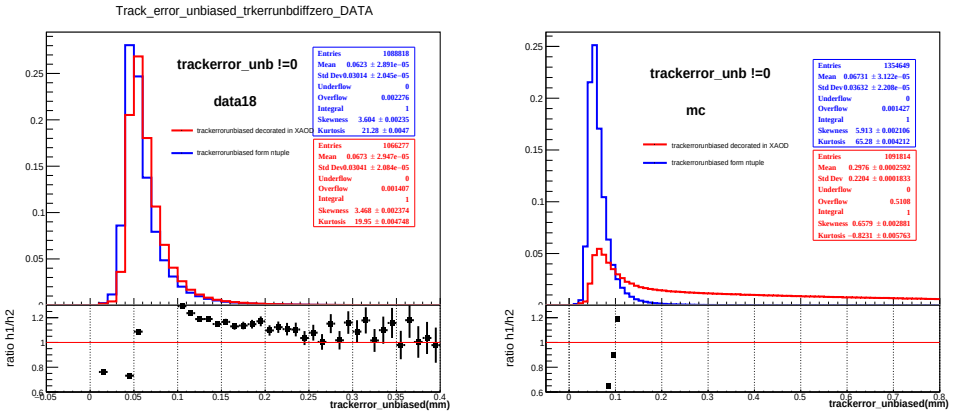


FIGURE A.40: TrackError_unbiased for TrackError_unbiased !=0 in DATA and MC

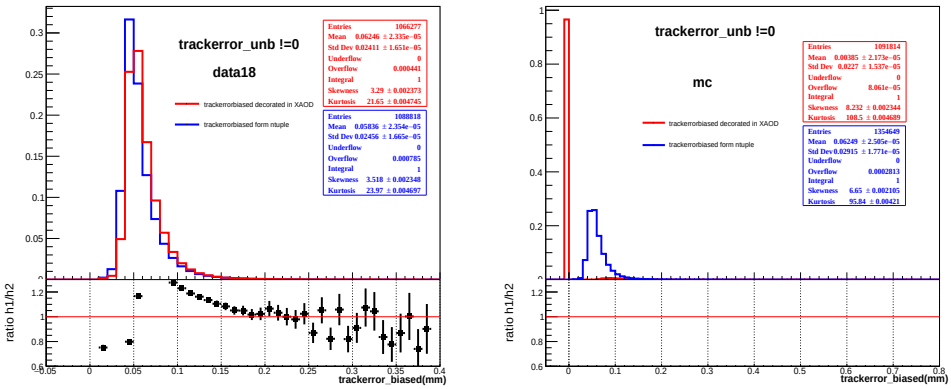


FIGURE A.41: TrackError_biased for TrackError_unbiased !=0 in DATA and MC

### A.4.3 Fixing the source of discrepancies and validation

In order to fix the source of these discrepancies, a study on how the track slimming affects the distributions of the problematic variables is needed. A systematic study of these variables, with and without the activation of the track slimming algorithms, is then performed on DATA and MC events.

#### Track slimming activated in DATA and MC

Figures A.42, A.43, A.44, A.45, A.46, A.47, A.48, A.49 show the distributions of all problematic variables with the Track slimming algorithm activated in DATA and MC events.

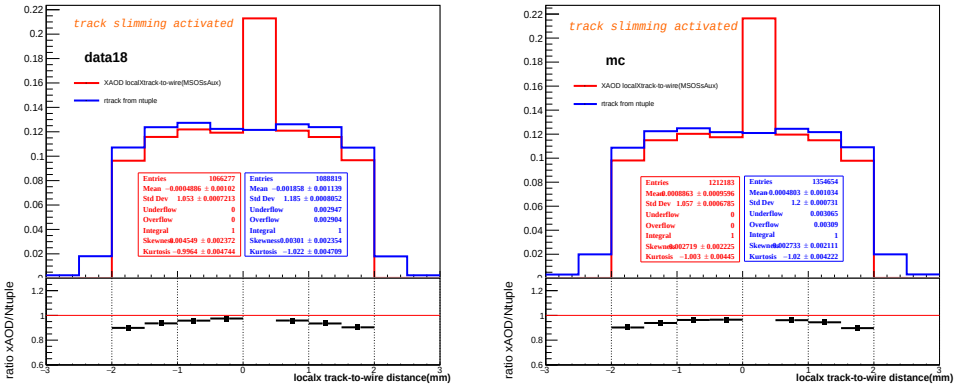


FIGURE A.42: localXtrack_to_wire(rtrack) for Track slimming activated in DATA and MC

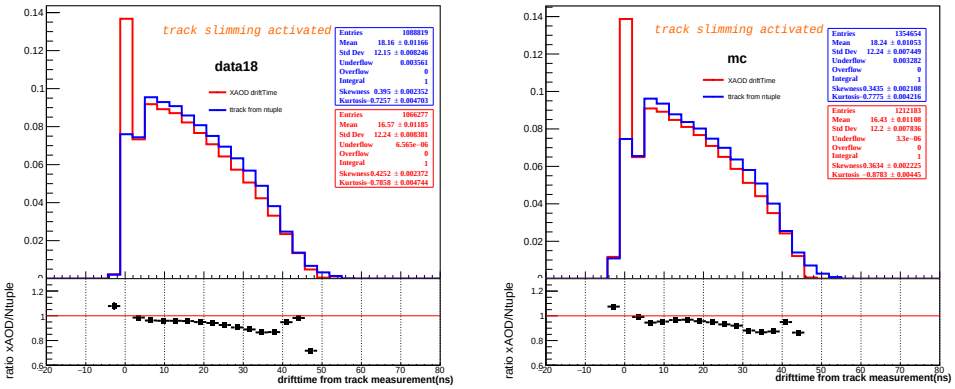


FIGURE A.43: driftTime(ttrack) for Track slimming activated in DATA and MC

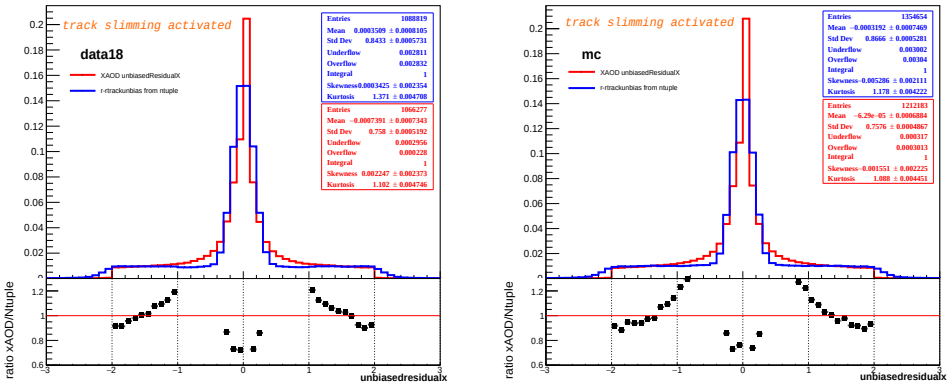


FIGURE A.44: unbiasedResidualX for Track slimming activated in DATA and MC

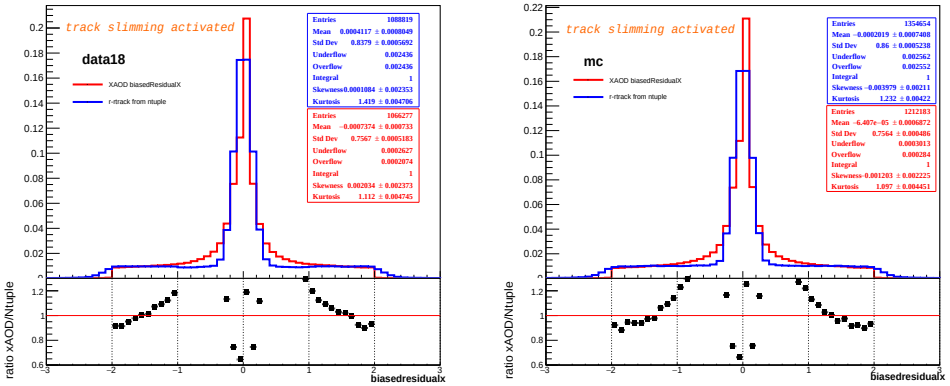


FIGURE A.45: biasedResidualX for Track slimming activated in DATA and MC

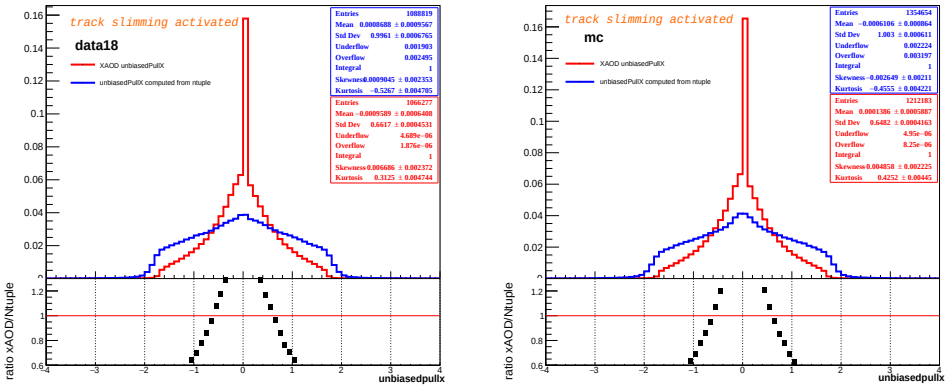


FIGURE A.46: unbiasedPullX for Track slimming activated in DATA and MC

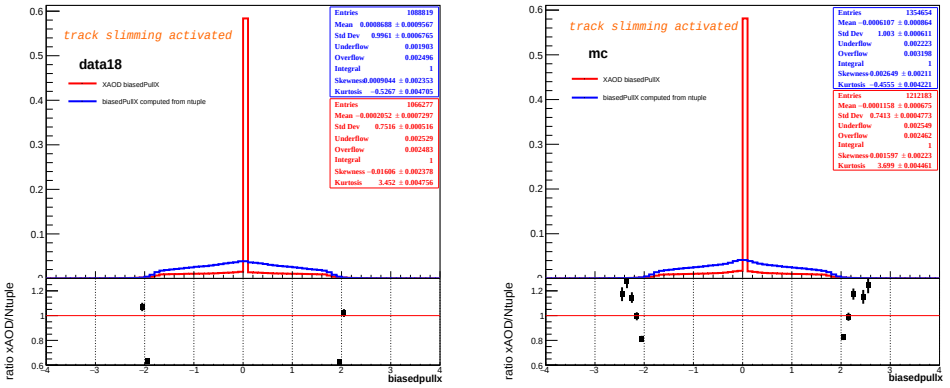


FIGURE A.47: biasedPullX for Track slimming activated in DATA and MC

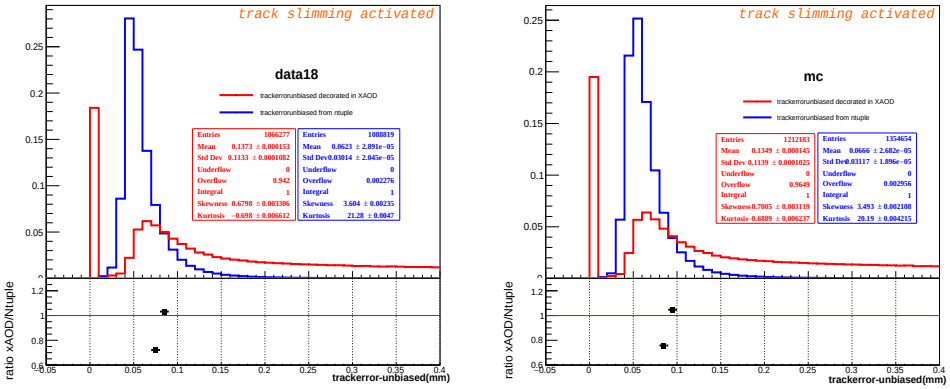


FIGURE A.48: TrackError_unbiased for Track slimming activated in DATA and MC

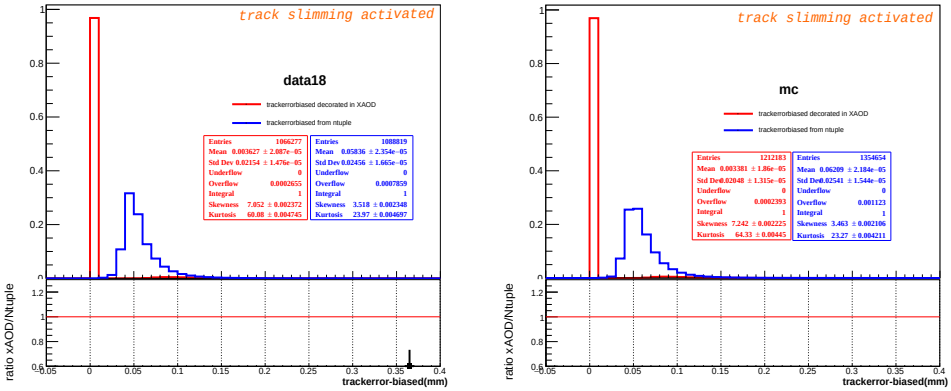


FIGURE A.49: TrackError_biased for Track slimming activated in DATA and MC

### Track slimming deactivated in DATA and MC

Figures A.50, A.51, A.52, A.53, A.54, A.55, A.56, A.57 show the distributions of problematic variables with the Track slimming algorithms deactivated in DATA and MC. Comparing Figures A.42, A.43, A.44, A.45, A.46, A.47, A.48, A.49, with Figures A.50, A.51, A.52, A.53, A.54, A.55, A.56, A.57 leads us to conclude that the source of the observed discrepancies originates from using the track slimming procedure in MC xAOD events while it was deactivated in data/ MC ntuples events as well as in data xAOD.

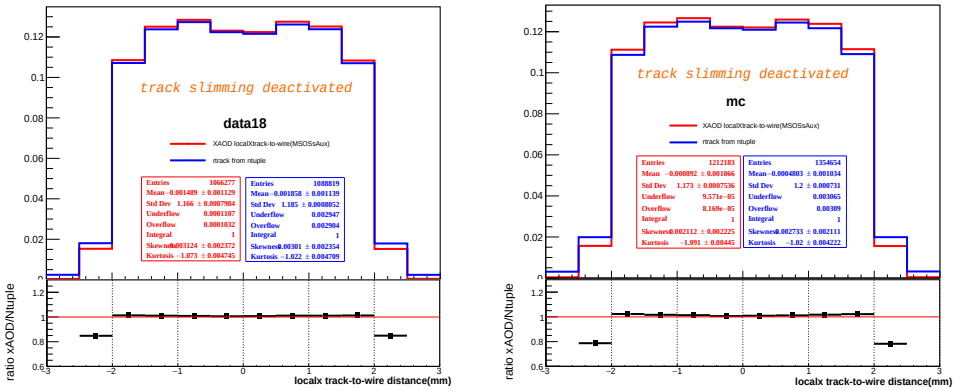


FIGURE A.50: localXtrack_to_wire(rtrack) for Track slimming deactivated in DATA and MC

## A.4.4 Drift circle error correction

The localXError from xAOD is named $dr^2$ in ntuple event format. It is defined in xAOD as the local covariance and its square root is used to calculate the drift radius uncertainty in straw with its value mostly laying within the [0.08-0.22] mm range. The error on drift radius from ntuple is defined as dr and Figure A.58 shows a clear disagreement between localXError and $dr^2$ in data and MC. After correcting the drift circle error, a new variable, called errDC, is added to the msos of xAOD format (through the decoration mechanism), using Athena 21.0.77 [trt107, trt108]. Figure A.59 shows a good agreement between errDC from xAOD and $dr^2$ in ntuple.

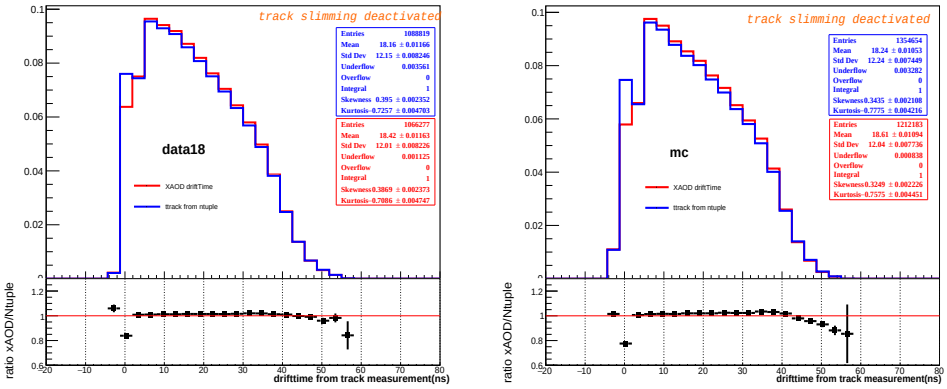


FIGURE A.51: driftTime(ttrack) for Track slimming deactivated in DATA and MC

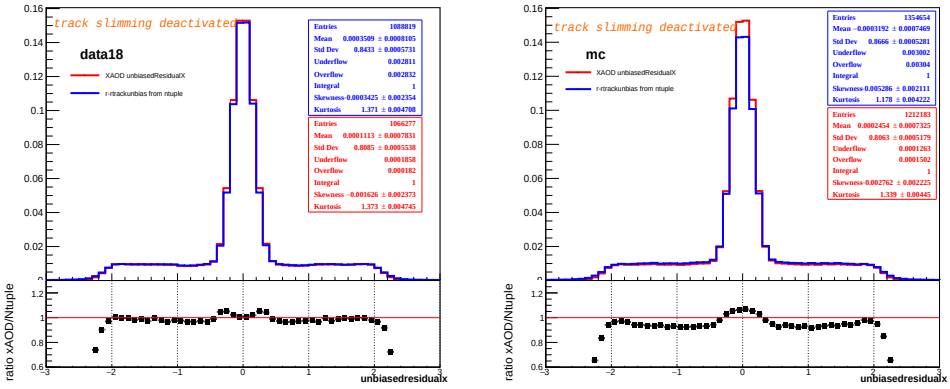


FIGURE A.52: unbiasedResidualX for Track slimming deactivated in DATA and MC

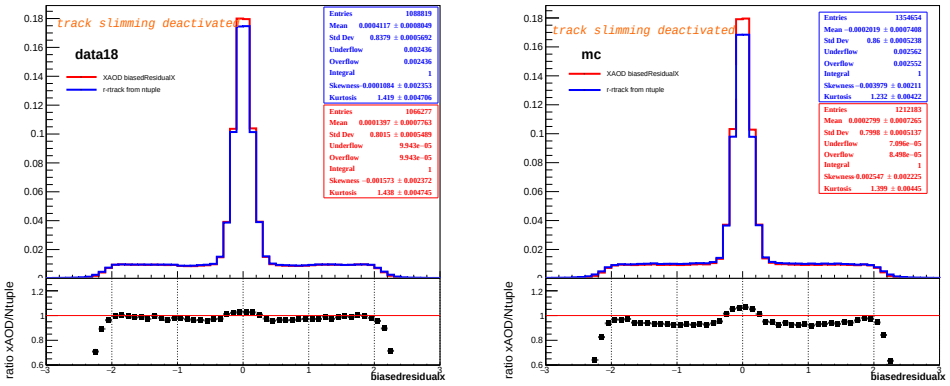


FIGURE A.53: biasedResidualX for Track slimming deactivated in DATA and MC

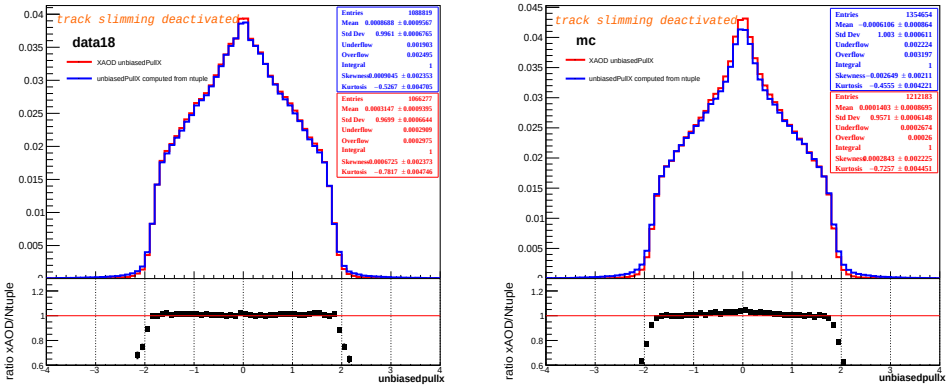


FIGURE A.54: unbiasedPullX for Track slimming deactivated in DATA and MC

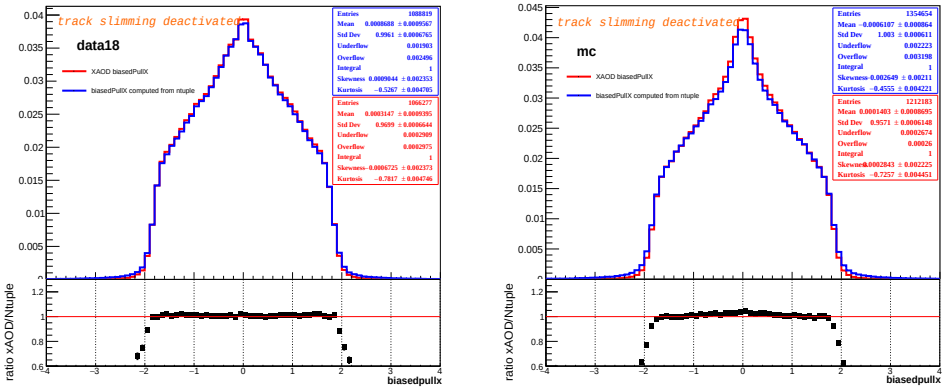


FIGURE A.55: biasedPullX for Track slimming deactivated in DATA and MC

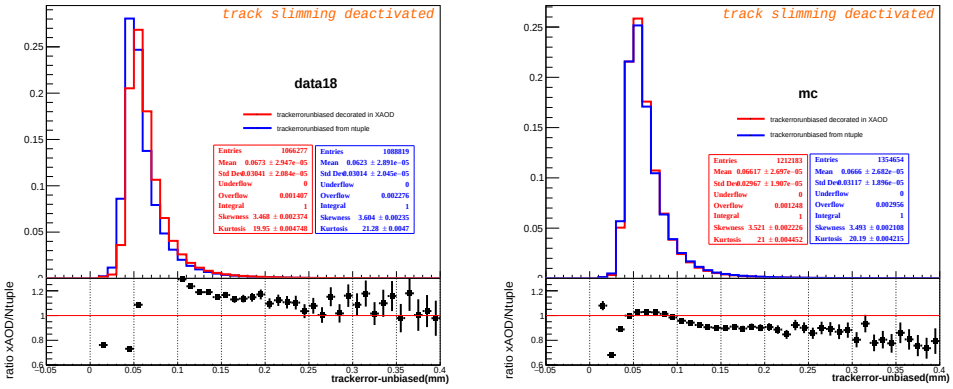


FIGURE A.56: TrackError_unbiased for Track slimming deactivated in DATA and MC

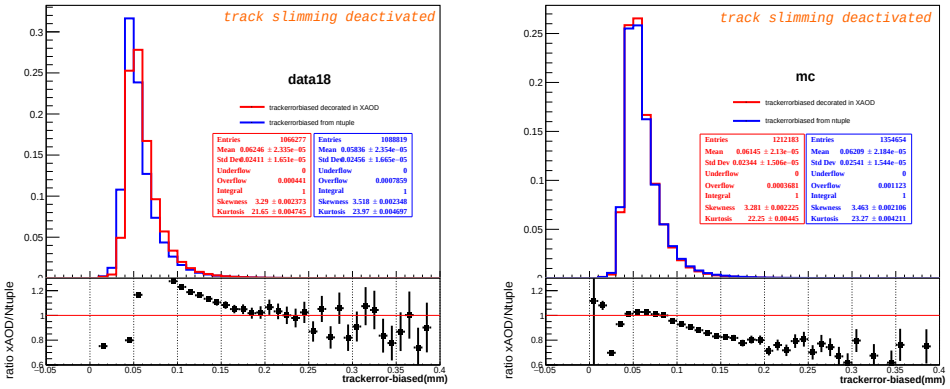


FIGURE A.57: TrackError_biased for Track slimming deactivated in DATA and MC

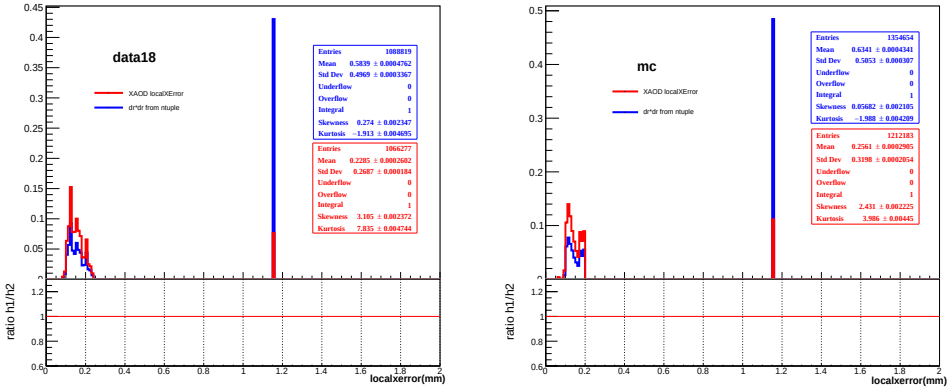


FIGURE A.58: Comparison of localXError and $dr^2$ for DATA and MC.

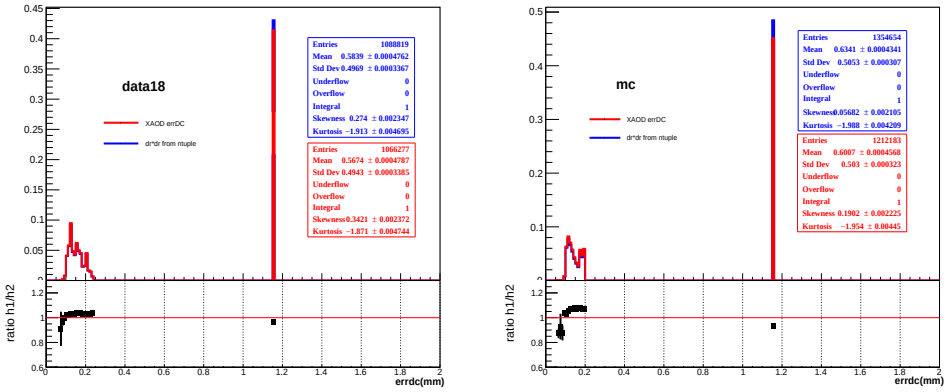


FIGURE A.59: Comparison of errdc and $dr^2$ for DATA and MC.

### A.4.5 Drifttime correction in ntuple

Figure A.23 shows an overall good agreement between xAOD and ntuple in Data. However, a disagreement in MC persists meaning that an extra correction needs to be applied to the whole [-1,1]ns range. This correction should be applied only to ntuple drifttime t>1 where the disagreement exists. Hence, a time correction called ephase, defined in range (-17.8,14.6ns) roughly, is applied to the drifttime. For t<1ns, variables from the ntuple format are kept. if (t < 1) drifttime->Fill(t); if (t > 1)drifttime->Fill(t+ephase);

Figure A.60 shows a good agreement for the variable drifttime after this new correction and based

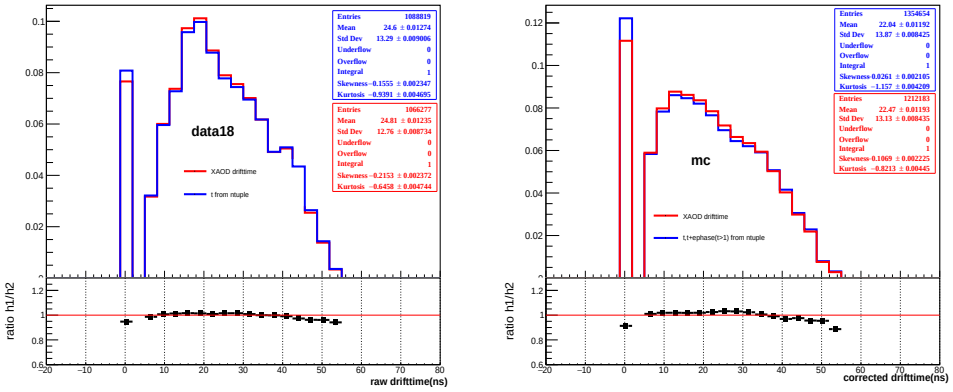


FIGURE A.60: drifttime(t) in DATA and the corrected drifttime in MC(t+ephase)

on it, the variable ephase from ntuple used in this correction is not the known ephase used for cosmic runs.

## A.5 Conclusion

A systematic study of TRT variables included in the xAOD and ntuple event formats are presented. The properties of these variables were carefully checked for both MC and data events in order to extract all possible discrepancies resulting in bad-quality TRT data. The results show first an incompatible naming of the same quantities in both xAOD's and ntuples leading to unphysical discrepancies. Once this naming problem has been sorted out, all the affected variables agreed in both formats. In addition, the track slimming algorithms were affecting some variables in xAOD's MC events. This was the source of the observed incompatibilities between the same variables in xAOD's and ntuples(buggy variables). Deactivating the track slimming algorithm in xAOD production has fixed the remaining discrepancies and a full agreement between TRT variables in xAOD and ntuple formats is achieved.

# B TRTxAOD variables description

The list of TRTxAOD variables used in this study and their description is given below in Table B.1. The word unbiased is used when the hit information was removed and then the track was refitted [300].

| variable name | Type | Description |
|---|---|---|
| bec | vector<int> | BEC = "Barrel/EndCap" 1: Barrel, 2: End-cap; positive (A-side), negative (C-side). |
| layer | vector<int> | Layer number (Barrel [0-2] ; End-cap [0-13]). |
| phi_module | vector<int> | Module phi sector [0-31]. |
| strawlayer | vector<int> | Straw layer in module (Barrel: [19, 24, 30], Endcap: [6x16, 8x8]). |
| strawnumber | vector<int> | Straw number in straw layer (Barrel: [0,14-17],[0,18-22],[0,22-27], Endcap: 6x[0,23], 8x[0,23]). |
| TRTboard | vector<int> | Board of straw hit (Barrel: [0-1],[2-4],[5-8], Endcap: [1]). |
| TRTchip | vector<int> | Chip of straw hit (Barrel: [1-21],[1-34],[1-50], Endcap: [84-107]...[204-227], [228-239]...[312-323]). |
| drifttime | vector<float> | The raw drift time. |
| tot | vector<float> | The Time-Over-Threshold of the Low-Threshold bits [0-75 ns]. |
| gasType | vector<char> | 0=Xe, 1=Ar, 2=Kr, 6=emulated Ar, 7=emulated Kr. |
| isHT | vector<char> | The High-Threshold hit indicator [0/1]. |
| highThreshold | vector<char> | The High-Threshold bit settings [0-7]. |
| T0 | vector<float> | The t0 of the straw (from calibration) [0-35 ns, mostly 6-12 ns]. |
| driftTimeToTCorrection | vector<float> | The TOT correction to the drift time [-3-6 ns]. |
| driftTimeHTCorrection | vector<float> | The HT correction to the drift time [0.0-1.5 ns]. |
| localX | vector<float> | The drift radius as obtained from the biased track ( aka track-to-wire distance) [-2.2-2.2 mm]. |
| localX | vector<float> | The estimated drift radius in straw [-2.0-2.0 mm]. |
| localXError | vector<float> | local covariance, use the square root of it to get the drift radius uncertainty in straw [0-1.2 mm, mostly 0.08-0.22 mm]. |
| globalX | vector<float> | The x-position of the hit [-1050-1050 mm]. |
| globalY | vector<float> | The y-position of the hit [-1050-1050 mm]. |
| unbiasedResidualX | vector<float> | The unbiased drift circle radius residual (i.e. NOT including this hit in track fit). |
| biasedResidualX | vector<float> | The biased drift circle radius residual (i.e. including this hit in track fit). |
| unbiasedPullX | vector<float> | The unbiased drift circle pull. |
| biasedPullX | vector<float> | The biased drift circle pull. |
| driftTime | vector<float> | Drift time from track measurement. |

TABLE B.1: Variables used from TRTxAOD's. The columns are the names of the TRTxAOD elements (left), their type (centre) and their descriptions (right).

# C Calibration Ntuple variable description

The ntuple is structured in such a way that each entry corresponds to one hit. The information kept for each hit is shown in Table C.1. All variables in the ntuple are declared as floats even information that would be better stored as integers [301].

| variable name | Description | Expected Range |
|---|---|---|
| det | detector part | $-1, -2, 1, 2$ |
| lay | layer | $[0, 2]$ for barrel $[0, 13]$ end-caps |
| mod | phi module | $[0, 31]$ |
| stl | straw layer | Barrel: $[0, 18]$, $[0, 24]$, $[0, 30]$, Endcap: for lay 0-5 : $[0, 15]$ for lay 6-13 :$[0, 7]$) |
| stw | straw number (within the straw layer) | |
| brd | Board of straw hit | (Barrel [0-1],[2-4],[5-8], Endcap [1]) |
| chp | Chip of straw hit | (Barrel [1,21],[1,34],[1,50], Endcap [84,107]...[204,227], [228,239]...[312,323]) |
| locx | position x (for the hit) | [-1075,+1075] |
| x | center of the specific detector element in x | same as locx |
| y | centre of the specific detector element in y | same as locy |
| r | drift radius | [0,2 mm] |
| dr | error on drift | radius |
| t | drift time | |
| rtrack | track to wire distance | (-3,3 mm) |
| drrtrack | error on track to wire distance | |
| rtrackunbias | track to wire distance unbiased | |
| drrtrackunbias | error on track to wire distance unbiased | |
| ttrack | track drift time | (-1,60 ns) |
| ttrackunbias | track drift time unbias | |
| t0 | $T_0$ | [0, 19 ns] roughly |
| ephase | time correction | (-17.8,14.6 ns) roughly |
| ToT | time over threshold | (0,56.7) discrete values |
| HT | High Threshold level (if exceeded) | 0 or 1 |
| ToTCorrection | time over threshold correction | [-3,6 ns] |
| HTCorrection | high threshold level correction | 0 (for MC) |
| isArgonStraw | is this straw filled with Argon | 0 or 1 |

TABLE C.1: Variables used from the calibration ntuple. The columns are the names of the ntuple elements (left), short descriptions of each element (centre) and the expected range of the element if available (right).

# Bibliography


[1] Douglas Clowe et al. “A Direct Empirical Proof of the Existence of Dark Matter”. In: *The Astrophysical Journal* 648.2 (2006), pp. L109–L113. DOI: 10.1086/508162. URL: https://doi.org/10.1086/508162.

[2] Marco Fabbrichesi, Emidio Gabrielli, and Gaia Lanfranchi. *The Physics of the Dark Photon*. 2021. DOI: 10.1007/978-3-030-62519-1. URL: http://dx.doi.org/10.1007/978-3-030-62519-1.

[3] P. Fayet. “Extra U(1)’s and New Forces,” in: *Nucl. Phys. B* 347 (1990), pp. 743–768. DOI: 10.1016/0550-3213(90)90381-M.

[4] H. Georgi, P. H. Ginsparg, and S. L. Glashow. “Photon Oscillations and the Cosmic Background Radiation,” in: *Nature* 306 (1983), pp. 765–766. DOI: 10.1038/306765a0.

[5] M. Raggi and V. Kozhuharov. “Results and perspectives in dark photon physics”. In: *Riv. Nuovo Cim* 38.10 (2015), pp. 449–505. DOI: 10.1393/ncr/i2015-10117-9.

[6] M. A. Deliyergiyev. “Recent Progress in Search for Dark Sector Signatures,” in: *Open Phys.* 14.1 (2015), pp. 281–303. DOI: 10.1515/phys-2016-0034. arXiv: 1510.06927 [hep-ph].

[7] P. Harris, P. Schuster, and J. Zupan. “Snowmass White Paper: New flavors and rich structures in dark sectors”. In: (2022). DOI: 10.48550/arXiv.2207.08990. arXiv: 2207.08990 [hep-ph]. URL: https://arxiv.org/abs/2207.08990.

[8] F. Curciarello. “Review on Dark Photon”. In: *Eur. Phys. J. Conf.* 118.10 (2016), p. 01008. DOI: 10.1051/epjconf/201611801008.

[9] J. Beacham et al. “Physics Beyond Colliders at CERN: Beyond the Standard Model Working Group Report”. In: *J. Phys. G: Nucl. Part. Phys.* 47.1 (2020), p. 010501. DOI: 10.1088/1361-6471/ab4cd2. arXiv: 1901.09966 [hep-ex].

[10] Marco Fabbrichesi, Emidio Gabrielli, and Gaia Lafranchi. “The Dark Photon”. In: (2020). DOI: 10.1007/978-3-030-62519-1. arXiv: 2005.01515v3 [hep-ph].

[11] JiJi Fan et al. “A Dark-Disk Universe”. In: *Phys. Rev. Lett.* 110.21 (2013), p. 211302. DOI: 10.1103/PhysRevLett.110.211302. arXiv: 1303.3271 [hep-ph].

[12] N. Arkani-Hamed et al. “A theory of dark matter”. In: *Phys. Rev. D* 79.1 (2009), p. 015014.

[13] Emidio Gabrielli et al. “Dark photons and resonant monophoton signatures in Higgs boson decays at the LHC”. In: *Phys. Rev. D* 90.5 (2014), p. 055032. DOI: 10.1103/PhysRevD.90.055032. arXiv: 1405.5196 [hep-ph].

[14] Sanjoy Biswas et al. “Dark-Photon searches via Higgs-boson production at the LHC”. In: *Phys. Rev. D* 93.9 (2016), p. 093011. DOI: 10.1103/PhysRevD.93.093011. arXiv: 1603.01377 [hep-ph].

[15] Emidio Gabrielli and Raidal Marti. "Exponentially spread dynamical Yukawa couplings from non-perturbative chiral symmetry breaking in the dark sector". In: *Phys. Rev. D* 89 (2014), p. 015008. DOI: 10.1103/PhysRevD.89.015008.

[16] K. J. Kelly and Y.-D. Tsai. "Proton fixed-target scintillation experiment to search for milicharged dark matter". In: *Phys. Rev. D* 100.1 (2019), p. 015043. DOI: 10.1103/PhysRevD.100.015043. arXiv: 1812.03998 [hep-ph]. URL: http://dx.doi.org/10.1103/PhysRevD.100.015043.

[17] J. Jaeckel, M. Jankowiak, and M. Spannowsky. *LHC probes the hidden sector*. 2013. DOI: 10.1016/j.dark.2013.06.001. arXiv: 1212.3620 [hep-ph]. URL: http://dx.doi.org/10.1016/j.dark.2013.06.001.

[18] ATLAS Collaboration. "Search for dark matter in association with an energetic photon in $pp$ collisions at $\sqrt{s} = 13\,\text{TeV}$ with the ATLAS detector". In: *JHEP* 02 (2021), p. 226. DOI: 10.1007/JHEP02(2021)226. arXiv: 2011.05259 [hep-ex].

[19] CMS Collaboration. "Search for new physics in the monophoton final state in proton–proton collisions at $\sqrt{s} = 13\,\text{TeV}$". In: *JHEP* 10 (2017), p. 073. DOI: 10.1007/JHEP10(2017)073. arXiv: 1706.03794 [hep-ex].

[20] ATLAS Collaboration. "Search for displaced photons produced in exotic decays of the Higgs boson using 13 TeV $pp$ collisions with the ATLAS detector". In: (2022). DOI: 10.48550/arXiv.2209.01029. arXiv: 2209.01029 [hep-ex].

[21] CMS Collaboration. "Search for dark photons in decays of Higgs bosons produced in association with $Z$ bosons in proton–proton collisions at $\sqrt{s} = 13\,\text{TeV}$". In: *JHEP* 10 (2019), p. 139. DOI: 10.1007/JHEP10(2019)139. arXiv: 1908.02699 [hep-ex].

[22] CMS Collaboration. "Search for dark photons in Higgs boson production via vector boson fusion in proton–proton collisions at $\sqrt{s} = 13\,\text{TeV}$". In: *JHEP* 03 (2021), p. 011. DOI: 10.1007/JHEP03(2021)011. arXiv: 2009.14009 [hep-ex].

[23] ATLAS Collaboration. "Observation of electroweak production of two jets in association with an isolated photon and missing transverse momentum, and search for a Higgs boson decaying into invisible particles at 13 TeV with the ATLAS detector". In: *Eur. Phys. J. C* 82 (2021), p. 105. DOI: 10.1140/epjc/s10052-021-09878-z. arXiv: 2109.00925 [hep-ex].

[24] H. Fritzsch. *Quantum Field Theory*. World Scientific, 2017. ISBN: 9789813141728. URL: https://books.google.fr/books?id=sPuIDAEACAAJ.

[25] J. Zinn-Justin. *Quantum Field Theory and Critical Phenomena: Fifth Edition*. International series of monographs on physics. Oxford University Press, 2021. ISBN: 9780198834625. URL: https://books.google.fr/books?id=ioskEAAAQBAJ.

[26] T. Lancaster, S.J. Blundell, and S. Blundell. *Quantum Field Theory for the Gifted Amateur*. OUP Oxford, 2014. ISBN: 9780199699339. URL: https://books.google.fr/books?id=Y-0kAwAAQBAJ.

[27] Ronald Kleiss. *Quantum Field Theory: A Diagrammatic Approach*. Cambridge University Press, 2021. DOI: 10.1017/9781108665209.

[28] Rodrigo Arouca, Andrea Cappelli, and Hans Hansson. "Quantum Field Theory Anomalies in Condensed Matter Physics". In: *SciPost Physics Lecture Notes* (2022). DOI: 10.21468/scipostphyslectnotes.62. URL: https://doi.org/10.21468%2Fscipostphyslectnotes.62.

[29] W.N. Cottingham and D.A. Greenwood. *An introduction to the standard model of particle physics*. Cambridge University Press, Apr. 2007. ISBN: 978-0-511-27136-6, 978-0-521-85249-4.

[30] P.A. Zyla et al. "Review of Particle Physics". In: *PTEP* 2020.8 (2020). and 2021 update, p. 083C01. DOI: 10.1093/ptep/ptaa104.

[31] M. Herrero. "The Standard model". In: *NATO Sci. Ser. C* 534 (1999). Ed. by T. Ferbel, pp. 1–59. DOI: 10.1007/978-94-011-4689-0_1. arXiv: hep-ph/9812242.

[32] URL: <ahref="https://www.kindpng.com/imgv/JbRoTm_standard-model-of-particle-physics-hd-png-download/"target="_blank">StandardModelOfParticlePhysics,HDPngDownload@kindpng.com</a>.

[33] Y. Fukuda et al. "Measurement of the flux and zenith angle distribution of upward through going muons by Super-Kamiokande". In: *Phys. Rev. Lett.* 82 (1999), pp. 2644–2648. DOI: 10.1103/PhysRevLett.82.2644. arXiv: hep-ex/9812014.

[34] Q.R. Ahmad et al. "Direct evidence for neutrino flavor transformation from neutral current interactions in the Sudbury Neutrino Observatory". In: *Phys. Rev. Lett.* 89 (2002), p. 011301. DOI: 10.1103/PhysRevLett.89.011301. arXiv: nucl-ex/0204008.

[35] K. Eguchi et al. "First results from KamLAND: Evidence for reactor anti-neutrino disappearance". In: *Phys. Rev. Lett.* 90 (2003), p. 021802. DOI: 10.1103/PhysRevLett.90.021802. arXiv: hep-ex/0212021.

[36] F. Englert and R. Brout. "Broken Symmetry and the Mass of Gauge Vector Mesons". In: *Phys. Rev. Lett.* 13 (1964). Ed. by J.C. Taylor, pp. 321–323. DOI: 10.1103/PhysRevLett.13.321.

[37] Peter W. Higgs. "Broken Symmetries and the Masses of Gauge Bosons". In: *Phys. Rev. Lett.* 13 (1964). Ed. by J.C. Taylor, pp. 508–509. DOI: 10.1103/PhysRevLett.13.508.

[38] Georges Aad et al. "Observation of a new particle in the search for the Standard Model Higgs boson with the ATLAS detector at the LHC". In: *Phys. Lett. B* 716 (2012), pp. 1–29. DOI: 10.1016/j.physletb.2012.08.020. arXiv: 1207.7214 [hep-ex].

[39] Serguei Chatrchyan et al. "Observation of a New Boson at a Mass of 125 GeV with the CMS Experiment at the LHC". In: *Phys. Lett. B* 716 (2012), pp. 30–61. DOI: 10.1016/j.physletb.2012.08.021. arXiv: 1207.7235 [hep-ex].

[40] C. Abel et al. "Measurement of the permanent electric dipole moment of the neutron". In: *Phys. Rev. Lett.* 124.8 (2020), p. 081803. DOI: 10.1103/PhysRevLett.124.081803. arXiv: 2001.11966 [hep-ex].

[41] M. Tanabashi et al. "Review of Particle Physics". In: *Phys. Rev. D* 98.3 (2018), p. 030001. DOI: 10.1103/PhysRevD.98.030001.

[42] R.N. Mohapatra. "Seesaw mechanism and its implications". In: *SEESAW25: International Conference on the Seesaw Mechanism and the Neutrino Mass*. Dec. 2004, pp. 29–44. DOI: 10.1142/9789812702210_0003. arXiv: hep-ph/0412379.

[43] Frank F. Deppisch, P.S. Bhupal Dev, and Apostolos Pilaftsis. "Neutrinos and Collider Physics". In: *New J. Phys.* 17.7 (2015), p. 075019. DOI: 10.1088/1367-2630/17/7/075019. arXiv: 1502.06541 [hep-ph].

[44] Benoit Famaey and Stacy McGaugh. "Modified Newtonian Dynamics (MOND): Observational Phenomenology and Relativistic Extensions". In: *Living Rev. Rel.* 15 (2012), p. 10. DOI: 10.12942/lrr-2012-10. arXiv: 1112.3960 [astro-ph.CO].

[45] P. G. Ferreira and G. D. Starkman. "Einstein's Theory of Gravity and the Problem of Missing Mass". In: *Science* 326.5954 (2009), pp. 812–815. ISSN: 1095-9203. DOI: 10.1126/science.1172245. URL: http://dx.doi.org/10.1126/science.1172245.

[46] Timothy Clifton et al. "Modified Gravity and Cosmology". In: *Phys. Rept.* 513 (2012), pp. 1–189. DOI: 10.1016/j.physrep.2012.01.001. arXiv: 1106.2476 [astro-ph.CO].

[47] Edvige Corbelli and Paolo Salucci. "The Extended Rotation Curve and the Dark Matter Halo of M33". In: *Mon. Not. Roy. Astron. Soc.* 311 (2000), pp. 441–447. DOI: 10.1046/j.1365-8711.2000.03075.x. arXiv: astro-ph/9909252.

[48] I.A. Yegorova et al. "Rotation curves of luminous spiral galaxies". In: *Astron. Astrophys. Trans.* 27 (2012), p. 335. arXiv: 1110.1925 [astro-ph.CO].

[49] Maxim Markevitch. "Chandra observation of the most interesting cluster in the universe". In: *ESA Spec. Publ.* 604 (2006), p. 723. arXiv: astro-ph/0511345.

[50] Marusa Bradac et al. "Revealing the properties of dark matter in the merging cluster MACSJ0025.4-1222". In: *Astrophys. J.* 687 (2008), p. 959. DOI: 10.1086/591246. arXiv: 0806.2320 [astro-ph].

[51] Adi Zitrin et al. "The Largest Known Einstein Radius: MACS J0717.5+3745 (z=0.546)". In: *Astrophys. J. Lett.* 707 (2009), p. L102. DOI: 10.1088/0004-637X/707/1/L102. arXiv: 0907.4232 [astro-ph.CO].

[52] Y. Akrami et al. "Planck 2018 results. I. Overview and the cosmological legacy of Planck". In: *Astron. Astrophys.* 641 (2020), A1. DOI: 10.1051/0004-6361/201833880. arXiv: 1807.06205 [astro-ph.CO].

[53] Y. Akrami et al. "Planck 2018 results. IV. Diffuse component separation". In: (2018). arXiv: 1807.06208 [astro-ph.CO].

[54] N. Aghanim et al. "Planck 2018 results. VI. Cosmological parameters". In: *Astron. Astrophys.* 641 (2020), A6. DOI: 10.1051/0004-6361/201833910. arXiv: 1807.06209 [astro-ph.CO].

[55] Scott Dodelson. *Modern Cosmology*. Amsterdam: Academic Press, 2003. ISBN: 978-0-12-219141-1.

[56] Bob Holdom. "Two U(1)'s and $\epsilon$ charge shifts". In: *Physics Letters B* 166.2 (1986), pp. 196–198. ISSN: 0370-2693. DOI: https://doi.org/10.1016/0370-2693(86)91377-8. URL: https://www.sciencedirect.com/science/article/pii/0370269386913778.

[57] F. del Aguila, M. Masip, and M. Pérez-Victoria. "Physical parameters and renormalization of U(1)a × U (1)b models". In: *Nuclear Physics B* 456.3 (1995), pp. 531–549. ISSN: 0550-3213. DOI: https://doi.org/10.1016/0550-3213(95)00511-6. URL: https://www.sciencedirect.com/science/article/pii/0550321395005116.

[58] Daniel Feldman, Zuowei Liu, and Pran Nath. "Stueckelberg $Z^{'}$ extension with kinetic mixing and millicharged dark matter from the hidden sector". In: *Phys. Rev. D* 75 (11 2007), p. 115001. DOI: 10.1103/PhysRevD.75.115001. URL: https://link.aps.org/doi/10.1103/PhysRevD.75.115001.

[59] Sacha Davidson, Steen Hannestad, and Georg Raffelt. "Updated bounds on milli-charged particles". In: *Journal of High Energy Physics* 2000.05 (2000), pp. 003–003. DOI: 10.1088/1126-6708/2000/05/003. URL: https://doi.org/10.1088%2F1126-6708%2F2000%2F05%2F003.

[60] HENRI RUEGG and MARTÍ RUIZ-ALTABA. "THE STUECKELBERG FIELD". In: *International Journal of Modern Physics A* 19.20 (2004), pp. 3265–3347. DOI: 10.1142/s0217751x04019755. URL: https://doi.org/10.1142%2Fs0217751x04019755.

[61] B. Grzadkowski et al. "Dimension-Six Terms in the Standard Model Lagrangian". In: *JHEP* 10 (2010), p. 085. DOI: 10.1007/JHEP10(2010)085. arXiv: 1008.4884 [hep-ph].

[62] Haim Goldberg and Lawrence J. Hall. "A New Candidate for Dark Matter". In: *Phys. Lett.* B174 (1986). [,467(1986)], p. 151. DOI: 10.1016/0370-2693(86)90731-8.

[63] Bob Holdom. "Searching for $\epsilon$ Charges and a New U(1)". In: *Phys. Lett.* B178 (1986), pp. 65–70. DOI: 10.1016/0370-2693(86)90470-3.

[64] Ben-Ami Gradwohl and Joshua A. Frieman. "Dark matter, long range forces, and large scale structure". In: *Astrophys. J.* 398 (1992), pp. 407–424. DOI: 10.1086/171865.

[65] Eric D. Carlson, Marie E. Machacek, and Lawrence J. Hall. "Self-interacting dark matter". In: *Astrophys. J.* 398 (1992), pp. 43–52. DOI: 10.1086/171833.

[66] Robert Foot. "Mirror matter-type dark matter". In: *Int. J. Mod. Phys.* D13 (2004), pp. 2161–2192. DOI: 10.1142/S0218271804006449. arXiv: astro-ph/0407623 [astro-ph].

[67] Jonathan L. Feng, Huitzu Tu, and Hai-Bo Yu. "Thermal Relics in Hidden Sectors". In: *JCAP* 0810 (2008), p. 043. DOI: 10.1088/1475-7516/2008/10/043. arXiv: 0808.2318 [hep-ph].

[68] Lotty Ackerman et al. "Dark Matter and Dark Radiation". In: *Phys. Rev.* D79 (2009). [,277(2008)], p. 023519. DOI: 10.1103/PhysRevD.79.023519, 10.1142/9789814293792_0021. arXiv: 0810.5126 [hep-ph].

[69] Jonathan L. Feng et al. "Hidden Charged Dark Matter". In: *JCAP* 0907 (2009), p. 004. DOI: 10.1088/1475-7516/2009/07/004. arXiv: 0905.3039 [hep-ph].

[70] Nima Arkani-Hamed et al. "A Theory of Dark Matter". In: *Phys. Rev.* D79 (2009), p. 015014. DOI: 10.1103/PhysRevD.79.015014. arXiv: 0810.0713 [hep-ph].

[71] David E. Kaplan et al. "Atomic Dark Matter". In: *JCAP* 1005 (2010), p. 021. DOI: 10.1088/1475-7516/2010/05/021. arXiv: 0909.0753 [hep-ph].

[72] Matthew R. Buckley and Patrick J. Fox. "Dark Matter Self-Interactions and Light Force Carriers". In: *Phys. Rev.* D81 (2010), p. 083522. DOI: 10.1103/PhysRevD.81.083522. arXiv: 0911.3898 [hep-ph].

[73] Dan Hooper, Neal Weiner, and Wei Xue. "Dark Forces and Light Dark Matter". In: *Phys. Rev.* D86 (2012), p. 056009. DOI: 10.1103/PhysRevD.86.056009. arXiv: 1206.2929 [hep-ph].

[74] Laura G. van den Aarssen, Torsten Bringmann, and Christoph Pfrommer. "Is dark matter with long-range interactions a solution to all small-scale problems of $\Lambda$ CDM cosmology?" In: *Phys. Rev. Lett.* 109 (2012), p. 231301. DOI: 10.1103/PhysRevLett.109.231301. arXiv: 1205.5809 [astro-ph.CO].

[75] James M. Cline, Zuowei Liu, and Wei Xue. "Millicharged Atomic Dark Matter". In: *Phys. Rev.* D85 (2012), p. 101302. DOI: 10.1103/PhysRevD.85.101302. arXiv: 1201.4858 [hep-ph].

[76] Sean Tulin, Hai-Bo Yu, and Kathryn M. Zurek. "Beyond Collisionless Dark Matter: Particle Physics Dynamics for Dark Matter Halo Structure". In: *Phys. Rev.* D87.11 (2013), p. 115007. DOI: 10.1103/PhysRevD.87.115007. arXiv: 1302.3898 [hep-ph].

[77] Emidio Gabrielli and Martti Raidal. "Exponentially spread dynamical Yukawa couplings from nonperturbative chiral symmetry breaking in the dark sector". In: *Phys. Rev.* D89.1 (2014), p. 015008. DOI: 10.1103/PhysRevD.89.015008. arXiv: 1310.1090 [hep-ph].

[78] Marco Baldi. "Structure formation in Multiple Dark Matter cosmologies with long-range scalar interactions". In: *Mon. Not. Roy. Astron. Soc.* 428 (2013), p. 2074. DOI: 10.1093/mnras/sts169. arXiv: 1206.2348 [astro-ph.CO].

[79] Francis-Yan Cyr-Racine and Kris Sigurdson. "Cosmology of atomic dark matter". In: *Phys. Rev.* D87.10 (2013), p. 103515. DOI: 10.1103/PhysRevD.87.103515. arXiv: 1209.5752 [astro-ph.CO].

[80] James M. Cline et al. "Composite strongly interacting dark matter". In: *Phys. Rev.* D90.1 (2014), p. 015023. DOI: 10.1103/PhysRevD.90.015023. arXiv: 1312.3325 [hep-ph].

[81] Xiaoyong Chu and Basudeb Dasgupta. "Dark Radiation Alleviates Problems with Dark Matter Halos". In: *Phys. Rev. Lett.* 113.16 (2014), p. 161301. DOI: 10.1103/PhysRevLett.113.161301. arXiv: 1404.6127 [hep-ph].

[82] Kimberly K. Boddy et al. "Self-Interacting Dark Matter from a Non-Abelian Hidden Sector". In: *Phys. Rev.* D89.11 (2014), p. 115017. DOI: 10.1103/PhysRevD.89.115017. arXiv: 1402.3629 [hep-ph].

[83] Manuel A. Buen-Abad, Gustavo Marques-Tavares, and Martin Schmaltz. "Non-Abelian dark matter and dark radiation". In: *Phys. Rev.* D92.2 (2015), p. 023531. DOI: 10.1103/PhysRevD.92.023531. arXiv: 1505.03542 [hep-ph].

[84] Prateek Agrawal et al. "Make Dark Matter Charged Again". In: *JCAP* 1705.05 (2017), p. 022. DOI: 10.1088/1475-7516/2017/05/022. arXiv: 1610.04611 [hep-ph].

[85] Douglas Clowe et al. "A direct empirical proof of the existence of dark matter". In: *Astrophys. J. Lett.* 648 (2006), pp. L109–L113. DOI: 10.1086/508162. arXiv: astro-ph/0608407.

[86] Jonathan L. Feng, Manoj Kaplinghat, and Hai-Bo Yu. "Halo Shape and Relic Density Exclusions of Sommerfeld-Enhanced Dark Matter Explanations of Cosmic Ray Excesses". In: *Phys. Rev. Lett.* 104 (2010), p. 151301. DOI: 10.1103/PhysRevLett.104.151301. arXiv: 0911.0422 [hep-ph].

[87] Tongyan Lin, Hai-Bo Yu, and Kathryn M. Zurek. "On Symmetric and Asymmetric Light Dark Matter". In: *Phys. Rev.* D85 (2012), p. 063503. DOI: 10.1103/PhysRevD.85.063503. arXiv: 1111.0293 [hep-ph].

[88] Annika H. G. Peter et al. "Cosmological Simulations with Self-Interacting Dark Matter II: Halo Shapes vs. Observations". In: *Mon. Not. Roy. Astron. Soc.* 430 (2013), p. 105. DOI: 10.1093/mnras/sts535. arXiv: 1208.3026 [astro-ph.CO].

[89] Maxim Pospelov and Tonnis ter Veldhuis. "Direct and indirect limits on the electromagnetic form-factors of WIMPs". In: *Phys. Lett. B* 480 (2000), pp. 181–186. DOI: 10.1016/S0370-2693(00)00358-0. arXiv: hep-ph/0003010.

[90] Kris Sigurdson et al. "Dark-matter electric and magnetic dipole moments". In: *Phys. Rev.* D70 (2004). [Erratum: Phys. Rev.D73,089903(2006)], p. 083501. DOI: 10.1103/PhysRevD.70.083501, 10.1103/PhysRevD.73.089903. arXiv: astro-ph/0406355 [astro-ph].

[91] Tom Banks, Jean-Francois Fortin, and Scott Thomas. "Direct Detection of Dark Matter Electromagnetic Dipole Moments". In: (2010). arXiv: 1007.5515 [hep-ph].

[92] Vernon Barger, Wai-Yee Keung, and Danny Marfatia. "Electromagnetic properties of dark matter: Dipole moments and charge form factor". In: *Phys. Lett. B* 696 (2011), pp. 74–78. DOI: 10.1016/j.physletb.2010.12.008. arXiv: 1007.4345 [hep-ph].

[93] N. Fornengo, P. Panci, and M. Regis. "Long-Range Forces in Direct Dark Matter Searches". In: *Phys. Rev. D* 84 (2011), p. 115002. DOI: 10.1103/PhysRevD.84.115002. arXiv: 1108.4661 [hep-ph].

[94] Eugenio Del Nobile et al. "Light Magnetic Dark Matter in Direct Detection Searches". In: *JCAP* 08 (2012), p. 010. DOI: 10.1088/1475-7516/2012/08/010. arXiv: 1203.6652 [hep-ph].

[95] Xiaoyong Chu, Jui-Lin Kuo, and Josef Pradler. "Dark sector-photon interactions in proton-beam experiments". In: *Phys. Rev. D* 101 (2020), p. 075035. DOI: 10.1103/PhysRevD.101.075035. arXiv: 2001.06042 [hep-ph].

[96] A. Liam Fitzpatrick et al. "The Effective Field Theory of Dark Matter Direct Detection". In: *JCAP* 1302 (2013), p. 004. DOI: 10.1088/1475-7516/2013/02/004. arXiv: 1203.3542 [hep-ph].

[97] Sebastian Liem et al. "Effective field theory of dark matter: a global analysis". In: *JHEP* 09 (2016), p. 077. DOI: 10.1007/JHEP09(2016)077. arXiv: 1603.05994 [hep-ph].

[98] Joachim Brod et al. "Effective Field Theory for Dark Matter Direct Detection up to Dimension Seven". In: *JHEP* 10 (2018), p. 065. DOI: 10.1007/JHEP10(2018)065. arXiv: 1710.10218 [hep-ph].

[99] Eduardo Cortina Gil et al. "The Beam and detector of the NA62 experiment at CERN". In: *JINST* 12.05 (2017), P05025. DOI: 10.1088/1748-0221/12/05/P05025. arXiv: 1703.08501 [physics.ins-det].

[100] M. Fabbrichesi, E. Gabrielli, and B. Mele. "Hunting down massless dark photons in kaon physics". In: *Phys. Rev. Lett.* 119.3 (2017), p. 031801. DOI: 10.1103/PhysRevLett.119.031801. arXiv: 1705.03470 [hep-ph].

[101] Eduardo Cortina Gil et al. "First search for $K^+ \to \pi^+ \nu\bar{\nu}$ using the decay-in-flight technique". In: *Phys. Lett. B* 791 (2019), pp. 156–166. DOI: 10.1016/j.physletb.2019.01.067. arXiv: 1811.08508 [hep-ex].

[102] J.K. Ahn et al. "Search for the $K_L \to \pi^0 \nu\bar{\nu}$ and $K_L \to \pi^0 X^0$ decays at the J-PARC KOTO experiment". In: *Phys. Rev. Lett.* 122.2 (2019), p. 021802. DOI: 10.1103/PhysRevLett.122.021802. arXiv: 1810.09655 [hep-ex].

[103] Marco Fabbrichesi and Emidio Gabrielli. "Dark-sector physics in the search for the rare decays $K^+ \to \pi^+ \nu\bar{\nu}$ and $K_L \to \pi^0 \nu\bar{\nu}$". In: *Eur. Phys. J. C* 80.6 (2020), p. 532. DOI: 10.1140/epjc/s10052-020-8103-7. arXiv: 1911.03755 [hep-ph].

[104] Jhih-Ying Su and Jusak Tandean. "Searching for dark photons in hyperon decays". In: (2019). arXiv: 1911.13301 [hep-ph].

[105] Jhih-Ying Su and Jusak Tandean. "Seeking massless dark photons in the decays of charmed hadrons". In: (2020). arXiv: 2005.05297 [hep-ph].

[106] J. P. Lees et al. "Improved Limits on $B^0$ Decays to Invisible Final States and to $\nu\bar{\nu}\gamma$". In: *Phys. Rev.* D86 (2012), p. 051105. DOI: 10.1103/PhysRevD.86.051105. arXiv: 1206.2543 [hep-ex].

[107] C. L. Hsu et al. "Search for $B^0$ decays to invisible final states". In: *Phys. Rev.* D86 (2012), p. 032002. DOI: 10.1103/PhysRevD.86.032002. arXiv: 1206.5948 [hep-ex].

[108] S. N. Gninenko and N. V. Krasnikov. "Invisible $K_L$ decays as a probe of new physics". In: *Phys. Rev.* D92.3 (2015), p. 034009. DOI: 10.1103/PhysRevD.92.034009. arXiv: 1503.01595 [hep-ph].

[109] S. N. Gninenko. "Search for invisible decays of $\pi^0, \eta, \eta', K_S$ and $K_L$: A probe of new physics and tests using the Bell-Steinberger relation". In: *Phys. Rev.* D91.1 (2015), p. 015004. DOI: 10.1103/PhysRevD.91.015004. arXiv: 1409.2288 [hep-ph].

[110] A. Sommerfeld. "Über die Beugung und Bremsung der Elektronen". In: *Annalen der Physik* 403 (1931), p. 257.

[111] E. Fermi. "An attempt of a theory of beta radiation. 1." In: *Zeitschrift für Physik* 88 (1934), p. 161.

[112] D. Barducci, M. Fabbrichesi, and E. Gabrielli. "Neutral Hadrons Disappearing into the Darkness". In: *Phys. Rev.* D98.3 (2018), p. 035049. DOI: 10.1103/PhysRevD.98.035049. arXiv: 1806.05678 [hep-ph].

[113] Sanjoy Biswas et al. "Higgs-boson production in association with a dark photon in $e^+e^?$ collisions". In: *JHEP* 06 (2015), p. 102. DOI: 10.1007/JHEP06(2015)102. arXiv: 1503.05836 [hep-ph].

[114] Sanjoy Biswas et al. "Dark-photon searches via $ZH$ production at $e^+e^-$ colliders". In: *Phys. Rev.* D96.5 (2017), p. 055012. DOI: 10.1103/PhysRevD.96.055012. arXiv: 1703.00402 [hep-ph].

[115] M. Fabbrichesi, E. Gabrielli, and B. Mele. "Z Boson Decay into Light and Darkness". In: *Phys. Rev. Lett.* 120.17 (2018), p. 171803. DOI: 10.1103/PhysRevLett.120.171803. arXiv: 1712.05412 [hep-ph].

[116] M. Cobal et al. "$Z$-boson decays into an invisible dark photon at the LHC, HL-LHC and future lepton colliders". In: *Phys. Rev. D* 102.3 (2020), p. 035027. DOI: 10.1103/PhysRevD.102.035027. arXiv: 2006.15945 [hep-ph].

[117] R. Barbieri et al. "Searching for galactic axions through magnetized media: the QUAX proposal". In: *Phys. Dark Univ.* 15 (2017), pp. 135–141. DOI: 10.1016/j.dark.2017.01.003. arXiv: 1606.02201 [hep-ph].

[118] So Chigusa, Takeo Moroi, and Kazunori Nakayama. "Detecting Light Boson Dark Matter through Conversion into Magnon". In: (2020). arXiv: 2001.10666 [hep-ph].

[119] Djuna Croon et al. "Hidden-Sector Spectroscopy with Gravitational Waves from Binary Neutron Stars". In: *Astrophys. J.* 858.1 (2018), p. L2. DOI: 10.3847/2041-8213/aabe76. arXiv: 1711.02096 [hep-ph].

[120] Stephon Alexander et al. "Hidden-Sector Modifications to Gravitational Waves From Binary Inspirals". In: *Class. Quant. Grav.* 35.23 (2018), p. 235012. DOI: 10.1088/1361-6382/aaeb5c. arXiv: 1808.05286 [gr-qc].

[121] Joachim Kopp et al. "Cuckoo's eggs in neutron stars: can LIGO hear chirps from the dark sector?" In: *JHEP* 11 (2018), p. 096. DOI: 10.1007/JHEP11(2018)096. arXiv: 1807.02527 [hep-ph].

[122] Marco Fabbrichesi and Alfredo Urbano. "Charged neutron stars and observational tests of a dark force weaker than gravity". In: (2019). arXiv: 1902.07914 [hep-ph].

[123] Fabienne Marcastel. "CERN's Accelerator Complex. La chaine des accélérateurs du CERN". In: (2013). General Photo. URL: https://cds.cern.ch/record/1621583.

[124] "LHC Design Report Vol.1: The LHC Main Ring". In: (2004). Ed. by Oliver S. Bruning et al. DOI: 10.5170/CERN-2004-003-V-1.

[125] "LHC Design Report. 2. The LHC infrastructure and general services". In: (2004). Ed. by O. Buning et al. DOI: 10.5170/CERN-2004-003-V-2.

[126] D. Boussard and T. Linnecar. "The LHC Superconducting RF System". In: *Adv. Cryog. Eng. A* 45 (2000). Ed. by Q.S. Shu et al., pp. 835–844.

[127] ATLAS Collaboration. *ATLAS online luminosity public plots*. 2018. URL: https://twiki.cern.ch/twiki/bin/view/AtlasPublic/LuminosityPublicResultsRun2 (visited on 09/14/2020).

[128] G. Aad et al. "The ATLAS Experiment at the CERN Large Hadron Collider". In: *JINST* 3 (2008), S08003. DOI: 10.1088/1748-0221/3/08/S08003.

[129] "ATLAS: Letter of intent for a general purpose p p experiment at the large hadron collider at CERN". In: (1992).

[130] W.W. Armstrong et al. "ATLAS: Technical proposal for a general-purpose p p experiment at the Large Hadron Collider at CERN". In: (1994).

[131] GEANT4 Collaboration, S. Agostinelli, et al. "GEANT4 – a simulation toolkit". In: *Nucl. Instrum. Meth. A* 506 (2003), p. 250. DOI: 10.1016/S0168-9002(03)01368-8.

[132] "ATLAS inner detector: Technical design report. Vol. 1". In: (1997).

[133] "ATLAS inner detector: Technical design report. Vol. 2". In: (1997).

[134] M.S. Alam et al. "ATLAS pixel detector: Technical design report". In: (1998).

[135] G. Aad et al. "ATLAS pixel detector electronics and sensors". In: *JINST* 3 (2008), P07007. DOI: 10.1088/1748-0221/3/07/P07007.

[136] M. Capeans et al. "ATLAS Insertable B-Layer Technical Design Report". In: (2010).

[137] Ashfaq Ahmad et al. "The silicon microstrip sensors of the ATLAS semiconductor tracker". In: *Nuclear Instruments and Methods in Physics Research Section A: Accelerators, Spectrometers, Detectors and Associated Equipment* 578 (2007), pp. 98–118. DOI: 10.1016/j.nima.2007.04.157.

[138] E. Abat et al. "The ATLAS TRT barrel detector". In: *JINST* 3 (2008), P02014. DOI: 10.1088/1748-0221/3/02/P02014.

[139] E. Abat et al. "The ATLAS TRT end-cap detectors". In: *JINST* 3 (2008), P10003. DOI: 10.1088/1748-0221/3/10/P10003.

[140] ATLAS Group et al. "Construction, assembly and tests of the ATLAS electromagnetic end-cap calorimeters". In: *Journal of Instrumentation* 3 (2008), P06002. DOI: 10.1088/1748-0221/3/06/P06002.

[141] *ATLAS liquid-argon calorimeter: Technical Design Report*. Technical Design Report ATLAS. Geneva: CERN, 1996. URL: https://cds.cern.ch/record/331061.

[142] Moustapha Thioye and Michael Rijssenbeek. "Topics in the measurement of electrons with the ATLAS detector at the LHC". In: (2008).

[143] C.W. Fabjan and F. Gianotti. "Calorimetry for particle physics". In: *Rev. Mod. Phys.* 75 (2003), pp. 1243–1286. DOI: 10.1103/RevModPhys.75.1243.

[144] "ATLAS tile calorimeter: Technical design report". In: (1996).

[145] "ATLAS muon spectrometer: Technical design report". In: (1997).

[146] *ATLAS magnet system: Technical Design Report, 1*. Technical Design Report ATLAS. Geneva: CERN, 1997. URL: https://cds.cern.ch/record/338080.

[147] Morad Aaboud et al. "Luminosity determination in pp collisions at $\sqrt{s}$ = 8 TeV using the ATLAS detector at the LHC". In: *Eur. Phys. J. C* 76.12 (2016), p. 653. DOI: 10.1140/epjc/s10052-016-4466-1. arXiv: 1608.03953 [hep-ex].

[148] "Luminosity determination in $pp$ collisions at $\sqrt{s} = 13$ TeV using the ATLAS detector at the LHC". In: (2019).

[149] Federico Lasagni Manghi. "LUCID: The ATLAS Luminosity Detector". In: *PoS* ICHEP2018 (2019), p. 280. DOI: 10.22323/1.340.0280.

[150] G. Avoni et al. "The new LUCID-2 detector for luminosity measurement and monitoring in ATLAS". In: *JINST* 13.07 (2018), P07017. DOI: 10.1088/1748-0221/13/07/P07017.

[151] V. Cindro et al. "The ATLAS beam conditions monitor". In: *JINST* 3 (2008), P02004. DOI: 10.1088/1748-0221/3/02/P02004.

[152] William Panduro Vazquez and ATLAS Collaboration. *The ATLAS Data Acquisition system in LHC Run 2*. Tech. rep. ATL-DAQ-PROC-2017-007. 3. Geneva: CERN, 2017. DOI: 10.1088/1742-6596/898/3/032017. URL: https://cds.cern.ch/record/2244345.

[153] G. Aad et al. "The ATLAS Simulation Infrastructure". In: *Eur. Phys. J.* C70 (2010), pp. 823–874. DOI: 10.1140/epjc/s10052-010-1429-9. arXiv: 1005.4568 [physics.ins-det].

[154] J. Alwall et al. "The automated computation of tree-level and next-to-leading order differential cross sections, and their matching to parton shower simulations". In: *JHEP* 07 (2014), p. 079. DOI: 10.1007/JHEP07(2014)079. arXiv: 1405.0301 [hep-ph].

[155] Johannes Bellm et al. "Herwig 7.0/Herwig++ 3.0 release note". In: *Eur. Phys. J. C* 76.4 (2016), p. 196. DOI: 10.1140/epjc/s10052-016-4018-8. arXiv: 1512.01178 [hep-ph].

[156] T. Cornelissen et al. "The new ATLAS track reconstruction (NEWT)". In: *J. Phys. Conf. Ser.* 119 (2008), p. 032014. DOI: 10.1088/1742-6596/119/3/032014.

[157] M. Aaboud et al. "Performance of the ATLAS Track Reconstruction Algorithms in Dense Environments in LHC Run 2". In: *Eur. Phys. J. C* 77.10 (2017), p. 673. DOI: 10.1140/epjc/s10052-017-5225-7. arXiv: 1704.07983 [hep-ex].

[158] Azriel Rosenfeld and John L. Pfaltz. "Sequential Operations in Digital Picture Processing." In: *J. ACM* 13.4 (1966), pp. 471–494. URL: http://dblp.uni-trier.de/db/journals/jacm/jacm13.html#Pfaltz66.

[159] R. Fruhwirth. "Application of Kalman filtering to track and vertex fitting". In: *Nucl. Instrum. Meth. A* 262 (1987), pp. 444–450. DOI: 10.1016/0168-9002(87)90887-4.

[160] Georges Aad et al. "Charged-particle distributions in $\sqrt{s}$ = 13 TeV pp interactions measured with the ATLAS detector at the LHC". In: *Phys. Lett. B* 758 (2016), pp. 67–88. DOI: 10.1016/j.physletb.2016.04.050. arXiv: 1602.01633 [hep-ex].

[161] Georges Aad et al. "Topological cell clustering in the ATLAS calorimeters and its performance in LHC Run 1". In: *Eur. Phys. J.* C77 (2017), p. 490. DOI: 10.1140/epjc/s10052-017-5004-5. arXiv: 1603.02934 [hep-ex].

[162] Matteo Cacciari, Gavin P. Salam, and Gregory Soyez. "The anti-$k_t$ jet clustering algorithm". In: *JHEP* 04 (2008), p. 063. DOI: 10.1088/1126-6708/2008/04/063. arXiv: 0802.1189 [hep-ph].

[163] Morad Aaboud et al. "Determination of jet calibration and energy resolution in proton-proton collisions at $\sqrt{s}$ = 8 TeV using the ATLAS detector". In: (Oct. 2019). arXiv: 1910.04482 [hep-ex].

[164] ATLAS Collaboration. "Jet energy scale measurements and their systematic uncertainties in proton-proton collisions at $\sqrt{s}$ = 13 TeV with the ATLAS detector". In: *Phys. Rev.* D96.7 (2017), p. 072002. DOI: 10.1103/PhysRevD.96.072002. arXiv: 1703.09665 [hep-ex].

[165] D. Buskulic et al. "Performance of the ALEPH detector at LEP". In: *Nucl. Instrum. Meth. A* 360 (1995), pp. 481–506. DOI: 10.1016/0168-9002(95)00138-7.

[166] Morad Aaboud et al. "Jet reconstruction and performance using particle flow with the ATLAS Detector". In: *Eur. Phys. J. C* 77.7 (2017), p. 466. DOI: 10.1140/epjc/s10052-017-5031-2. arXiv: 1703.10485 [hep-ex].

[167] The ATLAS collaboration. "Tagging and suppression of pileup jets". In: (2014).

[168] Andreas Hocker et al. "TMVA - Toolkit for Multivariate Data Analysis". In: (Mar. 2007). arXiv: physics/0703039.

[169] Georges Aad et al. "Electron and photon performance measurements with the ATLAS detector using the 2015–2017 LHC proton-proton collision data". In: *JINST* 14.12 (2019), P12006. DOI: 10.1088/1748-0221/14/12/P12006. arXiv: 1908.00005 [hep-ex].

[170] E. Hines. "Particle Identification with the ATLAS Transition Radiation Tracker". In: (Nov. 2011).

[171] Georges Aad et al. "Muon reconstruction performance of the ATLAS detector in proton–proton collision data at $\sqrt{s}$ =13 TeV". In: *Eur. Phys. J. C* 76.5 (2016), p. 292. DOI: 10.1140/epjc/s10052-016-4120-y. arXiv: 1603.05598 [hep-ex].

[172] Morad Aaboud et al. "Performance of missing transverse momentum reconstruction with the ATLAS detector using proton-proton collisions at $\sqrt{s}$ = 13 TeV". In: *Eur. Phys. J. C* 78.11 (2018), p. 903. DOI: 10.1140/epjc/s10052-018-6288-9. arXiv: 1802.08168 [hep-ex].

[173] "Data-driven determination of the energy scale and resolution of jets reconstructed in the ATLAS calorimeters using dijet and multijet events at $\sqrt{s} = 8$ *TeV*". In: (2015).

[174] ATLAS Collaboration. "ATLAS data quality operations and performance for 2015–2018 data-taking". In: *JINST* 15 (2020), P04003. DOI: 10.1088/1748-0221/15/04/P04003. arXiv: 1911.04632 [physics.ins-det].

[175] ATLAS Collaboration. "Performance of the ATLAS muon triggers in Run 2". In: *JINST* 15 (2020), P09015. DOI: 10.1088/1748-0221/15/09/p09015. arXiv: 2004.13447 [hep-ex].

[176] ATLAS Collaboration. "Performance of electron and photon triggers in ATLAS during LHC Run 2". In: *Eur. Phys. J. C* 80 (2020), p. 47. DOI: 10.1140/epjc/s10052-019-7500-2. arXiv: 1909.00761 [hep-ex].

[177] ATLAS Collaboration. "Operation of the ATLAS trigger system in Run 2". In: *JINST* 15 (2020), P10004. DOI: 10.1088/1748-0221/15/10/P10004. arXiv: 2007.12539 [hep-ex].

[178] ATLAS Collaboration. "The ATLAS Simulation Infrastructure". In: *Eur. Phys. J. C* 70 (2010), p. 823. DOI: 10.1140/epjc/s10052-010-1429-9. arXiv: 1005.4568 [physics.ins-det].

[179] T. Sjöstrand, S. Mrenna, and P. Skands. "A brief introduction to PYTHIA 8.1". In: *Comput. Phys. Commun.* 178 (2008), pp. 852–867. DOI: 10.1016/j.cpc.2008.01.036. arXiv: 0710.3820 [hep-ph].

[180] ATLAS Collaboration. *The Pythia 8 A3 tune description of ATLAS minimum bias and inelastic measurements incorporating the Donnachie–Landshoff diffractive model*. ATL-PHYS-PUB-2016-017. 2016. URL: https://cds.cern.ch/record/2206965.

[181] ATLAS Collaboration. "AtlFast3: The Next Generation of Fast Simulation in ATLAS". In: *Comput. Softw. Big Sci.* 6.7 (2022). DOI: 10.1007/s41781-021-00079-7. arXiv: 2109.02551 [hep-ex].

[182] T. Gleisberg et al. "Event generation with SHERPA 1.1". In: *JHEP* 02 (2009), p. 007. DOI: 10.1088/1126-6708/2009/02/007. arXiv: 0811.4622 [hep-ph].

[183] D. J. Lange. "The EvtGen particle decay simulation package". In: *Nucl. Instrum. Meth. A* 462 (2001), p. 152. DOI: 10.1016/S0168-9002(01)00089-4.

[184] D. de Florian et al. "Handbook of LHC Higgs Cross Sections: 4. Deciphering the Nature of the Higgs Sector". In: (2016). DOI: 10.23731/CYRM-2017-002. arXiv: 1610.07922 [hep-ph].

[185] John M. Campbell et al. "NLO Higgs boson production plus one and two jets using the POWHEG BOX, MadGraph4 and MCFM". In: *JHEP* 07 (2012), p. 092. DOI: 10.1007/JHEP07(2012)092. arXiv: 1202.5475 [hep-ph].

[186] Gionata Luisoni et al. "$HW^{\pm}/HZ$ + 0 and 1 jet at NLO with the POWHEG BOX interfaced to GoSam and their merging within MiNLO". In: *JHEP* 10 (2013), p. 083. DOI: 10.1007/JHEP10(2013)083. arXiv: 1306.2542 [hep-ph].

[187] Richard D. Ball et al. "Parton distributions for the LHC run II". In: *JHEP* 04 (2015), p. 040. DOI: 10.1007/JHEP04(2015)040. arXiv: 1410.8849 [hep-ph].

[188] J. Pumplin et al. "New Generation of Parton Distributions with Uncertainties from Global QCD Analysis". In: *JHEP* 07 (2002), p. 012. DOI: 10.1088/1126-6708/2002/07/012. arXiv: hep-ph/0201195.

[189] Stefano Goria, Giampiero Passarino, and Dario Rosco. "The Higgs Boson Lineshape". In: *Nucl. Phys. B* 864 (2012), pp. 530–579. DOI: 10.1016/j.nuclphysb.2012.07.006. arXiv: 1112.5517 [hep-ph].

[190] Lisa Carloni and Torbjörn Sjöstrand. "Visible effects of invisible Hidden Valley radiation". In: *Journal of High Energy Physics* 2010.9 (2010). DOI: 10.1007/jhep09(2010)105. URL: https://doi.org/10.1007/JHEP09(2010)105.

[191] Kirill Melnikov and Frank Petriello. "Electroweak gauge boson production at hadron colliders through $\mathcal{O}(\alpha_s^2)$". In: *Phys. Rev. D* 74 (2006), p. 114017. DOI: 10.1103/PhysRevD.74.114017. arXiv: hep-ph/0609070.

[192] LHCTopWG. *NNLO+NNLL top-quark-pair cross sections*. 2015. URL: https://twiki.cern.ch/twiki/bin/view/LHCPhysics/TtbarNNLO.

[193] LHCTopWG. *NLO single-top channel cross sections*. 2017. URL: https://twiki.cern.ch/twiki/bin/view/LHCPhysics/SingleTopRefXsec.

[194] Enrico Bothmann et al. "Event generation with Sherpa 2.2". In: *SciPost Phys.* 7.3 (2019), p. 034. DOI: 10.21468/SciPostPhys.7.3.034. arXiv: 1905.09127 [hep-ph].

[195] Tanju Gleisberg and Stefan Höche. "Comix, a new matrix element generator". In: *JHEP* 12 (2008), p. 039. DOI: 10.1088/1126-6708/2008/12/039. arXiv: 0808.3674 [hep-ph].

[196] Fabio Cascioli, Philipp Maierhöfer, and Stefano Pozzorini. "Scattering Amplitudes with Open Loops". In: *Phys. Rev. Lett.* 108 (2012), p. 111601. DOI: 10.1103/PhysRevLett.108.111601. arXiv: 1111.5206 [hep-ph].

[197] Steffen Schumann and Frank Krauss. "A parton shower algorithm based on Catani–Seymour dipole factorisation". In: *JHEP* 03 (2008), p. 038. DOI: 10.1088/1126-6708/2008/03/038. arXiv: 0709.1027 [hep-ph].

[198] Stefan Höche et al. "QCD matrix elements + parton showers. The NLO case". In: *JHEP* 04 (2013), p. 027. DOI: 10.1007/JHEP04(2013)027. arXiv: 1207.5030 [hep-ph].

[199] Torbjörn Sjöstrand et al. "An introduction to PYTHIA 8.2". In: *Comput. Phys. Commun.* 191 (2015), p. 159. DOI: 10.1016/j.cpc.2015.01.024. arXiv: 1410.3012 [hep-ph].

[200] Leif Lönnblad and Stefan Prestel. "Matching tree-level matrix elements with interleaved showers". In: *JHEP* 2012.3 (2012). ISSN: 1029-8479. DOI: 10.1007/jhep03(2012)019. arXiv: 1109.4829v3 [hep-ex]. URL: http://dx.doi.org/10.1007/JHEP03(2012)019.

[201] Stefano Frixione. "Isolated photons in perturbative QCD". In: *Phys. Lett. B* 429 (1998), pp. 369–374. DOI: 10.1016/S0370-2693(98)00454-7. arXiv: hep-ph/9801442.

[202] Stefano Frixione et al. "Single-top hadroproduction in association with a $W$ boson". In: *JHEP* 07 (2008), p. 029. DOI: 10.1088/1126-6708/2008/07/029. arXiv: 0805.3067 [hep-ph].

[203] ATLAS Collaboration. *Vertex Reconstruction Performance of the ATLAS Detector at $\sqrt{s} =$ 13 TeV*. ATL-PHYS-PUB-2015-026. 2015. URL: https://cds.cern.ch/record/2037717.

[204] ATLAS Collaboration. "Electron and photon performance measurements with the ATLAS detector using the 2015–2017 LHC proton–proton collision data". In: *JINST* 14 (2019), P12006. DOI: 10.1088/1748-0221/14/12/P12006. arXiv: 1908.00005 [hep-ex].

[205] ATLAS Collaboration. "Muon reconstruction and identification efficiency in ATLAS using the full Run 2 $pp$ collision data set at $\sqrt{s} = 13\,\text{TeV}$". In: *Eur. Phys. J. C* 81 (2021), p. 578. DOI: 10.1140/epjc/s10052-021-09233-2. arXiv: 2012.00578 [hep-ex].

[206] Matteo Cacciari, Gavin P. Salam, and Gregory Soyez. "FastJet user manual". In: *Eur. Phys. J. C* 72 (2012), p. 1896. DOI: 10.1140/epjc/s10052-012-1896-2. arXiv: 1111.6097 [hep-ph].

[207] ATLAS Collaboration. "Jet reconstruction and performance using particle flow with the ATLAS Detector". In: *Eur. Phys. J. C* 77 (2017), p. 466. DOI: 10.1140/epjc/s10052-017-5031-2. arXiv: 1703.10485 [hep-ex].

[208] ATLAS Collaboration. "Jet energy scale and resolution measured in proton–proton collisions at $\sqrt{s} = 13\,\text{TeV}$ with the ATLAS detector". In: *Eur. Phys. J. C* 81 (2020), p. 689. DOI: 10.1140/epjc/s10052-021-09402-3. arXiv: 2007.02645 [hep-ex].

[209] ATLAS Collaboration. *Tagging and suppression of pileup jets with the ATLAS detector*. ATLAS-CONF-2014-018. 2014. URL: https://cds.cern.ch/record/1700870.

[210] ATLAS Collaboration. *Forward Jet Vertex Tagging: A new technique for the identification and rejection of forward pileup jets*. ATL-PHYS-PUB-2015-034. 2015. URL: https://cds.cern.ch/record/2042098.

[211] ATLAS Collaboration. *Forward jet vertex tagging using the particle flow algorithm*. ATL-PHYS-PUB-2019-026. 2019. URL: https://cds.cern.ch/record/2683100.

[212] ATLAS Collaboration. "Measurements of $b$-jet tagging efficiency with the ATLAS detector using $t\bar{t}$ events at $\sqrt{s} = 13\,\text{TeV}$". In: *JHEP* 08 (2018), p. 089. DOI: 10.1007/JHEP08(2018)089. arXiv: 1805.01845 [hep-ex].

[213] ATLAS Collaboration. "Performance of missing transverse momentum reconstruction with the ATLAS detector using proton–proton collisions at $\sqrt{s} = 13\,\text{TeV}$". In: *Eur. Phys. J. C* 78 (2018), p. 903. DOI: 10.1140/epjc/s10052-018-6288-9. arXiv: 1802.08168 [hep-ex].

[214] ATLAS Collaboration. *Object-based missing transverse momentum significance in the ATLAS Detector*. ATLAS-CONF-2018-038. 2018. URL: https://cds.cern.ch/record/2630948.

[215] ATLAS Collaboration. *Selection of jets produced in 13 TeV proton–proton collisions with the ATLAS detector*. ATLAS-CONF-2015-029. 2015. URL: https://cds.cern.ch/record/2037702.

[216] Tianqi Chen and Carlos Guestrin. "XGBoost: A Scalable Tree Boosting System". In: *CoRR* abs/1603.02754 (2016). DOI: 10.1145/2939672.2939785. arXiv: 1603.02754 [cs.LG]. URL: http://arxiv.org/abs/1603.02754.

[217] ATLAS Collaboration. *Luminosity determination in pp collisions at $\sqrt{s} = 13\,\text{TeV}$ using the ATLAS detector at the LHC*. ATLAS-CONF-2019-021. 2019. URL: https://cds.cern.ch/record/2677054.

[218] G. Avoni et al. "The new LUCID-2 detector for luminosity measurement and monitoring in ATLAS". In: *JINST* 13.07 (2018), P07017. DOI: 10.1088/1748-0221/13/07/P07017.

[219] ATLAS Collaboration. "Measurement of the photon identification efficiencies with the ATLAS detector using LHC Run 2 data collected in 2015 and 2016". In: *Eur. Phys. J. C* 79 (2019), p. 205. DOI: 10.1140/epjc/s10052-019-6650-6. arXiv: 1810.05087 [hep-ex].

[220] ATLAS Collaboration. *Tagging and suppression of pileup jets*. ATL-PHYS-PUB-2014-001. 2014. URL: https://cds.cern.ch/record/1643929.

[221] ATLAS Collaboration. *Optimisation and performance studies of the ATLAS b-tagging algorithms for the 2017-18 LHC run*. ATL-PHYS-PUB-2017-013. 2017. URL: https://cds.cern.ch/record/2273281.

[222] ATLAS Collaboration. *Deep Sets based Neural Networks for Impact Parameter Flavour Tagging in ATLAS*. ATL-PHYS-PUB-2020-014. 2020. URL: https://cds.cern.ch/record/2718948.

[223] M. Baak et al. "HistFitter software framework for statistical data analysis". In: *Eur. Phys. J.* C75 (2015), p. 153. DOI: 10.1140/epjc/s10052-015-3327-7. arXiv: 1410.1280 [hep-ex].

[224] A L Read. "Presentation of search results: the $CL_s$ technique". In: *J. Phys. G* 28.10 (2002), p. 2693. DOI: 10.1088/0954-3899/28/10/313.

[225] Glen Cowan et al. "Asymptotic formulae for likelihood-based tests of new physics". In: *Eur. Phys. J. C* 71 (2011), p. 1554. DOI: 10.1140/epjc/s10052-011-1554-0. arXiv: 1007.1727 [physics.data-an].

[226] Kyle Cranmer and Itay Yavin. "RECAST — extending the impact of existing analyses". In: *Journal of High Energy Physics* 2011.4 (2011). DOI: 10.1007/jhep04(2011)038. URL: https://doi.org/10.1007%2Fjhep04%282011%29038.

[227] ATLAS Collaboration. "Search for dark matter in association with an energetic photon in collisions at $\sqrt{s}$ = 13 TeV with the ATLAS detector". In: *JHEP* 02 (2021). DOI: 10.1007/JHEP02(2021)226. arXiv: 2011.05259 [hep-ex].

[228] Paolo Nason. "A new method for combining NLO QCD with shower Monte Carlo algorithms". In: *JHEP* 11 (2004), p. 040. DOI: 10.1088/1126-6708/2004/11/040. arXiv: hep-ph/0409146.

[229] Stefano Frixione, Paolo Nason, and Carlo Oleari. "Matching NLO QCD computations with parton shower simulations: the POWHEG method". In: *JHEP* 11 (2007), p. 070. DOI: 10.1088/1126-6708/2007/11/070. arXiv: 0709.2092 [hep-ph].

[230] Simone Alioli et al. "A general framework for implementing NLO calculations in shower Monte Carlo programs: the POWHEG BOX". In: *JHEP* 06 (2010), p. 043. DOI: 10.1007/JHEP06(2010)043. arXiv: 1002.2581 [hep-ph].

[231] Keith Hamilton et al. "NNLOPS simulation of Higgs boson production". In: *JHEP* 10 (2013), p. 222. DOI: 10.1007/JHEP10(2013)222. arXiv: 1309.0017 [hep-ph].

[232] Keith Hamilton, Paolo Nason, and Giulia Zanderighi. "Finite quark-mass effects in the NNLOPS POWHEG+MiNLO Higgs generator". In: *JHEP* 05 (2015), p. 140. DOI: 10.1007/JHEP05(2015)140. arXiv: 1501.04637 [hep-ph].

[233] Charalampos Anastasiou et al. "High precision determination of the gluon fusion Higgs boson cross-section at the LHC". In: *JHEP* 05 (2016), p. 058. DOI: 10.1007/JHEP05(2016)058. arXiv: 1602.00695 [hep-ph].

[234] Charalampos Anastasiou et al. "Higgs Boson Gluon-Fusion Production in QCD at Three Loops". In: *Phys. Rev. Lett.* 114 (2015), p. 212001. DOI: 10.1103/PhysRevLett.114.212001. arXiv: 1503.06056 [hep-ph].

[235] Falko Dulat, Achilleas Lazopoulos, and Bernhard Mistlberger. "iHixs 2 – Inclusive Higgs cross sections". In: *Comput. Phys. Commun.* 233 (2018), pp. 243–260. DOI: 10.1016/j.cpc.2018.06.025. arXiv: 1802.00827 [hep-ph].

[236] Robert V. Harlander and Kemal J. Ozeren. "Finite top mass effects for hadronic Higgs production at next-to-next-to-leading order". In: *JHEP* 11 (2009), p. 088. DOI: 10.1088/1126-6708/2009/11/088. arXiv: 0909.3420 [hep-ph].

[237] Robert V. Harlander and Kemal J. Ozeren. "Top mass effects in Higgs production at next-to-next-to-leading order QCD: Virtual corrections". In: *Phys. Lett. B* 679 (2009), pp. 467–472. DOI: 10.1016/j.physletb.2009.08.012. arXiv: 0907.2997 [hep-ph].

[238] Robert V. Harlander et al. "Higgs production in gluon fusion at next-to-next-to-leading order QCD for finite top mass". In: *Eur. Phys. J. C* 66 (2010), pp. 359–372. DOI: 10.1140/epjc/s10052-010-1258-x. arXiv: 0912.2104 [hep-ph].

[239] Alexey Pak, Mikhail Rogal, and Matthias Steinhauser. "Finite top quark mass effects in NNLO Higgs boson production at LHC". In: *JHEP* 02 (2010), p. 025. DOI: 10.1007/JHEP02(2010)025. arXiv: 0911.4662 [hep-ph].

[240] Stefano Actis et al. "NLO electroweak corrections to Higgs boson production at hadron colliders". In: *Phys. Lett. B* 670 (2008), pp. 12–17. DOI: 10.1016/j.physletb.2008.10.018. arXiv: 0809.1301 [hep-ph].

[241] Stefano Actis et al. "NNLO computational techniques: The cases $H \to \gamma\gamma$ and $H \to gg$". In: *Nucl. Phys. B* 811 (2009), pp. 182–273. DOI: 10.1016/j.nuclphysb.2008.11.024. arXiv: 0809.3667 [hep-ph].

[242] Marco Bonetti, Kirill Melnikov, and Lorenzo Tancredi. "Higher order corrections to mixed QCD-EW contributions to Higgs boson production in gluon fusion". In: *Phys. Rev. D* 97.5 (2018), p. 056017. DOI: 10.1103/PhysRevD.97.056017. arXiv: 1801.10403 [hep-ph].

[243] Jon Butterworth et al. "PDF4LHC recommendations for LHC Run II". In: *J. Phys. G* 43 (2016), p. 023001. DOI: 10.1088/0954-3899/43/2/023001. arXiv: 1510.03865 [hep-ph].

[244] Peter Skands, Stefano Carrazza, and Juan Rojo. "Tuning PYTHIA 8.1: the Monash 2013 Tune". In: *Eur. Phys. J. C* 74.8 (2014), p. 3024. DOI: 10.1140/epjc/s10052-014-3024-y. arXiv: 1404.5630 [hep-ph].

[245] Baptiste Cabouat and Torbjörn Sjöstrand. "Some dipole shower studies". In: *The European Physical Journal C* 78.3 (2018). ISSN: 1434-6052. DOI: 10.1140/epjc/s10052-018-5645-z. URL: http://dx.doi.org/10.1140/epjc/s10052-018-5645-z.

[246] D. de Florian et al. "Handbook of LHC Higgs Cross Sections: 4. Deciphering the Nature of the Higgs Sector". In: *CERN Yellow Reports* (2017). DOI: 10.48550/arXiv.1610.07922. arXiv: 1610.07922 [hep-ph]. URL: https://arxiv.org/abs/1610.07922.

[247] Enrico Bothmann, Marek Schönherr, and Steffen Schumann. "Reweighting QCD matrix-element and parton-shower calculations". In: *Eur. Phys. J. C* 76.11 (2016), p. 590. DOI: 10.1140/epjc/s10052-016-4430-0. arXiv: 1606.08753 [hep-ph].

[248] ATLAS Collaboration. *ATLAS Pythia 8 tunes to 7 TeV data*. ATL-PHYS-PUB-2014-021. 2014. URL: https://cds.cern.ch/record/1966419.

[249] Kyle Cranmer et al. "HistFactory: A tool for creating statistical models for use with RooFit and RooStats". In: (2012).

[250] Glen Cowan et al. "Asymptotic formulae for likelihood-based tests of new physics". In: *Eur. Phys. J.* C71 (2011). [Erratum: Eur. Phys. J.C73,2501(2013)], p. 1554. DOI: 10.1140/epjc/s10052-011-1554-0,10.1140/epjc/s10052-013-2501-z. arXiv: 1007.1727 [physics.data-an].

[251] *Technical Design Report: A High-Granularity Timing Detector for the ATLAS Phase-II Upgrade*. Tech. rep. CERN-LHCC-2020-007. ATLAS-TDR-031. Geneva: CERN, 2020. URL: https://cds.cern.ch/record/2719855.

[252] "High-Luminosity Large Hadron Collider (HL-LHC) : Preliminary Design Report". In: (Dec. 2015). Ed. by G Apollinari et al. DOI: 10.5170/CERN-2015-005.

[253] P. Azzi et al. "Report from Working Group 1: Standard Model Physics at the HL-LHC and HE-LHC". In: *CERN Yellow Rep. Monogr.* 7 (2019). Ed. by Andrea Dainese et al., pp. 1–220. DOI: 10.23731/CYRM-2019-007.1. arXiv: 1902.04070 [hep-ph].

[254] M. Cepeda et al. "Report from Working Group 2: Higgs Physics at the HL-LHC and HE-LHC". In: *CERN Yellow Rep. Monogr.* 7 (2019). Ed. by Andrea Dainese et al., pp. 221–584. DOI: 10.23731/CYRM-2019-007.221. arXiv: 1902.00134 [hep-ph].

[255] Xabier Cid Vidal et al. "Report from Working Group 3: Beyond the Standard Model physics at the HL-LHC and HE-LHC". In: *CERN Yellow Rep. Monogr.* 7 (2019). Ed. by Andrea Dainese et al., pp. 585–865. DOI: 10.23731/CYRM-2019-007.585. arXiv: 1812.07831 [hep-ph].

[256] ATLAS Collaboration. *Technical Design Report for the ATLAS Inner Tracker Pixel Detector*. Tech. rep. CERN-LHCC-2017-021. Geneva: CERN, 2018. URL: https://cds.cern.ch/record/2285585.

[257] ATLAS Collaboration. *Technical Design Report for the ATLAS Inner Tracker Strip Detector*. Tech. rep. CERN-LHCC-2017-005 ; ATLAS-TDR-025. CERN, 2017. URL: https://cds.cern.ch/record/2257755.

[258] N.J. Buchanan et al. "Design and implementation of the Front End Board for the readout of the ATLAS liquid argon calorimeters". In: *JINST* 3 (2008), P03004. DOI: 10.1088/1748-0221/3/03/P03004.

[259] T. Zakareishvili. "Upgrade of the ATLAS Hadronic Tile Calorimeter for the High Luminosity LHC". In: *JINST* 15.09 (2020), p. C09003. DOI: 10.1088/1748-0221/15/09/C09003.

[260] ATLAS Collaboration. *Technical Proposal: A High-Granularity Timing Detector for the ATLAS Phase-II Upgrade*. Tech. rep. CERN-LHCC-2018-023. Geneva: CERN, 2018. URL: https://cds.cern.ch/record/2623663.

[261] Frederick Bordry et al. *Machine Parameters and Projected Luminosity Performance of Proposed Future Colliders at CERN*. Tech. rep. CERN-ACC-2018-0037. Geneva: CERN, 2018. URL: https://cds.cern.ch/record/2645151.

[262] Lucio Rossi and Oliver Sim Brüning. "High Luminosity Large Hadron Collider : A description for the European Strategy Preparatory Group". In: 2012.

[263] Apollinari G. et al. *High-Luminosity Large Hadron Collider (HL-LHC): Technical Design Report V. 0.1*. CERN Yellow Reports: Monographs. Geneva: CERN, 2017. DOI: 10.23731/CYRM-2017-004. URL: http://cds.cern.ch/record/2284929.

[264] *Technical Proposal: A High-Granularity Timing Detector for the ATLAS Phase-II Upgrade*. Tech. rep. Geneva: CERN, 2018. DOI: 10.17181/CERN.CIUJ.KS4H. URL: https://cds.cern.ch/record/2623663.

[265] ATLAS Collaboration. "The ATLAS Experiment at the CERN Large Hadron Collider". In: *JINST* 3 (2008), S08003. DOI: 10.1088/1748-0221/3/08/S08003.

[266] G. Pellegrini et al. "Technology developments and first measurements of Low Gain Avalanche Detectors (LGAD) for high energy physics applications". In: *Nucl. Instrum. Meth. A* 765 (2014). Ed. by Yoshinobu Unno et al., pp. 12–16. DOI: 10.1016/j.nima.2014.06.008.

[267] C. de La Taille et al. "A 20 pico-second time resolutions ASIC for the ATLAS High Granularity Timing Detector (HGTD)". In: *Topical Workshop on Electronics for Particle Physics, TWEPP-17, Santa Cruz, California*. 2018. URL: https://pos.sissa.it/313/006.

[268] C. Agapopoulou et al. "Performance of a Front End prototype ASIC for picosecond precision time measurements with LGAD sensors". In: *Journal of Instrumentation* 15.07 (2020), P07007–P07007. DOI: 10.1088/1748-0221/15/07/p07007. URL: https://doi.org/10.1088%2F1748-0221%2F15%2F07%2Fp07007.

[269] A. Gerbershagen and B. Rae. "CERN SPS North Area". In: (2019). URL: http://sba.web.cern.ch/sba/BeamsAndAreas/H6/H6_presentation.html.

[270] R. Diener et al. "The DESY II test beam facility". In: *Nucl. Instr. Meth. A* 922 (2019), pp. 265–286.

[271] C. Allaire et al. "Beam test measurements of Low Gain Avalanche Detector single pads and arrays for the ATLAS High Granularity Timing Detector". In: *Journal of Instrumentation* 13.06 (2018), P06017–P06017. DOI: 10.1088/1748-0221/13/06/p06017. URL: https://doi.org/10.1088%2F1748-0221%2F13%2F06%2Fp06017.

[272] J. Lange et al. "Gain and time resolution of 45 µm thin Low Gain Avalanche Detectors before and after irradiation up to a fluence of $10^{15}$ $n_{eq}/cm^2$". In: *JINST* 12 (2017), pp. 265–286. DOI: P05003/arXiv.1703.09004. arXiv: 1703.09004.

[273] M. Carulla et al. "First 50 $\mu$m thick LGAD fabrication at CNM". In: (2016). URL: https://agenda.infn.it/getFile.py/access?contribId=20&sessionId=8&resId=0&materialId=slides&confId=11109.

[274] *RD50 - Radiation hard semiconductor devices for very high luminosity colliders*. URL: http://rd50.web.cern.ch/rd50/.

[275] Hidalgo. S et al. "CNM activities on LGADs for ATLAS/CMS Timing Layers". In: (2018). URL: https://indico.cern.ch/event/719814/contributions/3022492/.

[276] G. Kramberger et al. "Radiation Hardness of Thin Low Gain Avalanche Detectors". In: (2017). arXiv: 1711.06003. URL: http://rd50.web.cern.ch/rd50/.

[277] L. Castillo García. "A High-Granularity Timing Detector for the Phase-II upgrade of the ATLAS Calorimeter system". In: *Journal of Instrumentation* 15.09 (2020), p. C09047. DOI: 10.1088/1748-0221/15/09/C09047. URL: https://dx.doi.org/10.1088/1748-0221/15/09/C09047.

[278] Hendrik Jansen et al. "Performance of the EUDET-type beam telescopes". In: *EPJ Techniques and Instrumentation* 3.1 (2016). DOI: 10.1140/epjti/s40485-016-0033-2. URL: https://doi.org/10.1140%2Fepjti%2Fs40485-016-0033-2.

[279] Olga Vladlena Posopkina, Vagelis Gkougkousis, and Lucia Castillo Garcia. "Design and integration of a SiPM based Timing Reference for ATLAS HGTD test beam". In: (2018). URL: https://cds.cern.ch/record/2635107.

[280] Z. Galloway et al. "Properties of HPK UFSD after neutron irradiation up to 6e15 n/cm2". In: (2017). arXiv: 1707.04961 [physics.ins-det].

[281] T Isidori et al. "Performance of a low gain avalanche detector in a medical linac and characterisation of the beam profile". In: *Physics in Medicine and Biology* 66.13 (2021), p. 135002. DOI: 10.1088/1361-6560/ac0587. URL: https://dx.doi.org/10.1088/1361-6560/ac058.

[282] N. Cartiglia. *Beam test studies of the LGAD sensors at FNAL*. URL: https://indico.cern.ch/event/637212/contributions/2608659/.

[283] SensL TM. "C-Series datacheet: Low Noise, Blue-Sensitive Silicon Photomultipliers". In: (). URL: https://www.mouser.com/datasheet/2/308/DS-MicroCseries-1489568.pdf.

[284] D. Renker. "Geiger-mode avalanche photodiodes, history, properties and problems". In: *Nuclear Instruments and Methods in Physics Research Section A: Accelerators, Spectrometers, Detectors and Associated Equipment* 567.1 (2006). Proceedings of the 4th International Conference on New Developments in Photodetection, pp. 48–56. ISSN: 0168-9002. DOI: https://doi.org/10.1016/j.nima.2006.05.060. URL: https://www.sciencedirect.com/science/article/pii/S0168900206008680.

[285] "SMT/MLP SMA and SMTPA Board Reference Designs". In: (). URL: https://www.onsemi.com/pub/Collateral/AND9809-D.PDF.

[286] "Gali-52+ Sourface Mount Monolithic Amplifier Datasheet". In: (). URL: https://www.minicircuits.com/pdfs/GALI-52+.pdf.

[287] I. Rubinskiy U. Koetz. *User Manual: ATLAS FE-I4A Pixel Module as a Trigger Plane for the Beam Telescope*. URL: https://telescopes.desy.de/images/0/08/131014_koetz-rubinsky_FEI4_as_trigger_plane.pdf.

[288] D. Cussans. *Description of the JRA1 Trigger Logic Unit (TLU), v0.2c, Tech. Rep*. 2009. URL: http://www.eudet.org/e26/e28/e42441/e57298/EUDET-MEMO-2009-04.pdf.

[289] P. Ahlburg et al. "EUDAQ—a data acquisition software framework for common beam telescopes". In: *Journal of Instrumentation* 15.01 (2020), P01038. DOI: 10.1088/1748-0221/15/01/P01038. URL: https://dx.doi.org/10.1088/1748-0221/15/01/P01038.

[290] M. Backhaus et al. "Development of a versatile and modular test system for ATLAS hybrid pixel detectors". In: *Nuclear Instruments and Methods in Physics Research Section A: Accelerators, Spectrometers, Detectors and Associated Equipment* 650.1 (2011). International Workshop on Semiconductor Pixel Detectors for Particles and Imaging 2010, pp. 37–40. ISSN: 0168-9002. DOI: https://doi.org/10.1016/j.nima.2010.12.087. URL: https://www.sciencedirect.com/science/article/pii/S0168900210028676.

[291] *LGADUtils: A C++ based framework for waveform analysis*. URL: https://gitlab.cern.ch/egkougko/lgadutils.

[292] Igor Rubinskiy and Mimosa. "Offline track reconstruction and DUT analysis software". In: 2011.

[293] *EUTelescope: A Generic Pixel Telescope Data Analysis Framework*. URL: https://eutelescope.github.io.

[294] Lucía Castillo García et al. "Characterization of Irradiated Boron, Carbon-Enriched and Gallium Si-on-Si Wafer Low Gain Avalanche Detectors". In: *Instruments* 6.1 (2021), p. 2. DOI: 10.3390/instruments6010002.

[295] Alejandro Alonso, Oxana Smirnova, and Akesson Torsten. "Transition Radiation Tracker calibration, searches beyond the Standard Model and multiparticle correlations in ATLAS". Presented 20 May 2012. 2012. URL: https://cds.cern.ch/record/1452211.

[296] *ATLAS inner detector: Technical Design Report, 1*. Technical Design Report ATLAS. Geneva: CERN, 1997. URL: https://cds.cern.ch/record/331063.

[297] Andrew Buckley et al. *Implementation of the ATLAS Run 2 event data model*. Tech. rep. ATL-SOFT-PROC-2015-003. 7. Geneva: CERN, 2015. URL: https://cds.cern.ch/record/2014150.

[298] S SNYDER et al. "The Run 2 ATLAS Analysis Event Data Model". In: (2014). URL: https://cds.cern.ch/record/1752598.

[299] Andreas Salzburger, Dietmar Kuh, and Markus Elsing. "Track Simulation and Reconstruction in the ATLAS experiment". 2008. URL: https://cds.cern.ch/record/2224514.

[300] PhilippeCalfayan. *TrtxAOD*. https://twiki.cern.ch/twiki/bin/viewauth/Atlas/TrtxAOD. [Online; accessed 2018-11-06]. 2018.

[301] EleniSkorda. *TRTCalibrationNtupleDoc*. https://twiki.cern.ch/twiki/bin/viewauth/Atlas/TRTCalibrationNtupleDoc. [Online; accessed 2018-11-27]. 2018.